2014

# Studying Short-Period Comets and Long-Period Comets Detected by WISE/NEOWISE

Emily Kramer
*University of Central Florida*

# Studying Short-Period Comets and Long-Period Comets Detected by WISE/NEOWISE

by

Emily Anne Kramer
B.S. Massachusetts Institute of Technology, 2008

A dissertation submitted in partial fulfillment of the requirements
for the degree of Doctor of Philosophy
in the Department of Physics
in the College of Sciences
at the University of Central Florida
Orlando, Florida

Fall Term
2014

Major Professor: Yanga R. Fernández

# ABSTRACT

The Wide-field Infrared Survey Explorer (WISE) mission surveyed the sky in four infrared wavelength bands (3.4, 4.6, 12 and 22 $\mu$m) between January 2010 and February 2011. During the mission, WISE serendipitously observed 160 comets, including 21 newly discovered objects. About 89 of the comets observed by WISE displayed a significant dust tail in the 12 and 22 $\mu$m (thermal emission) bands, showing a wide range of activity levels and dust morphology. Since the observed objects are a mix of both long-period comets (LPCs) and short-period comets (SPCs), differences in their activity can be used to better understand the thermal evolution that each of these populations has undergone. For the comets that displayed a significant dust tail, we have estimated the sizes and ages of the particles using dynamical models based on the Finson-Probstein method [Finson and Probstein, 1968]. For a selection of 40 comets, we have then compared these models to the data using a novel tail-fitting method that allows the best-fit model to be chosen analytically rather than subjectively. For comets that were observed multiple times by WISE, the particle properties were estimated separately, and then compared. We find that the dust tails of both LPCs and SPCs are primarily comprised of $\sim$mm-cm sized particles, which were the result of emission that occurred several months to several years prior to the observations. The LPCs nearly

all have strong emission close to the comet's perihelion distance, and the SPCs mostly have strong emission close to perihelion, but some have strong emission well before perihelion.

To my parents, who always encouraged my passion for science.

# ACKNOWLEDGMENTS

I would like to first and foremost thank my advisor, Yan Fernández, for his excellent advice and guidance throughout my graduate career. Thank you to the other members of my committee (Joshua Colwell, Viatcheslav Kokoouline, Richard Klemm, and Casey Lisse) for their insights and helpful ideas as I developed this project. In particular, than you to Casey for the models which inspired the code used in this project.

Thank you to Jim Elliot of MIT (RIP) for giving me the opportunity, when I was only a rising sophomore undergraduate, to work on a top-notch astronomical project, thereby hooking me into the field of planetary sciences, and thank you to Susan Benecchi (née Kern) for introducing me to him. Thank you to Elisabeth Adams for helping me to learn how to "massage the data", and to Amanda Gulbis for helping me to learn the finer points of ground-based observational astronomy. Thank you to Rick Binzel for encouraging me to go to UCF for graduate school.

Thank you to Jean-Luc Margot for being my REU advisor and introducing me to many aspects of small body studies which I continue to use to this day. Thank you to Dave Schleicher for getting me hooked on comets when I was still an undergraduate. They've continued to "activate" my interest ever since!

Thank you to the NEOWISE team (Gerbs, Amy, Rach, Joe, Tommy, Carrie and Sonnett) for providing me access to this incredible data set, and for helping me to understand some of its nuances.

A big thank you to Martin Michalak for his emotional support and mathematical ideas throughout my graduate career.

Thank you to Nate Lust for help with python and mac issues over my entire graduate career, Charles for providing me with an air mattress on which to nap while writing this dissertation, and all the other UCF planetary graduate students for their moral support and scientific ideas. Thank you to Sabine for providing me with coffee, company, and figs during the final stages of writing. Thank you to Sondy and Steve for last-minute BibTex help.

Thank you to my siblings Abby and Jeff for always being there for me, and taking care of things back home while I went to graduate school.

I would also like to thank Daniel Gallagher for publishing his LaTeX template online as a Git repository at: `https://bitbucket.org/dgallagher/ucf-thesis-latex-template`.

Finally, I would like to thank my sponsoring organizations. The research here was funded by a NASA Earth and Space Sciences Fellowship. The research here was also funded in part by a JPL Graduate Student Fellowship and NASA's Planetary Astronomy program. This publication makes use of data products from (1) WISE, which is a joint project of UCLA and JPL/Caltech, funded by NASA; and (2) NEOWISE, which is a project of JPL/Caltech, funded by the Planetary Science Division of NASA. This research has also made use of NASA's Astrophysics Data System.

# TABLE OF CONTENTS

# LIST OF FIGURES

# LIST OF TABLES

# CHAPTER 1
# INTRODUCTION

## 1.1 Why study comets?

A central goal of astronomy is to understand the formation of the Earth and the Solar System. Since comets contain primordial materials from the protoplanetary disk, they are excellent resources for understanding the early Solar System, as well as other planetary systems. However, comets still have undergone some alterations via different heating processes, such as impacts and insolation [Prialnik and Bar-Nun, 1987], after their relatively recent entry into the inner Solar System. These processes can cause significant structural changes in the comet from its original form of conglomerated icy planetesimals on timescales which, for short-period comets, are shorter than the $\sim 10^4$-$10^5$ year dynamical lifetime of the comets [Lisse, 2002, Levison and Duncan, 1994]. In order to understand what comets were like when they formed, we therefore must understand how they have evolved over time.

We will now investigate two methods of classifying comets: based on their orbital dynamics, and based on the composition and chemistry of the volatiles and dust.

## 1.2 Orbital dynamical taxonomy

Dynamical taxonomy is the classification of comets based on the orbital elements which describe the shape and position of their orbit. Historically, comets were grouped into two broad categories, with short-period comets (SPCs) defined as having an orbital period ($P$) of <200 years, and long-period comets (LPCs) having $P$ >200 years. The SPCs were further split into Jupiter-family (JFC) ($P$ <20 years) and Halley-type (HTC) comets (20 years $\leq P \leq$ 200 years). However, numerical integrations suggest that this definition is too loose, since a comet may evolve in and out of the traditional JFC definition many times over the course of its dynamical lifetime [Levison and Duncan, 1994, Duncan et al., 2004]. A more precise way to categorize comets is to use the Tisserand parameter, $T$, which is approximately conserved in the 3-body problem and thus does not vary substantially over a comet's lifetime once it is in the inner Solar System [Levison and Duncan, 1994]. The Tisserand parameter with respect to the Sun-Jupiter-comet 3-body problem is defined as:

$$T = a_J/a + 2\sqrt{(1-e^2)a/a_J}cos(i) \tag{1.1}$$

where $a_J$ is the semi-major axis of Jupiter, and $a$, $e$, and $i$ are the semi-major axis, eccentricity and inclination, respectively, of the object. The Tisserand parameter is calculated with respect to Jupiter since Jupiter contains most of the angular momentum in the Solar System and thus controls the dynamical orbital evolution of inner Solar System comets. Comets with $T$ <2 are defined as nearly isotropic comets and primarily originate from the Oort cloud,

while comets with $T > 2$ are defined as ecliptic comets since they mostly have low inclinations [Levison, 1996]. The ecliptic comets can be parsed into three groups. Comets with $2 < T < 3$ have dynamics that are dominated by interactions with Jupiter, and are as such named the Jupiter-family comets. Centaurs have $T > 3$ and $a > a_J$, meaning that their orbit is exterior that of Jupiter, and Encke-type comets have $T > 3$ and $a < a_J$. The Tisserand parameter is thus a useful tool for understanding how comets can be grouped within the broad dynamical classes of LPCs and SPCs. In this dissertation we are concerned with the behavior of the comets in a broad sense, thus, for the remainder of this work, we will use the *du jour* comet taxonomy, i.e., LPCs and SPCs.

Up until about 2005, dynamical models of the early solar system (e.g. [Duncan et al., 2004]) suggested that the LPCs formed in the giant planet region ($5 < r_h < 30$ AU) and were subsequently scattered out to the Oort Cloud, and JFCs were thought to originate in the Kuiper Belt ($r_h > 30$ AU) [Mumma and Charnley, 2011]. This would suggest that, since the two main populations had distinct source regions at different heliocentric distances, LPCs and SPCs should have distinctly different volatile and refractory makeup [Mumma et al., 1993, Boss, 1998].

However, more recent models which include migration of the giant planets (i.e. the "Nice" model, [Gomes et al., 2005, Morbidelli et al., 2005] and the "Grand Tack" model, [Walsh et al., 2012]) suggest that there may have been significant radial mixing in the protoplanetary disk. The Grand Tack model [Walsh et al., 2012] suggests that, during the final million years of the primordial gaseous solar nebula (approximately 5-10 Myr after calcium aluminum

inclusion (CAI) formation), Jupiter and Saturn migrated inward to about 1.5 AU, truncating the protoplanetary disk in the terrestrial planet forming region before migrating outwards again. This would also re-populate the asteroid belt with a mix of planetesimals from near Jupiter's orbit and also from beyond the orbits of the giant planets. This, then, sets up the initial conditions necessary for the Nice model to begin 400-600 Myr later, with planetesimals from the outer region of the disk ($15 < r_h < 35$ AU) being scattered and ejected to form the current Kuiper belt structure and a minority fraction of the Oort cloud, and planetesimals in the giant planet region ($5 < r_h < 15$ AU) being ejected to the Oort cloud [Mumma and Charnley, 2011]. This would mean that LPCs and SPCs had overlapping source regions in the protoplanetary disk, and, thus, may have similar unaltered volatiles and refractory materials. Moreover, Levison et al. [2010] recently found that in order to explain the number of Oort cloud comets currently in our solar system, up to 90% of these objects may have originated from the protoplanetary disks of other stars in the Sun's birth cluster. Modern models have taken us beyond the historical view of the solar system as a slowly evolving, spinning in place structure.

### 1.3 Using volatiles to understand the early Solar System

In addition to the dynamical taxonomy described above, we can also classify comets based on the composition and chemistry of their volatiles and dust. This classification can help us to better understand the formation of the dynamical reservoirs of the current comet

population by using observational data to examine whether different dynamical populations have different physical characteristics. The comae of comets are comprised of volatiles which can be categorized as "primary" or "parent", meaning that they were stored in the nuclear ice in their current form, or "product" or "daughter", meaning that they are the result of some chemical or physical process [Mumma and Charnley, 2011]. Compositional surveys have been carried out in optical, radio, and infrared wavelengths, each of which measures a different aspect of cometary chemistry.

The compositional surveys which are most complete are based on optical observations of product species, with ∼2/3 of the 246 (as of 2011) SPCs having data, and ∼60 unnumbered LPCs having data [A'Hearn et al., 1995, Schleicher and Bair, 2014]. A'Hearn et al. [1995] used narrowband optical photometry to observe 5 product species (OH, CN, $C_2$, $C_3$, and NH) in 85 comets, 41 of which had sufficiently robust data to classify. They found that comets could be placed into two groups based on composition: those that were carbon-chain ($C_2$ and $C_3$) normal, and those that were carbon chain depleted. While carbon-chain depleted group was primarily comprised of JFCs, not all JFCs were carbon-chain depleted. Additionally, their results suggest that water and other ices are mixed as individual pure chunks at the grain level (as opposed to being heterogeneous ices mixed at the molecular level), which has significant implications for the formation mechanism for comets as a whole, and that cometary activity seems to depend most strongly on the perihelion distance of the comet's orbit.

The optical A'Hearn et al. [1995] results have recently been built upon by Schleicher and Bair [2014]. The previous data have been re-analyzed in a uniform manner, and more comets have been added to the database, which now stands at 167 total, with 101 comets having sufficiently robust measurements to classify. Using cluster and principle component analysis, Schelicher and Bair have found 7 compositional classes, some of which are subgroups of A'Hearn et al.'s original carbon-chain-depleted class. As with the A'Hearn et al.'s study, these results suggest that carbon-chain depletion is primordial in nature and not due to thermal evolution, due to the fact that there is no correlation between depletion and dynamical age of the comets, and that nearly all of the carbon-chain depleted comets are JFCs, but not all JFCs are carbon-chain depleted. An intriguing additional result is the discovery of a group of comets which are depleted in ammonia ($NH_3$) but not in carbon-chain molecules. Since only 5 comets fall into this category, it is still too soon to tell whether this depletion is primordial or evolutionary.

Whereas optical observations have been used to study product volatiles, radio observations have been used to categorize comets based on the primary species present in their comae. Radio surveys are advantageous since they allow large molecules to be easily detected, and high spectral resolution to be achieved. However, only one species can be measured at a time, and measuring different species requires using a different instrument or even a different observatory. Thus far, 10 primary volatile species, 3 product species, and 1 (likely) coma product have been measured in >35 comets [Biver et al., 2002, Crovisier et al., 2009]. No correlation has been found between composition and dynamical class. However, there are

two caveats to take into consideration: (1) HCN is taken as a proxy for water production, but its abundance relative to water varies wildly [Mumma and Charnley, 2011]; (2) since the relative abundances of different molecules may vary as a function of heliocentric distance [Biver et al., 2011], comparing production rates of different molecules that were not measured simultaneously may not be valid.

Infrared spectral surveys of primary cometary volatiles are advantageous since they can measure several species simultaneously, including water or OH. Using data from a number of ground-based studies to look at the abundance ratios of several primary volatile species, Mumma and Charnley [2011] (and references therein) find the comets under consideration can be categorized into three compositional groups: organics-normal, organics-enriched, and organics-depleted. There does not appear to be any correlation between compositional group and dynamical class [Mumma et al., 2011]. Space-based infrared measurements of cometary volatiles can be particularly useful, since the presence of $CO_2$ in the Earth's atmosphere prevents this important molecule from being measured reliably using ground-based observatories [Ootsubo et al., 2012]. Using the 2.5 to 5 $\mu$m spectrometer on the *AKARI* spacecraft, Ootsubo et al. [2012] measured the abundances of CO, $CO_2$, and $H_2O$ in 18 comets, creating the largest uniform set of $CO_2/H_2O$ production rate ratios to date. They found that within 2.5 AU, $CO_2/H_2O$ production rate ratios range from ∼5-25% for both JFCs and Oort Cloud (OC) comets, rising substantially outside of 2.5 AU as water production rates drop off. A survey by Reach et al. [2013] used the 3.6 and 4.5 $\mu$m channels on the Infrared Array Camera (IRAC) on *Spitzer* to measure CO and $CO_2$ production rates on 23 comets. Using some

assumptions about water production rates, they found that the comets could be placed into two groups: $CO_2$-rich, and $CO_2$-poor. Their results are consistent with those of A'Hearn et al. [1995], with many of the $CO_2$-rich comets in the Reach et al. [2013] study being categorized as carbon-chain normal by A'Hearn et al. [1995]. Reach et al. [2013] also found that all of the comets studied by Ootsubo et al. [2012] would be classified as $CO_2$-rich.

### 1.4 Cometary activity drivers and thermal regimes

We have seen that comets have a wide variety of volatiles present in their nuclei and comae. We will now briefly discuss the effect of thermal evolution on those volatiles. With each perihelion passage through the inner Solar System, a comet undergoes thermal evolution when it receives a significant burden of insolation containing orders of magnitude more energy than during the rest of its orbit. The heat from the Sun warms up the comet, causing volatiles to be released, and intermixed dust particles to be carried along with the escaping gas. There are three primary drivers of cometary volatile activity driven by insolation: $H_2O$ sublimation, $CO/CO_2$ sublimation and the amorphous to crystalline (a-to-c) water ice transition. The a-to-c transition does not produce any volatiles directly, and thus will not be discussed further here. Water is the most abundant volatile [Festou et al., 2004] but CO and $CO_2$ are significant, $\sim$10% as abundant on average. Since each of the three drivers becomes important at different temperatures and heliocentric distances [Meech and Svoren, 2004], cometary activity in different thermal regimes is dominated by different volatiles. Notably,

$H_2O$ ice sublimation becomes strong within $\sim$ 3 AU, $CO_2$ ice sublimation becomes strong within $\sim$13 AU, and CO ice sublimation becomes strong within $\sim$120 AU. Note that the distances listed are not "turn on" points. That is, sublimation of these ices will occur outside of these heliocentric distances, just to a much lesser degree than within them.

As previously mentioned, Ootsubo et al. [2012] found evidence that $CO_2$ is a significant activity driver for both JF and OC comets. Thus, we can expect that cometary activity should be significant even outside the region where water-ice sublimation is strong. While it would be ideal to measure the volatiles directly, this is difficult and time consuming to do, and thus we will use cometary dust activity as a proxy for activity driver, as described below.

One way to study this phenomenon would be to monitor a single comet over a large fraction of its orbit, taking data as it moved through different thermal regimes. This type of observation has been carried out for a few comets, including C/1995 O1 (Hale-Bopp) [Kramer et al., 2014, Szabó et al., 2008, 2011] and 1P/Halley [Hainaut et al., 1995, 2004]. Although this type of observation gives us a good insight into the physical properties of an individual comet, it does not do a good job of characterizing the properties of the comet population as a whole. Additionally, it is time-intensive to study an individual comet for several years, and can only be done rarely. An alternative method, which is used in this investigation, is to study a large number of comets at a wide range of heliocentric distances. Vagaries of individual comets are thus de-emphasized, letting us search for trends and correlations of

cometary behavior and dust properties with other orbital and photometric properties in a way that has not been possible before.

## 1.5 Cometary dust as an indicator of activity driver

Cometary dust tails are a useful proxy for understanding the volatiles in cometary nuclei. As seen in the recent flyby of comet 103P/Hartley 2, $H_2O$ sublimation can cause coma morphology and dust emission that are significantly different from that caused by $CO_2$ sublimation. The particles carried out by $CO_2$ are large and slow moving, while the particles carried out by $H_2O$ are small and faster moving [A'Hearn et al., 2011]. This suggests that if the activity on the comet is driven by something other than water, i.e. something that is not the main volatile constituent, the dust grains that are dragged off the nucleus by that volatile will have different properties. This may be due to the fact that if $CO_2$ is causing the grains to be lifted off the nucleus, the grains still contain abundant $H_2O$ ice in solid form, keeping the grains bound and large. The grains then proceed to sublimate their $H_2O$ ice and fragment into smaller grains, releasing substantial coma gas as they do so. Thus, if we can remotely characterize the size and speed of cometary materials, we can potentially determine which volatile is driving the activity.

## 1.6 Other infrared surveys of cometary dust

Several previous studies have used infrared observations of comets to characterize the dust in the tails/trails, including IRAS [Matson, 1986, Sykes et al., 1986, Sykes and Walker, 1992], COBE [Lisse et al., 1998], MSX [Lisse et al., 2004, Kraemer et al., 2005], ISO [Müller et al., 2005], Spitzer [Reach et al., 2007], Akari [Ootsubo et al., 2012], and SEPPCoN (with Spitzer) [Kelley et al., 2013]. The results from Akari were already mentioned in Section 1.3, and the results from the other surveys will be discussed here.

Comets have been studied by a number of other space-based infrared telescopes, both all-sky surveys and targeted missions, beginning with the Infrared Astronomical Satellite (IRAS) in 1983. IRAS observed 24 comets during its all-sky survey, and also heralded the beginning of the study of comet dust trails, with the discovery of 8 trails consisting of large ($>\sim$cm-sized) particles [Matson, 1986, Sykes et al., 1986, Sykes and Walker, 1992].

COBE/DIRBE [Lisse et al., 1998] all-sky survey found 4 comets, 3 LPC and 1 SPC. Each comet was imaged repeatedly, thereby giving some insight into the long-term behavior of cometary activity. Two of the LPCs (C/OLR and C/Austin) were found to have only large, dark grains, one of the LPCs (C/Levy) was found to have small grains, and the SPC (73P/S-W 3) was only detected as a point source, but was an unexpected find, since it is optically faint. The results of this work were integrated with a literature review by [Lisse, 2002] to conclude that, in general, LPCs emit dust which is small and high albedo, while SPCs emit dust which is large and dark (low albedo). The result is consistent within their

original sample of 9 comets and the consistency is maintained when extended to the literature review of an additional 46 comets. They also found that all comets with a perihelion distance >5 AU have small particle dominated emission.

In addition to all-sky surveys, three space-based infrared telescopes have done pointed observations of comets. The Infrared Space Observatory (ISO) observed 20 comets, including both spectroscopy and imaging, allowing for both dust and gas to be studied [Müller et al., 2005]. Of those 20 comets, 4 were imaged using ISOCAM in order to study the morphology of the dust [Colangeli et al., 1998, Epifani et al., 2001, Lisse et al., 2004]. The Midcourse Space Experiment (MSX) observed 8 comets in four infrared wavelength bands with a relatively small effective beam size and highly robust calibrations [Lisse et al., 2004, Kraemer et al., 2005]. Of those 8 comets, 5 showed extended dust emission. Interestingly, C/1996 B2 (Hyakutake) was shown to have both a tail of small particles and a trail-like structure likely comprised of large particles [Kraemer et al., 2005].

Using the *Spitzer* Space Telescope, Reach et al. [2007] observed 34 Jupiter-Family Comets with the 24 $\mu$m MIPS camera. They found that comets with a smaller perihelion distance($q$) had more massive dust trails than those with a larger $q$. The authors suggest that while this may seem inconsistent with visible light surveys (e.g., [A'Hearn et al., 1995]) which show that comets with a smaller $q$ have a lower dust-to-gas ratio, the effect could be due to the evolution of the size of the particles ejected from the comets due to long-term thermal evolution from spending more time in the inner Solar System. This result agrees with the result found by Lisse [2002]. While not discussed in Reach et al. [2007], this would suggest

that LPC dust tails should be composed of smaller particles, since these objects have spent significantly less time in the inner solar system.

The Survey of the Ensemble Physical Properties of Cometary Nuclei (SEPPCoN) used Spitzer to observe 89 Jupiter-Family comets in its targeted survey, detecting ongoing activity in 21 [Kelley et al., 2013] . This survey found that the comets in the study with relatively small perihelion distances ($q$<1.8 AU) were inactive, and that cometary activity is much more common post-perihelion than pre-perihelion. The study also found that comets whose perihelion distance has been recently decreased (within the past 150 years) are much more likely to be active. In a complementary study of the same data set, Reach et al. [2013] investigated the abundance of CO and $CO_2$ in 23 comets in order to better understand the role of activity drivers over a range of heliocentric distances. They found that there was not a marked transition between $CO_2$ and $H_2O$ dominated activity as a function of heliocentric distance (i.e., the transition between the two regimes was smooth), which is consistent with the results found by the Ootsubo et al. [2012] with the Akari spacecraft data. Currently, SEPPCoN is the most complete picture we have of the Jupiter-Family comets, and serves as a valuable comparison to the work described in this dissertation. While the scope of SEPPCoN is similar to the work described here, the biggest advantage of the WISE data set is that it was a non-targeted survey, and contains both LPCs and SPCs as targets of study. Thus, since the comets in the WISE survey were not specifically selected for study, we expect to see a wider range of activity levels than was seen by SEPPCoN.

Concerning the work presented here, several of the comets found to have tails in the WISE data were also studied by the other infrared surveys described in this section, providing important overlapping datasets and the possibility of comparisions between our work and the work of previous groups. Namely, IRAS [Matson, 1986] observed 5 (all short-period), COBE and the University of Maryland follow-up ground based survey [Lisse, 2002] observed 6 SPCs, Spitzer [Reach et al., 2007] observed 7 SPCs, SEPPCoN [Kelley et al., 2013] observed 11 SPCs, Akari [Ootsubo et al., 2012] observed 14 (7 short-period and 7 long-period). These comets are marked in Chapter 2 in Table 2.1.

## 1.7 Outline of the rest of this dissertation

In this dissertation, we study the 89 comets with extended emission that were observed by the WISE (Wide-Field Infrared Survey Explorer) mission. Most previous surveys (e.g. with Spitzer) used targeted observations of selected objects; in contrast, WISE observed the sky in a relatively unbiassed manner and detected any and all comets brighter than a given flux level. We describe the WISE mission and the comets under investigation here in more detail in Chapter 2.

Chapter 3 describes the modeling techniques used to help us characterize the dust tails, and the novel tail-fitting technique developed to help us constrain the results more rigorously. Chapter 4 shows the results of those dynamical models and fits, with a detailed description of the results for a selection of comets. Chapter 5 gives some interpretations of these results,

and compares our conclusions to those found by other scientists. Finally, Chapter 6 discusses further work that could be done with this data set, and suggests some interesting possibilities for the future of cometary studies.

# CHAPTER 2
# DATA

## 2.1 The WISE mission

The data used in this research were collected by the Wide-field Infrared Survey Explorer (hereafter, WISE, [Wright et al., 2010]). WISE is a NASA Medium Class Explorer Mission that surveyed the sky from January 2010 to February 2011 [Mainzer et al., 2011] using a 40 cm diameter telescope, positioned in sun-synchronous polar orbit. The telescope and detectors were cooled using a solid hydrogen cryostat, which cooled the telescope down to 12K, and the detectors down to 7.5K.

WISE collected data in four infrared bands named, in order of wavelength, "W1", "W2", "W3", and "W4". The spectral response of each band is shown in Figure 2.1 with the band centers at 3.4, 4.6, 12 and 22 $\mu$m. Despite the fact that W4 was the least sensitive band, this was the band in which cometary dust was most readily detected. The reason for this becomes clear when we examine the spectral energy distribution (SED) for sample cometary dust at a range of heliocentric distances, as shown in Figure 2.2. This figure was generated using Mie modeling, and includes the following assumptions: grain radius = 50 $\mu$m; number of grains = 1 x $10^{20}$; emissivity = 0.95 at all wavelengths; bond albedo = 0.05

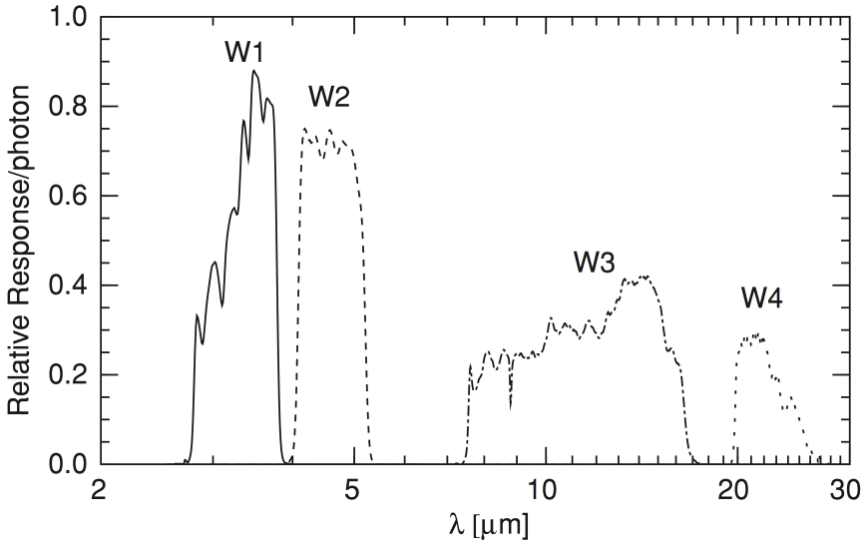


Figure 2.1: Response function of the four WISE wavebands (from [Wright et al., 2010])

at all wavelengths; observations are made at quadrature (as with the WISE observations), but no phase corrections are made; the grains are assumed to be isothermal and emit a Planck function (Yanga Fernandez, personal communication, September 24, 2014). We can see from this figure that for all heliocentric distances, flux from cometary dust will be seen most strongly in the W4 (22 $\mu$m) band. This effect becomes stronger as the sample comet increases in heliocentric distance, due to the decrease in insolation causing the peak in thermal emission to shift towards longer wavelengths.

During the fully-cryogenic phase of the mission, WISE continuously scanned the sky in all 4 wavebands, using a beam splitter to image them all simultaneously. Each individual frame is 47'x47', with a scale of 2.75"/pixel for W1, W2, and W3, and a scale of 5.5"/pixel for W4, with the W4 images binned 2x2 on board the spacecraft. The W1 and W2 images were 7.7 s exposures, and the W3 and W4 images were 8.8 s. Due to WISE's polar orbit, the sky was imaged in a series of overlapping strips. Due to the overlap of the strips, each

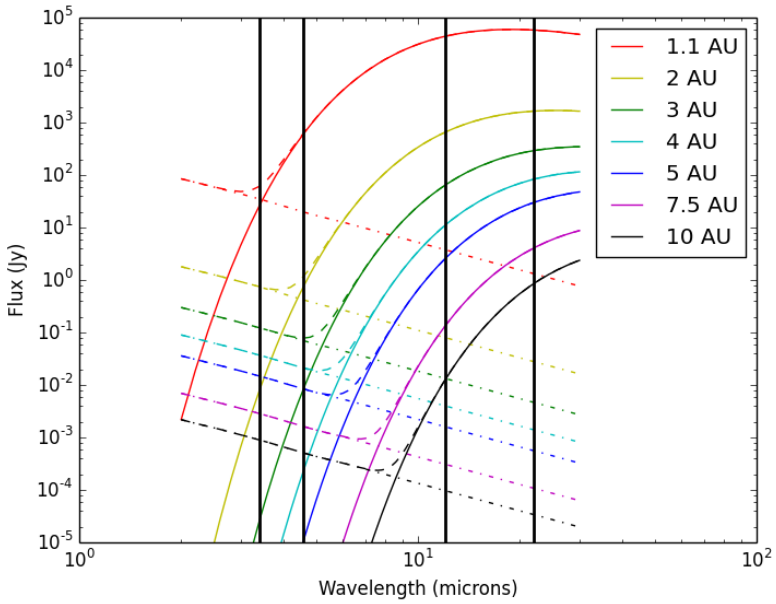


Figure 2.2: Sample of spectral energy distribution (SED) for sample cometary dust at a range of heliocentric distances. For each heliocentric distance, thermal flux is shown in a solid line, reflected flux is shown in a dot-dash line, and the total flux is shown in a dashed line. The band centers for each of the WISE wavebands are shown with the vertical black lines.

patch of sky was imaged at least 8 times (at the equator), up to hundreds of times at the poles [Wright et al., 2010]. As WISE precessed around the Earth, the strips built up a map of the sky. The strips completed 1.2 circuits around the sky in all four wavebands.

The cryogen began to run out in August 2010 after which time the 22$\mu$m images were no longer useful. The 12$\mu$m integration times were cut down after 14 August and were no longer useful after 29 September 2010 [Wright et al., 2010]. At this time, the spacecraft continued to operate with only W1 and W2 as the NEOWISE post-cryogenic mission until 1 February 2011 [Mainzer et al., 2011]. For more details on the WISE mission, we suggest the reader consult Wright et al. [2010] and Mainzer et al. [2011].

### 2.1.1 Detecting comets using WISE/WMOPS

While the WISE mission was originally designed as an astrophysics mission to survey and map the sky in mid-infrared wavelengths [Mainzer et al., 2005], the NEOWISE (Near-Earth Object WISE, [Mainzer et al., 2011]) enhancement to the mission allowed individual images to be saved and searched for moving objects, that is, asteroids and comets. Using the WISE Moving Object Processing Software (WMOPS, [Mainzer et al., 2011]), over 150,000 asteroids and 160 comets were found in the WISE images, including over 34,000 newly discovered asteroids and 21 comets that were either newly discovered or were objects with previously unknown activity.

### 2.1.2 Image stacking using AWAIC

In order to boost the signal-to-noise of the cometary dust tails seen in W3 and W4, the images for each comet were stacked using A WISE Astronomical Image Co-adder (AWAIC; [Masci and Fowler, 2009]). This program co-adds all the frames found by WMOPS, using background matching and outlier rejection to produce a mosaic image. The input images are interpolated such that the final mosaic is 1800x1800 pixels, with a pixel scale of 1"/pixel (thus the final image is 30' per side, as opposed to the original images which were 47' per side). The nucleus of the comet is centered in the image, and the mosaic is rotated such that North is up and East is left.

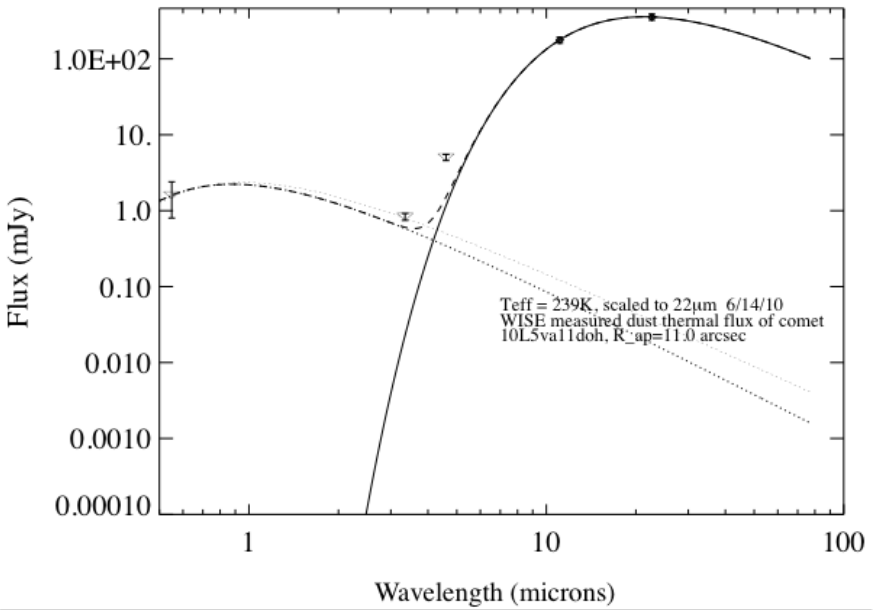


Figure 2.3: Example SED for C/2010 L5 (WISE) showing the excess of W2 flux from $CO/CO_2$ emission (J. Bauer, personal communication, October 2013).

## 2.2 Comets detected by WISE

WISE detected 160 comets during its prime mission [Bauer et al., 2011]. Of these, 89 (34 LPC and 55 SPC) had a dust tail or trail detected in W3 and/or W4 (or W1/W2, for the case of C/2009 K2), and 40 of those had tails or trails that could readily be modeled using the techniques described in Section 3.2. Table 2.1 (shown at the end of this chapter) lists the comets with a detected dust tail/trail, and lists some relevant physical parameters. The individual mosaicked images for each comet are shown with their respective models in Chapter 4.

The vast majority of the comets detected by WISE have detections in both W3 and W4, which will allow thermal parameters and temperatures to be constrained. About 20% of the 160 detected comets also have detections in W1 and W2. It is useful to note that light from

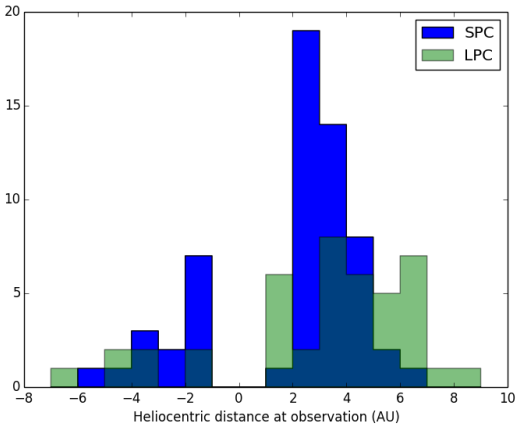


(a) All 89 comet with tails/trails.

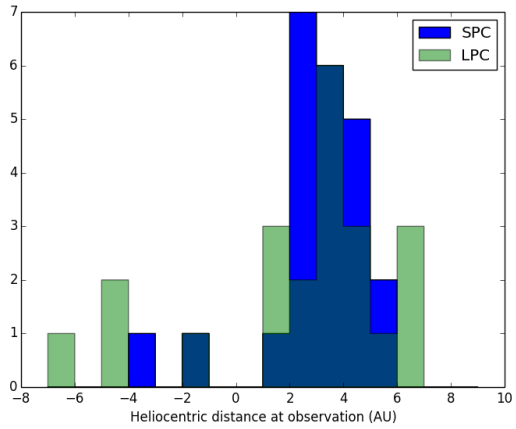


(b) Subset of 40 comets with well-fit tails

Figure 2.4: Histograms showing the heliocentric distance at which the comets with tails were observed. Negative values correspond to pre-perihelion observations, and positive values correspond to post-perihelion observations. SPCs are shown in blue, LPCs are shown in green, and the overlap between the two is shown in darker blue.

comets in the W1 band is mostly reflected light, while the light from comets in the W3 and W4 bands is thermal emission. The light from comets in the W2 band is a combination of reflected light and thermal emission, but also contains emission lines from CO and $CO_2$, thereby allowing the production rates for these gasses to be constrained [Bauer et al., 2011]. An example of a comet with W2 excess is C/2010 L5 (WISE), shown in Figure 2.3. The $CO/CO_2$ excess is evident by the fact that the 4.6$\mu$m flux value is well above the SED models, shown in solid and dashed lines (J. Bauer, personal communication, October 2013).

In order to better understand the nature of the comets with tails detected by WISE, the orbital parameters in Table 2.1 can be shown as histograms. Figure 2.4 shows the heliocentric distance at which the comets were observed. We can see that, both for the full set of comets and the subset of well-fit comets, there is a strong bias towards post-perihelion

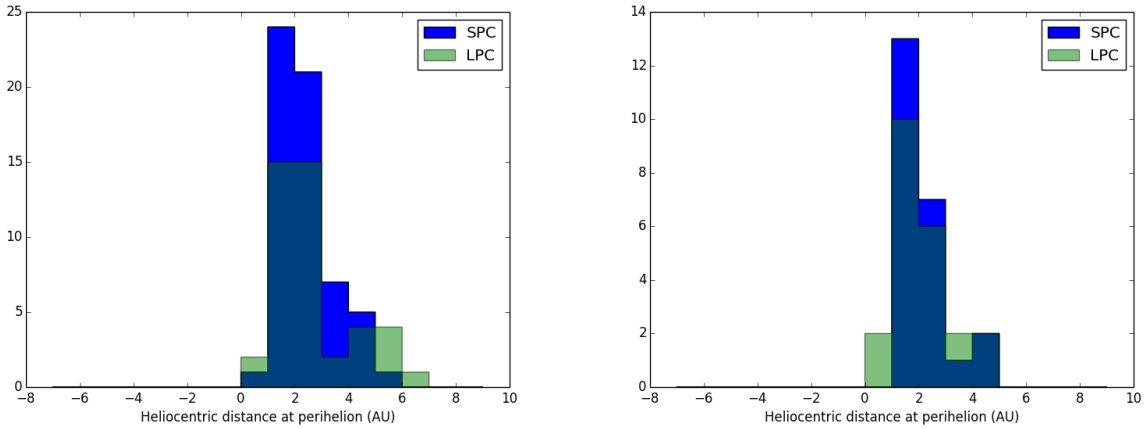


(a) All 89 comet with tails/trails.

(b) Subset of 40 comets with well-fit tails

Figure 2.5: Histograms showing the perihelion distances of the comets. SPCs are shown in blue, LPCs are shown in green, and the overlap between the two is shown in darker blue.

observations, shown on the right half of the plots. While we do see some comets before they reach perihelion, significantly more comets were observed after perihelion.

Figure 2.5 shows the perihelion distance of the observed comets. We can see that while most of the comets have perihelion distances between 1 and 3 AU, several observed comets have large perihelion distances of >4 AU, even when we only look at the 40 comets with well-fit tails.

Figure 2.6 shows the orbit plane angle separation at the time of observation for the comets. We can see that, as expected, the SPCs have a much smaller distribution of orbit plane angle separations than the LPCs, due to the smaller inclination distribution of the SPCs. We note that subset of 40 comets with well-fit tails still has a wide range of orbit plane angle separations; that is, WISE observed comets with dust tails at a wide range of latitudes. However, we can also see from this figure that comets with small orbit plane angles

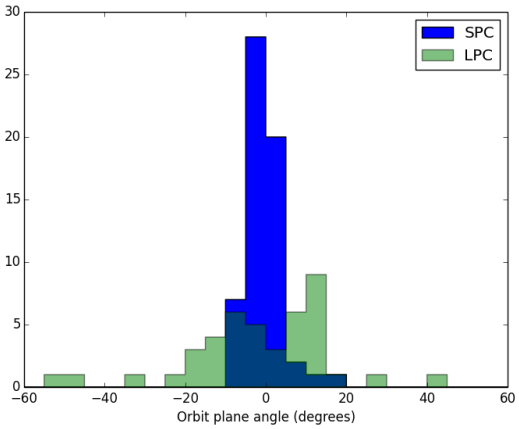


(a) All 89 comet with tails/trails.

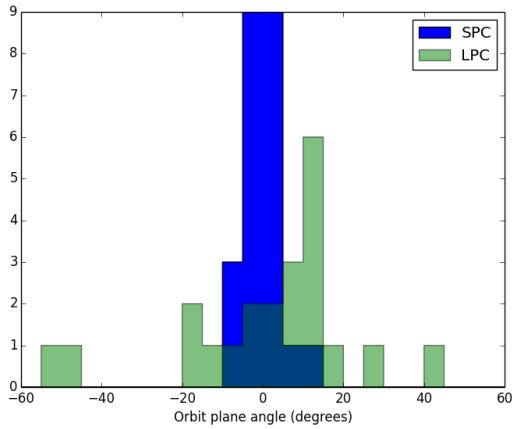


(b) Subset of 40 comets with well-fit tails

Figure 2.6: Histograms showing orbit plane angle separation at the time of observation. SPCs are shown in blue, LPCs are shown in green, and the overlap between the two is shown in darker blue.

are selected against with respect to the well-fit tails, due to the fact that this causes the models to become ambiguous.

### 2.2.1 Selection effect due to wavelength of observations

When considering the dust tails seen in this survey, it is important to remember that the WISE data is not sensitive to small particles [Bauer et al., 2012], due to the fact that particles cannot emit at wavelengths longer than

$$s = \frac{\lambda}{2\pi} \tag{2.1}$$

where $\lambda$ is the wavelength of the observations, and $s$ is the particle radius [Burns et al., 1979]. For the W4 images, this means that the data are not sensitive to particles with a

radius smaller than $\sim$3.5$\mu$m. That is, if a comet happened to only emit very small dust grains, then its tail would not show up in the images under consideration here. Thus, due to the wavelength of the observations, we have selected against comets that only have small dust grains in their tails.

Table 2.1: List of comets with dust tails detected by WISE

| **Name** | **Date Obs** | **Type** | **Bands** | **r (AU)** | **q (AU)** | $\alpha$ (°) | **Other Surveys[1]** |
|---|---|---|---|---|---|---|---|
| C/2005 L3 | 2010-05-24 | LP | 1,2,3,4 | 8.20+ | 5.59 | -3.39 | - |
| C/2006 OF2 | 2010-05-11 | LP | 3,4 | 6.30+ | 2.43 | 4.75 | O12 |
| C/2006 Q1 | 2010-04-15 | LP | 1,2,3,4 | 6.59+ | 2.76 | -0.67 | O12 |
| C/2006 S3 | 2010-05-23 | LP | 1,2,3,4 | 7.23+ | 5.13 | -0.76 | O12 |
| C/2006 W3 | 2010-04-20 | LP | 1,2,3,4 | 4.10+ | 3.13 | 11.45 | - |
| C/2007 B2 | 2010-05-20 | LP | 3,4 | 6.46+ | 2.98 | 2.91 | - |
| C/2007 G1 | 2010-02-14 | LP | 3,4 | 5.17+ | 2.65 | 10.43 | O12 |
| C/2007 N3 | 2010-02-23 | LP | 3,4 | 5.12+ | 1.21 | 0.03 | O12 |
| C/2007 Q3 | 2010-06-04 | LP | 1,2,3,4 | 3.46+ | 2.25 | -15.91 | O12 |
| C/2007 VO53 | 2010-01-25 | LP | 1,2,3,4 | 4.89- | 4.84 | 10.84 | - |
| C/2008 A1 | 2010-02-20 | LP | 1,2,3,4 | 6.12+ | 1.07 | 7.54 | - |
| C/2008 FK75 | 2010-03-19 | LP | 1,2,3,4 | 4.78- | 4.51 | 6.96 | - |
| C/2008 N1 | 2010-02-03 | LP | 1,2,3,4 | 3.08+ | 2.78 | 12.21 | - |
| ” | 2010-06-05 | LP | 1,2,3,4 | 3.75+ | 2.78 | -14.59 | - |
| C/2008 Q1 | 2010-01-15 | LP | 3,4 | 4.67+ | 2.95 | 10.66 | - |
| ” | 2010-06-09 | LP | 3,4 | 5.68+ | 2.95 | -8.65 | - |
| C/2008 Q3 | 2010-04-23 | LP | 1,2,3,4 | 3.96+ | 1.79 | -1.23 | O12 |
| C/2008 T2 | 2010-04-28 | LP | 3,4 | 4.25+ | 1.20 | 11.68 | - |
| C/2009 F2 | 2010-01-26 | LP | 3,4 | 5.90+ | 5.87 | 8.42 | - |
| ” | 2010-07-11 | LP | 3,4 | 6.11+ | 5.87 | -8.14 | - |
| C/2009 F5 | 2010-02-16 | LP | 3,4 | 5.23+ | 2.24 | 10.58 | - |
| ” | 2010-07-19 | LP | 4 | 6.40+ | 2.24 | -9.03 | - |
| C/2009 F6 | 2010-03-02 | LP | 3,4 | 4.01+ | 1.28 | 13.17 | - |
| C/2009 G1 | 2010-01-12 | LP | 3,4 | 3.78+ | 1.13 | -2.31 | - |
| C/2009 K2 | 2010-05-09 | LP | 3,4 | 3.36+ | 3.25 | -16.42 | - |

Continued on next page

| Name | Date Obs | Type | Bands | r (AU) | q (AU) | $\alpha$ (°) | Other Surveys[1] |
|---|---|---|---|---|---|---|---|
| C/2009 K5[2] | 2010-10-14 | LP | 1,2 | 2.65+ | 1.42 | 19.33 | - |
| C/2009 P1 | 2010-06-06 | LP | 1,2,3,4 | 6.35- | 1.55 | -8.45 | - |
| C/2009 T1 | 2010-01-15 | LP | 1,2,3,4 | 6.26+ | 6.23 | 8.01 | - |
| C/2009 U3 | 2010-01-17 | LP | 1,2,3,4 | 1.67- | 1.41 | -33.27 | - |
| C/2009 Y1 | 2010-04-10 | LP | 3,4 | 3.94- | 2.52 | -9.34 | - |
| C/2010 A4 | 2010-04-29 | LP | 3,4 | 3.20- | 2.74 | -15.18 | - |
| C/2010 DG56[3] | 2010-07-27 | LP | 1,2,3,4 | 1.86+ | 1.59 | -10.87 | - |
| C/2010 FB87[3] | 2010-07-23 | LP | 3,4 | 3.04+ | 2.84 | -9.77 | - |
| C/2010 G3[3] | 2010-04-15 | LP | 3,4 | 4.91+ | 4.91 | -10.83 | - |
| ” | 2010-07-04 | LP | 3,4 | 4.95+ | 4.91 | 6.1 | - |
| C/2010 J1 | 2010-04-02 | LP | 1,2,3,4 | 1.84+ | 1.69 | -23.95 | - |
| ” | 2010-07-01 | LP | 1,2,3,4 | 2.48+ | 1.69 | 7.77 | - |
| C/2010 J4 [3] | 2010-05-01 | LP | 1,2,3,4 | 1.09- | 1.09 | -45.56 | - |
| ” | 2010-05-12 | LP | 1,2,3,4 | 1.10+ | 1.09 | -54.98 | - |
| C/2010 L4 [3] | 2010-06-16 | LP | 3,4 | 3.04+ | 2.83 | -13.14 | - |
| C/2010 L5 [3] | 2010-06-14 | LP | 1,2,3,4 | 1.21+ | 0.79 | 44.33 | - |
| ” | 2010-07-16 | LP | 1,2,3,4 | 1.62+ | 0.79 | 28.22 | - |
| 10P | 2010-04-29 | SP | 1,2,3,4 | 1.58- | 1.42 | -9.66 | M86, L02, R07 |
| 17P | 2010-05-15 | SP | 3,4 | 5.13+ | 2.06 | 3.84 | - |
| 19P | 2010-02-12 | SP | 3,4 | 4.54+ | 1.35 | -6.02 | L02, O12 |
| ” | 2010-07-25 | SP | 3,4 | 5.11+ | 1.35 | 4.29 | ” |
| 29P | 2010-05-04 | SP | 1,2,3,4 | 6.21+ | 5.73 | 1.56 | M86, L02, O12 |
| 30P | 2010-03-08 | SP | 1,2,3,4 | 1.92- | 1.88 | -3.81 | - |
| 47P | 2010-02-28 | SP | 3,4 | 3.45+ | 2.81 | -1.12 | K13 |
| 64P | 2010-05-04 | SP | 3,4 | 3.47+ | 1.38 | 2.72 | O12 |
| 65P | 2010-04-25 | SP | 1,2,3,4 | 2.46+ | 2.46 | -2.59 | M86, R07 |
| 67P | 2010-01-19 | SP | 3,4 | 3.32+ | 1.24 | -2.05 | M86, L02, R07, O12 |
| ” | 2010-06-29 | SP | 3,4 | 4.18+ | 1.24 | 1.3 | ” |
| 68P | 2010-02-20 | SP | 3,4 | 3.85+ | 1.76 | 1.25 | K13 |
| 74P | 2010-01-19 | SP | 1,2,3,4 | 3.61+ | 3.56 | -1.26 | M86, K13 |
| ” | 2010-07-07 | SP | 1,2,3,4 | 3.74+ | 3.56 | 0.88 | ” |
| 77P | 2010-05-07 | SP | 1,2,3,4 | 2.99+ | 2.31 | 4.39 | K13 |
| 81P[2] | 2010-08-07 | SP | 1,2,3 | 2.22+ | 1.60 | -0.06 | L02, O12 |
| 89P | 2010-08-06 | SP | 3,4 | 3.24+ | 2.28 | 3.95 | K13 |

Continued on next page

| Name | Date Obs | Type | Bands | r (AU) | q (AU) | $\alpha$ (°) | Other Surveys[1] |
|---|---|---|---|---|---|---|---|
| 94P | 2010-05-22 | SP | 1,2,3,4 | 2.27+ | 2.24 | -0.58 | R07, K13 |
| 100P | 2010-04-17 | SP | 2,3,4 | 2.23+ | 1.98 | -2.45 | - |
| 103P | 2010-05-11 | SP | 2,3,4 | 2.29- | 1.06 | -1.16 | L02, R07 |
| 116P | 2010-04-17 | SP | 1,2,3,4 | 2.82+ | 2.17 | 0.13 | R07, O12 |
| 117P | 2010-03-18 | SP | 3,4 | 5.13- | 3.06 | -1.55 | - |
| 118P | 2010-03-25 | SP | 1,2,3,4 | 2.08+ | 1.98 | -2.58 | O12, K13 |
| 127P | 2010-01-09 | SP | 1,2,3,4 | 2.26+ | 2.20 | -6.99 | R07, K13 |
| 142P | 2010-07-25 | SP | 3,4 | 2.52+ | 2.49 | -4.35 | - |
| 145P | 2010-04-28 | SP | 3,4 | 2.62+ | 1.89 | 0.59 | - |
| 158P | 2010-04-14 | SP | 3,4 | 4.71- | 4.58 | -1.58 | - |
| 186P | 2010-06-09 | SP | 4 | 4.77+ | 4.26 | 5.68 | - |
| 195P | 2010-06-19 | SP | 2,3,4 | 4.99+ | 4.44 | -2.92 | - |
| 199P | 2010-07-19 | SP | 3,4 | 4.25+ | 2.94 | 2.32 | - |
| 203P | 2010-02-25 | SP | 1,2,3,4 | 3.18+ | 3.18 | 0.71 | - |
| 213P | 2010-01-21 | SP | 3,4 | 3.67- | 2.12 | -0.59 | K13 |
| ” | 2010-07-06 | SP | 3,4 | 3.08- | 2.12 | 1.78 | ” |
| 215P | 2010-04-28 | SP | 3,4 | 3.22- | 3.22 | -2.58 | K13 |
| 217P | 2010-03-17 | SP | 2,3,4 | 2.46+ | 1.22 | -4.58 | - |
| 219P [2] | 2010-08-13 | SP | 3 | 2.58+ | 2.36 | -4.87 | K13 |
| 226P | 2010-04-12 | SP | 3,4 | 3.23+ | 1.77 | -7.14 | - |
| 230P | 2010-05-16 | SP | 3,4 | 2.91+ | 1.48 | -4.72 | - |
| 232P | 2010-05-01 | SP | 3,4 | 3.21+ | 2.98 | -1.35 | - |
| 233P | 2010-02-07 | SP | 3,4 | 1.81- | 1.79 | -6.88 | - |
| 234P | 2010-01-16 | SP | 3,4 | 2.86+ | 2.86 | 3.83 | - |
| 236P | 2010-06-22 | SP | 1,2,3,4 | 1.96- | 1.83 | -4.03 | - |
| ” | 2010-07-04 | SP | 3,4 | 1.93- | 1.83 | -6.19 | - |
| 237P | 2010-06-11 | SP | 3,4 | 2.70+ | 2.39 | -0.82 | - |
| 240P [2] | 2010-09-25 | SP | 1,2,3 | 2.13- | 2.12 | 11.67 | - |
| 245P [3] | 2010-06-04 | SP | 2,3,4 | 2.34+ | 2.13 | 9.04 | - |
| P/2008 J3 | 2010-03-16 | SP | 3,4 | 3.33+ | 2.29 | -2.03 | - |
| P/2008 Y3 | 2010-01-16 | SP | 3,4 | 4.86+ | 4.43 | 4.07 | - |
| P/2009 Q4 | 2010-05-28 | SP | 3,4 | 2.32+ | 1.32 | -4.84 | - |
| P/2009 T2 | 2010-01-24 | SP | 1,2,3,4 | 4.53+ | 1.76 | 19.55 | - |
| P/2009 WX51 | 2010-04-03 | SP | 3,4 | 1.25+ | 0.80 | -4.02 | - |

Continued on next page

| Name | Date Obs | Type | Bands | r (AU) | q (AU) | $\alpha$ (°) | Other Surveys[1] |
|---|---|---|---|---|---|---|---|
| P/2010 A1 | 2010-04-22 | SP | 3,4 | 2.92+ | 1.95 | -1.07 | - |
| P/2010 A2 | 2010-04-03 | SP | 3,4 | 2.07+ | 2.00 | 2.41 | - |
| P/2010 A3 | 2010-01-16 | SP | 1,2,3,4 | 1.85- | 1.62 | -7.61 | - |
| P/2010 A5 | 2010-01-21 | SP | 1,2,3,4 | 1.95- | 1.72 | 1.34 | - |
| P/2010 D1[3] | 2010-02-18 | SP | 3,4 | 3.03+ | 2.67 | 0.71 | - |
| P/2010 H2 | 2010-07-07 | SP | 1,2,3,4 | 3.15+ | 3.11 | 3.19 | - |
| P/2010 J5 | 2010-02-26 | SP | 3,4 | 3.76+ | 3.75 | -2.01 | - |
| P/2010 P4 [3] | 2010-08-07 | SP | 3,4 | 1.88+ | 1.86 | 11.3 | - |
| P/2010 U1 | 2010-07-27 | SP | 3,4 | 4.93+ | 4.90 | -0.65 | - |

[1] M86: [Matson, 1986]; L02: [Lisse, 2002]; R07: [Reach et al., 2007]; O12: [Ootsubo et al., 2012]; K13: [Kelley et al., 2013]

[2] These comets are from the post-cryo part of the mission

[3] These comets were discovered by WISE

# CHAPTER 3
# DYNAMICAL MODELING METHODS

## 3.1 Finson-Probstein modeling

Note: Parts of this section are based on the analysis published in Kramer et al. [2014]'s Spitzer study of comet C/1995 O1 (Hale-Bopp) at high heliocentric distances.

The morphology of cometary comae, tails, and trails can be used to derive physical properties of their constituent grains such as grain size distribution, grain speeds, activity history, and dust production rate. In order to constrain some of these parameters in dust tails, we employ the Finson-Probstein method, which assumes that the motion of cometary dust particles, once they have left the collisionally thick region (i.e. decoupled from the comet's gas outflow) and been accelerated to a terminal outflow velocity, is controlled only by solar gravity and solar radiation pressure, both of which are central forces acting along the Sun-dust particle vector [Finson and Probstein, 1968]. The particle motion can then be parameterized using the ratio of these two forces, called $\beta$:

$$\beta = \frac{F_{rad}}{F_{grav}} \tag{3.1}$$

where

$$F_{rad} = \frac{Q_{pr}}{c}\left(\frac{E_s}{4\pi r^2}\right)\frac{\pi d^2}{4} \tag{3.2}$$

$$F_{grav} = \frac{GM_s}{r^2}\left(\frac{\rho_d \pi d^3}{6}\right) \tag{3.3}$$

and where $Q_{pr}$ is the scattering efficiency for radiation pressure, $c$ is the speed of light (2.99 x $10^8$ m $s^{-1}$), $E_s$ is the mean total solar luminosity (3.846 x $10^{26}$ W), $r$ is the distance from the Sun, $d$ is the particle diameter, $G$ is the universal gravitational constant (6.673 x $10^{-11}$ N $m^2$ $kg^{-2}$), $M_s$ is the mass of the Sun (1.98855 x $10^{30}$ kg), and $\rho_d$ is the mass density of the particle. Putting 3.2 and 3.3 into 3.1, collecting the constant terms, changing particle diameter to particle radius, and converting to cgs units gives:

$$\beta = \frac{CQ_{pr}}{\rho_d a} \tag{3.4}$$

where $\rho_{\mathrm{d}}$ is now in units of g $cm^{-3}$, $a$ is the particle radius in cm, and the factor of $C$ = 5.78 x $10^{-5}$ g $cm^{-2}$ comes from collecting all the constants into a single term [Finson and Probstein, 1968] (note that the value for $C$ is slightly different than that presented in Finson and Probstein [1968], due to differences in the measured value of $E_s$).

Thus $\beta$ depends on the inverse of particle radius; i.e. for small grains, $\beta$ is larger, meaning the radiation pressure pushing the particles outwards has a proportionally larger effect than for larger particles. Figure 3.1, from Reach et al. [2007], shows a schematic of how small ($\beta$

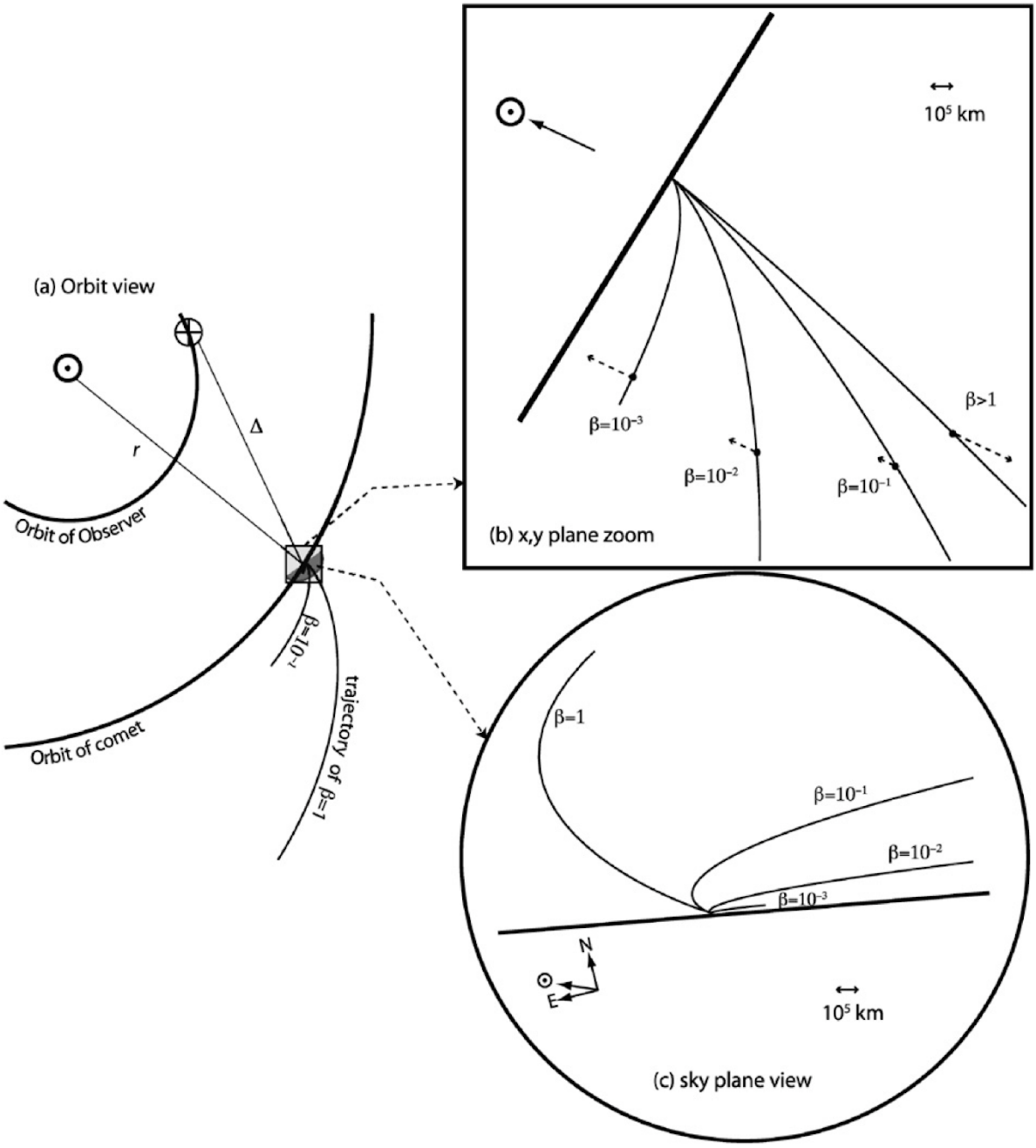


Figure 3.1: Schematic showing how $\beta$ affects particle motion. From Reach et al. [2007].

= 1) and large ($\beta = 10^{-3}$) particles are affected by solar radiation pressure in different ways. From this figure, we can see that small particles move in a nearly anti-solar direction, while large particles move close to the orbit of the comet from which they were emitted.

$\beta$ is incorporated into the equation of motion in the heliocentric coordinate system in the following way:

$$\ddot{\vec{x}} + (1 - \beta)\frac{GM_s}{|\vec{x}|^3}\vec{x} = 0 \tag{3.5}$$

where $\vec{x}$ is the vector position of the particle. This is a simple equation of motion that can then be integrated to track the motion of particles with different $\beta$ values.

The computations were carried out by creating a numerical integrator (based on the work of Lisse et al. [1998]) in the language Python. The comet state vectors (positions, velocities and accelerations) were calculated using software developed by the NEOWISE team, called "pyPlanetary". The dynamical modeling software takes in a set of $\beta$ values and comet state vectors, and integrates the motion of the dust particles over the designated time interval, using the comet positions and velocities as the initial conditions for the dust particles. The calculations are carried out in a 3-D heliocentric coordinate system, and the final positions of the dust particles are then transformed to the cometrocentic coordinate system, projecting the relative positions of the particles onto the observer's (WISE's) plane of sky. The software thus returns a matrix of points which can then be plotted as curves of constant beta (syndynes) or curves of constant particle emission date (synchrones). Figure

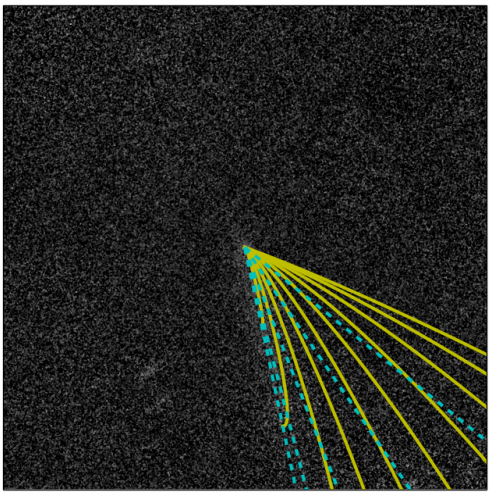

Figure 3.2: Example of full syndyne-synchrone model, for C/2008 T2. Syndynes are show in solid yellow curves and range from $\beta = 3$ to $\beta = 10^{-4}$, and synchrones are shown in dashed cyan curves and are shown for emission occurring 1, 2, 3, 4, and 5 years before the observations took place.

3.2 shows an example of the full syndyne-synchrone modeling results, showing how different $\beta$ values affect the final shape of the tail.

Each syndyne corresponds to dust with a particular $\beta$ that was released continuously from some given time ago up to the time of the image. Since the forces on particles of different $\beta$ are different, the syndynes will tend to fan out in the comet's orbital plane. If the data are well modeled by the syndynes, the curves will span the width of the dust tail when overplotted on the data image. In the most general case, the relative velocity of the grains from the comet's surface can be included into the integration, giving individual $\beta$ curves a spread of some finite width. Here, we are concerned with general shape matching, so the particles were given no initial velocity relative to the nucleus.

## 3.2 Tail Fitting Method

In the field of cometary science, the general method for deriving the results of Finson-Probstein modeling is to overlay the resulting models on an image, and then select "by hand" which model most closely matches the morphology of the dust in the image. While we were examining the results of the dynamical models for the comets in the data presented in this dissertation, it became clear that this technique was insufficient for a population study, since it is (1) slow, and (2) subjective, since two competing models might "win" for different team members examining the results.

In order to mathematically constrain the best-fit syndyne and synchrone of each dust tail, we developed a novel analytical method to collapse a diffuse tail into a set of points which can then be automatically and systematically compared to the syndynes and synchrones. This process allows the best-fit models to be chosen in a much more uniform manner than could be achieved by the "by hand" process. We will first set out a general outline for the method, then explain each step in greater detail.

1. Split the image into concentric annuli of width $a$.

2. Unwrap the annulus into r-$\theta$ space.

3. Bin the points into radial bins of width $b$.

4. Fit a Gaussian to the binned points, using the center as the best-fit tail location for that annulus.

5. Transform the best-fit tail location back to x-y coordinates.

6. Repeat steps 1-5 for a range of $a$ and $b$.

7. Use a clustering algorithm to remove points that are far from the tail.

8. Use a least-squares fitting method to determine separately the best-fit syndyne and synchrone.

### 3.2.1 Split the image into concetric annuli

Our first task is to split the image into a series of concentric annuli, centered on the comet. For the WISE data, this is somewhat simplified since the AWAIC program puts the nucleus at the center of the image (900, 900) during the stacking process. For an annulus of width $a$, we first omit the region within $a$ pixels of the center, in order to avoid confusion from an extended coma around the nucleus. The remainder of the image is then divided up into concentric annuli out to about halfway to the edge of the image. For the work presented here, we have used annuli of width 20, 30 and 40 pixels, corresponding to 24, 16 and 12 annuli, respectively. See panel B of Figure 3.3.

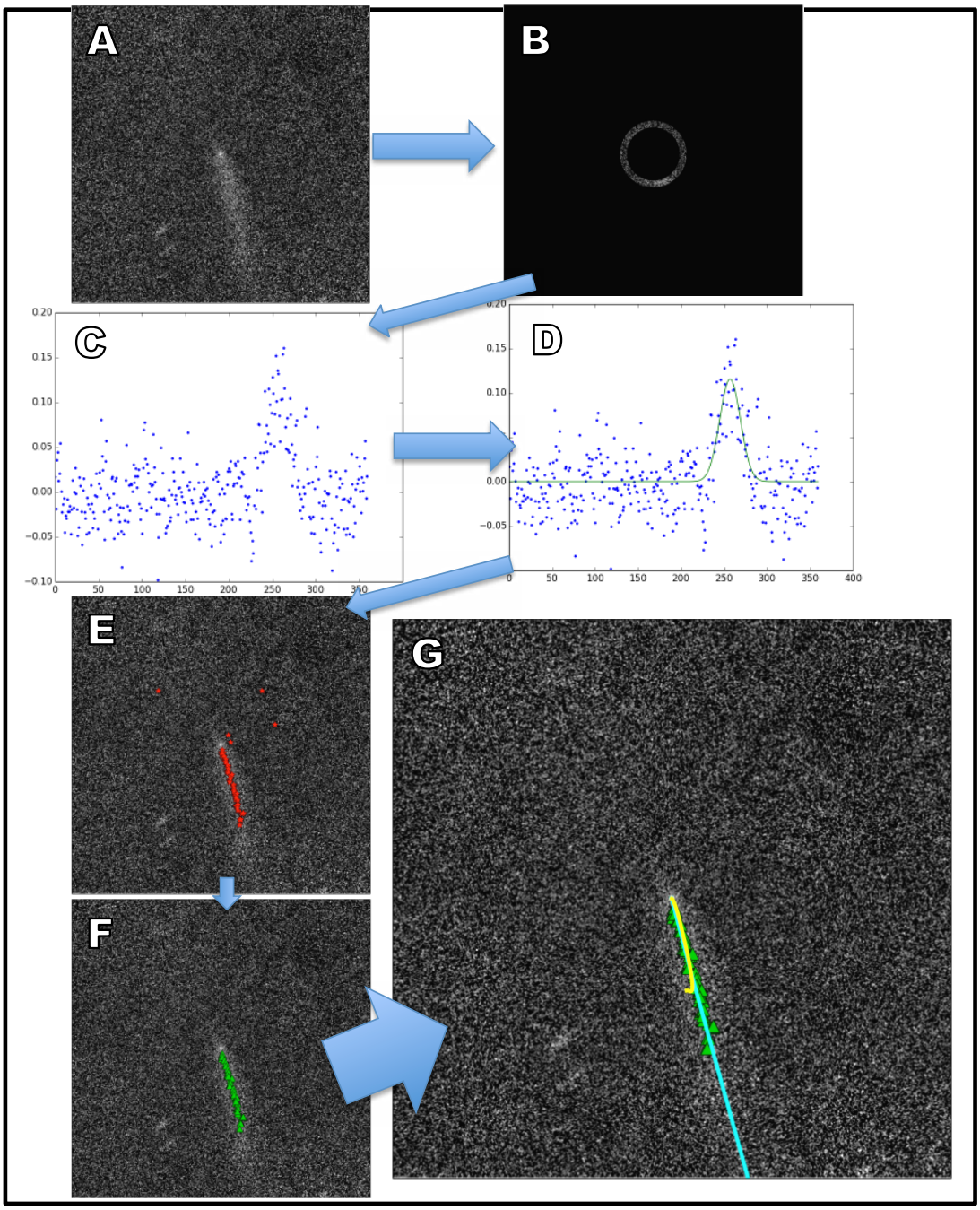


Figure 3.3: Flow chart of tail fitting process. (A) Original image, (B) A selected annulus, (C) Unwrapped annulus after binning, (D) Gaussian fit, (E) Fitted points superimposed on the image, (F) Fitted points with outliers discarded, and (G) Best-fit syndyne (yellow) and synchrone (cyan) overlaid on the image.

### 3.2.2 Unwrap the annulus into r-$\theta$ space

Next we unwrap the annulus into r-$\theta$ space by first calculating the distance from each pixel location to the location of the nucleus. We then find the angle of each pixel relative to the +x axis.

### 3.2.3 Bin the points into radial bins of width $b$

In order to boost the signal to noise ratio and thus give a better fit, we then collect the pixels into radial wedges. That is, for a 1° bin, we collect all the pixels with $\theta$ between 0-1°, adding the value of all the pixels together and dividing by the number of pixels in that radial bin. For the work presented here, we have used radial bins of 1, 2, and 3°. See panel C of Figure 3.3.

### 3.2.4 Fit a Gaussian to the binned points, using the center as the best-fit tail location for that annulus

In order to aid in the Gaussian fitting, we first subtract the median of all the bins in the annulus. We then (a) fit a Gaussian to these points, saving the results to an array and (b) create a synthetic Gaussian using the fitted parameters, and subtract that from the points.

Steps (a) and (b) are repeated twice more, for a total of three times. This is necessary since occasionally a background star or background noise may be strong enough that the tail signal will be overwhelmed. The best fit to the tail is usually found among the three fitted Gaussians.

We then find the median Gaussian center across the entire set of annuli. If we assume that the comet's tail is the strongest signal in the image, then that Gaussian center value should show up in each set of three values for each annulus. For each annulus, we then select the fitted Gaussian whose center value is closest to the median previously calculated. See panel D of Figure 3.3.

### 3.2.5 Transform the best-fit tail location back to x-y coordinates

We next transform the best-fit tail location for each annulus from r-$\theta$ space back to x-y coordinates.

### 3.2.6 Repeat steps 1-5 for a range of $a$ and $b$

We repeat the process described above for a range of annular widths and radial wedge sizes. Since the comet tails exhibit a wide range of morphologies, there is no one set of $a$ and $b$ that works for all the comets. See panel E of Figure 3.3.

### 3.2.7 Use a clustering algorithm to remove points that are far from the tail

In order to boost the strength of the fitted tail and to automatically remove points which are not part of the tail, we employ a clustering algorithm. This algorithm works by first gathering all the fitted tail points (from the entire range of $a$ and $b$) into a single list. Then, the distance between each point and all the others is computed. If there are any points that do not fall within 40 pixels of two other points, that point is discarded. The value of 40 pixels was chosen because this was the width of the widest annulus used in our analysis. See panel F of Figure 3.3.

### 3.2.8 Use a least-squares fitting method to determine separately the best-fit syndyne and synchrone

Before comparing the fitted tail points to the models, model points which are far from the center of the image (>2100 pixels from the center in either coordinate) are trimmed to speed up computing time. Next, the synchrones are interpolated, since they only have at most 10 points each, thus making it difficult to compare to the fitted tail points.

We first describe the process for finding the best-fit synchrone. The process is similar for finding the best-fit syndyne. In order to compare the fitted tail points to the models, all the points (both fitted and model) are first converted to polar coordinates. Since the tail is roughly radial from the center, using a simple Cartesian comparison of data to model would unfairly penalize points which are far from the nucleus. Then, for each fitted tail point, we find the model point for each model that is closest in $r$, and then find the difference in $\theta$ between the fitted tail point and that model point. This is repeated for each synchrone, yielding a list of $\theta$ difference values between each model and each fitted tail point. Those $\theta$ difference values are squared and added for each synchrone, called "*diffsq*" for convenience. The synchrone with the lowest *diffsq* is thus chosen as the best-fit synchrone. See panel G of Figure 3.3.

## 3.3 Interpretation of the Results

Once the tail fitting method described above gives us the best-fit syndyne and synchrone for each comet, we must then interpret these results as physical characteristics of the cometary activity.

### 3.3.1 Interpretation of Syndynes

The interpretation of the parameter $\beta$ must be taken with care. To a first order approximation, it can be used as a proxy for the size of dust particles emitted by the comet by rearranging the terms in Equation 3.1 to get

$$a = \frac{CQ_{pr}}{\rho_d \beta} \tag{3.6}$$

which gives the particle size in cm when the appropriate values for $C$, $Q_{pr}$, $\rho_d$, and $\beta$ are inserted. Thus, for a dust particle with $\rho_d = 0.5$ g cm$^{-3}$ and $Q_{pr} = 1$, the particle radius in microns is roughly equal to $1/\beta$ (recall that 1 micron = $10^{-5}$ cm).

#### 3.3.1.1 The use of $Q_{pr}$

In the calculations and discussion presented in this dissertation, I have included the assumption that $Q_{pr} = 1$, which is not strictly true for all cases. However, I will now demonstrate that for the particle size and wavelength regimes under consideration here, this is a good approximation. The size parameter

$$X = \frac{2\pi a}{\lambda} \tag{3.7}$$

where $a$ is the particle radius and $\lambda$ is the wavelength under consideration, is used to asses how the size of the particles under consideration compare to the characteristic wavelength [Burns et al., 1979]. For cases where $X \gg 1$, geometrical optics can be used, thereby simplifying the problem. Since the solar spectrum is concentrated near $\sim 0.5\mu$m, we can then say that geometric optics holds for particles larger than $\sim 0.8\mu$m (by saying that $X > 1$). Since the WISE detectors all observe at wavelengths larger than $0.8\mu$m, and we can only observe particles on the order of or larger than the wavelengths being observed, we can thus say that the geometrical optics case holds for the observations presented here. The effect of this can be seen in Figure 3.4, with the geometrical optics case (solid line) showing a linear relationship across the entire plot, and all the other materials showing a near linear trend for particles larger than $\sim 0.1\mu$m.

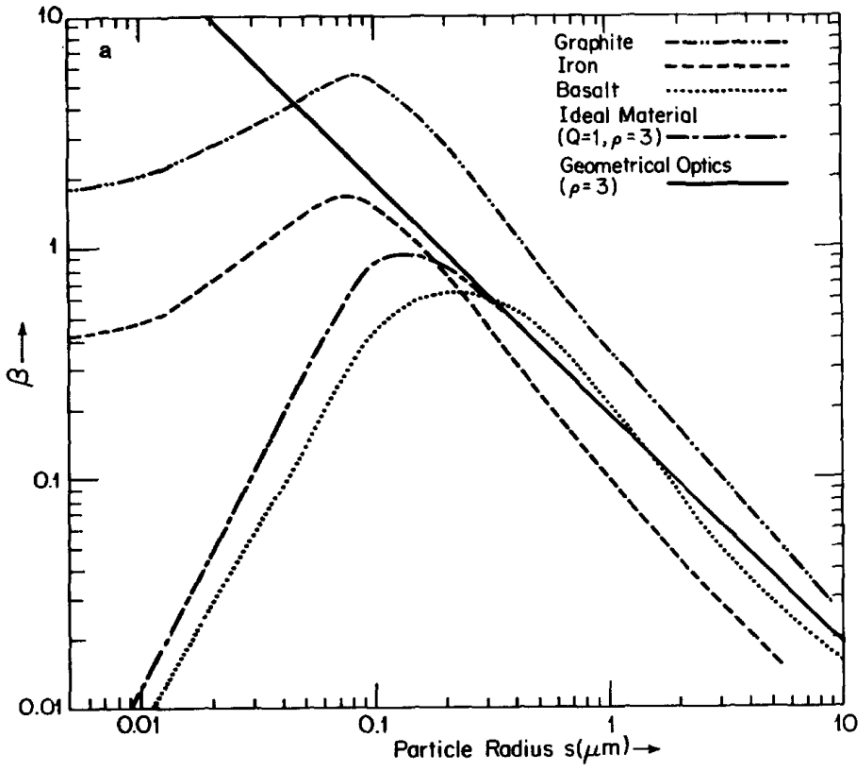


Figure 3.4: A log-log plot of $\beta$ as a function of particle size for a selection of real and ideal materials. For the data under consideration here, the geometrical optics case (solid line) holds true. (From Burns et al. [1979])

### 3.3.2 Interpretation of Synchrones

The best-fit synchrone is a measure of the age of the dust in the tail in terms of number of days before the observations took place. For example, if the observations took place on 15 April 2010, and the tail-fitting method yields a best-fit synchrone of 180 days, that means that the dust we are seeing was primarily emitted 180 days before the observations took place, or on 17 October 2009. Using the JPL Horizons web tool (http://ssd.jpl.nasa.gov/horizons.cgi), we can then calculate the heliocentric distance at which the emission occurred by using the calculated emission date.

### 3.3.3 Effect of Initial Particle Velocity

While the analysis done in this dissertation has neglected the effect of the initial particle velocity, we can do some quick calculations to study how particle velocity may affect the interpretation of the results. The velocity at which a particle leaves the surface of a comet is dependent on the particle size and the heliocentric distance in the following way:

$$v_i = A\left(\frac{\beta}{r}\right)^{0.5} \tag{3.8}$$

where $r$ is the heliocentric distance at which the particles were emitted and $A$ is taken to be 0.3 [Lisse et al., 1998]. Since the comet images are all 1800" x 1800" with the comet at the center, the distance from the comet to the edge of the frame is 900". We can thus calculate the angular size in km between the center and the edge of the frame using some simple trigonometry:

$$D = \frac{\delta\Delta}{206265"} km \tag{3.9}$$

where $D$ is the angular size in km, $\delta$ is the angular size of the the frame in arcseconds, (here, 900"), $\Delta$ is the distance between the Earth and the comet, and the factor of 206265 comes from converting radians to arcseconds (60x60x180/$\pi$). We can use these equations to calculate the maximum number of days that particles of a particular size would spend in the field of view. Note that this is a **maximum** time, since this calculation neglects the additional affects of acceleration due to solar radiation pressure. While this will affect the final speed of the particle significantly, the purpose of this discussion is to demonstrate that small particles will leave the field of view much more quickly than large particles. Thus, if all the dust emission for a comet occurs simultaneously (as a synchrone), then the small particles will leave the field of view of the image quickly compared to the large particles.

Table 3.1: Calculated number of days a particle would stay in the field of view, as a function of heliocentric distance and $\beta$

| $\beta$ value | | | | | |
|---|---|---|---|---|---|
| - | - | 0.0001 | 0.01 | 0.1 | 1 |

| | | | | | |
|---|---|---|---|---|---|
| Distance (AU) | 1 | 2518 | 252 | 80 | 25 |
| | 2 | 7123 | 712 | 225 | 71 |
| | 4 | 20146 | 2015 | 637 | 201 |
| | 6 | 37011 | 3701 | 1170 | 370 |

## 3.4 Error Estimation

In order to understand the significance of the results that are being presented here, we must estimate the errors on best-fit syndynes and synchrones. We do this by exploiting the fact that the best-fit tail points were chosen using a Gaussian fit: we use the width of the Gaussian (calculated above in Section 3.2.4) as an estimate of the spread in the tail at a given point. The steps used to estimate the spread in the tail are given here:

1. Use the Gaussian width of the best-fit tail points (that is, the standard deviation) as a measure of the error in the fit.

2. Subtract (add) the Gaussian width (in pixels) for each best-fit tail point to the (unwrapped) best-fit center location.

3. Build up a positive and negative tail by repeating this process along the entire length of the fitted tail (see Figure 3.5a.

4. Do the normal least-squares fitting from the data to the models (described in Section 3.2.8) for the positive and negative tails (see Figure 3.5c and 3.5b).

This process gives us a best-fit syndyne and synchrone for the nominal, +1 sigma, and -1 sigma tails. Thus, we can use this analysis method to assess the goodness of the fit yielded by this process. In the example shown in Figure 3.5 for C/2006 OF2, we can see in (a) that the +/- 1 sigma fitted tail points span the width of the tail, and that the least-squares fitting process finds syndynes (shown in (b)) and synchrones (shown in (c)) that span the width of the tail. Thus, this process does a good job of estimating the error in the fitting process.

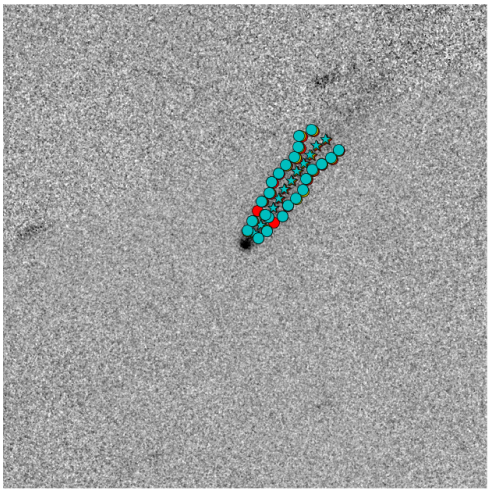

(a) Positive and negative tail points (circles) and nominal tail points (stars) plotted on C/2006 OF2 W4 data.

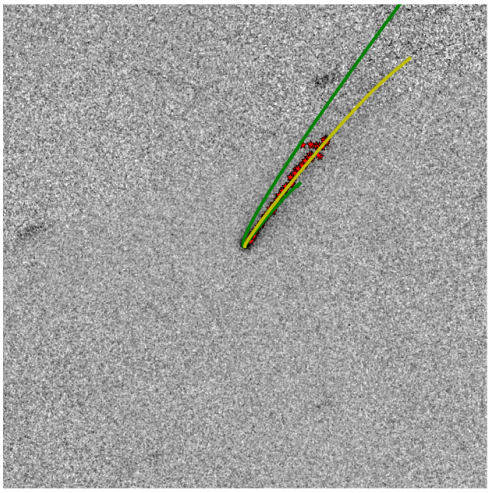

(b) Syndyne models fit to the positive and negative tail points (green) and the nominal tail points (yellow) for C/2006 OF2 W4 data

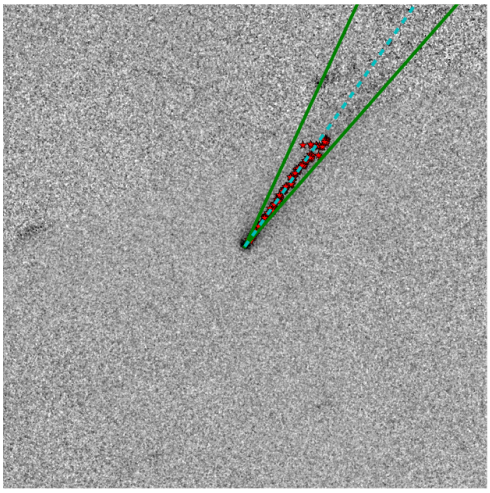

(c) Synchrone models fit to the positive and negative tail points (green) and the nominal tail points (cyan) for C/2006 OF2 W4 data

Figure 3.5: Example of the error estimation process for C/2006 OF2.

# CHAPTER 4
# RESULTS

We have employed the methods described in Chapter 3 to characterize the dust tails of the comets listed in Table 2.1. We have completed a preliminary analysis of all the comets (below, Section 4.3), and used the tail-fitting method on a subset of 40 comets on which the method worked with no user influence.

Before we dive in to the results, it is important to recall that synchrones are curves of constant particle emission date, and syndynes are curves of constant $\beta$ (particle size). Care must be taken when interpreting the results of the tail-fitting method. The best-fit synchrone (BFSc) is not necessarily a measure of the when all of the dust emission occurred. Rather, it is a measure of the time in the comet's orbit during when the dust emission was **strongest**. That is, for most comets, dust emission likely occurred both before and after the time (and thus heliocentric distance) indicated by the BFSc, but the BFSc is a useful measure of when the activity was most vigorous.

Similarly, the best-fit syndyne (BFSd) is a measure of the $\beta$ value of the brightest part of a comet's tail. That is, the tail contains particles which are both larger and smaller than

that suggested by the BFSd, but the BFSd can be used as a proxy for understanding the average particle size in a comet's tail.

## 4.1 Comets of particular interest

There are several comets among the entire data set to which we will now draw your attention. Two comets in particular, C/2006 W3 (Christensen) (see Section 4.2.1.2 and Figure 4.2)and C/2007 Q3 (Siding Spring) (see Section 4.2.1.5 and Figure 4.5), displayed dust tails which were significantly brighter and more fanned out than the rest of the comets in this study. These comet will be the subject of an in-depth analysis to occur at a later time.

Among the entire data set of 89 comets, 13 were observed to have dust tails when they were imaged twice by WISE. Among those 13, 5 were successfully run through the tail-fitting method. The well-fit comets with tails at multiple epochs are:

- C/2008 N1: Section 4.2.1.9 and Figures 4.9 and 4.10
- C/2010 J4: Section 4.2.1.18 and Figures 4.19 and 4.20
- C/2010 L5: Section 4.2.1.19 and Figures 4.21 and 4.22
- 19P: Section 4.2.2.3 and Figures 4.26 and 4.27
- 67P: Section 4.2.2.5 and Figures 4.29 and 4.30

The other 8 comets (some of which had one observation with a well-fit tail) that were observed to have a dust tail in two observations by WISE are:

- C/2008 Q1: Figures 4.50 and 4.51
- C/2009 F2: Figures 4.52 and 4.53
- C/2009 F5: Figures 4.54 and 4.55
- C/2010 G3: Figures 4.62 and 4.63
- C/2010 J1: Figures 4.64 and 4.18
- 74P: Figures 4.70 and 4.71
- 213P: Figures 4.82 and 4.39
- 236P: Figures 4.88 and 4.89

## 4.2 Results for individual comets with well-fit tails

We will now present a brief description of the results for individual comets. For each comet, the W3 and W4 data images are shown, the full syndyne/synchrone models are overlaid on the image, and the best-fit syndyne and synchrone are overlaid on the image. The results

are summarized in Table 4.1. We note that the results listed in the table are significant to the first two digits.

### 4.2.1 Long-Period Comets

#### 4.2.1.1 C/2006 OF2 (Broughton)

This comet has a faint dust tail in W3, and a strong dust tail in W4. The tail fitting works reasonably well for W3, and very well for W4. The BFSc for W3 suggests that strong activity occurred before perihelion at ∼2.8 AU, while the BFSc for W4 suggests that strong activity occurred just before perihelion (2.43 AU) at ∼2.5 AU. Both W3 and W4 have a BFSd of $\beta$ = 0.0003, suggesting that the tail particles are ∼3 mm in diameter.

#### 4.2.1.2 C/2006 W3 (Christensen)

This comet was extremely bright in both W3 and W4. The tail fitting had odd (but consistent) results for both W3 and W4 due to the brightness of the tail. The BFSc for both W3 and W4 suggest that strong activity began at ∼3.2 AU, just before perihelion (3.13 AU). Both W3 and W4 have a BFSd of $\beta = 0.003$, suggesting that the tail particles are ∼300$\mu$m in diameter.

#### 4.2.1.3 C/2007 B2 (Skiff)

This comet was barely visible in W3, but had a faint tail in W4. The tail fitting did not work well for W3, but worked well for W4. The BFSc for W4 suggests that strong activity occurred at ∼3.6 AU, well before the comet's perihelion at 2.98 AU. The BFSd for W4 is $\beta$ = 0.001, suggesting that the tail particles are ∼1 mm in diameter.

#### 4.2.1.4 C/2007 G1 (LINEAR)

This comet has a very faint dust tail in W3, and a strong dust tail in W4. The tail fitting did not work well for W3, but worked well for W4. The BFSc for W4 suggests that strong activity occurred at ∼2.7 AU, just before the comet's perihelion at 2.65 AU. the BFSd for W4 is $\beta = 0.0003$, suggesting that the tail particles are ∼3mm in diameter.

#### 4.2.1.5 C/2007 Q3 (Siding Spring)

This comet was extremely bright in both W3 and W4. In both W3 and W4, the tail appears to be comprised of two components, a younger one (estimated by hand) which is ∼175 days old with $\beta = 0.01$, and the fitted component which is ∼230 days old with $\beta = 0.001$. This

fitted component corresponds to strong activity occurring at ∼2.25 AU, which is precisely at the comet's perihelion, and a particle size of about 1 mm.

#### 4.2.1.6 C/2007 VO53 (Spacewatch)

This comet has a very short and faint tail in W3, and a strong but short tail in W4. The fitting does not work for W3, but works well for W4. The BFSc for W4 suggests that strong activity occurred at ∼ 6.0 AU, about 1.25 years before the comet reached its perihelion of 4.84 AU (note that this comet was observed pre-perihelion). This is one of the few LPCs that had strong emission well before perihelion. The BFSd for W4 is $\beta = 0.001$, suggesting that the tail particles are ∼1 mm in diameter.

#### 4.2.1.7 C/2008 A1 (McNaught)

This comet was hardly detected in W3, and presented a strong but diffuse tail in W4. The fitting does not work for W3, but works well for W4. The BFSc for W4 suggests that strong activity occurred at ∼1.2 AU, not too much before the comet's perihelion at 1.07 AU. The BFSd for W4 is $\beta = 0.0001$, suggesting that the tail particles are ∼1 cm in diameter. There appears to be some infrared emission to the west (left) of the nucleus on the image which

is not in the comet's orbital plane and cannot be explained by the presence of very small particles.

#### 4.2.1.8 C/2008 FK75 (Lemmon-Siding Spring)

This comet has a faint, short tail in W3 and a strong, but still short tail in W4. The fitting does not work well for W3, but works well for W4. The BFSc for W4 suggests that strong activity occurred at ∼5.2 AU, well before the comet's perihelion distance of 4.51 AU (note that this comet was observed pre-perihelion). The BFSd for W4 is $\beta = 0.03$, suggesting the tail particles are ∼30 $\mu$m in diameter.

#### 4.2.1.9 C/2008 N1 (Holmes)

This comet was observed twice by WISE during the course of it mission, once during February 2010 and a second time in June 2010. The two sets of observations will be discussed separately, then compared.

In February 2010 when the comet was at 3.08 AU, it had a faint, but long tail in W3, and a somewhat strong and long tail in W4. The fitting worked well for both W3 and W4. The BFSc for both W3 and W4 suggests that strong activity occurred at ∼3.2 AU, compared to

the comet's perihelion distance of 2.78 AU. The BFSd for both W3 and W4 is $\beta = 0.001$, suggesting that the tail particles are $\sim$1 mm in diameter.

In June 2010 when the comet was at 3.75 AU, it had a very faint tail in W3, and a somewhat faint tail in W4. The fitting did not work well for W3, but did work well for W4. The BFSc for W4 suggests that strong activity occurred at $\sim$ 2.9 AU, compared to the comet's perihelion distance of 2.78 AU. The BFSd for W4 is $\beta = 0.0003$, suggesting that the tail particles are $\sim$3 mm in diameter.

While the BFSc from the two observations may seem inconsistent, it must be noted that the tail is significantly fainter in the June observations. It is interesting that the grains are found to be slightly larger in the June data; this may suggest that the smaller grains have been swept away in the 3 months between observations. We do note, however, that the orbit plane angle separation is very different in the two observations: in February, it is 12.21°, while in June it is -14.59°.

#### 4.2.1.10 C/2008 Q3 (Garradd)

This comet has a very strong and long tail in both W3 and W4, and the fitting works well for both images. However, due to a relatively small orbit plane angle separation (-1.23°), the W3 and W4 results do not match well. The BSFc for W3 suggests that strong activity

occurred at ∼3.3 AU, while the BSFc for W4 suggests that strong activity occurred at ∼1.9 AU; both results are well before the perihelion distance of 1.79 AU. The W3 BSFd is $\beta$ = 0.1, while the W4 BSFd is $\beta$ = 0.001, suggesting tail particles of ∼10$\mu$m and ∼1 mm in diameter, respectively.

#### 4.2.1.11 C/2008 T2 (Cardinal)

This comet has an extremely faint and long tail in W3, and a somewhat faint and long tail in W4. The tail fitting did not work well for W3, but worked well for W4. The BFSc for W4 suggests that strong activity occurred at ∼1.5 AU, before the perihelion distance of 1.20 AU. The BFSd for W4 is $\beta$ = 0.0001, suggesting that the tail particles are ∼1 cm in diameter.

#### 4.2.1.12 C/2009 F6 (Yi-SWAN)

This comet has a long and faint tail in both W3 and W4, and the tail fitting worked well for both wavelength bands, though a background star may have interfered with the W3 fit. The BFSc for W3 suggests strong activity occurring at ∼3.3 AU, while the BFSc for W4 suggests strong activity occurring at the perihelion distance of 1.28 AU. The BDFd for both W3 and W4 is $\beta$ = 0.0001, suggesting that the tail particles are ∼1 cm in diameter.

#### 4.2.1.13 C/2009 G1 (STEREO)

This comet has a faint, medium length tail in W3, and a somewhat faint and long tail in W4. The tail fitting did not work well for W3 due to background stars, but worked well for W4. The BFSc for W4 suggests that strong activity occurred at ∼1.3 AU, before the perihelion distance of 1.13 AU. The BFSd for W4 is $\beta = 0.0001$, suggesting that the tail particles are ∼1 cm in diameter.

#### 4.2.1.14 C/2009 K2 (Catalina)

This comet has a faint, somewhat curved tail in W3, and a stronger, curved tail in W4. The tail fitting did not work well for W3 due to the faintness of the tail, but worked well for W4. The BFSc for W4 suggests that strong activity occurred at ∼3.7 AU, well before the perihelion distance of 3.25 AU. The BFSd for W4 is $\beta = 0.001$, suggesting that the tail particles are ∼1 mm in diameter.

#### 4.2.1.15 C/2009 K5 (McNaught)

This comet was observed during the post-cryogenic phase of the mission only in bands W1 and W2. However, a strong dust tail was still readily visible in the images. The comet has

a faint, diffuse tail in W1, and an even fainter tail in W2. However, the tail fitting worked well for both W1 and W2, despite background stars being present in the stacked images. The BFSc for W1 suggests that strong activity occurred at ∼1.5 AU, while the BFSc for W2 suggests that strong activity occurred at ∼1.7 AU. Both of these are before the perihelion distance of 1.42 AU, though the W1 BFSc is very close. The BFSd for both W1 and W2 is $\beta = 0.0003$, suggesting that the tail particles are ∼3 mm in diameter. It is interesting to see that the best-fit particle size for these W1 and W2 images is within the same range as for the other comets which all used W3 and W4 data.

#### 4.2.1.16 C/2009 P1 (Garradd)

This comet was observed at 6.35 AU pre-perihelion, making it the most-distant inbound comet in our dataset with an apparent dust tail.

This comet has a bright coma in both W3 and W4, and a short, but strong, tail in W4. The fitting does not work for W3, but works well for W4 despite the tail being very short. The BFSc for W4 suggests that strong activity occurred at a very-distant ∼17.1 AU, compared to the perihelion distance of 1.55 AU (note that this comet was observed about 1.5 years pre-perihelion). The BFSd for W4 is $\beta = 0.0001$, suggesting that the tail particles are

$\sim$1 cm in diameter. While this may sound extremely far for emission to begin, the dynamical models show quite clearly that the tail must be old and comprised of very large dust grains.

#### 4.2.1.17 C/2010 J1 (Boattini)

The comet was observed in both April and July 2010, but the tail was only well-fit in the July data. The comet has a long, thin tail in both the W3 and W4 data, however, background noise in W3 caused the fitting algorithm to select a BFSc and BFSd which was definitely incorrect. The BFSc for W4 suggests that strong activity occurred at $\sim$1.7 AU, essentially at the perihelion distance of 1.69 AU. The BFSd for W4 was $\beta = 0.001$, suggesting that the tail particles are $\sim$1 mm in diameter.

#### 4.2.1.18 C/2010 J4 (WISE)

This comet was observed twice by WISE, on May 1 and on May 12, 2010. The two sets of observations will be discussed separately, then compared.

On May 1, the comet was 2 days pre-perihelion, and was imaged in a crowded star field, but a faint, medium length tail is present in both W3 and W4. The fitting did not work well for W3 due to confusion from field stars, but worked well for W4 where the stars were

somewhat fainter. The BFSc for W4 suggested that strong activity occurred at ∼1.1 AU (17 days before perihelion), just before the perihelion distance of 1.09 AU. The BFSd for W4 was $\beta = 0.03$, suggesting that the tail particles are ∼30$\mu$m in diameter.

On May 12, the comet was 9 days post-perihelion, and medium-strength, medium-length dust tail was seen in both W3 and W4. The fitting worked well for both W3 and W4. The BFSc for W3 and W4 suggested that strong activity occurred at ∼1.2 (23 days pre-perihelion) and ∼1.1 AU (16 days pre-perihelion), respectively, again just before the perihelion distance of 1.09 AU. The BFSd for both W3 and W4 was $\beta = 0.01$, suggesting that the tail particles are ∼100$\mu$m in diameter.

The consistency of the two fits (both showing the dust was emitted 16-20 days pre-perihelion) is a testament to the accuracy of the dynamical models and tail-fitting method. It is interesting that the dust grains seem to be somewhat larger during the second set of observations on May 12. It is possible that the smaller grains got quickly swept away after they were emitted.

#### 4.2.1.19 C/2010 L5 (WISE)

This comet was also observed twice by WISE, in June and July 2010. The two sets of observations will be discussed separately, then compared. A preliminary version of this

result was presented by Kramer et al. [2013] at the Division for Planetary Sciences annual meeting.

In June, the comet has a wide, nearly conically shaped tail in both W3 and W4. The fitting worked well for both W3 and W4. The BFSc for both W3 and W4 suggested that strong emission occurred at $\sim$0.79 AU, corresponding precisely to the comet's perihelion distance and date. The BFSd for both W3 and W4 was $\beta = 0.003$, suggesting that the dust tail particles are on average $\sim 300\mu$m in diameter.

In July, the tail was significantly narrower and fainter in both W3 and W4. The W3 fitting did not work well due to some background emission, but the W4 fitting worked very well. The BFSc for W4 suggested that strong emission occurred at $\sim$0.79 AU, again corresponding precisely to the comet's perihelion distance and date. The BFSd for W4 was $\beta = 0.001$, suggesting that the dust particles are on average $\sim$1 mm in diameter.

Once again, the consistency in the fitted emission date and perihelion distance is remarkable, as is the fact that the emission seems to have occurred nearly entirely and exactly at perihelion. As was the case with C/2010 J4, the average size of the dust grains in the tail seemed to have increased somewhat between observations.

### 4.2.2 Short-Period Comets

#### 4.2.2.1 10P/Tempel 2

In the WISE data, 10P had an extremely bright dust trail in both W3 and W4. The tail was well fit in both W3 and W4. The BFSc for both W3 and W4 corresponded strong emission occurring at ∼4.7 AU, which is the comet's aphelion distance. The BFSd for both W3 and W4 was $\beta = 0.0001$, suggesting that the tail particles are ∼1 cm in diameter. We note, however, that this comet will be studied in greater detail at a later time by another member of the NEOWISE team who specializes in dust trails.

#### 4.2.2.2 17P/Holmes

In the WISE data, 17P had an extremely faint dust tail in W3, and a faint but easily detectable dust tail in W4. The fitting did not work well for W3, but did work well for W4. The BFSc for W4 corresponded to strong emission occurring at ∼2.06 AU, precisely at the comet's perihelion distance. The BFSd for W4 is $\beta = 0.0001$, suggesting that the tail particles are ∼1 cm in diameter.

A preliminary version of the results presented here was presented in Stevenson et al. [2014], with the tail modeling work done by the author of this dissertation. The results in

this dissertation differ than those in the paper primarily due to improvements in the tail fitting method, however, they are consistent within the error bars presented in Stevenson et al. [2014].

#### 4.2.2.3 19P/Borrelly

This comet was observed twice by WISE during the course of its mission, once during February 2010 and a second time in July 2010. The two sets of observations will be discussed separately, then compared.

In February, the comet showed a distinct but diffuse tail as well as a trail in both W3 and W4. The fitting worked well for both W3 and W4, primarily finding the tail rather than the trail. The BFSc for W3 and W4 suggests strong emission occurring at $\sim$1.4 AU and $\sim$2.1 AU, respectively, before the perihelion distance of 1.35 AU. The distance for W4 is higher likely due to contamination from the trail. The BFSd for both W3 and W4 is $\beta = 0.0001$, suggesting that the tail particles are $\sim$1 cm in diameter.

In July, the tail and trail were still clearly visible in both W3 and W4, though they were noticeably fainter. The fitting worked well for both W3 and W4. The BFSc for W3 and W4 suggest strong emission occurring at $\sim$1.6 AU and $\sim$1.5 AU, respectively, well outside the

perihelion distance of 1.35 AU. The BFSd for both W3 and W4 is $\beta = 0.0001$, suggesting that the tail particles are $\sim$1 cm in diameter.

We can see here again that the results are quite consistent between the two observations in terms of the distance at which strong emission occurs. It is interesting to note that the size of the tail particles does not seem to change between observations.

#### 4.2.2.4 64P/Swift-Gehrels

This comet had an extremely faint dust tail in W3 and a moderately faint dust tail in W4. The tail fitting worked well for W3, despite the faintness of the comet, and moderately well for W4 despite some erroneous points from background emission. The BFSc for W3 and W4 suggest strong emission occurring at $\sim$1.4 AU and $\sim$1.9 AU, respectively, before the comet's perihelion of 1.38 AU. The BFSd for W3 is $\beta = 0.0003$, suggesting that the tail particles are $\sim$3 mm in diameter; the BFSd for W4 is $\beta = 0.003$, suggesting that the tail particles are $\sim 300\mu$m in diameter. We note that the W3 results seem to match the fitted tail points better than the W4 results.

#### 4.2.2.5 67P/Churymov-Gerasimenko

This comet was observed twice by WISE during the course of it mission, once during January 2010 and a second time in June 2010. The two sets of observations will be discussed separately, then compared.

In January, the comet had a long, thin, bright tail in both W3 and W4, with a hint of a trail in both bands. The fitting worked well for both W3 and W4. The BFSc for W3 and W4 suggest strong emission occurring at ∼5.3 AU and ∼4.4 AU, respectively, which is closer to the comet's aphelion (5.68 AU) than its perihelion (1.24 AU). However, due to unfavorable viewing geometry, it is difficult to distinguish between synchrones which are widely separated in time. The BFSd for both W3 and W4 was $\beta = 0.0001$, suggesting that the tail particles are ∼1 cm in diameter.

In June, the tail was somewhat fainter than in January, but was still long, thin, and visible in both W3 and W4. The fitting worked well for both W3 and W4. The BFSc for W3 and W4 both suggest strong emission occurring at ∼1.3 AU, near the comet's perihelion of 1.24 AU. The BFSd for both W3 and W4 was $\beta = 0.0001$, suggesting that the tail particles are ∼1 cm in diameter.

We can see here that while the age of the dust is not consistent between the two observations (likely due to ambiguities due to unfavorable viewing geometry in January), the size of the dust particles is consistent.

A preliminary version of the results presented here was published by Bauer et al. [2012], with the tail modeling word done by the author of this dissertation. The results presented here differ slightly from those in the paper primarily because that work was done before the development of the tail-fitting method used in this dissertation.

#### 4.2.2.6 68P/Klemola

This comet had a clear nucleus signal in both W3 and W4, with only a hint of a tail in W3, and a long, diffuse tail in W4. The fitting did not work for W3, but did work for W4. the BFSc for W4 suggests that strong emission occurred at $\sim$2.2 AU, well before the perihelion distance of 1.76 AU. The BFSd for W4 is $\beta = 0.001$, suggesting that the tail particles are $\sim$1mm in diameter.

#### 4.2.2.7 77P/Longmore

This comet has a long, medium-width tail in both W3 and W4. The fitting worked well for both W3 and W4, but, as is apparent in Figure 4.32, the model chosen by the fitting algorithm does not seem to match up with the fitted tail points very well. However, we include it as an example of how the fitting method may sometimes give less-than-optimal results. The BFSc for W3 and W4 suggest that strong emission occurred at ∼2.3 AU and ∼2.8 AU, respectively, at the comet's perihelion distance for W3, and well before perihelion for W4. The BFSd for W3 was $\beta = 0.001$, suggesting that the tail particles are ∼1 mm in diameter; the BFSd for W4 was $\beta = 0.3$ suggesting that the tail particles are ∼30$\mu$m in diameter.

#### 4.2.2.8 94P/Russell 4

This comet appears to have a neck-line structure in both W3 and W4, with tail-like emission as well. The fitting did not work well for W3 due to the faintness of the emission, but did work well for W4. The BFSc for W4 suggests that strong emission occurred at ∼2.6 AU, well before the perihelion distance of 2.24 AU. The BFSd for W4 is $\beta = 0.0003$, suggesting that the tail particles are ∼3 mm in diameter.

#### 4.2.2.9 100P/Hartley 1

This comet has a medium-length, medium-brightness tail in both W3 and W4. The tail fitting worked well for both W3 and W4, but we note that the orbit plane angle for this comet is small (-2.45°), and thus the results may be misleading. The BFSc for W3 and W4 suggests that strong emission occurred at ∼2.7 AU and ∼4.7 AU, respectively, both well outside the perihelion distance of 1.98 AU. The BFSd for W3 was $\beta = 0.0003$, suggesting that the tail particles are ∼3 mm in diameter; the BFSd for W4 was $\beta = 0.0001$, suggesting that the tail particles are ∼1 cm in diameter.

#### 4.2.2.10 118P/Shoemaker-Levy 4

This comet has a very bright and large coma in both W3 and W4, shows a tail in both bands, and possibly a trail as well. The fitting works well in both W3 and W4. The BFSc for W3 and W4 suggest that strong emission occurred at ∼2.3 AU and ∼2.5 AU, respectively, both well outside the perihelion distance of 1.98 AU. The BFSc for W3 was $\beta = 0.001$, suggesting that the tail particles are ∼1 mm in diameter; the BFSd for W4 was $\beta = 0.0003$, suggesting that the tail particles are ∼3 mm in diameter.

Interestingly, the position angle of the tail appears quite different in the two wavelength bands. This is the only comet in our data set which seems to have this property.

#### 4.2.2.11 186P/Garradd

This comet was not seen in W3, and had a very faint, but long tail in W4. The fitting worked well for W4. The BFSc for W4 suggests that strong emission occurred at ∼4.3 AU, just outside its perihelion distance of 4.26 AU. Note that this comet's orbit is nearly circular; that is, $e$=0.12, so the difference in heliocentric distance between perihelion and aphelion is much smaller than for the vast majority of comets. The BFSd for W4 is $\beta = 0.0003$, suggesting that the tail particles are ∼3 mm in diameter.

#### 4.2.2.12 195P/Hill

This comet has an extremely faint tail in W3, and a faint, medium-length tail in W4. The fitting did not work well for W3, but did work well for W4. The BFSc for W4 suggests that strong activity occurred at ∼5.8 AU, nearly 2.5 years before the perihelion distance of 4.44 AU. The BFSd for W4 is $\beta = 0.0001$, suggesting that the tail particles are ∼1 cm in diameter.

#### 4.2.2.13 199P/Shoemaker 4

This comet had a faint, medium-length tail in W3, and a faint, long tail in W4. The fitting worked well for both W3 and W4. The BFSc for W3 and W4 suggest that strong activity occurred at ∼3.2 AU and 3.0 AU, respectively, both outside the perihelion distance of 2.94 AU. The BFSd for both W3 and W4 is $\beta = 0.0003$, suggesting that the tail particles are ∼3 mm in diameter.

#### 4.2.2.14 213P/Van Ness

This comet was observed twice by WISE during the course of it mission, once during January 2010 and a second time in July 2010.

The January images were captured when the comet was at an extremely low orbit plane angle separation ($\alpha$ = -0.59°), and thus it is impossible to distinguish between the different models. However, the comet did have a long, thing tail in both the W3 and W4 images, with the tail being brighter in W4.

In July, the comet had a long, thin tail in both W3 and W4. The fitting worked well for both W3 and W4. The BFSc for both W3 and W4 suggested that strong emission occurred

at ∼4.7 AU, closer to the comet's aphelion (4.73 AU) than perihelion (2.12 AU). The BFSd for both W3 and W4 is $\beta = 0.0003$, suggesting that the tail particles are ∼3 mm in diameter.

For both sets of observations and in both W3 and W4, extended emission was present in the comet's orbit plane. This may have something to do with the fragmentation event that was detected in 2011.

#### 4.2.2.15 217P/LINEAR

This comet was observed while it was in a field with a good deal of background infrared emission, but a medium-strength tail was present in both W3 and W4. Due to the background emission, the tail was not well fit in W3, but was fit reasonably well in W4. The BFSc for W4 suggests that strong emission occurred at ∼1.28 AU, just before the comet's perihelion of 1.28 AU. The BFSd for W4 was $\beta = 0.001$, suggesting that the tail particles are ∼1 mm in diameter.

#### 4.2.2.16 226P/Pigott-LINEAR-Kowalski

This comet had an extremely faint tail in both W3 and W4. The fitting did not work well for W3, but seemed to find the tail reasonably well in W4. The BFSc for W4 suggests that

strong emission occurred at ∼1.9 AU, before the comet's perihelion distance of 1.77 AU. The BFSd for W4 is $\beta = 0.0003$, suggesting that the tail particles are ∼3 mm in diameter.

#### 4.2.2.17 232P/Hill

This comet has a relatively bright coma, and a short tail in both W3 and W4. The W3 data seems to suggest a neckline type structure. The fitting worked well for both W3 and W4. The BFSc for W3 and W4 was ∼3.1 AU and ∼3.0 AU, respectively, just before the comet's perihelion at 2.98 AU. The BFSd for W3 was $\beta = 0.001$, suggesting that the tail particles are ∼1 mm in diameter; the BFSd for W4 was $\beta = 0.003$, suggesting that the tail particles are ∼300$\mu$m in diameter.

#### 4.2.2.18 237P/LINEAR

This comet had a long, thin tail in both W3 and W4. The fitting worked well for both W3 and W4. The BFSc for W3 and W4 are ∼4.6 AU and ∼4.9 AU, respectively, closer to the comet's aphelion distance (5.05 AU) than its perihelion distance (2.39 AU). The BFSd for both W3 and W4 was $\beta = 0.0001$, suggesting that the tail particles are ∼1 cm in diameter.

#### 4.2.2.19 P/2009 Q4 (Boattini)

This comet had a faint, medium-length tail in both W3 and W4. The fitting did not work well in W3 due to contamination from a field star, but worked well in W4. The BFSc for W4 suggested that strong activity occurred at ∼1.4 AU, just before the comet's perihelion at 1.32 AU. The BFSd for W4 was $\beta = 0.0003$, suggesting that the tail particles are ∼3 mm in diameter.

#### 4.2.2.20 P/2010 H2 (Vales)

This comet had a very bright, wide, diffuse tail in both W3 and W4. The fitting worked very well for both W3 and W4. The BFSc for both W3 and W4 suggests that strong activity occurred at ∼3.12 AU (outbound), a couple of months after the comet's perihelion of 3.11 AU. The BFSd for both W3 and W4 was $\beta = 0.3$, suggesting that the tail particles are ∼3$\mu$m in diameter. These were the smallest particles definitively found during this work.

The BFSc for W3 and W4 corresponds to emission dates of 14 and 17 May 2010, respectively. This is inconsistent with the comet's known outburst date of 16 April 2010 [Yang and Sarid, 2010]. This comet will require further investigation to fully understand the discrepancy between the results obtained here and the comet's actual outburst date.

#### 4.2.2.21 P/2010 P4 (WISE)

The comet had a faint, diffuse tail in both W3 and W4. The fitting worked well for W3, but did not work for W4 since these images were taken when the cryogen was beginning to run out on the spacecraft, so the background levels for W4 were higher than before. The BFSc for W3 suggested that strong emission occurred at $\sim$2.8 AU, well before the comet's perihelion at 1.86 AU. The BFSd for W3 is $\beta = 0.0003$, suggesting that the tail particles are $\sim$3 mm in diameter.

Table 4.1: Results for comets with well-fit tails

| **Name** | **W3 Fit?** | **W4 Fit?** | **W3 Beta** | **W4 Beta** | **W3 Synch (days)** | **W4 Synch (days)** | **Days since Peri** | **W3 R at Emission Start (AU)** | **W4 R at Emission Start (AU)** |
|---|---|---|---|---|---|---|---|---|---|
| C/2006 OF2 | Y | Y | 0.0003 | 0.0003 | 480 | 569 | 602 | 2.763 | 2.456 |
| C/2006 W3 | Y | Y | 0.003 | 0.003 | 208 | 222 | 287 | 3.215 | 3.186 |
| C/2007 B2 | N | Y | - | 0.001 | - | 432 | 638 | - | 3.577 |
| C/2007 G1 | N | Y | - | 0.0003 | - | 511 | 455 | - | 2.718 |
| C/2007 Q3 | Y | Y | 0.001 | 0.001 | 232 | 230 | 240 | 2.253 | 2.253 |
| C/2007 VO53 | N | Y | - | 0.001 | - | 371 | -92 | - | 6.008 |
| C/2008 A1 | N | Y | - | 0.0001 | - | 533 | 509 | - | 1.157 |
| C/2008 FK75 | N | Y | - | 0.03 | - | 121 | -194 | - | 5.178 |
| C/2008 N1 | Y | Y | 0.001 | 0.001 | 279 | 288 | 130 | 3.179 | 3.223 |
| ” | N | Y | - | 0.0003 | - | 337 | 252 | - | 2.922 |
| C/2008 Q3 | Y | Y | 0.1 | 0.001 | 65 | 260 | 304 | 3.348 | 1.876 |
| C/2008 T2 | N | Y | - | 0.0001 | - | 375 | 319 | - | 1.499 |
| C/2009 F6 | Y | Y | 0.0001 | 0.0001 | 528 | 292 | 299 | 3.331 | 1.276 |
| C/2009 G1 | N | Y | - | 0.0001 | - | 302 | 270 | - | 1.251 |
| C/2009 K2 | N | Y | - | 0.001 | - | 276 | 91 | - | 3.696 |
| C/2009 K5 | W1 | W2 | 0.0003 | 0.0003 | 190 | 231 | 167 | 1.467 | 1.703 |
| C/2009 P1 | N | Y | - | 0.0001 | - | 1613 | -566 | - | 17.079 |
| C/2010 J1 | N | Y | - | 0.001 | - | 134 | 146 | - | 1.701 |
| C/2010 J4 | N | Y | - | 0.03 | - | 15 | -2 | - | 1.13 |
| ” | Y | Y | 0.01 | 0.01 | 32 | 25 | 9 | 1.161 | 1.126 |
| C/2010 L5 | Y | Y | 0.003 | 0.003 | 49 | 53 | 52 | 0.791 | 0.793 |
| ” | N | Y | - | 0.001 | - | 78 | 84 | - | 0.794 |
| 10P | Y | Y | 0.0001 | 0.0001 | 1024 | 943 | -66 | 4.672 | 4.713 |

Continued on next page

| Name | W3 Fit? | W4 Fit? | W3 Beta | W4 Beta | W3 Synch (days) | W4 Synch (days) | Days since Peri | W3 R at Emission Start (AU) | W4 R at Emission Start (AU) |
|---|---|---|---|---|---|---|---|---|---|
| 17P | N | Y | - | 0.0001 | - | 1095 | 1107 | - | 2.055 |
| 19P | Y | Y | 0.0001 | 0.0001 | 612 | 719 | 570 | 1.449 | 2.118 |
| ” | Y | Y | 0.0001 | 0.0001 | 659 | 678 | 733 | 1.582 | 1.484 |
| 64P | Y | Y | 0.0003 | 0.003 | 331 | 204 | 323 | 1.382 | 1.935 |
| 67P | Y | Y | 0.0001 | 0.0001 | 1126 | 858 | 324 | 5.275 | 4.406 |
| ” | Y | Y | 0.0001 | 0.0001 | 495 | 456 | 485 | 1.254 | 1.292 |
| 68P | N | Y | - | 0.001 | - | 259 | 395 | - | 2.213 |
| 77P | Y | Y | 0.001 | 0.3 | 268 | 39 | 303 | 2.321 | 2.852 |
| 94P | N | Y | - | 0.0003 | - | 260 | 53 | - | 2.634 |
| 100P | Y | Y | 0.0003 | 0.0001 | 384 | 1059 | 132 | 2.711 | 4.71 |
| 118P | Y | Y | 0.001 | 0.0003 | 233 | 289 | 82 | 2.31 | 2.533 |
| 186P | N | Y | - | 0.0003 | - | 570 | 742 | - | 4.317 |
| 195P | N | Y | - | 0.0001 | - | 1391 | 514 | - | 5.764 |
| 199P | Y | Y | 0.0003 | 0.0003 | 661 | 404 | 465 | 3.248 | 2.966 |
| 213P | Y | Y | 0.0003 | 0.0003 | 656 | 714 | -345 | 4.665 | 4.702 |
| 217P | N | Y | - | 0.001 | - | 158 | 189 | - | 1.28 |
| 226P | N | Y | - | 0.0003 | - | 267 | 335 | - | 1.875 |
| 232P | Y | Y | 0.001 | 0.003 | 355 | 226 | 211 | 3.097 | 2.985 |
| 237P | Y | Y | 0.0001 | 0.0001 | 1037 | 1823 | 187 | 4.601 | 4.852 |
| P/2009 Q4 | N | Y | - | 0.0003 | - | 216 | 189 | - | 1.361 |
| P/2010 H2 | Y | Y | 0.3 | 0.3 | 54 | 51 | 121 | 3.12 | 3.121 |
| P/2010 P4 | Y | N | 0.0003 | - | 294 | - | 32 | 2.827 | - |

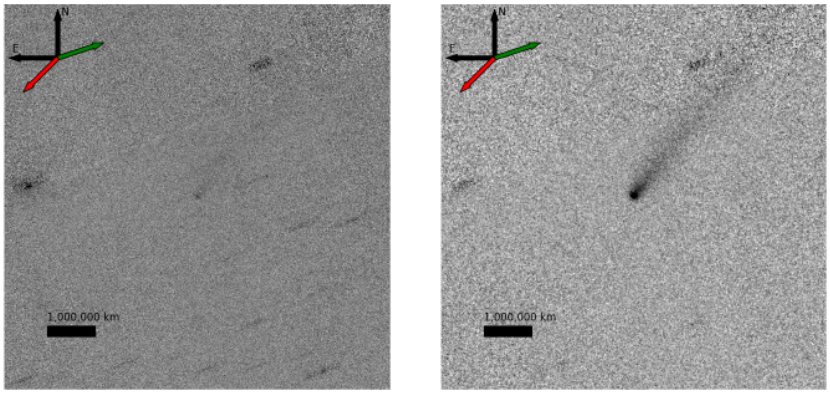


(a) W3 data

(b) W4 data

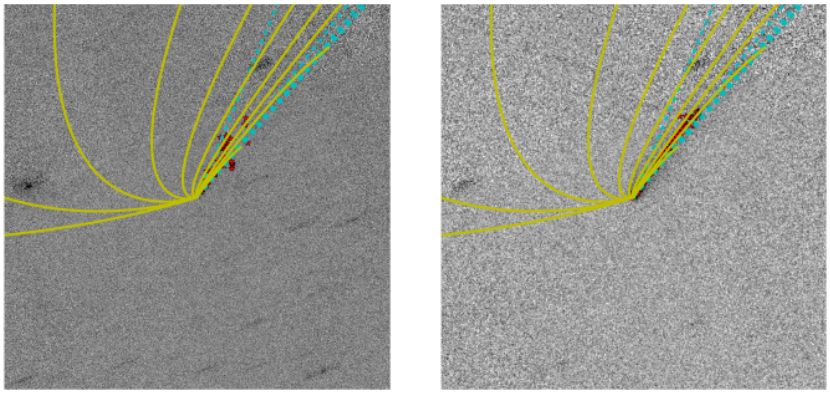

(c) W3 all syndynes and synchrones

(d) W4 all syndynes and synchrones

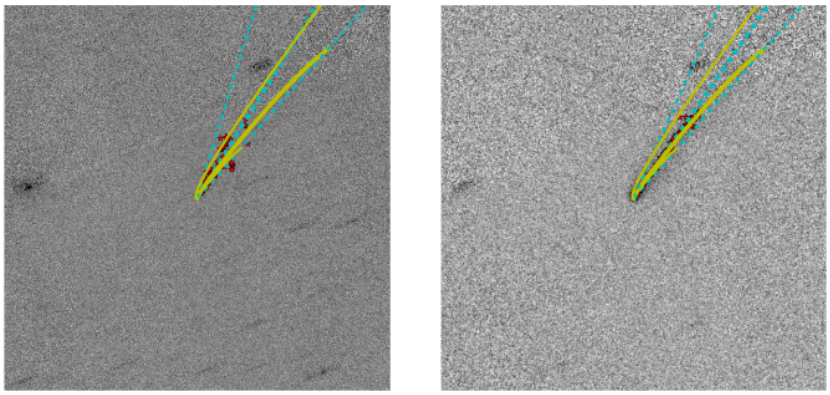

(e) W3 best-fit model

(f) W4 best-fit model

Figure 4.1: The data and results for C/2006 OF2. (a) Included are an inset of the coordinate axes, where N is North, E is East, the green arrow is the sunward direction, and the red arrow is the heliocentric orbit velocity direction. The black bar represents a projected distance 1,000,000 km at the comet's location. For (c)-(f), cyan (dashed line) are synchrones, yellow (solid line) are syndynes, and the red-stars are the fitted tail points. In (c) and (d) are shown W3 and W4 (respectively) images with 5-year Finson-Probstein models and fitted tail points. The $\beta$ values are (3, 1, 0.3, 0.1, 0.03, 0.01, 0.003, 0.001, 0.0003, and 0.0001). The synchrones are 1, 2, 3, 4, and 5 years. In (e) and (f) are shown best-fit syndynes and synchrones for W3 and W4, respectively, with the thick lines showing the nominal best-fit models, and the thinner lines showing the +/- 1 $\sigma$ error analysis results.

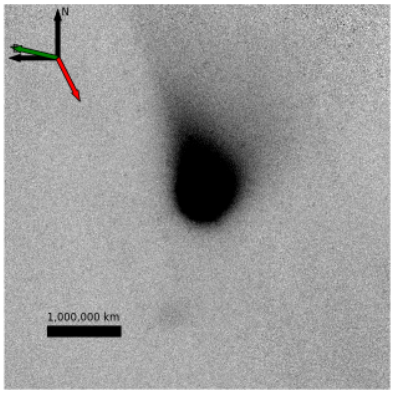


(a) W3 data

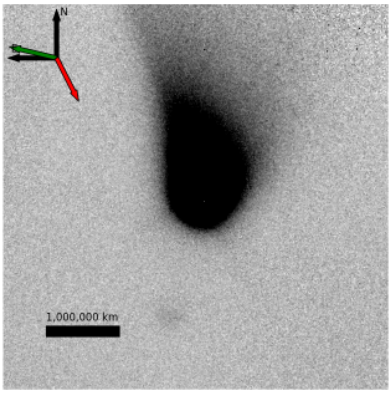


(b) W4 data

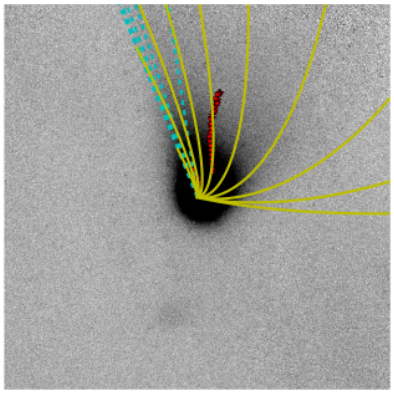

(c) W3 all syndynes and synchrones

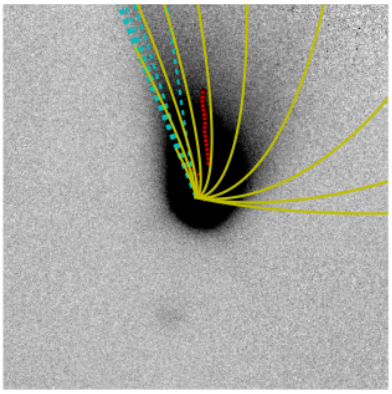

(d) W4 all syndynes and synchrones

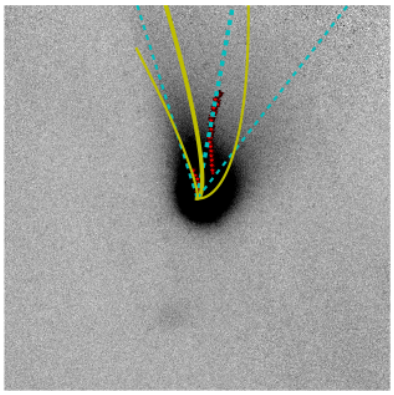

(e) W3 best-fit model

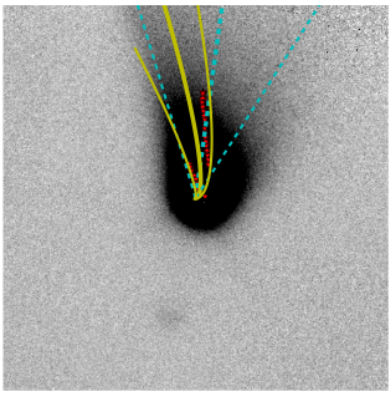

(f) W4 best-fit model

Figure 4.2: The data and results for C/2006 W3. The overlays are the same as in Figure 4.1

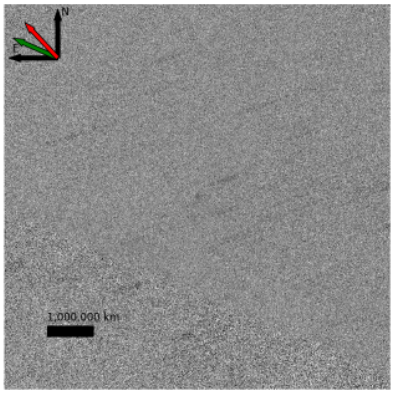


(a) W3 data

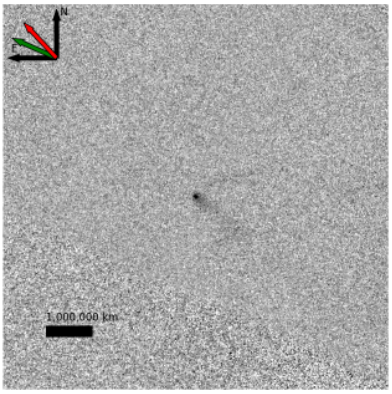


(b) W4 data

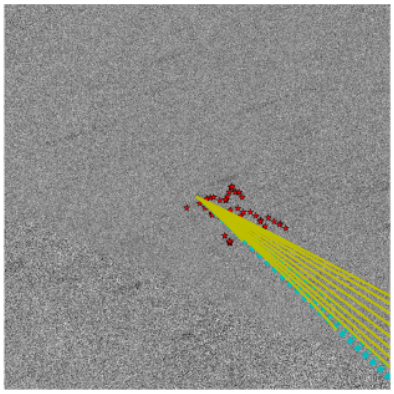

(c) W3 all syndynes and synchrones

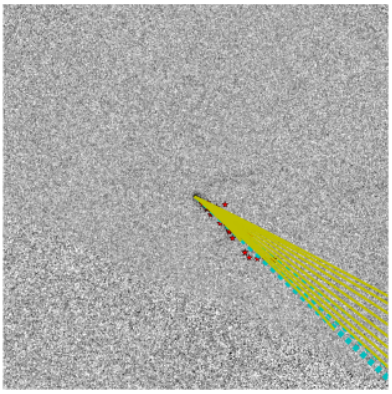

(d) W4 all syndynes and synchrones

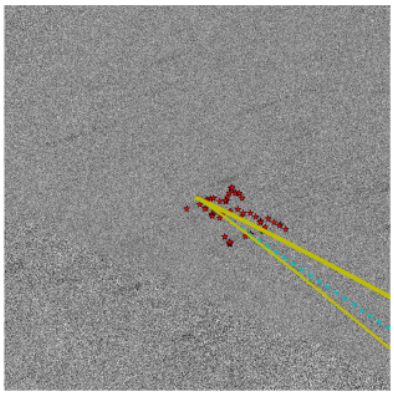

(e) W3 best-fit model

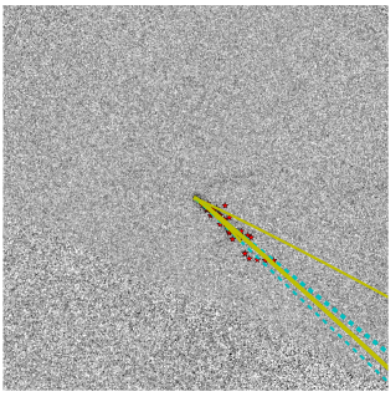

(f) W4 best-fit model

Figure 4.3: The data and results for C/2007 B2. The overlays are the same as in Figure 4.1

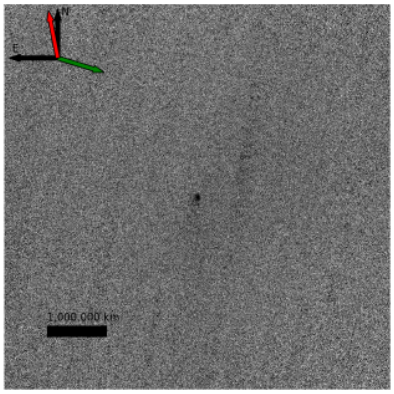


(a) W3 data

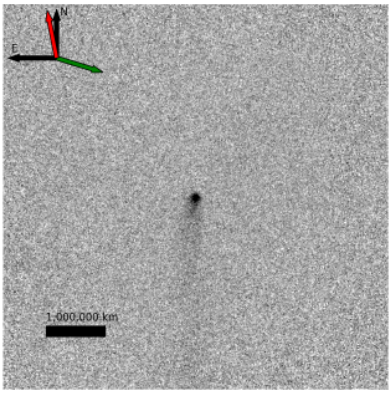


(b) W4 data

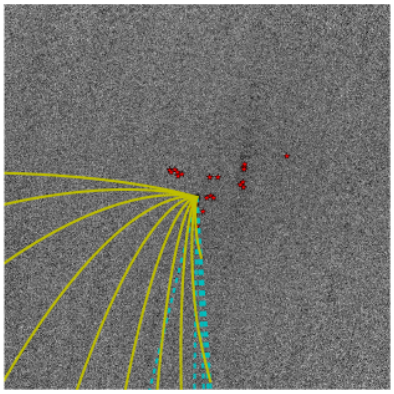

(c) W3 all syndynes and synchrones

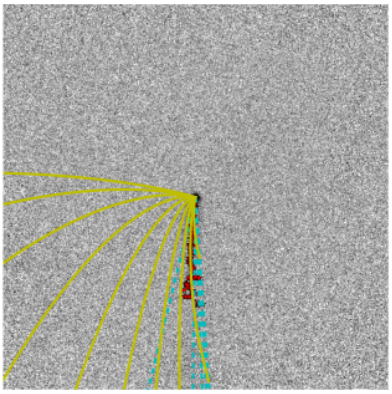

(d) W4 all syndynes and synchrones

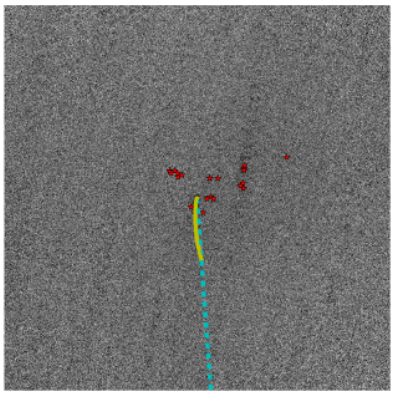

(e) W3 best-fit model

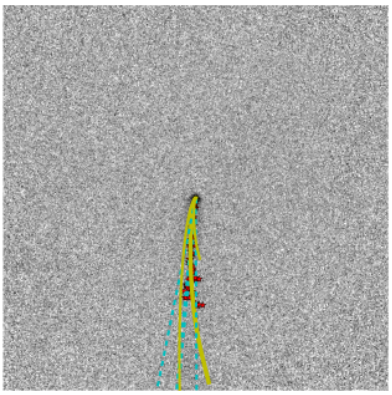

(f) W4 best-fit model

Figure 4.4: The data and results for C/2007 G1. The overlays are the same as in Figure 4.1

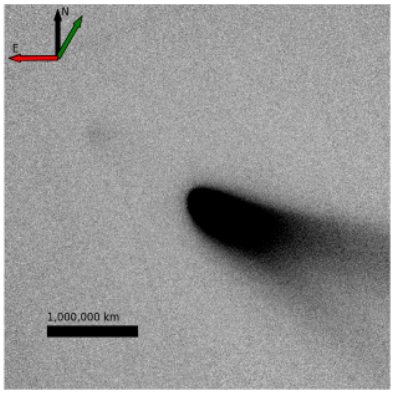


(a) W3 data

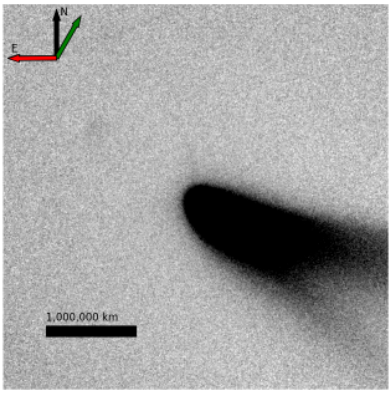


(b) W4 data

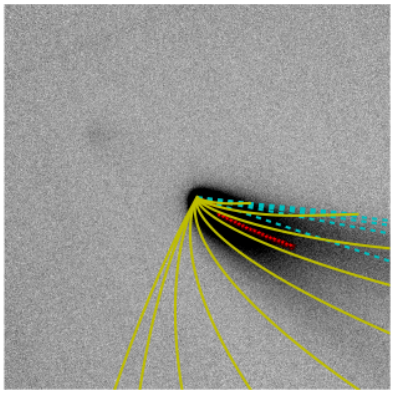

(c) W3 all syndynes and synchrones

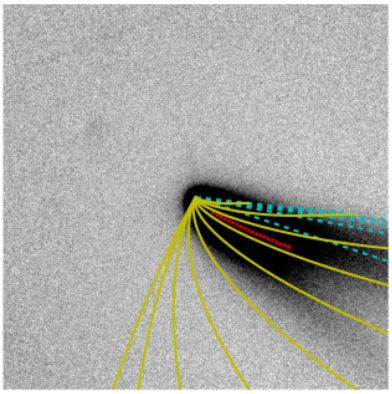

(d) W4 all syndynes and synchrones

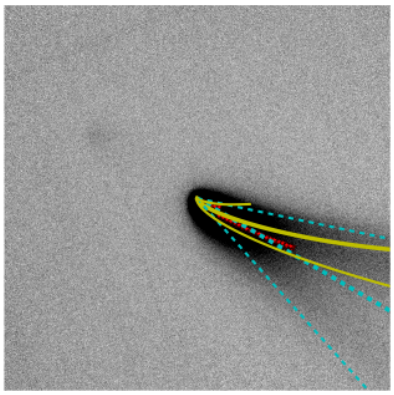

(e) W3 best-fit model

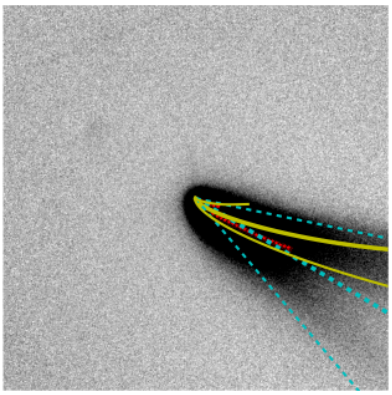

(f) W4 best-fit model

Figure 4.5: The data and results for C/2007 Q3. The overlays are the same as in Figure 4.1

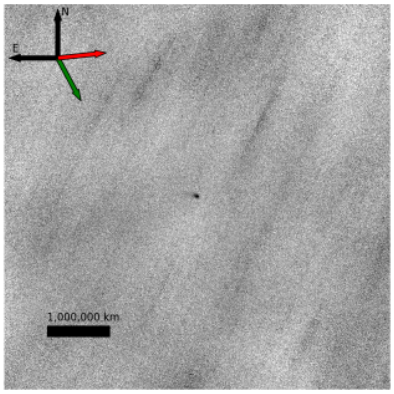


(a) W3 data

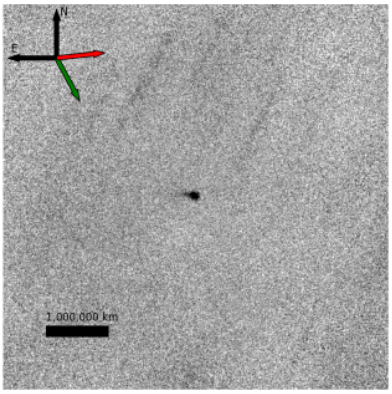


(b) W4 data

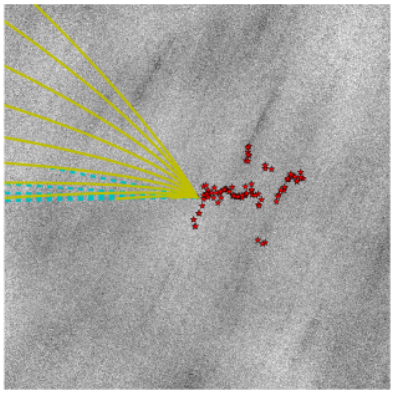

(c) W3 all syndynes and synchrones

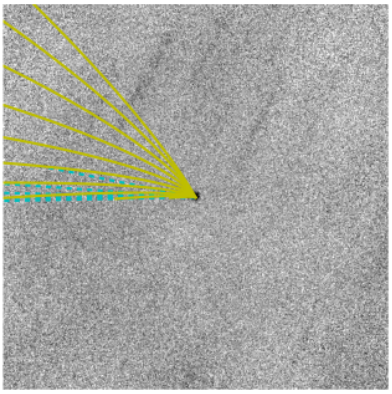

(d) W4 all syndynes and synchrones

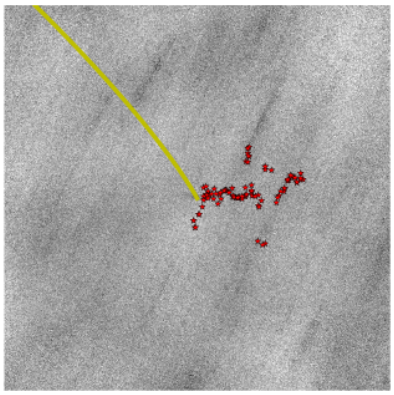

(e) W3 best-fit model

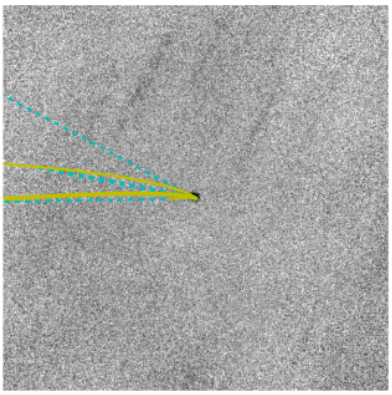

(f) W4 best-fit model

Figure 4.6: The data and results for C/2007 VO53. The overlays are the same as in Figure 4.1

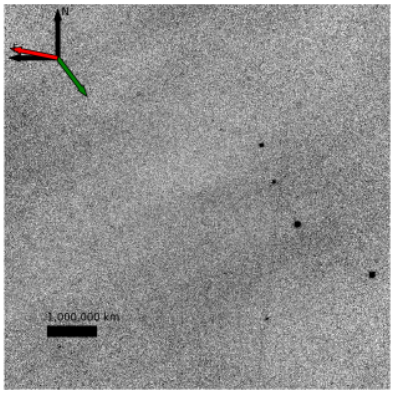

(a) W3 data

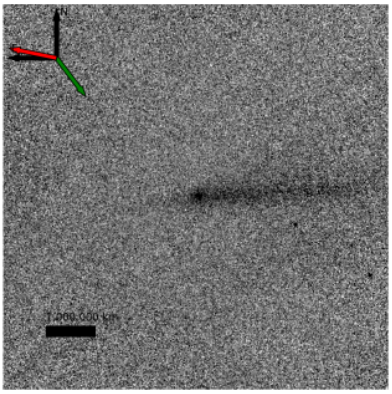

(b) W4 data

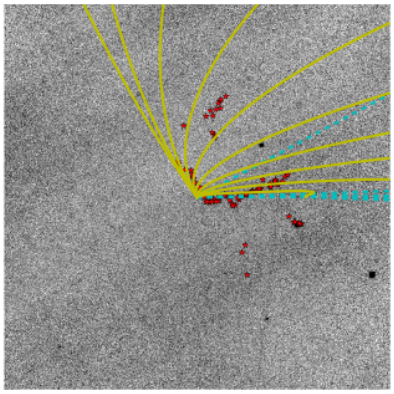

(c) W3 all syndynes and synchrones

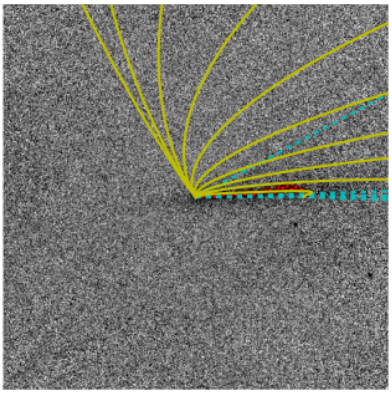

(d) W4 all syndynes and synchrones

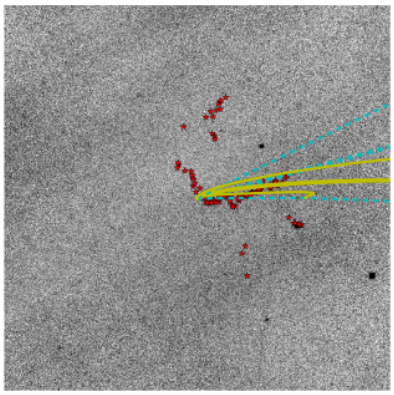

(e) W3 best-fit model

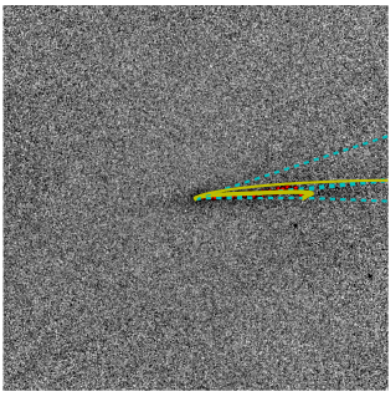

(f) W4 best-fit model

Figure 4.7: The data and results for C/2008 A1. The overlays are the same as in Figure 4.1

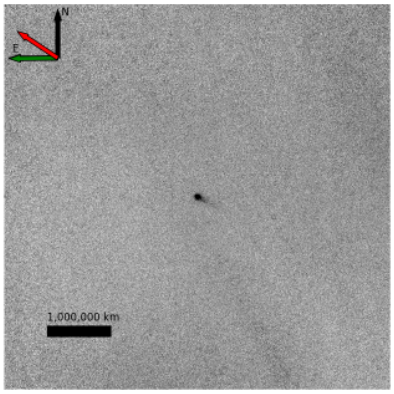


(a) W3 data

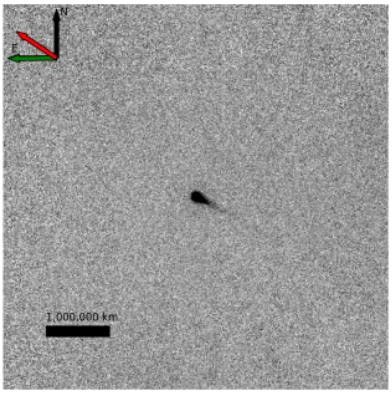


(b) W4 data

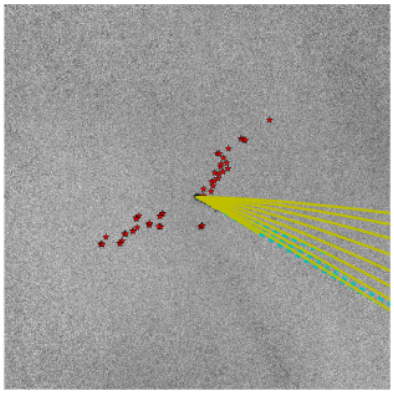

(c) W3 all syndynes and synchrones

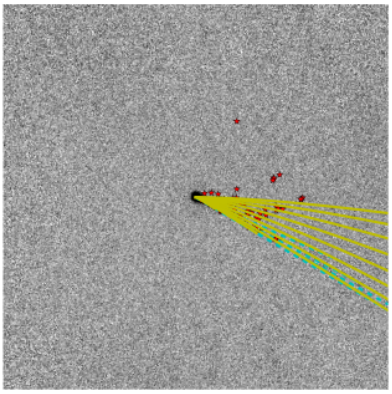

(d) W4 all syndynes and synchrones

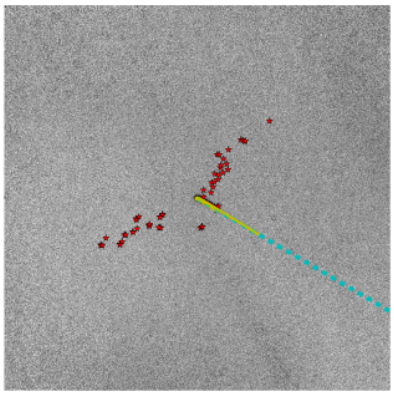

(e) W3 best-fit model

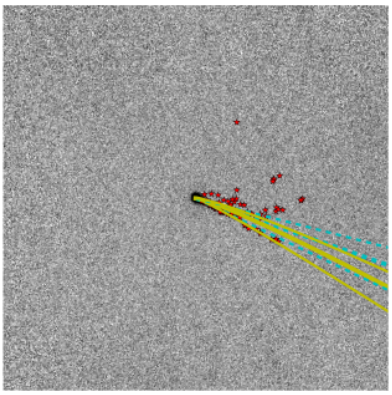

(f) W4 best-fit model

Figure 4.8: The data and results for C/2008 FK75. The overlays are the same as in Figure 4.1

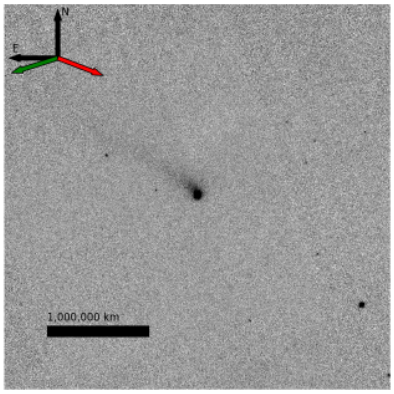


(a) W3 data

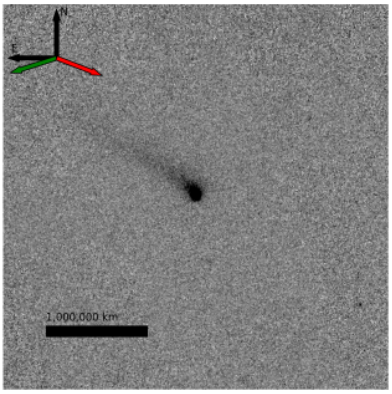


(b) W4 data

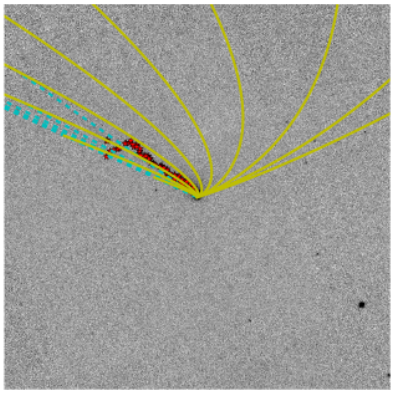

(c) W3 all syndynes and synchrones

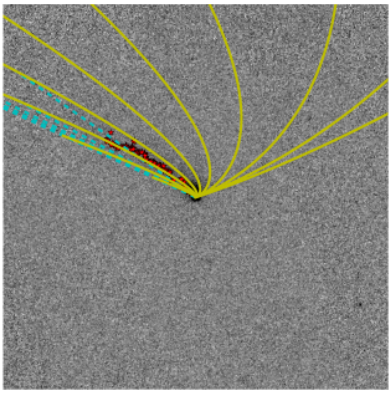

(d) W4 all syndynes and synchrones

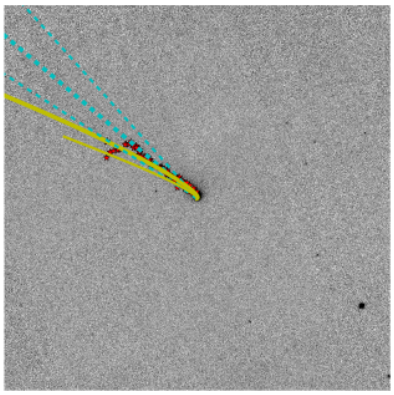

(e) W3 best-fit model

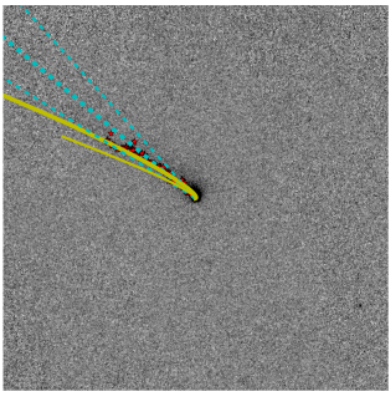

(f) W4 best-fit model

Figure 4.9: The data and results for C/2008 N1 Feb. The overlays are the same as in Figure 4.1

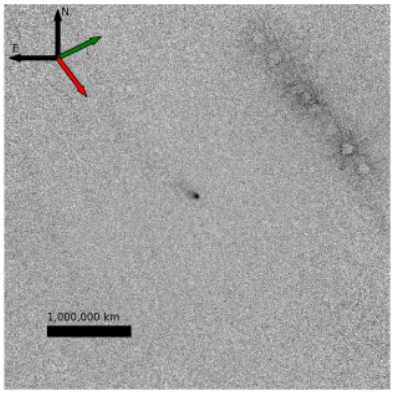


(a) W3 data

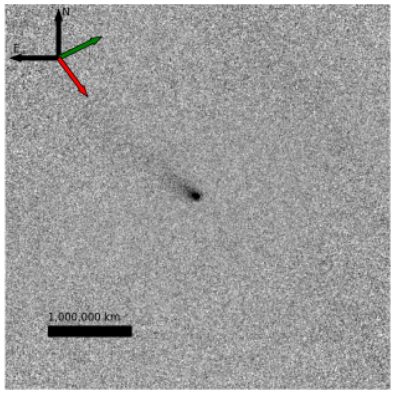


(b) W4 data

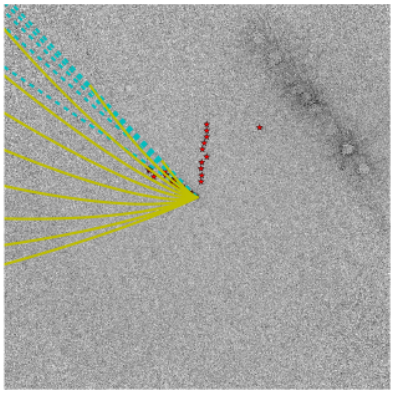

(c) W3 all syndynes and synchrones

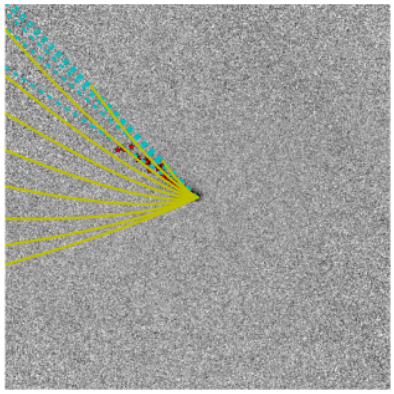

(d) W4 all syndynes and synchrones

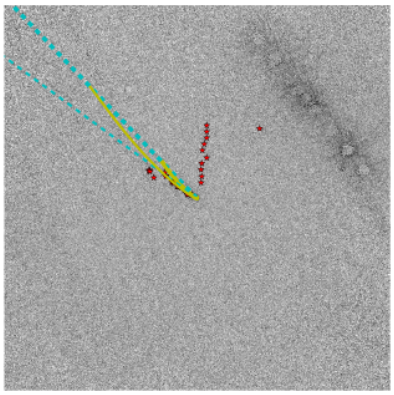

(e) W3 best-fit model

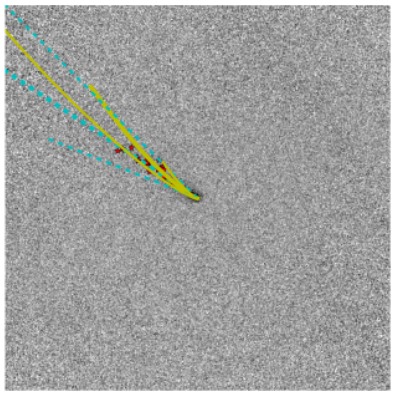

(f) W4 best-fit model

Figure 4.10: The data and results for C/2008 N1 June. The overlays are the same as in Figure 4.1

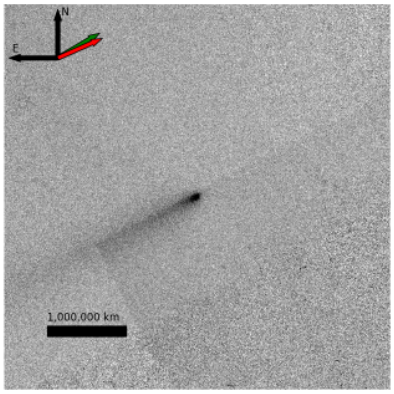


(a) W3 data

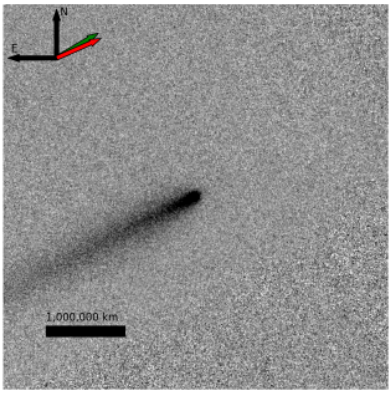


(b) W4 data

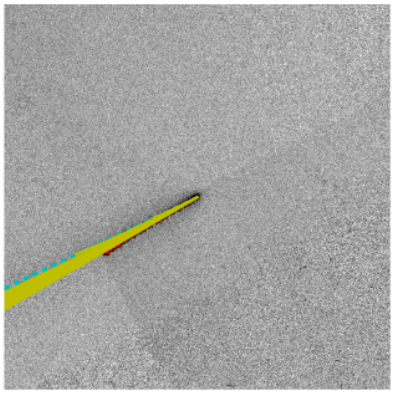

(c) W3 all syndynes and synchrones

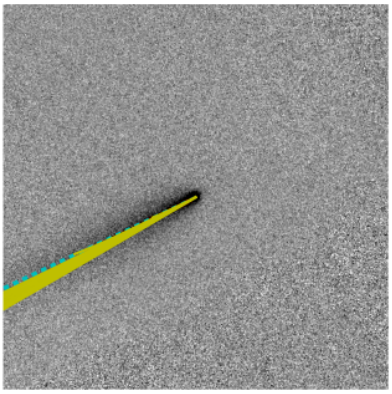

(d) W4 all syndynes and synchrones

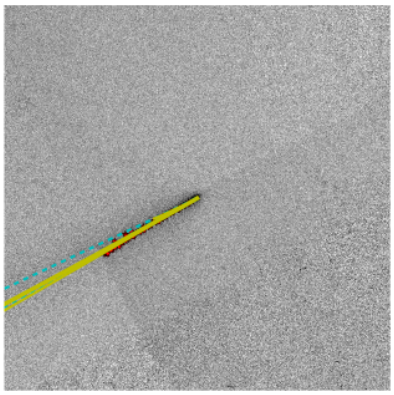

(e) W3 best-fit model

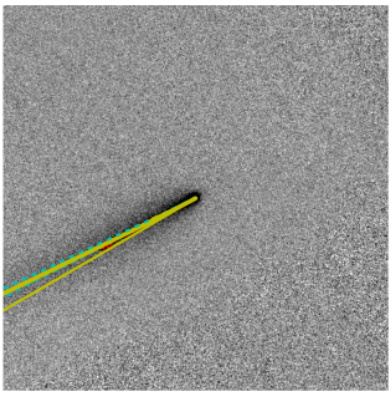

(f) W4 best-fit model

Figure 4.11: The data and results for C/2008 Q3. The overlays are the same as in Figure 4.1

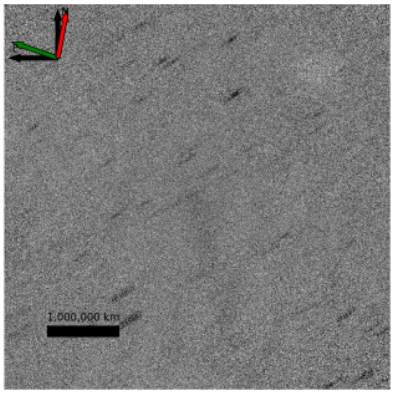

(a) W3 data

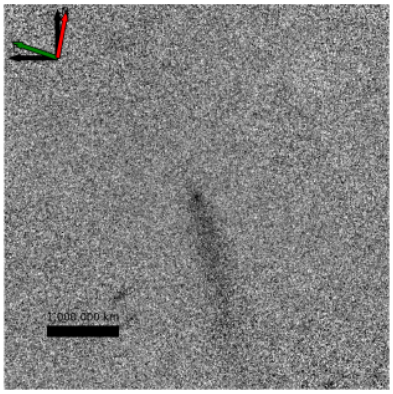

(b) W4 data

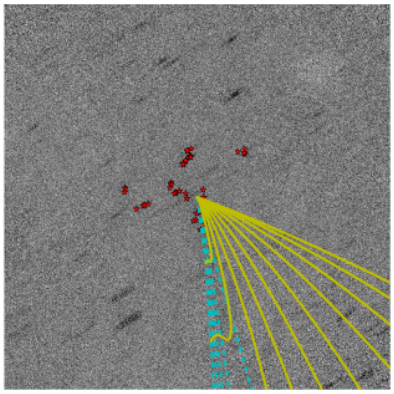

(c) W3 all syndynes and synchrones

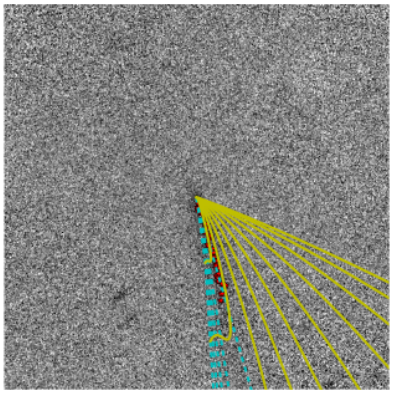

(d) W4 all syndynes and synchrones

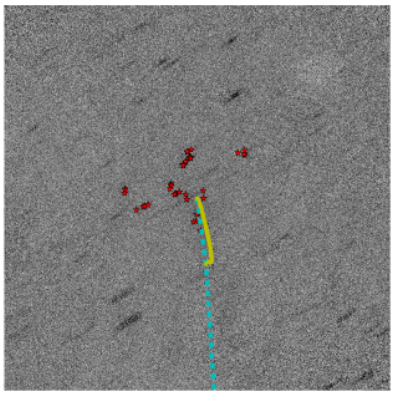

(e) W3 best-fit model

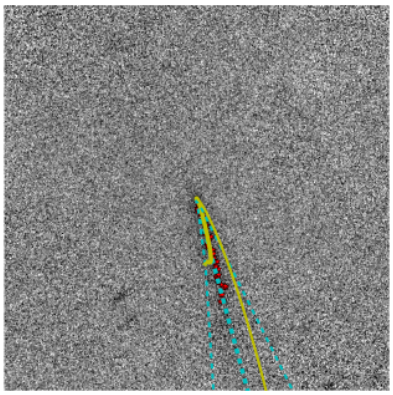

(f) W4 best-fit model

Figure 4.12: The data and results for C/2008 T2. The overlays are the same as in Figure 4.1

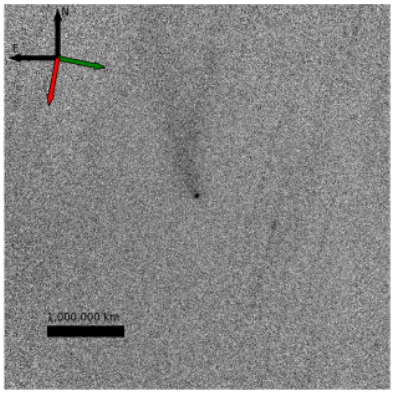


(a) W3 data

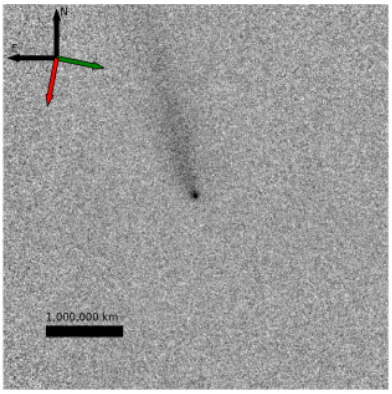


(b) W4 data

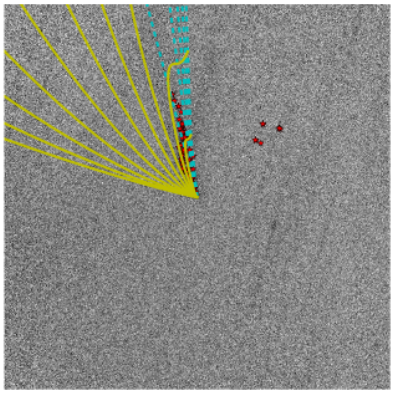

(c) W3 all syndynes and synchrones

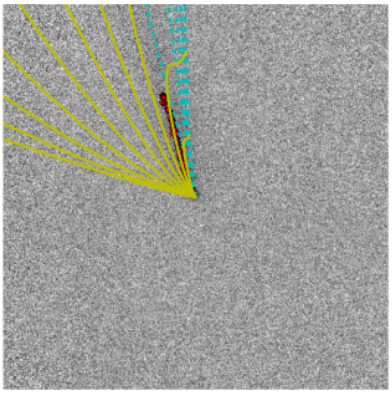

(d) W4 all syndynes and synchrones

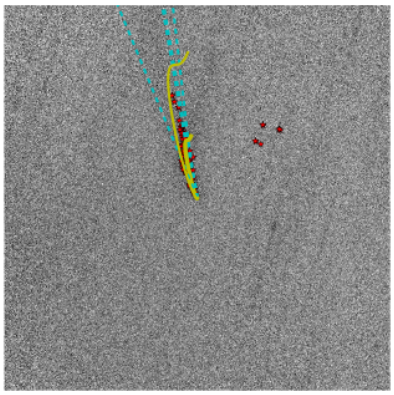

(e) W3 best-fit model

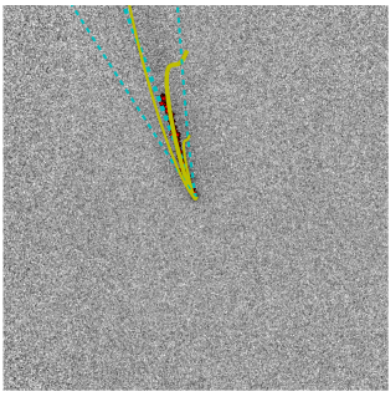

(f) W4 best-fit model

Figure 4.13: The data and results for C/2009 F6. The overlays are the same as in Figure 4.1

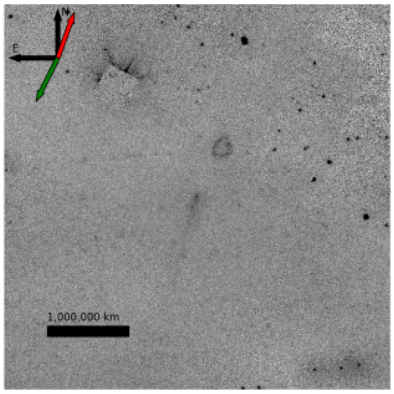


(a) W3 data

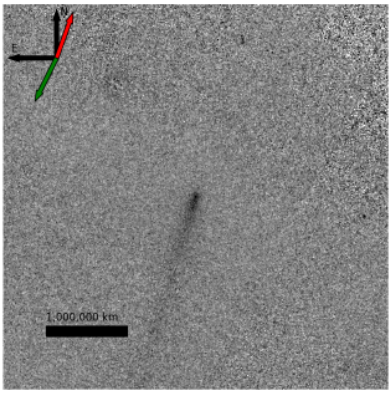


(b) W4 data

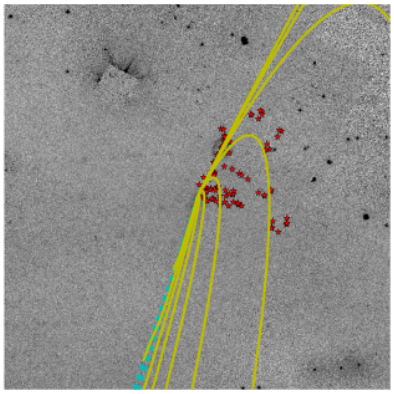

(c) W3 all syndynes and synchrones

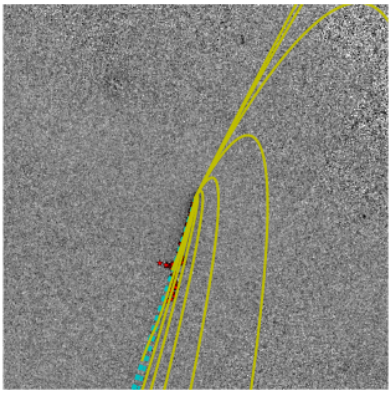

(d) W4 all syndynes and synchrones

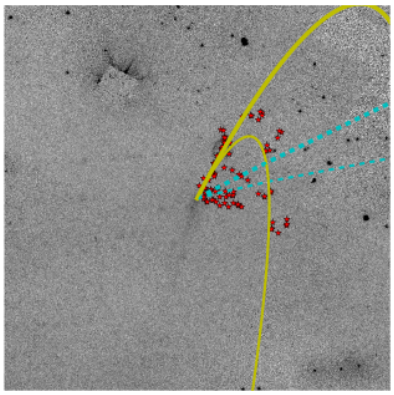

(e) W3 best-fit model

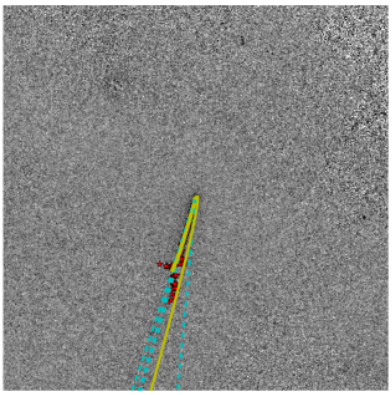

(f) W4 best-fit model

Figure 4.14: The data and results for C/2009 G1. The overlays are the same as in Figure 4.1

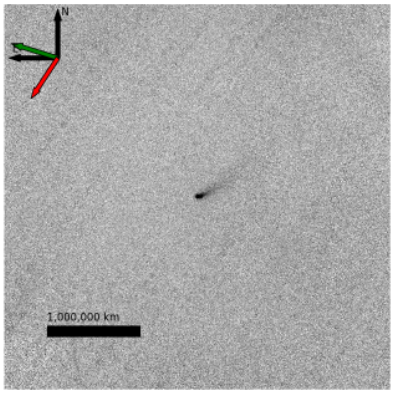


(a) W3 data

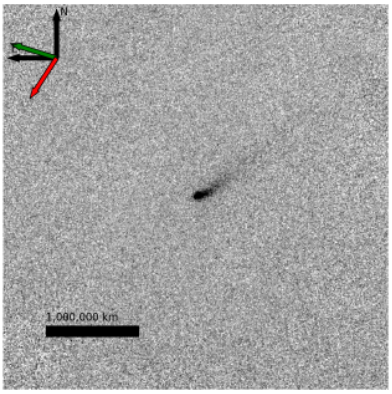


(b) W4 data

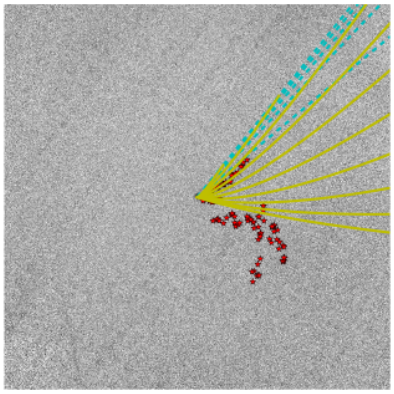

(c) W3 all syndynes and synchrones

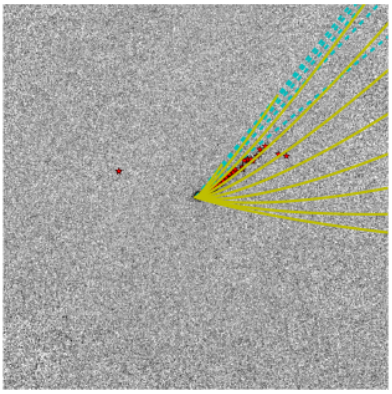

(d) W4 all syndynes and synchrones

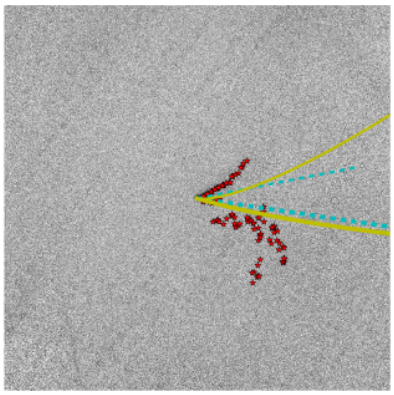

(e) W3 best-fit model

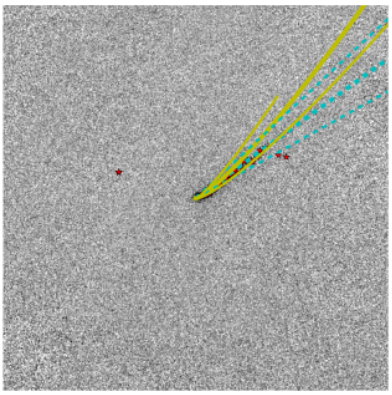

(f) W4 best-fit model

Figure 4.15: The data and results for C/2009 K2. The overlays are the same as in Figure 4.1

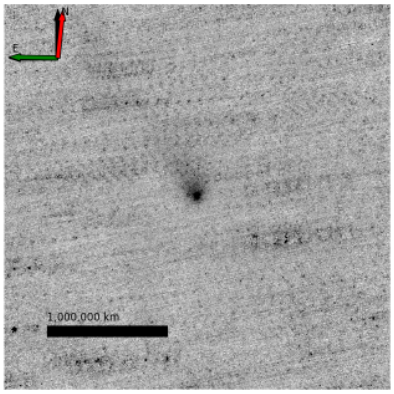


(a) W1 data

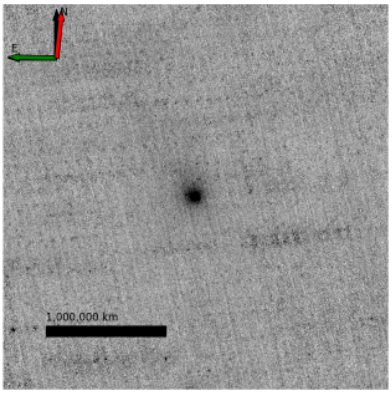


(b) W2 data

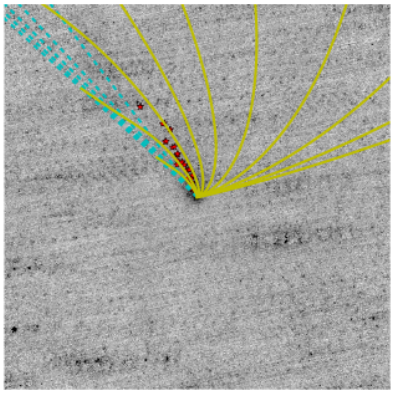

(c) W1 all syndynes and synchrones

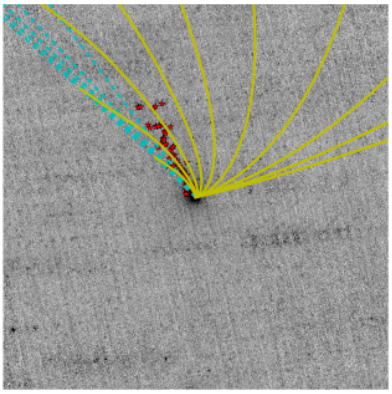

(d) W2 all syndynes and synchrones

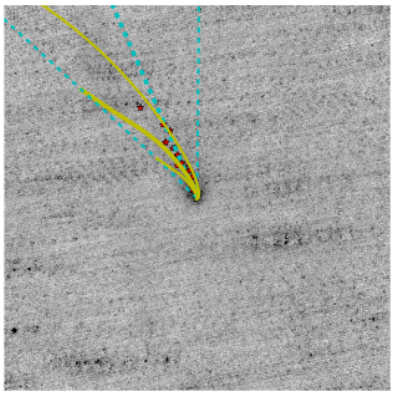

(e) W1 best-fit model

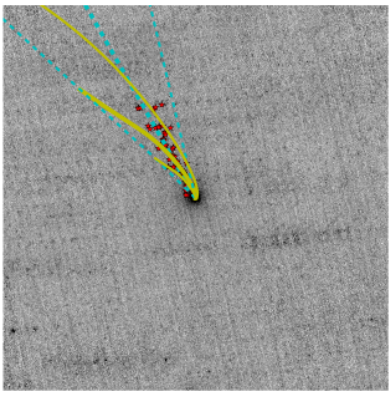

(f) W2 best-fit model

Figure 4.16: The data and results for C/2009 K5. The overlays are the same as in Figure 4.1

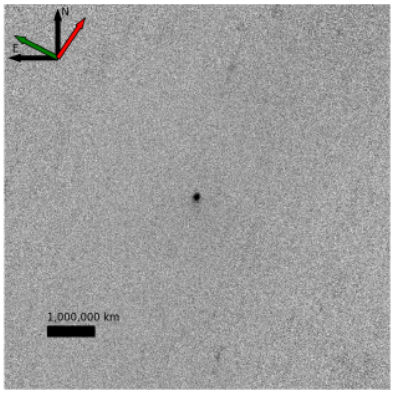


(a) W3 data

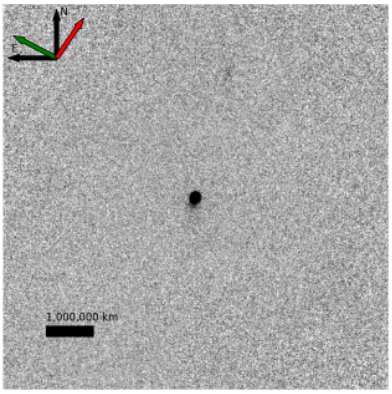


(b) W4 data

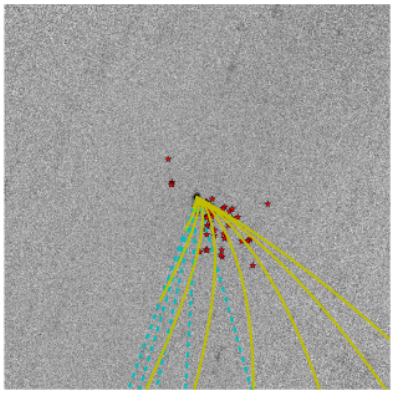

(c) W3 all syndynes and synchrones

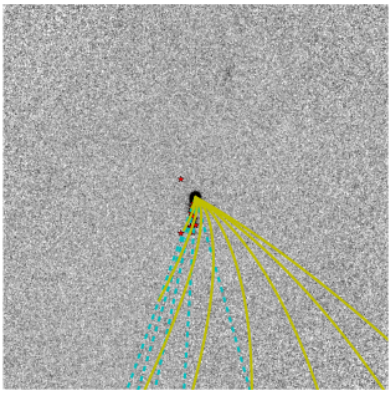

(d) W4 all syndynes and synchrones

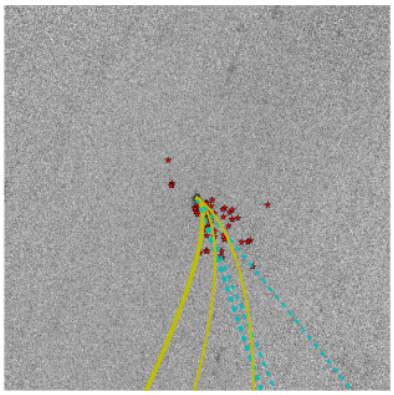

(e) W3 best-fit model

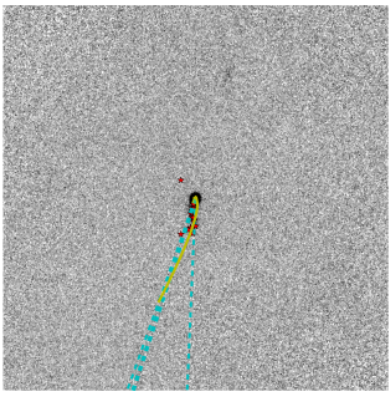

(f) W4 best-fit model

Figure 4.17: The data and results for C/2009 P1. The overlays are the same as in Figure 4.1

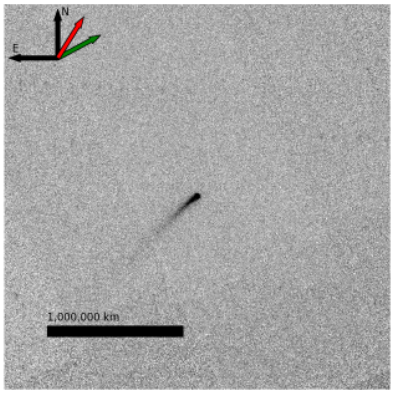


(a) W3 data

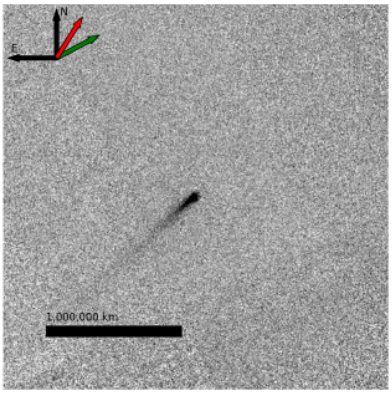


(b) W4 data

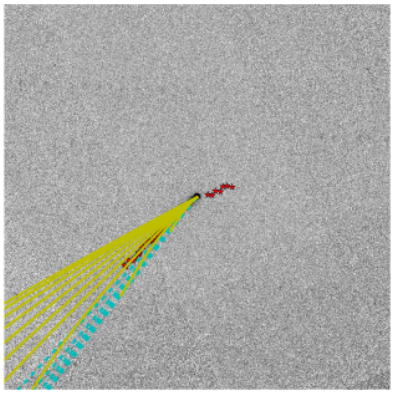

(c) W3 all syndynes and synchrones

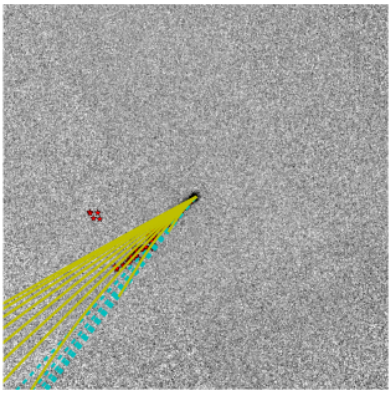

(d) W4 all syndynes and synchrones

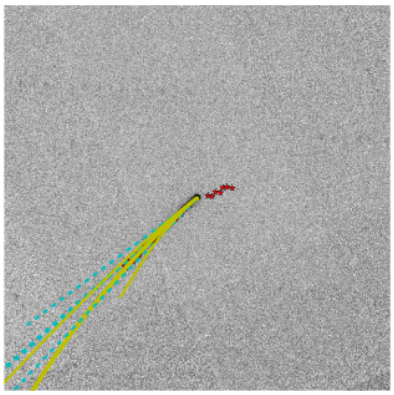

(e) W3 best-fit model

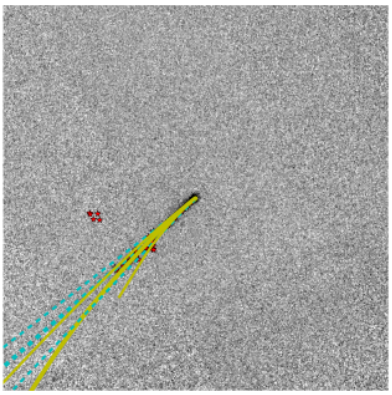

(f) W4 best-fit model

Figure 4.18: The data and results for C/2010 J1 July. The overlays are the same as in Figure 4.1

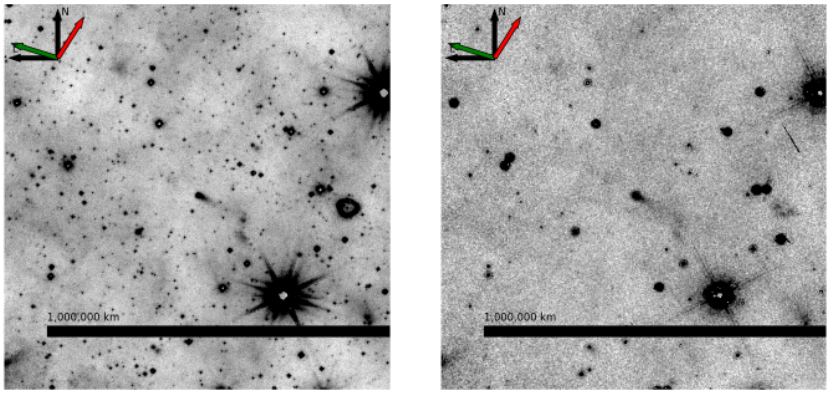


(a) W3 data

(b) W4 data

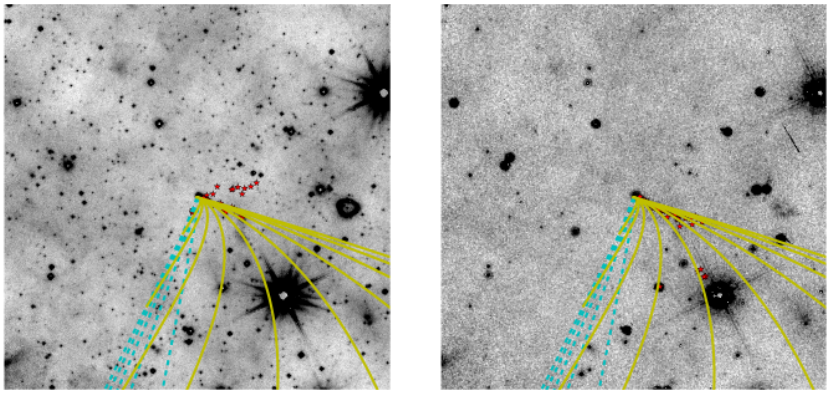

(c) W3 all syndynes and synchrones

(d) W4 all syndynes and synchrones

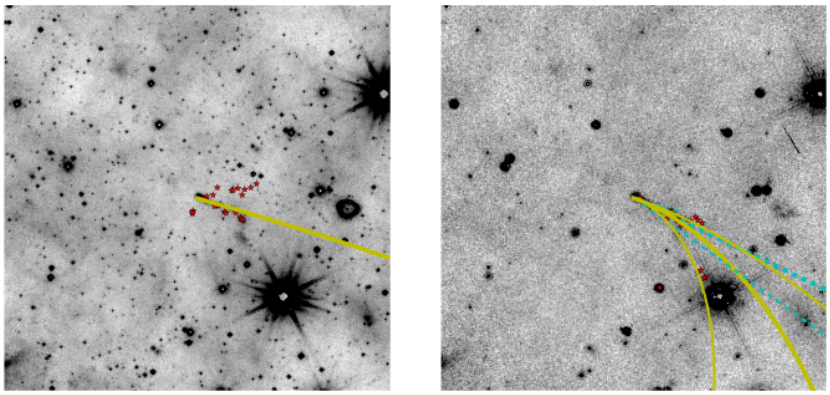

(e) W3 best-fit model

(f) W4 best-fit model

Figure 4.19: The data and results for C/2010 J4 May 1. The overlays are the same as in Figure 4.1

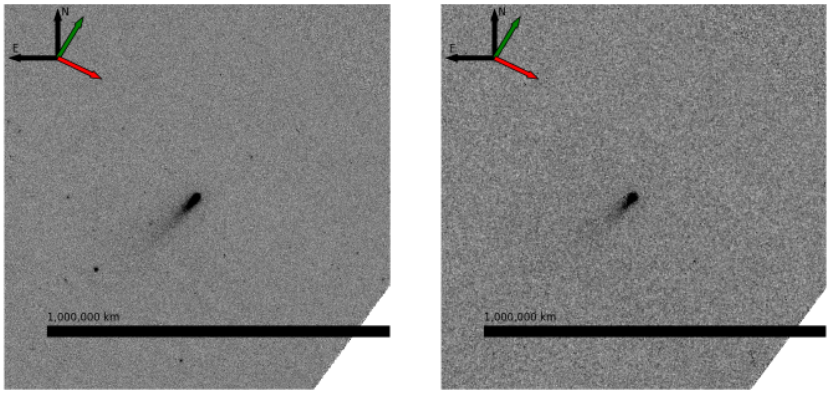


(a) W3 data

(b) W4 data

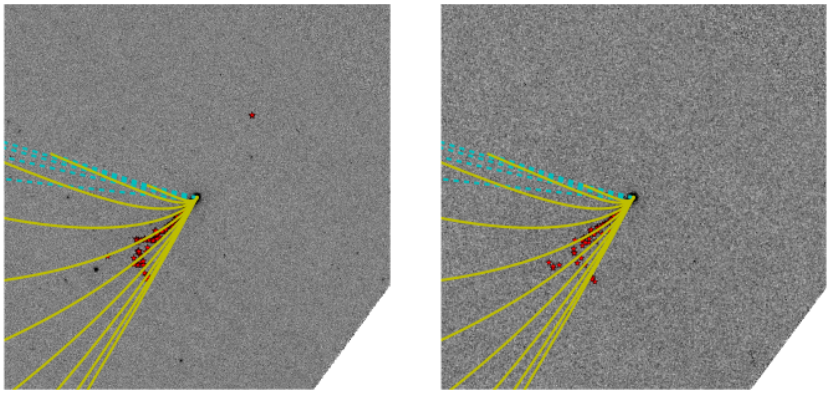

(c) W3 all syndynes and synchrones

(d) W4 all syndynes and synchrones

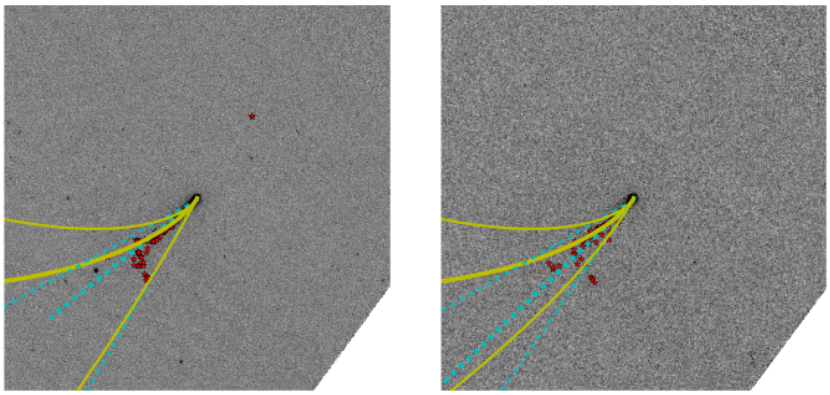

(e) W3 best-fit model

(f) W4 best-fit model

Figure 4.20: The data and results for C/2010 J4 May 12. The overlays are the same as in Figure 4.1

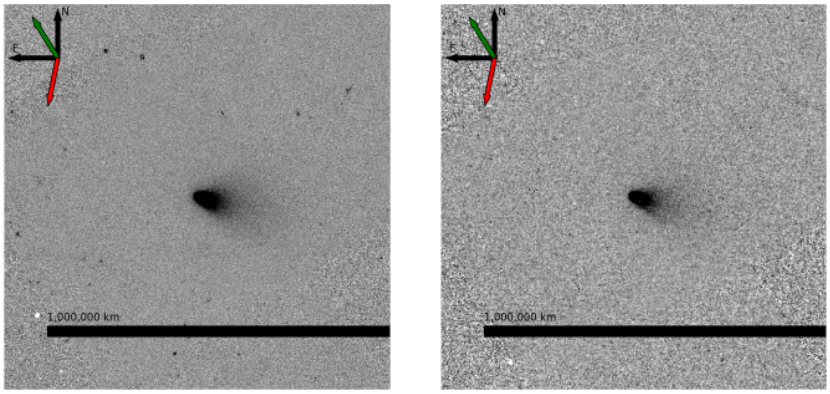


(a) W3 data

(b) W4 data

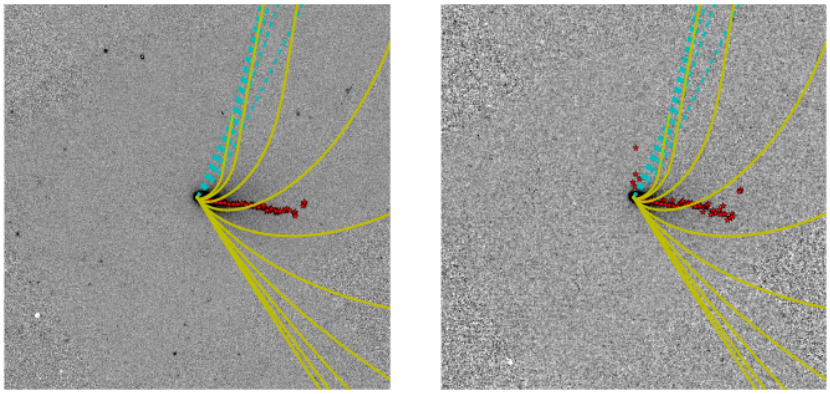

(c) W3 all syndynes and synchrones

(d) W4 all syndynes and synchrones

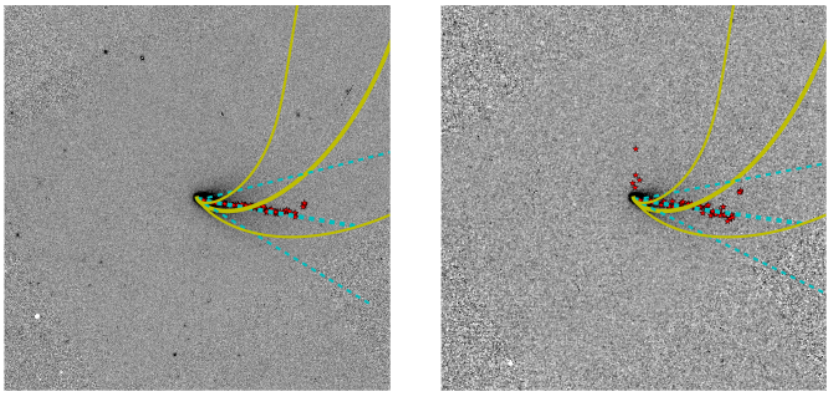

(e) W3 best-fit model

(f) W4 best-fit model

Figure 4.21: The data and results for C/2010 L5 June. The overlays are the same as in Figure 4.1

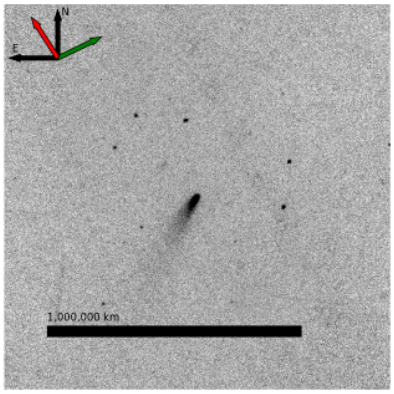


(a) W3 data

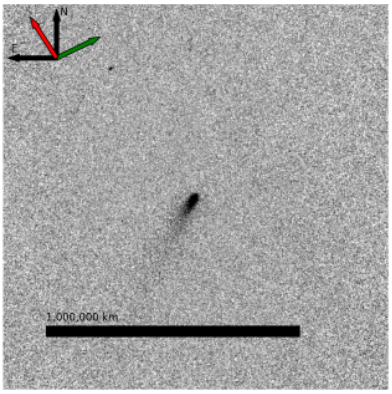


(b) W4 data

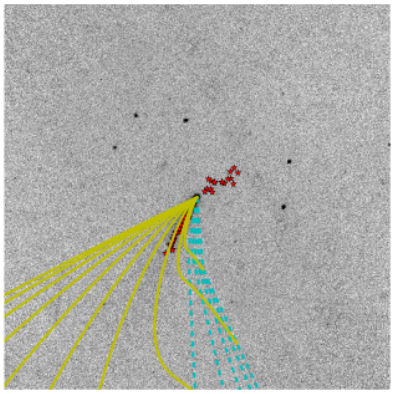

(c) W3 all syndynes and synchrones

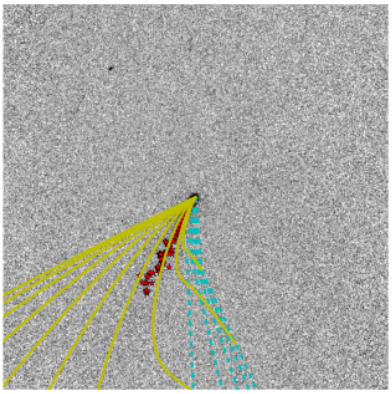

(d) W4 all syndynes and synchrones

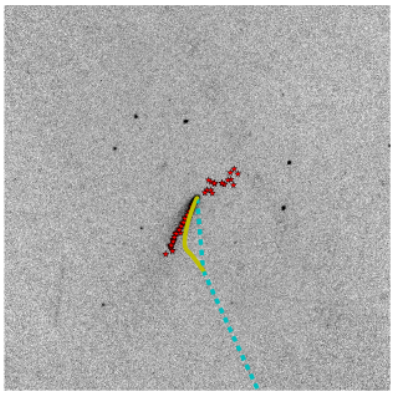

(e) W3 best-fit model

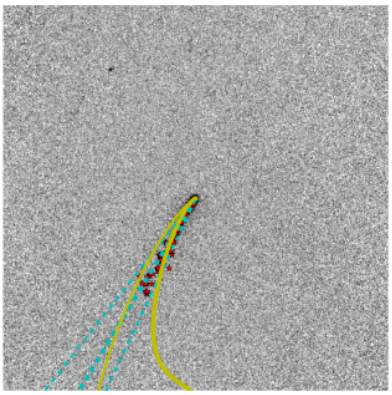

(f) W4 best-fit model

Figure 4.22: The data and results for C/2010 L5 July. The overlays are the same as in Figure 4.1

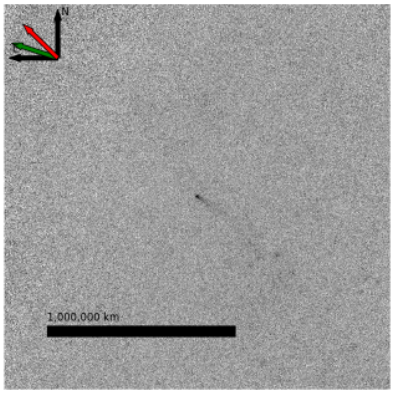


(a) W3 data

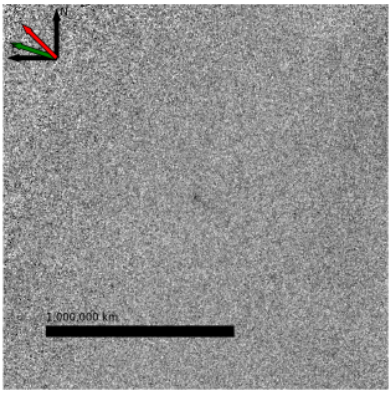


(b) W4 data

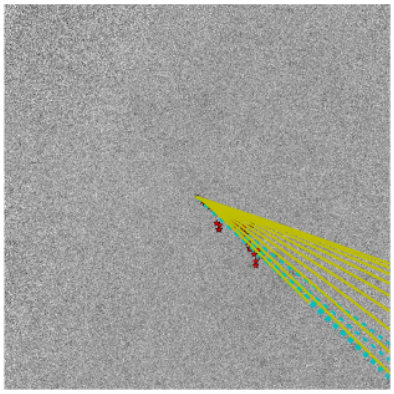

(c) W3 all syndynes and synchrones

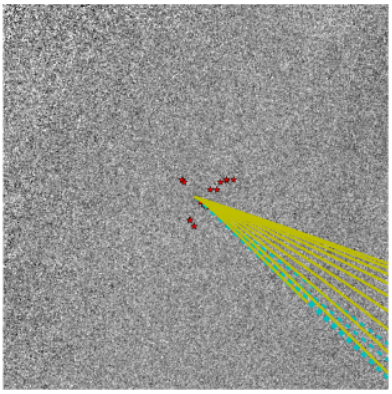

(d) W4 all syndynes and synchrones

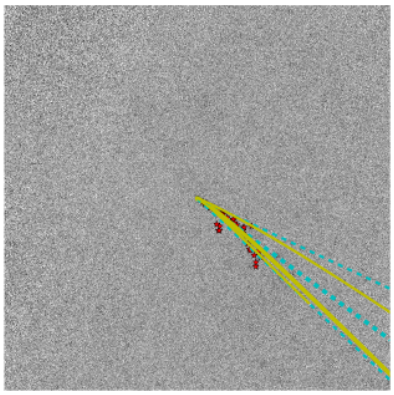

(e) W3 best-fit model

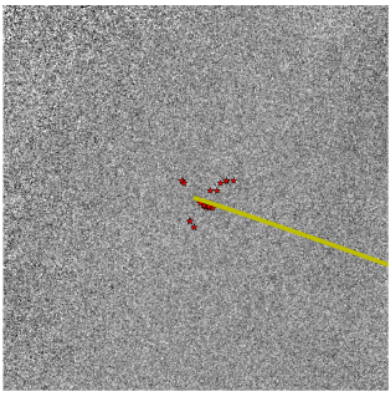

(f) W4 best-fit model

Figure 4.23: The data and results for P/2010 P4. The overlays are the same as in Figure 4.1

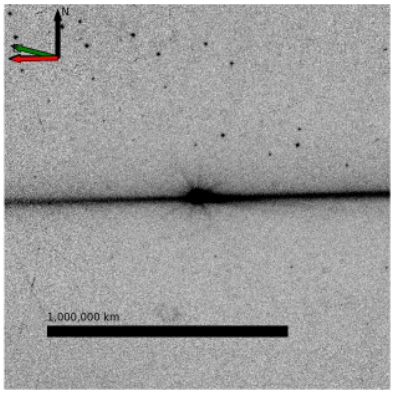


(a) W3 data

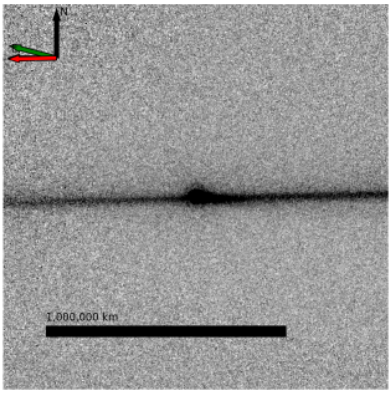


(b) W4 data

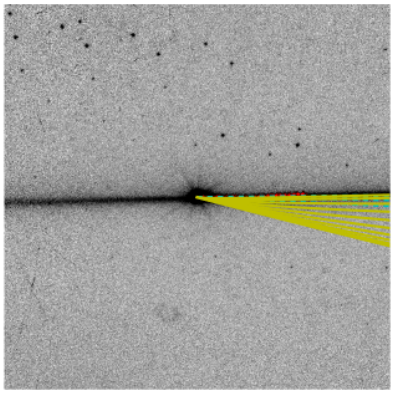

(c) W3 all syndynes and synchrones

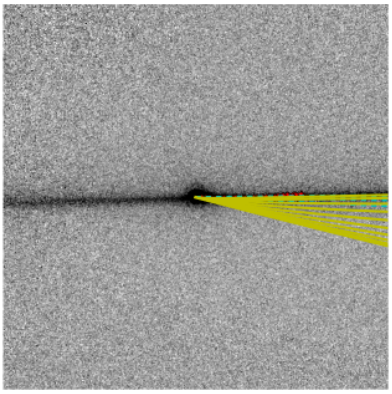

(d) W4 all syndynes and synchrones

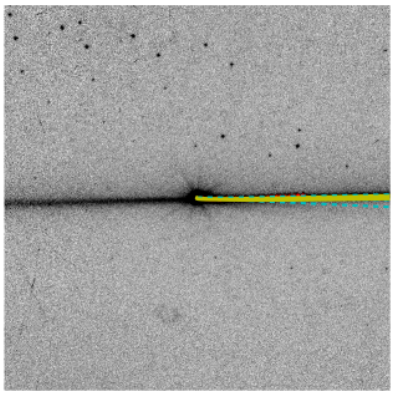

(e) W3 best-fit model

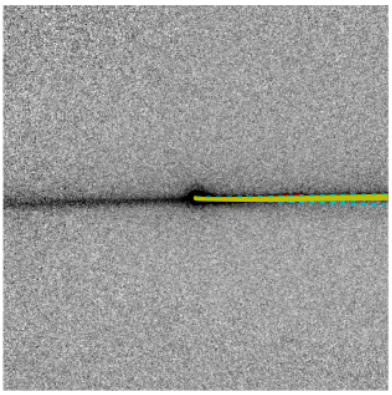

(f) W4 best-fit model

Figure 4.24: The data and results for 10P. The overlays are the same as in Figure 4.1

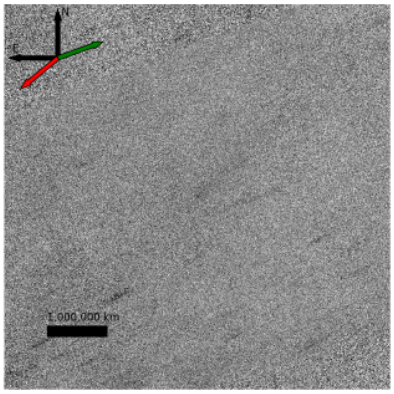


(a) W3 data

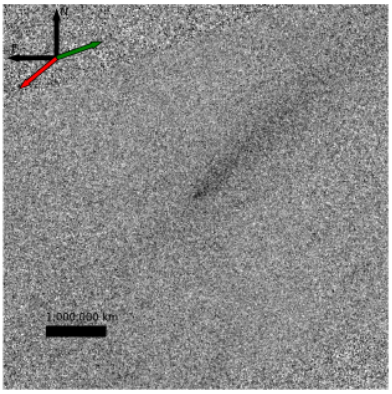


(b) W4 data

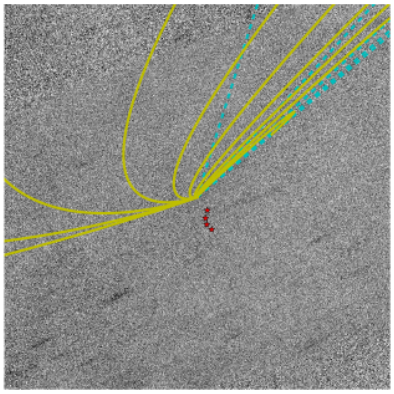

(c) W3 all syndynes and synchrones

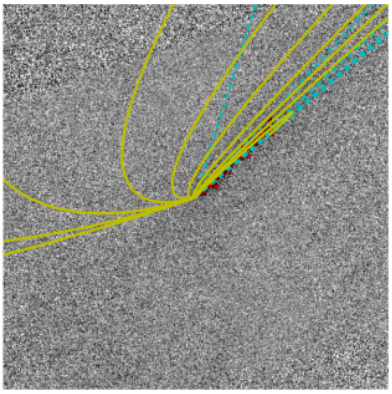

(d) W4 all syndynes and synchrones

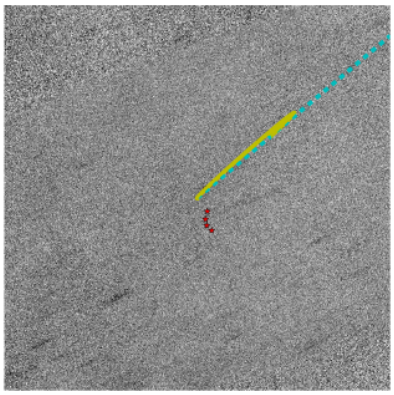

(e) W3 best-fit model

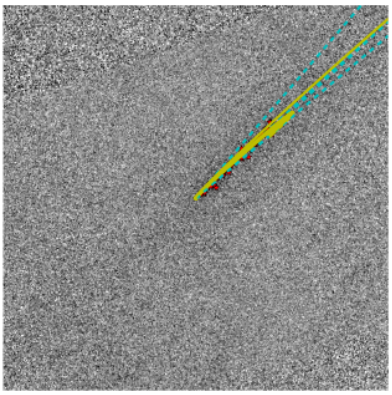

(f) W4 best-fit model

Figure 4.25: The data and results for 17P. The overlays are the same as in Figure 4.1

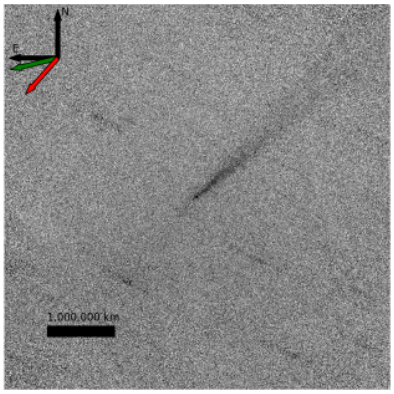


(a) W3 data

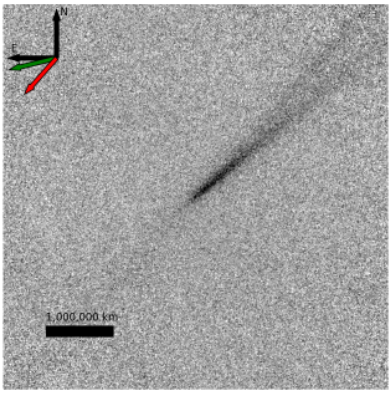


(b) W4 data

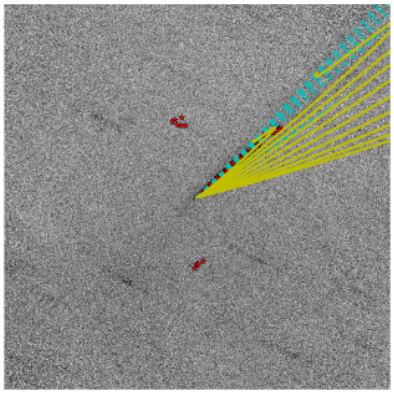

(c) W3 all syndynes and synchrones

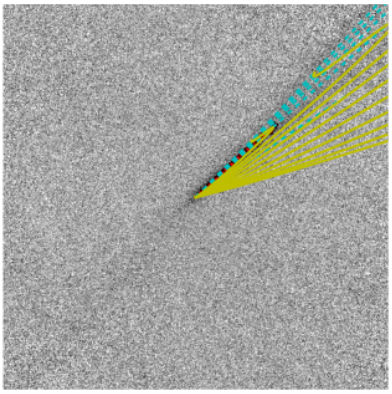

(d) W4 all syndynes and synchrones

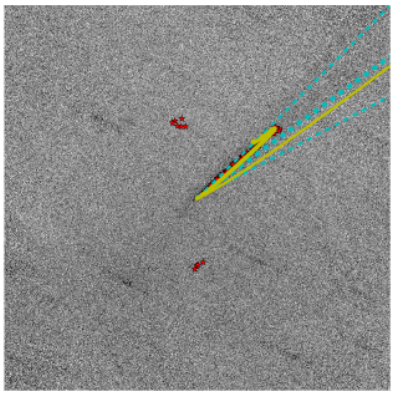

(e) W3 best-fit model

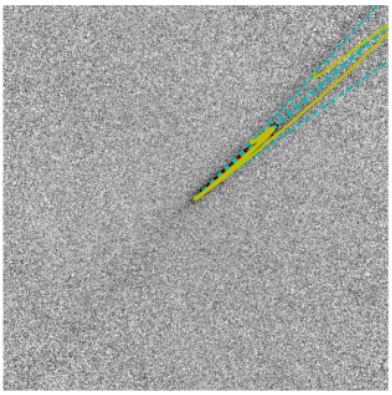

(f) W4 best-fit model

Figure 4.26: The data and results for 19P Feb. The overlays are the same as in Figure 4.1

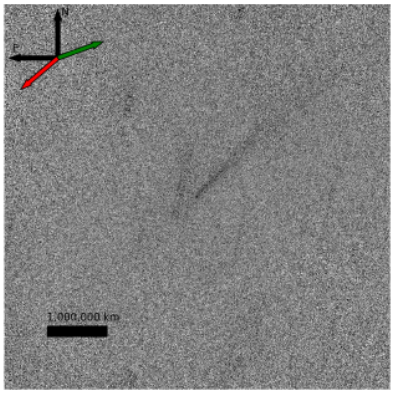


(a) W3 data

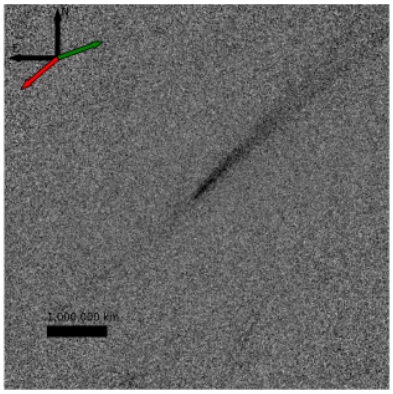


(b) W4 data

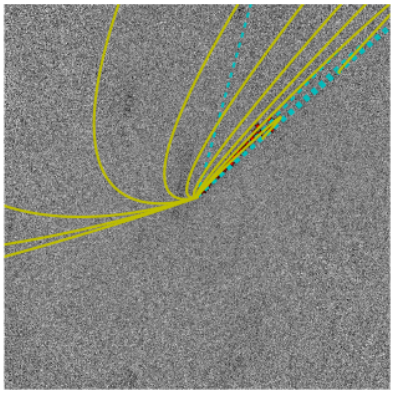

(c) W3 all syndynes and synchrones

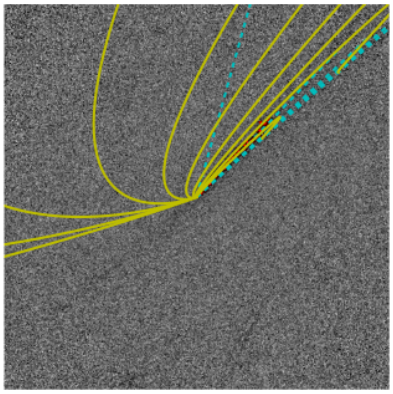

(d) W4 all syndynes and synchrones

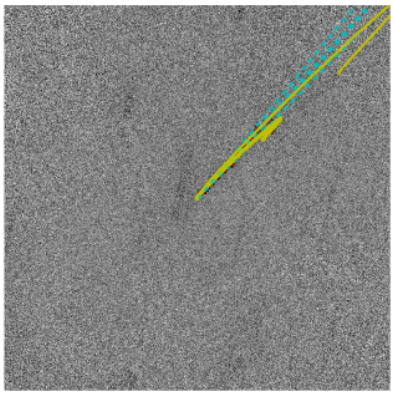

(e) W3 best-fit model

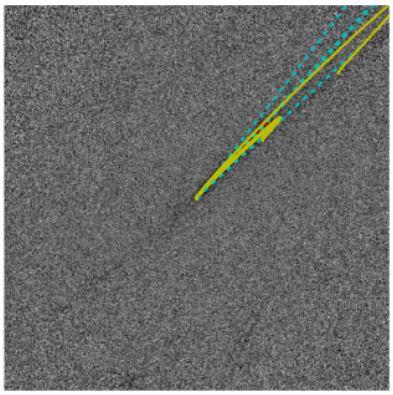

(f) W4 best-fit model

Figure 4.27: The data and results for 19P July. The overlays are the same as in Figure 4.1

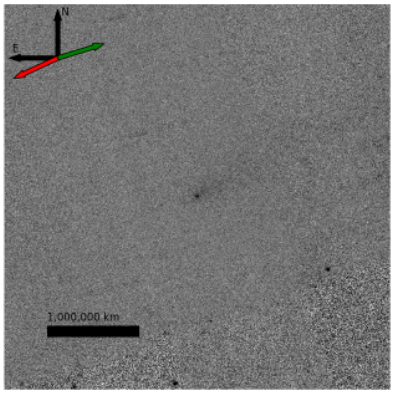


(a) W3 data

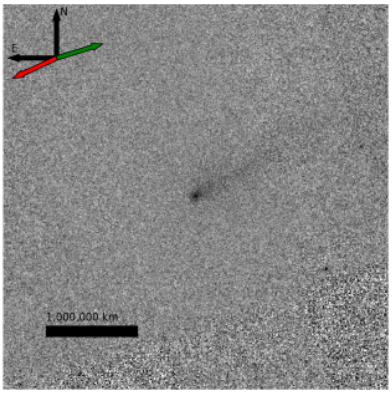


(b) W4 data

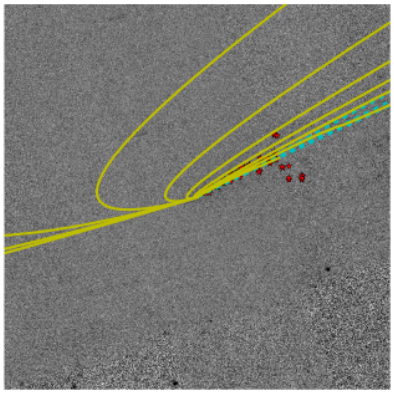

(c) W3 all syndynes and synchrones

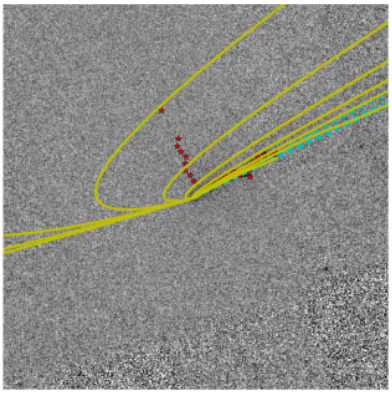

(d) W4 all syndynes and synchrones

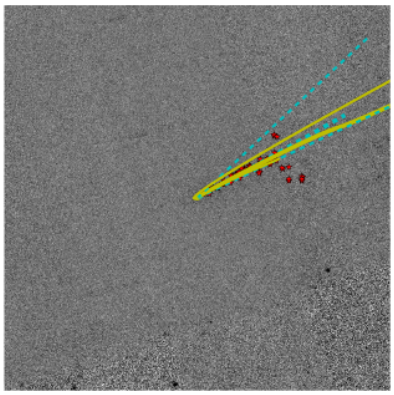

(e) W3 best-fit model

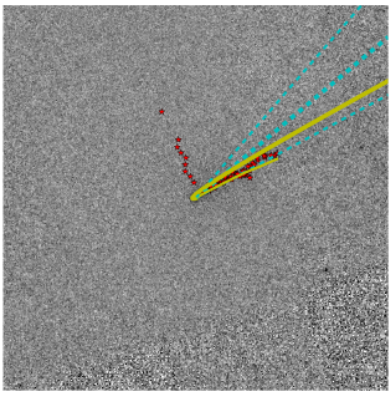

(f) W4 best-fit model

Figure 4.28: The data and results for 64P. The overlays are the same as in Figure 4.1

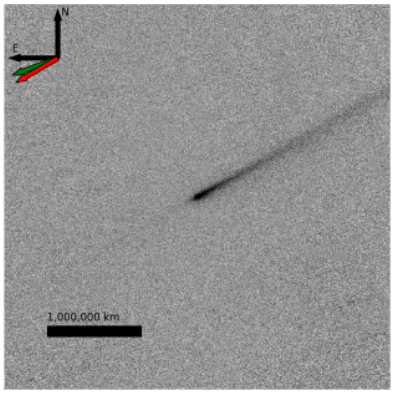


(a) W3 data

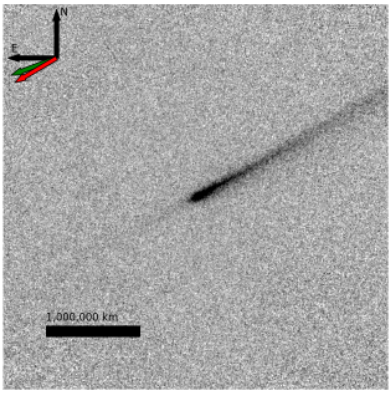


(b) W4 data

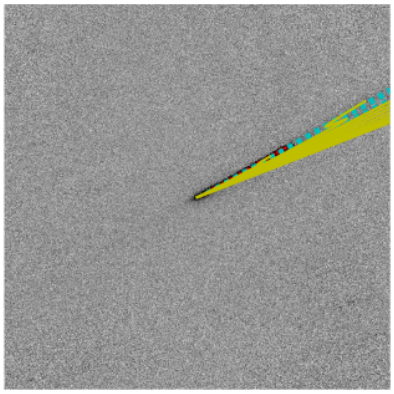

(c) W3 all syndynes and synchrones

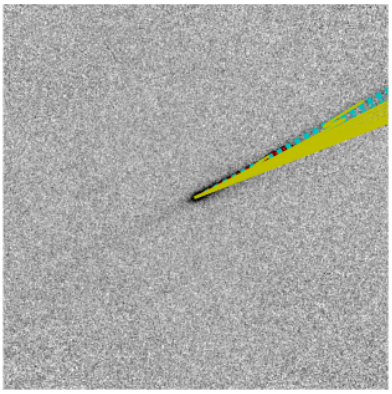

(d) W4 all syndynes and synchrones

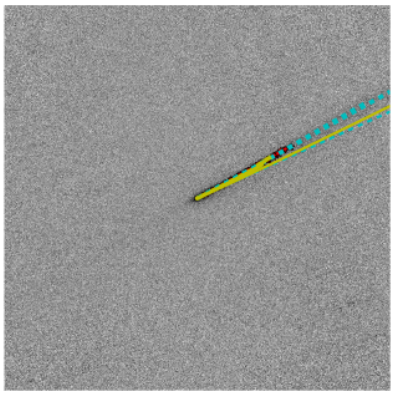

(e) W3 best-fit model

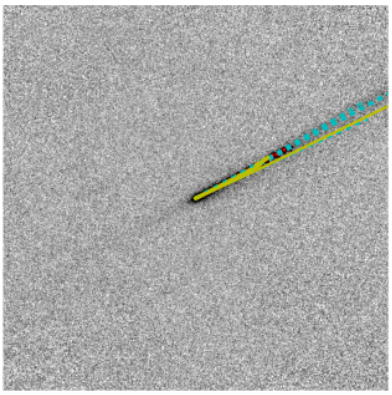

(f) W4 best-fit model

Figure 4.29: The data and results for 67P Jan. The overlays are the same as in Figure 4.1

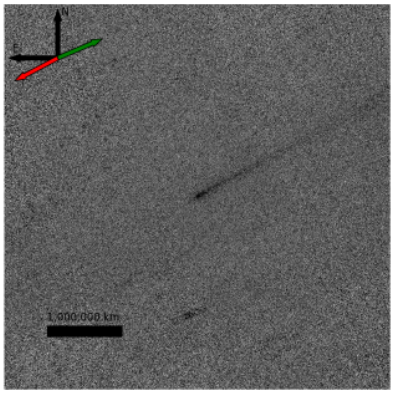


(a) W3 data

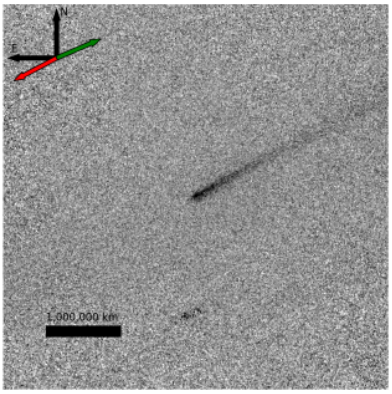


(b) W4 data

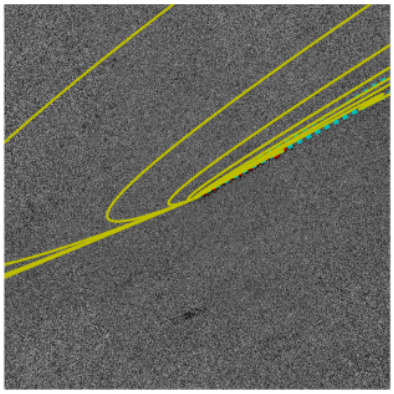

(c) W3 all syndynes and synchrones

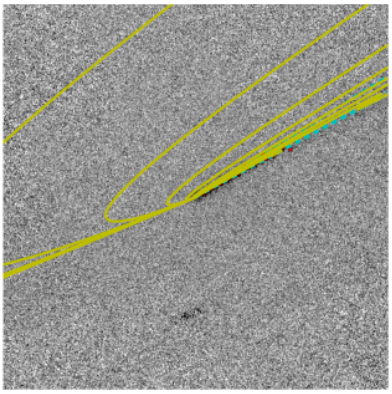

(d) W4 all syndynes and synchrones

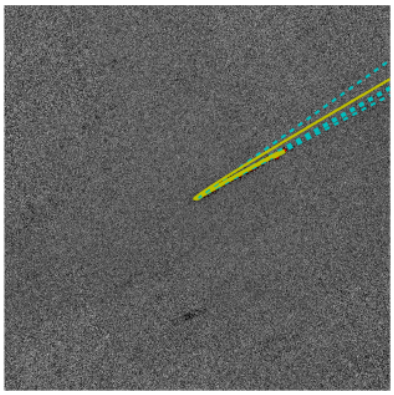

(e) W3 best-fit model

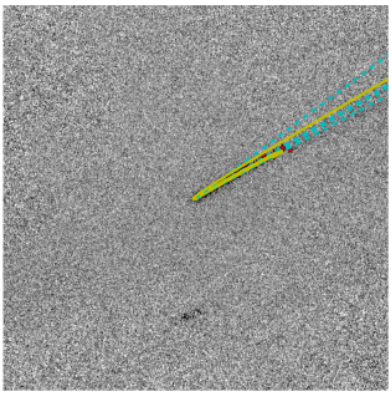

(f) W4 best-fit model

Figure 4.30: The data and results for 67P June. The overlays are the same as in Figure 4.1

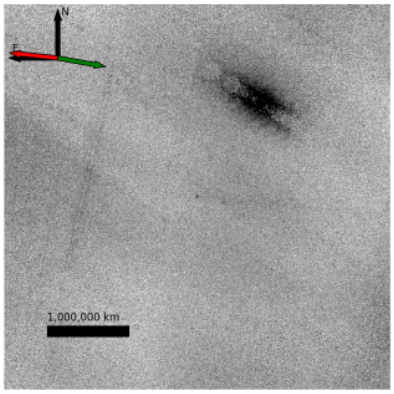


(a) W3 data

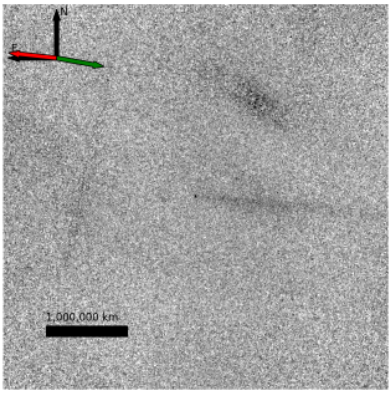


(b) W4 data

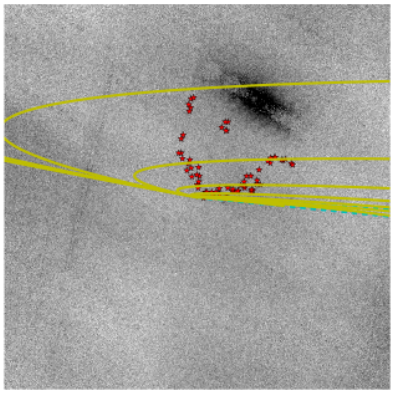

(c) W3 all syndynes and synchrones

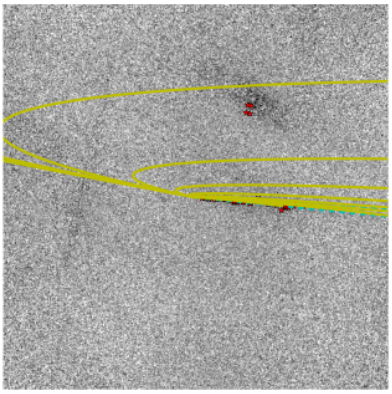

(d) W4 all syndynes and synchrones

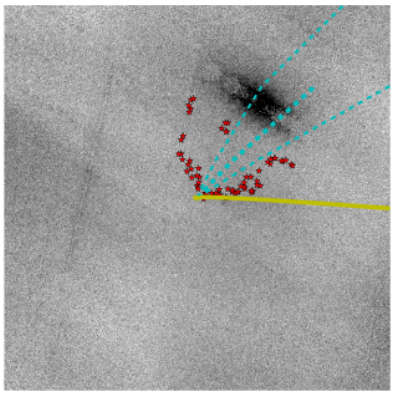

(e) W3 best-fit model

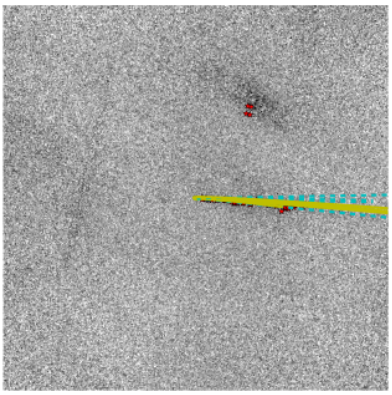

(f) W4 best-fit model

Figure 4.31: The data and results for 68P. The overlays are the same as in Figure 4.1

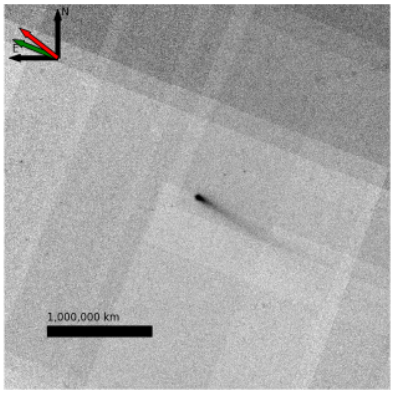


(a) W3 data

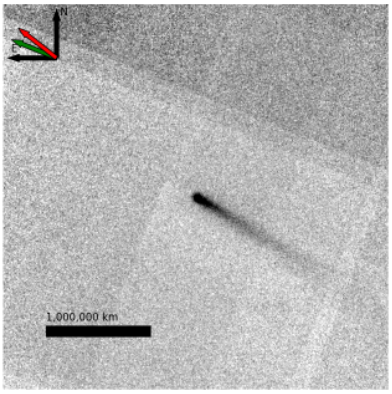


(b) W4 data

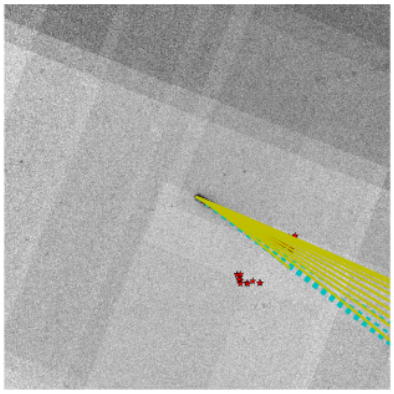

(c) W3 all syndynes and synchrones

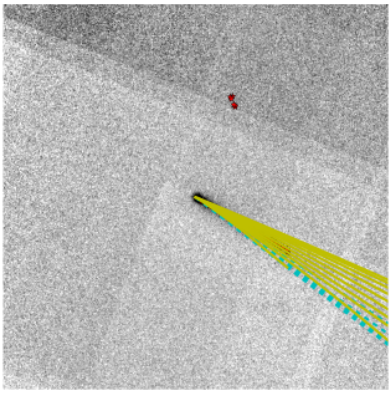

(d) W4 all syndynes and synchrones

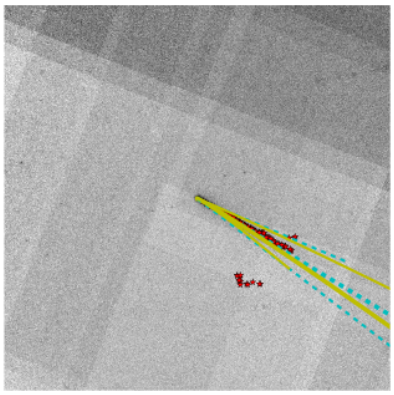

(e) W3 best-fit model

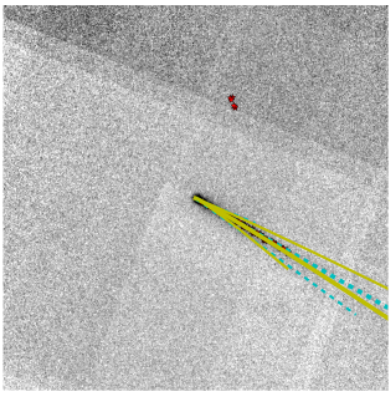

(f) W4 best-fit model

Figure 4.32: The data and results for 77P. The overlays are the same as in Figure 4.1

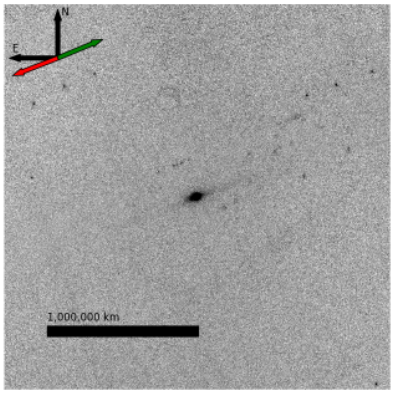


(a) W3 data

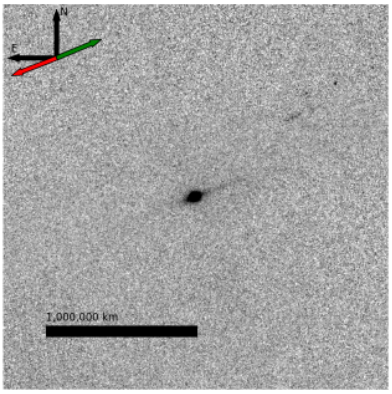


(b) W4 data

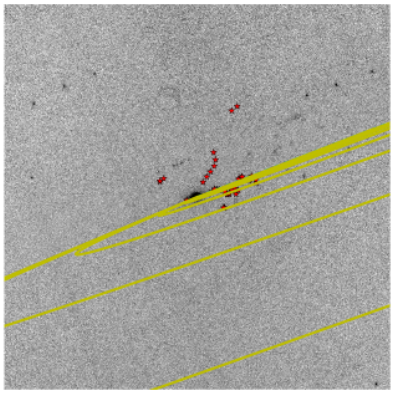

(c) W3 all syndynes and synchrones

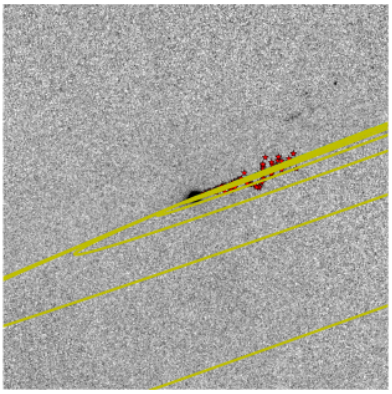

(d) W4 all syndynes and synchrones

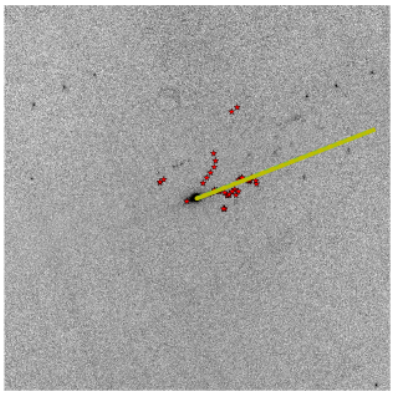

(e) W3 best-fit model

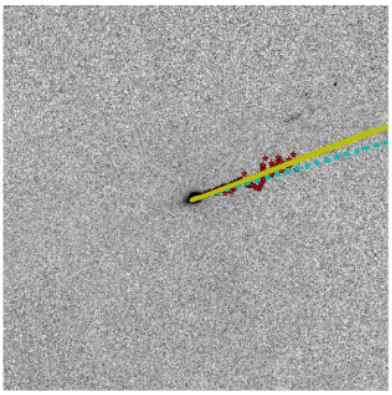

(f) W4 best-fit model

Figure 4.33: The data and results for 94P. The overlays are the same as in Figure 4.1

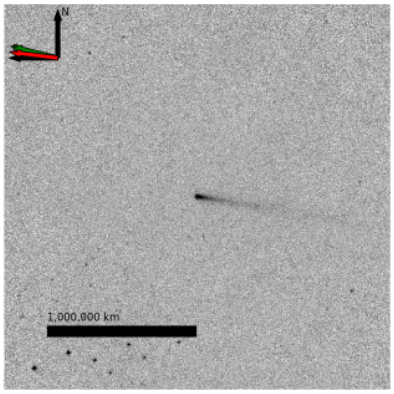


(a) W3 data

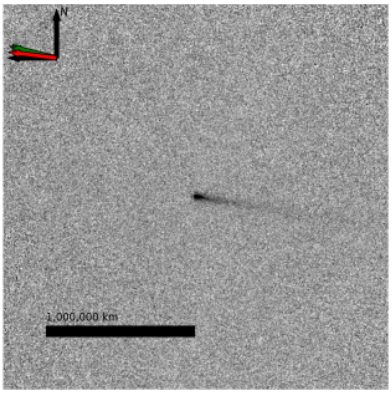


(b) W4 data

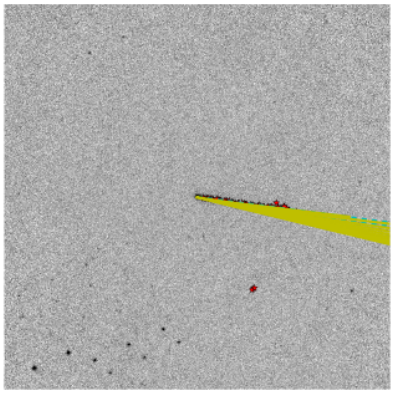

(c) W3 all syndynes and synchrones

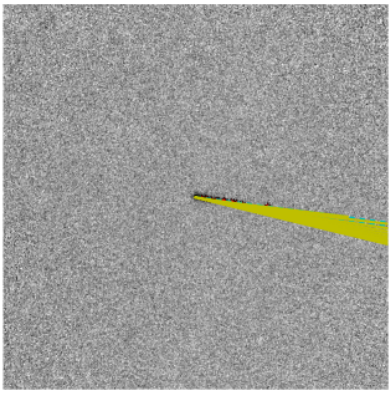

(d) W4 all syndynes and synchrones

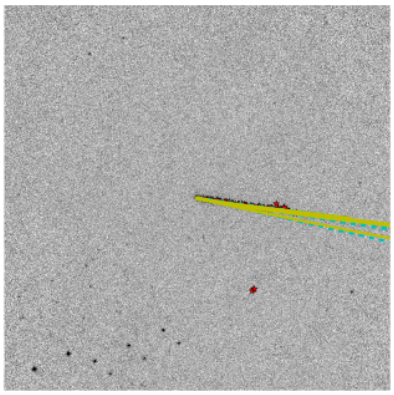

(e) W3 best-fit model

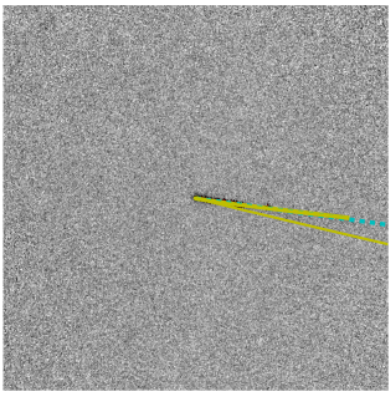

(f) W4 best-fit model

Figure 4.34: The data and results for 100P. The overlays are the same as in Figure 4.1

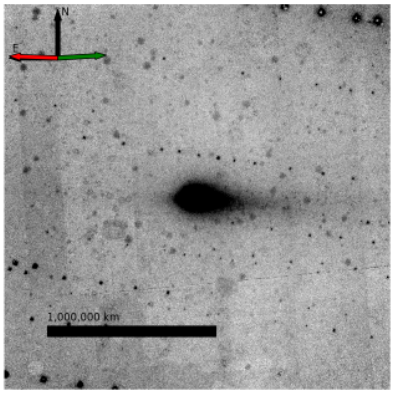


(a) W3 data

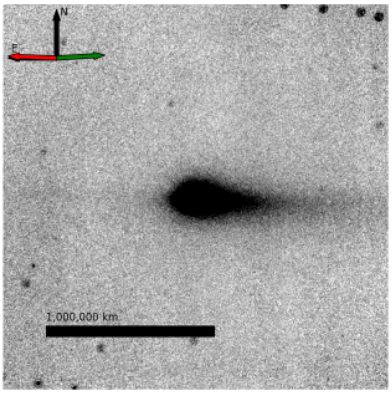


(b) W4 data

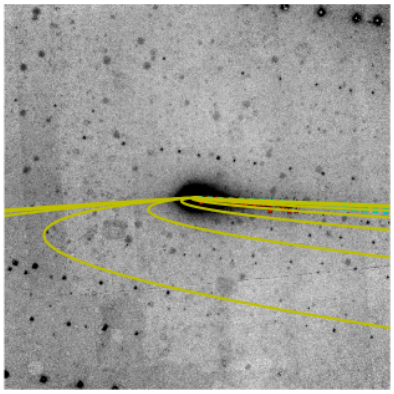

(c) W3 all syndynes and synchrones

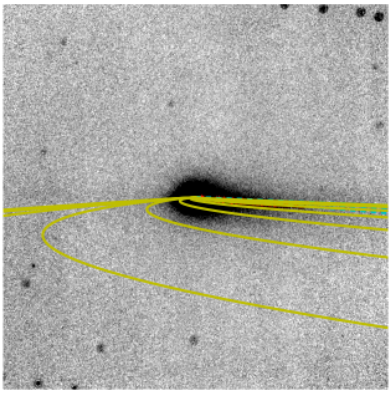

(d) W4 all syndynes and synchrones

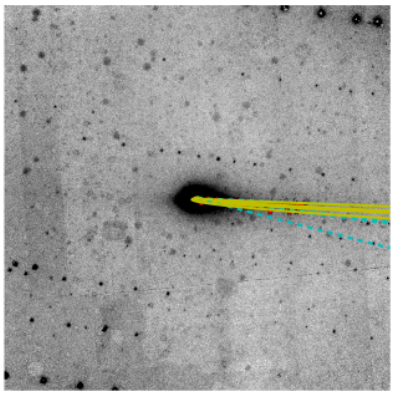

(e) W3 best-fit model

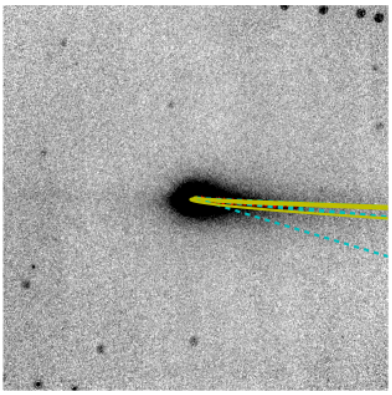

(f) W4 best-fit model

Figure 4.35: The data and results for 118P. The overlays are the same as in Figure 4.1

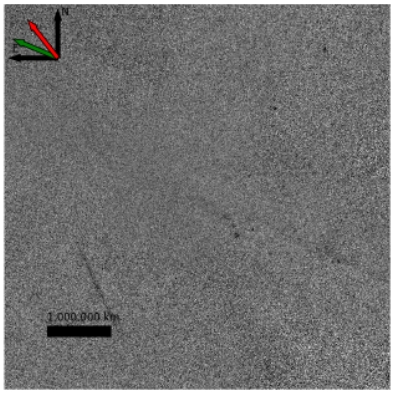

(a) W3 data

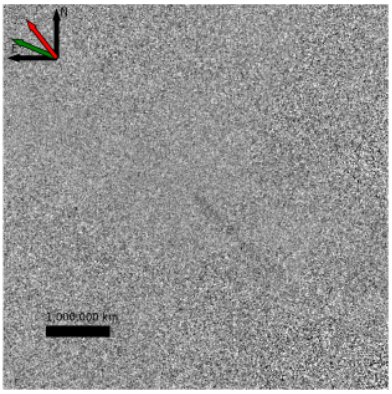

(b) W4 data

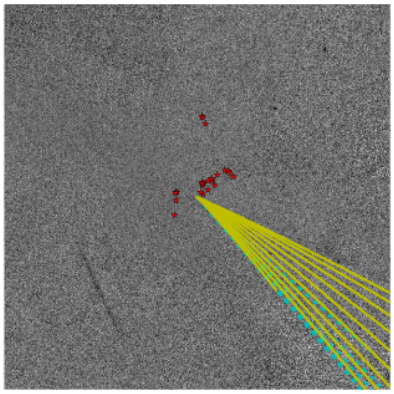

(c) W3 all syndynes and synchrones

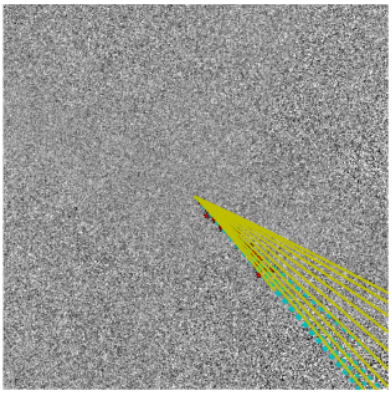

(d) W4 all syndynes and synchrones

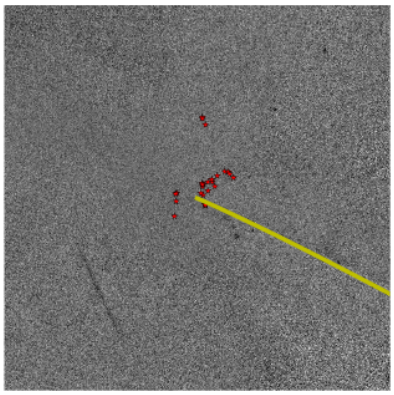

(e) W3 best-fit model

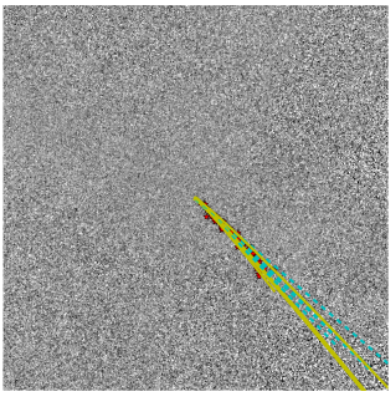

(f) W4 best-fit model

Figure 4.36: The data and results for 186P. The overlays are the same as in Figure 4.1

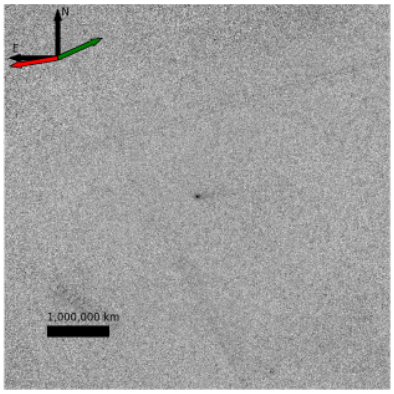


(a) W3 data

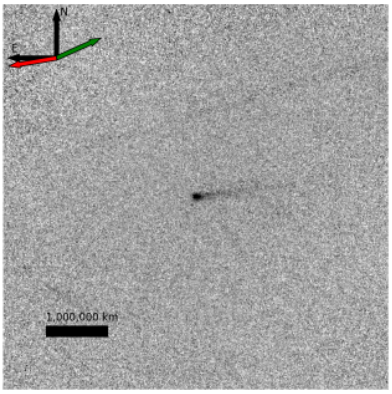


(b) W4 data

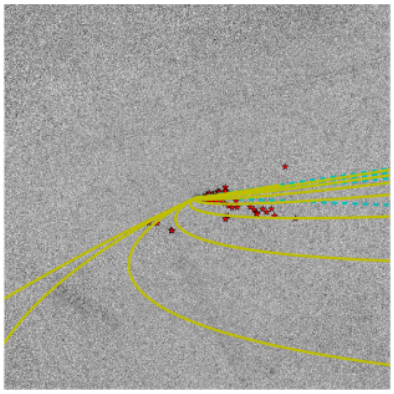

(c) W3 all syndynes and synchrones

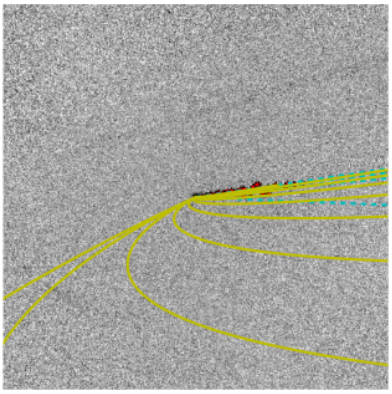

(d) W4 all syndynes and synchrones

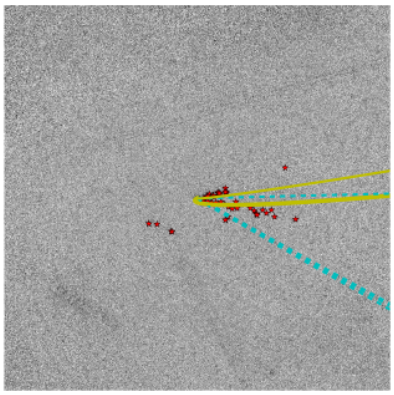

(e) W3 best-fit model

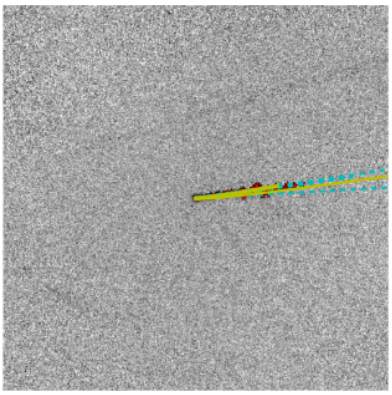

(f) W4 best-fit model

Figure 4.37: The data and results for 195P. The overlays are the same as in Figure 4.1

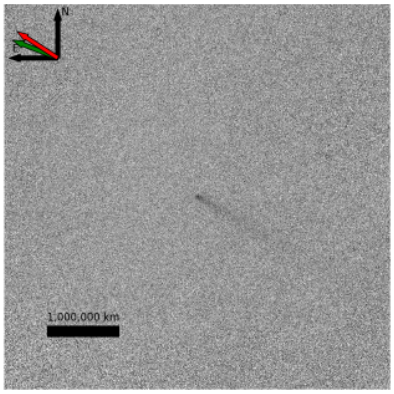


(a) W3 data

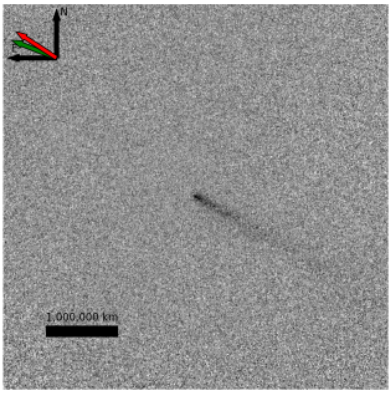


(b) W4 data

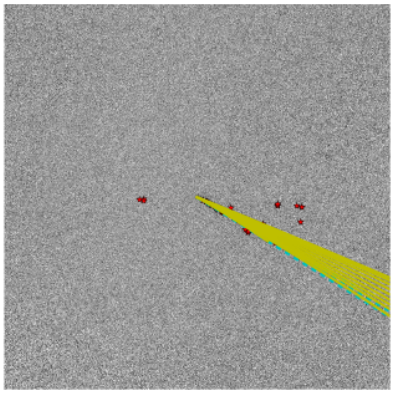

(c) W3 all syndynes and synchrones

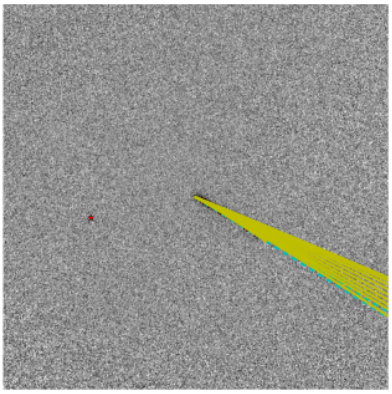

(d) W4 all syndynes and synchrones

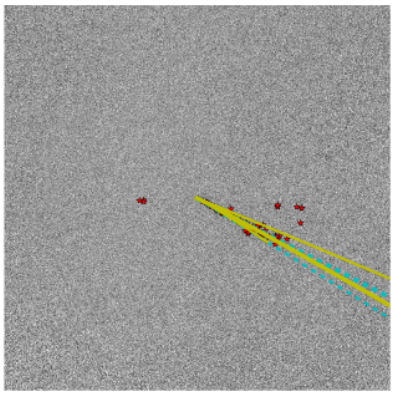

(e) W3 best-fit model

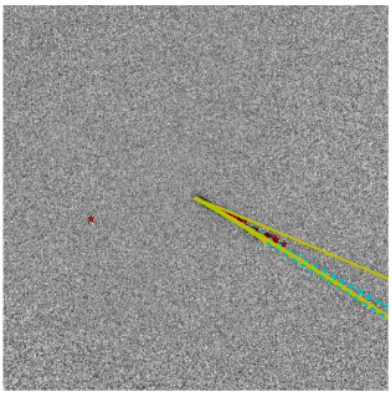

(f) W4 best-fit model

Figure 4.38: The data and results for 199P. The overlays are the same as in Figure 4.1

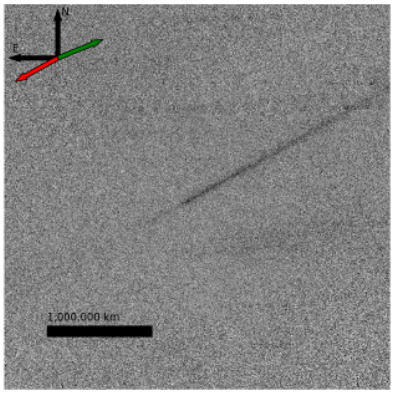


(a) W3 data

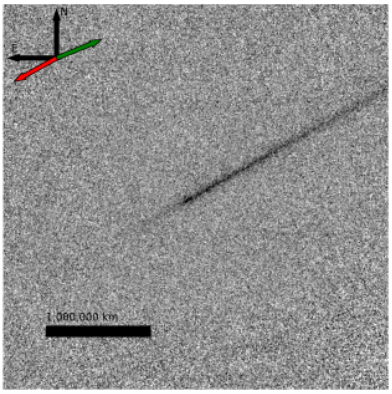


(b) W4 data

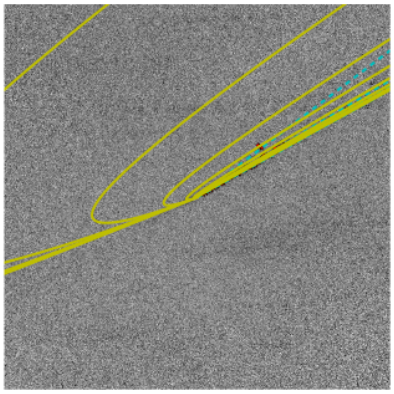

(c) W3 all syndynes and synchrones

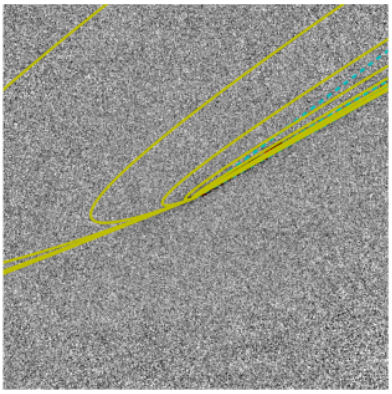

(d) W4 all syndynes and synchrones

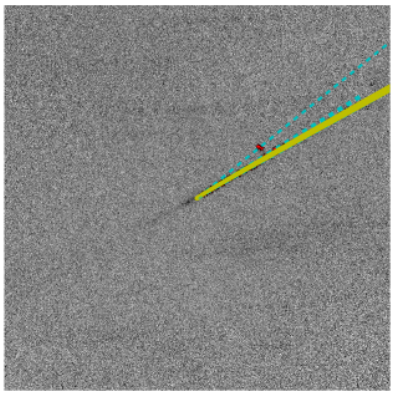

(e) W3 best-fit model

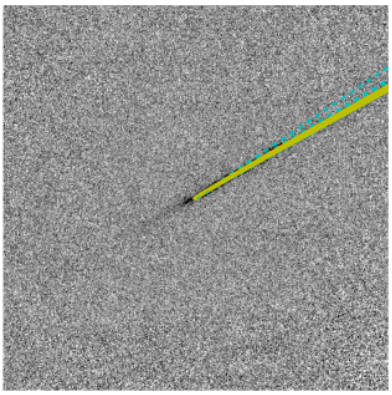

(f) W4 best-fit model

Figure 4.39: The data and results for 213P July. The overlays are the same as in Figure 4.1

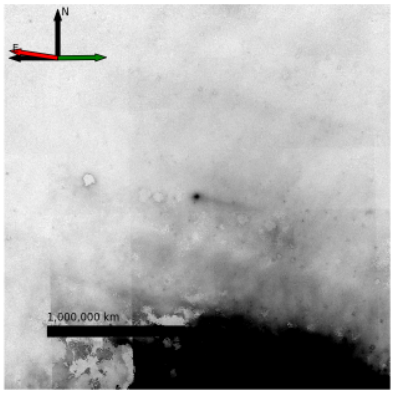


(a) W3 data

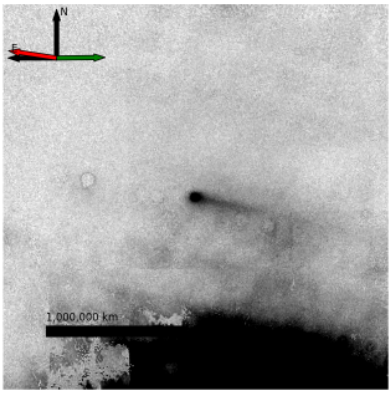


(b) W4 data

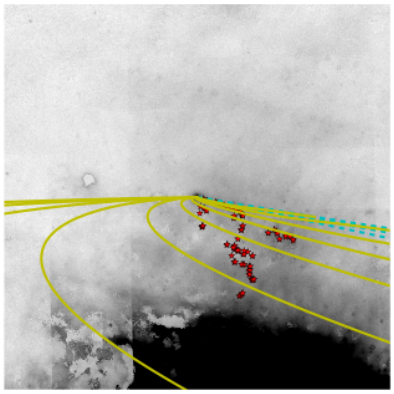

(c) W3 all syndynes and synchrones

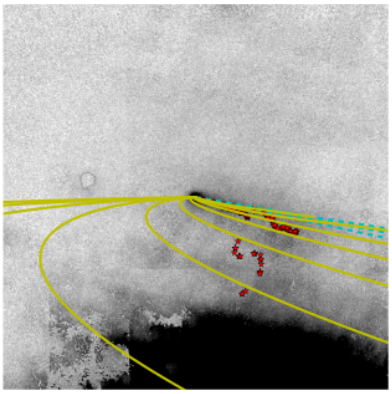

(d) W4 all syndynes and synchrones

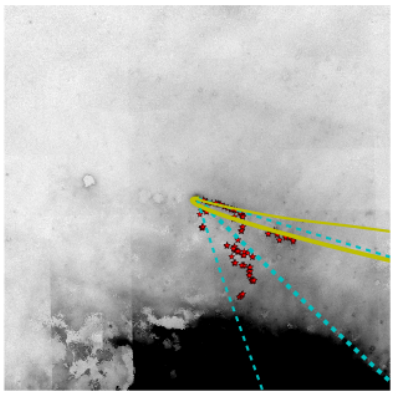

(e) W3 best-fit model

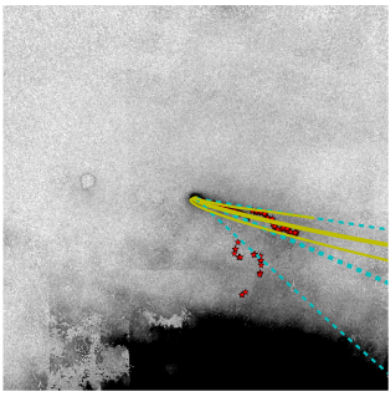

(f) W4 best-fit model

Figure 4.40: The data and results for 217P. The overlays are the same as in Figure 4.1

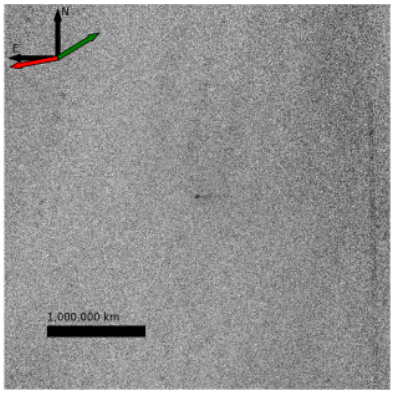


(a) W3 data

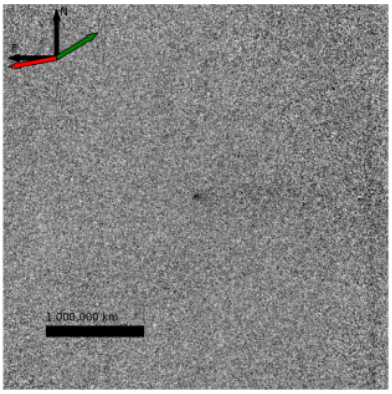


(b) W4 data

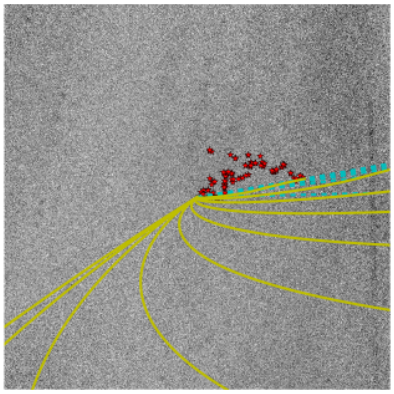

(c) W3 all syndynes and synchrones

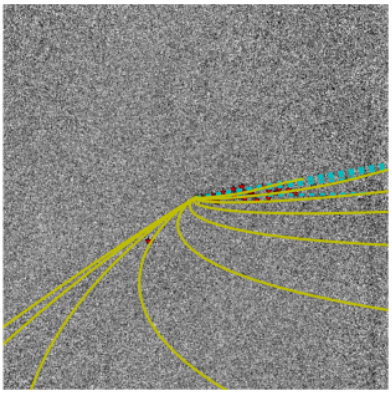

(d) W4 all syndynes and synchrones

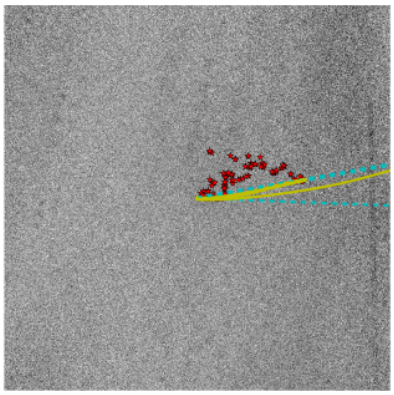

(e) W3 best-fit model

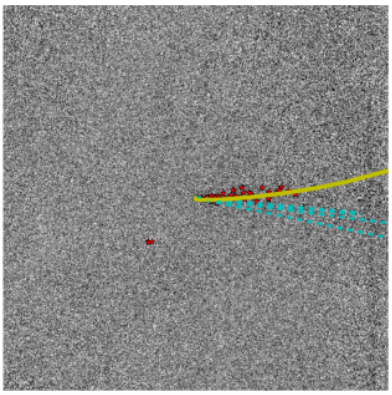

(f) W4 best-fit model

Figure 4.41: The data and results for 226P. The overlays are the same as in Figure 4.1

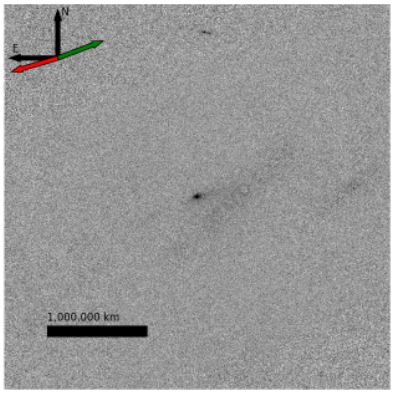


(a) W3 data

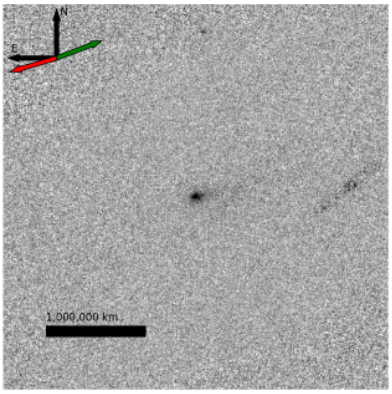


(b) W4 data

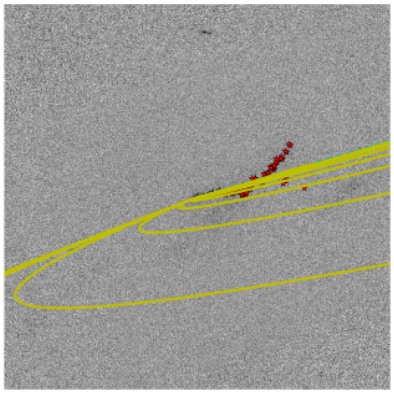

(c) W3 all syndynes and synchrones

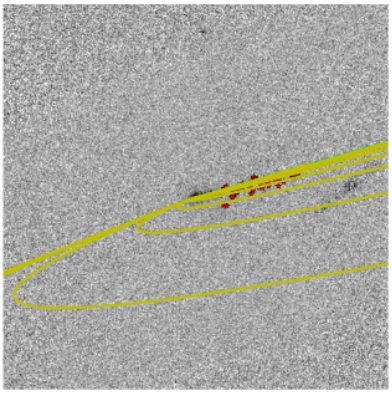

(d) W4 all syndynes and synchrones

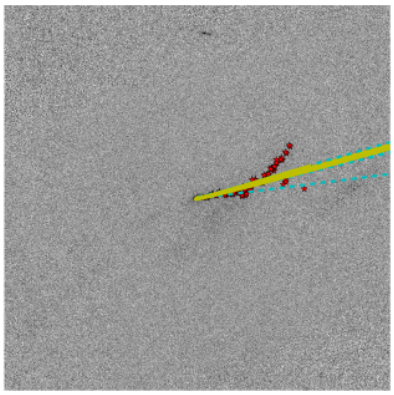

(e) W3 best-fit model

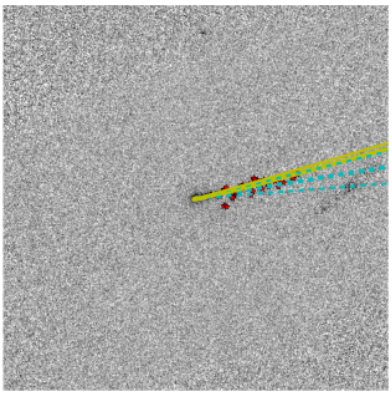

(f) W4 best-fit model

Figure 4.42: The data and results for 232P. The overlays are the same as in Figure 4.1

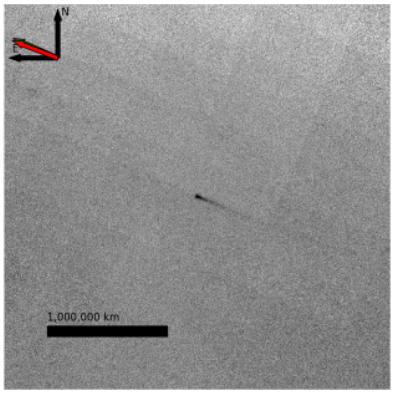


(a) W3 data

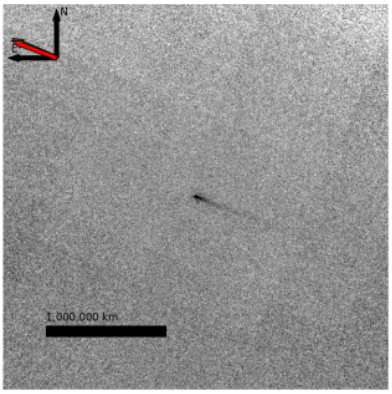


(b) W4 data

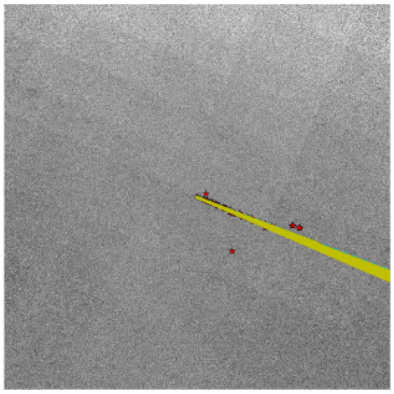

(c) W3 all syndynes and synchrones

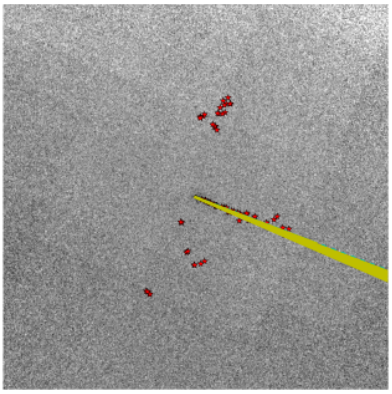

(d) W4 all syndynes and synchrones

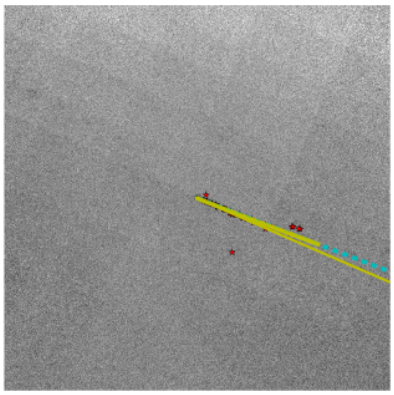

(e) W3 best-fit model

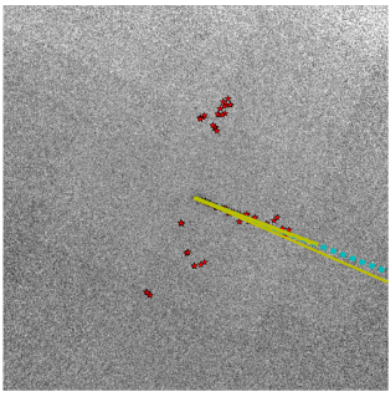

(f) W4 best-fit model

Figure 4.43: The data and results for 237P. The overlays are the same as in Figure 4.1

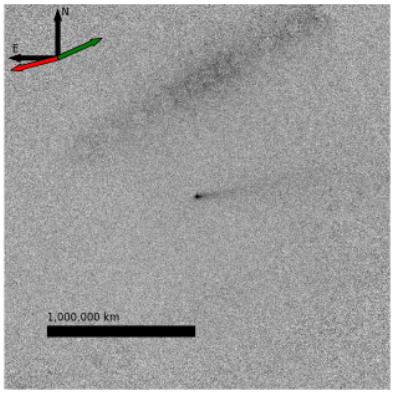


(a) W3 data

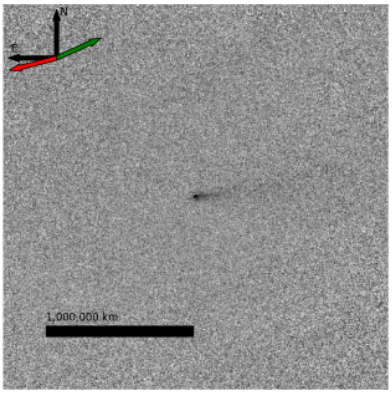


(b) W4 data

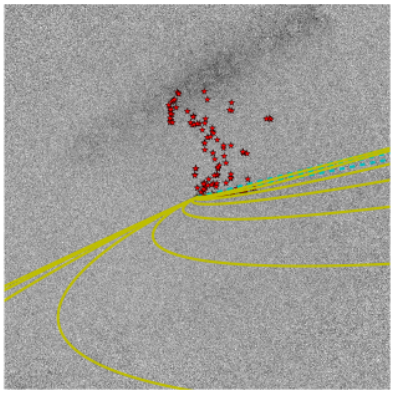

(c) W3 all syndynes and synchrones

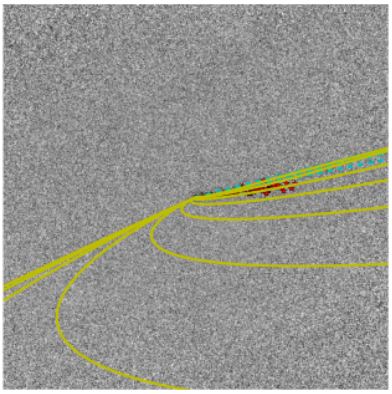

(d) W4 all syndynes and synchrones

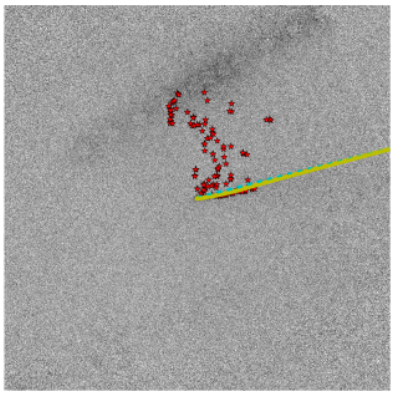

(e) W3 best-fit model

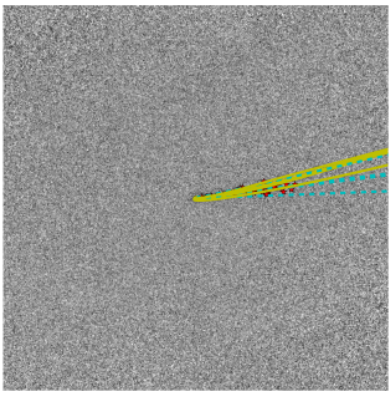

(f) W4 best-fit model

Figure 4.44: The data and results for P/2009 Q4. The overlays are the same as in Figure 4.1

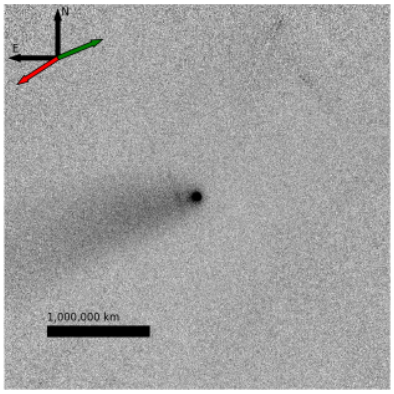


(a) W3 data

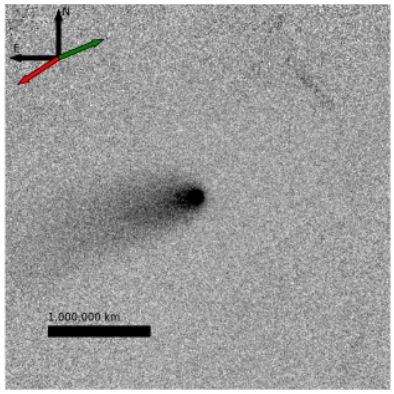


(b) W4 data

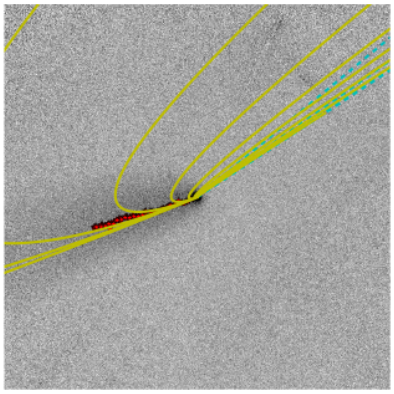

(c) W3 all syndynes and synchrones

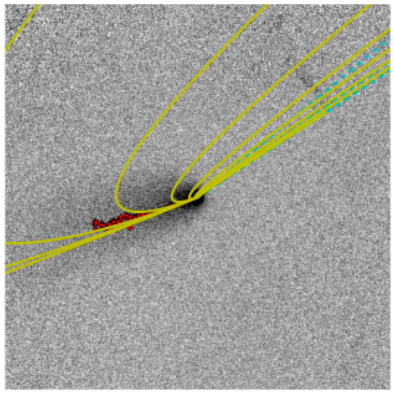

(d) W4 all syndynes and synchrones

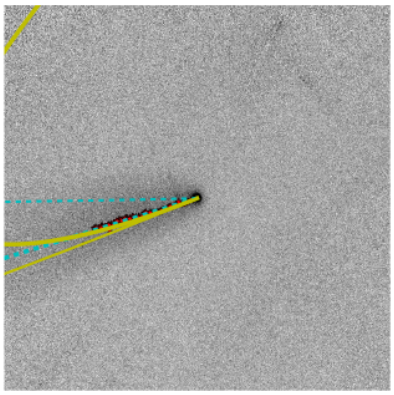

(e) W3 best-fit model

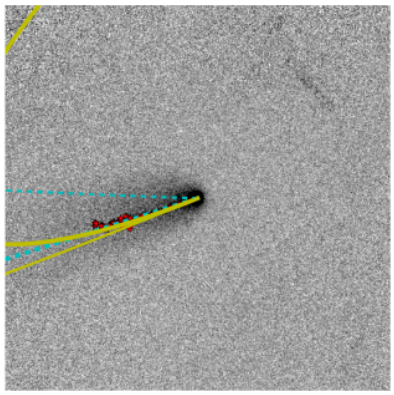

(f) W4 best-fit model

Figure 4.45: The data and results for P/2010 H2. The overlays are the same as in Figure 4.1

## 4.3 Results for individual comets: tails fit by hand

Before the tail-fitting method was developed, the best syndyne and synchrone was selected in our work for each comet by overlaying the entire set on the image, then selecting the syndyne and synchrone that appeared to match the data the best. Although these results are not as rigorously derived at the fitted results described above, they are included for completeness, and to give the reader a sense for why the tail fitting method may not have worked well on these objects.

For each comet, including those which were well-fit by the fitting method, Table 4.2 lists the approximate beta value, approximate number of years since the dust was emitted (listed as a fraction of a year where applicable), the approximate number of days since emission (the number of years x 365), the number of days since perihelion for comparison, and the approximate heliocentric distance at the time of emission. Note that for some comets, even this careful, hands-on treatment could not yield even an estimate of particle size or the heliocentric distance at time of strong emission. For most cases, this was due to a very small angle between the comet's orbit plane, which contains most of its emitted dust (recall that the two main forces acting on the dust, radiation pressure and gravity, are both central so the dust's angular momentum about the Sun is conserved and the dust tends to stay in the orbital plane), and the observer's line of sight, leading to a highly foreshortened dust

tail that shows little structure (see Table 2.1). For each case where no estimates could be derived, the footnote describes for the reader a potential reason.

The individual comets without well-fit tails are shown in the figures below. For each comet, the W3 and W4 data images are shown, the full syndyne/synchrone models are overlaid on the image, and, where applicable, the hand-selected syndyne and synchrone are overlaid on the image. These comets are not discussed individually; rather the reader is directed to Table 4.2 for interpretation of the figures.

Table 4.2: Hand-fit results for all comets

| **Name** | **Approx. Beta** | **Approx. Em. Yrs** | **Approx. Em. Days** | **Days Since Peri** | **Approx. R at Em. (AU)** |
|---|---|---|---|---|---|
| C/2005 L3 | 0.003 | 3 | 1095 | 859 | 5.85 |
| C/2006 OF2 | 0.001 | 2.5 | 912.5 | 602 | 2.51 |
| C/2006 Q1 | -[1] | - | - | 651 | - |
| C/2006 S3 | 0.01 | 3 | 1095 | 37 | 13.01 |
| C/2006 W3 | 0.01 | 3 | 1095 | 287 | 7.64 |
| C/2007 B2 | 0.01 | 1 | 365 | 638 | 5.21 |
| C/2007 G1 | 0.001 | 2.5 | 912.5 | 455 | 5.21 |
| C/2007 N3 | -[1] | - | - | 409 | - |
| C/2007 Q3 | 0.01 | 2 | 730 | 240 | 5.47 |
| C/2007 VO53 | 0.003 | 1 | 365 | -92 | 5.97 |
| C/2008 A1 | 0.001 | 1.5 | 547.5 | 509 | 1.26 |
| C/2008 FK75 | 0.003 | 1.5 | 547.5 | -194 | 7.27 |
| C/2008 N1 | 0.003 | 1.5 | 547.5 | 130 | 4.91 |
| ” | 0.003 | 1 | 365 | 252 | 3.01 |
| C/2008 Q1 | 0.003 | 1 | 365 | 380 | 2.96 |

Continued on next page

[1] Very small orbit plane angle separation; models too stacked up to differentiate between them

| Name | Approx. Beta | Approx. Em. Yrs | Approx. Em. Days | Days Since Peri | Approx. R at Em. (AU) |
|---|---|---|---|---|---|
| ” | 0.0003 | 2 | 730 | 525 | 3.57 |
| C/2008 Q3 | -[1] | - | - | 304 | - |
| C/2008 T2 | 0.001 | 1 | 365 | 319 | 1.4 |
| C/2009 F2 | 0.003 | 1 | 365 | 74 | 6.22 |
| ” | 0.001 | 2 | 730 | 240 | 6.79 |
| C/2009 F5 | 0.0003 | 2 | 730 | 469 | 3.6 |
| ” | -[2] | - | - | 622 | - |
| C/2009 F6 | 0.001 | 1 | 365 | 299 | 1.61 |
| C/2009 G1 | 0.003 | 1 | 365 | 270 | 1.84 |
| C/2009 K2 | 0.01 | 1 | 365 | 91 | 4.13 |
| C/2009 K5 | 0.001 | 0.75 | 273.75 | 167 | 2.05 |
| C/2009 P1 | 0.003 | 4 | 1460 | -566 | 16.21 |
| C/2009 T1 | 0.0003 | 3 | 1095 | 98 | 9.07 |
| C/2009 U3 | 0.003 | 1 | 365 | -62 | 5.17 |
| C/2009 Y1 | 0.003 | 1 | 365 | -294 | 6.69 |
| C/2010 A4 | 0.003 | 1 | 365 | -163 | 5.83 |
| C/2010 DG56 | 0.003 | 0.2 | 73 | 73 | 1.59 |
| C/2010 FB87 | 0.01 | 0.25 | 90 | -107 | 3.46 |
| C/2010 G3 | 0.001 | 2 | 730 | 4 | 7.3 |
| ” | 0.001 | 2.25 | 821.25 | 84 | 7.35 |
| C/2010 J1 | 0.001 | 0.5 | 182.5 | 56 | 2.31 |
| ” | 0.003 | 0.75 | 273.75 | 146 | 2.32 |
| C/2010 J4 | 0.003 | 0.1 | 30 | -2 | 1.21 |
| ” | 0.01 | 0.1 | 30 | 9 | 1.14 |
| C/2010 L4 | 0.003 | 1 | 365 | 112 | 3.75 |
| C/2010 L5 | 0.001 | 0.2 | 60 | 52 | 0.81 |
| ” | 0.001 | 0.25 | 90 | 84 | 0.8 |
| 10P | 0.0003 | -[3] | - | -66 | - |
| 17P | 0.0003 | 3 | 1095 | 1107 | 2.05 |
| 19P | 0.001 | 1.5 | 547.5 | 570 | 1.38 |
| ” | 0.001 | 2 | 730 | 733 | 1.36 |

Continued on next page

[2] Tail is present, but too short or faint to make a determination.

[3] Dust emission is closer to a trail than a tail; too old to say for sure.

| Name | Approx. Beta | Approx. Em. Yrs | Approx. Em. Days | Days Since Peri | Approx. R at Em. (AU) |
|---|---|---|---|---|---|
| 29P | -[4] | - | - | 2123 | - |
| 30P | 0.01 | 1 | 365 | -43 | 3.55 |
| 47P | 0.003 | 1 | 365 | 372 | 2.8 |
| 64P | 0.001 | 0.75 | 273.75 | 323 | 1.51 |
| 65P | -[3] | - | - | 47 | - |
| 67P | 0.001 | 2 | 730 | 324 | 3.79 |
| ” | 0.001 | 2 | 730 | 485 | 2.79 |
| 68P | 0.001 | 3 | 1095 | 395 | 5.43 |
| 74P | 0.003 | 1.5 | 547.5 | 173 | 3.78 |
| ” | 0.003 | 2 | 730 | 342 | 3.79 |
| 77P | 0.003 | 1 | 365 | 303 | 2.35 |
| 81P | -[1] | - | - | 165 | - |
| 89P | 0.001 | 1 | 365 | 354 | 2.28 |
| 94P | 0.003 | 0.75 | 273.75 | 53 | 2.57 |
| 100P | 0.003 | 0.5 | 182.5 | 132 | 2.02 |
| 103P | -[1] | - | - | -170 | - |
| 116P | -[1] | - | - | 272 | - |
| 117P | 0.001 | 4 | 1460 | 1553[5] | 3.07 |
| 118P | 0.003 | 1 | 365 | 82 | 2.85 |
| 127P | 0.001 | 0.75 | 273.75 | 79 | 2.53 |
| 142P | 0.001 | 1 | 365 | 56 | 3.35 |
| 145P | 0.003 | 1 | 365 | 397 | 1.91 |
| 158P | 0.01 | 1 | 365 | -893 | 4.79 |
| 186P | 0.003 | 1.5 | 547.5 | 742 | 4.33 |
| 195P | 0.001 | 3 | 1095 | 514 | 5.12 |
| 199P | 0.001 | 2 | 730 | 465 | 3.46 |
| 203P | 0.001 | 2 | 730 | 16 | 4.63 |
| 213P | -[1] | - | - | -511 | - |
| ” | 0.0003 | 4 | 1460 | -345 | 3.67 |
| 215P | 0.001 | 1 | 365 | -51 | 3.61 |
| 217P | 0.0003 | 1 | 365 | 189 | 2.35 |

Continued on next page

[4] Dust emission is nearly spherical; more like an extended coma than a tail.

[5] This comet is near aphelion. This is the duration since the previous perihelion.

| Name | Approx. Beta | Approx. Em. Yrs | Approx. Em. Days | Days Since Peri | Approx. R at Em. (AU) |
|---|---|---|---|---|---|
| 219P | 0.001 | 1 | 365 | 160 | 2.7 |
| 226P | 0.001 | 1 | 365 | 335 | 1.79 |
| 230P | 0.0003 | 0.75 | 273.75 | 280 | 1.49 |
| 232P | 0.001 | 1 | 365 | 211 | 3.11 |
| 233P | 0.1 | 0.1 | 36.5 | -34 | 1.87 |
| 234P | -[2] | - | - | 24 | - |
| 236P | 0.001 | 0.25 | 91.25 | -79 | 2.35 |
| ” | 0.001 | 0.5 | 182.5 | -67 | 2.75 |
| 237P | -[1] | - | - | 187 | - |
| 240P | 0.001 | 0.5 | 182.5 | -9 | 2.27 |
| 245P | 0.003 | 0.25 | 90 | 119 | 2.16 |
| P/2008 J3 | 0.003 | 1 | 365 | 370 | 2.29 |
| P/2008 Y3 | 0.01 | 1 | 365 | 370 | 4.43 |
| P/2009 Q4 | 0.001 | 1 | 365 | 189 | 2.23 |
| P/2009 T2 | -[6] | - | - | 11 | - |
| P/2009 WX51 | -[1] | - | - | 62 | - |
| P/2010 A1 | 0.003 | 0.75 | 273.75 | 257 | 1.95 |
| P/2010 A2 | 0.0003 | 1 | 365 | 120 | 2.2 |
| P/2010 A3 | -[2] | - | - | -78 | - |
| P/2010 A5 | -[1] | - | - | -88 | - |
| P/2010 D1 | -[2] | - | - | 238 | - |
| P/2010 H2 | 1 | 0.167 | 60 | 121 | 3.12 |
| P/2010 J5 | -[2] | - | - | 115 | - |
| P/2010 P4 | 0.001 | 1 | 365 | 32 | 3.18 |
| P/2010 U1 | -[2] | - | - | 124 | - |

[6] Poor image quality, hard to discern best model.

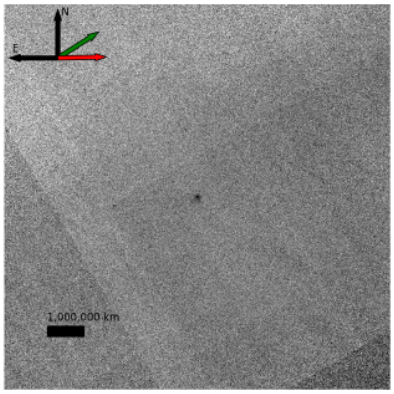


(a) W3 data

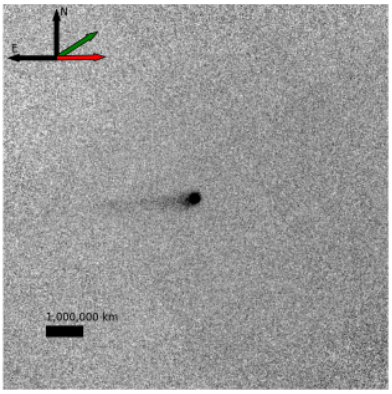


(b) W4 data

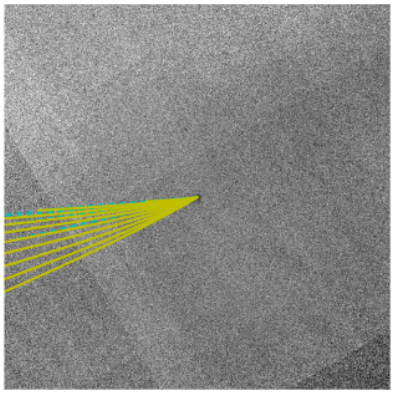

(c) W3 all syndynes and synchrones

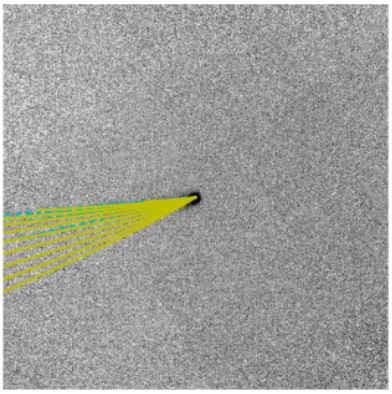

(d) W4 all syndynes and synchrones

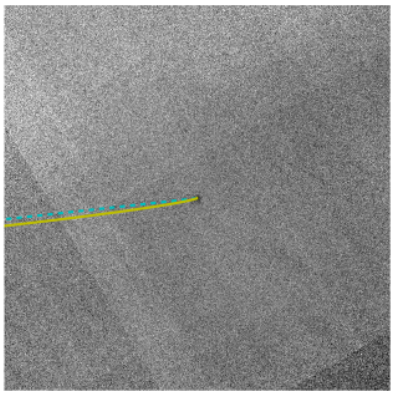

(e) W3 hand-fit model

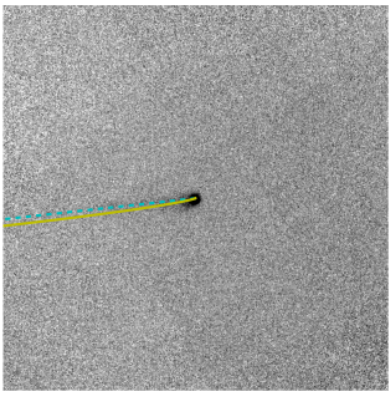

(f) W4 hand-fit model

Figure 4.46: The data and results for C/2005 L3. (a) Included are an inset of the coordinate axes, where N is North, E is East, the green arrow is the sunward direction, and the red arrow is the heliocentric orbit velocity direction. The black bar represents a projected distance of 1,000,000 km at the comet's location. For (c)-(f), cyan (dashed line) are synchrones, and yellow (solid line) are syndynes. In (c) and (d) are shown W3 and W4 (respectively) images with 5-year Finson-Probstein models. The $\beta$ values are (3, 1, 0.3, 0.1, 0.03, 0.01, 0.003, 0.001, 0.0003, and 0.0001). The synchrones are 1, 2, 3, 4, and 5 years. (e) and (f) hand-fit syndynes and synchrones for W3 and W4, respectively.

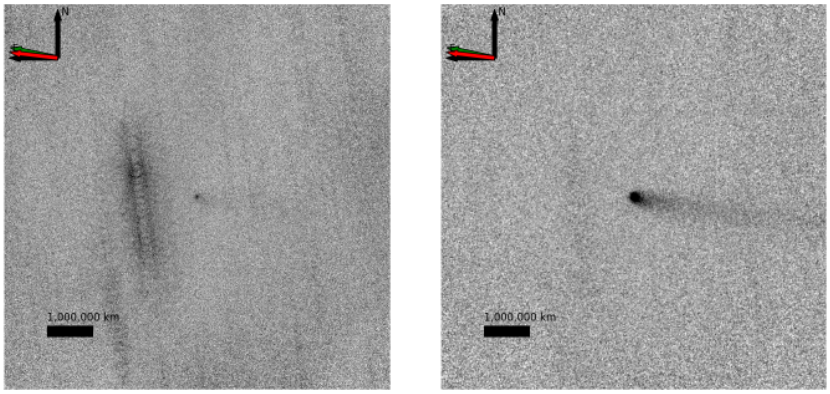


(a) W3 data (b) W4 data

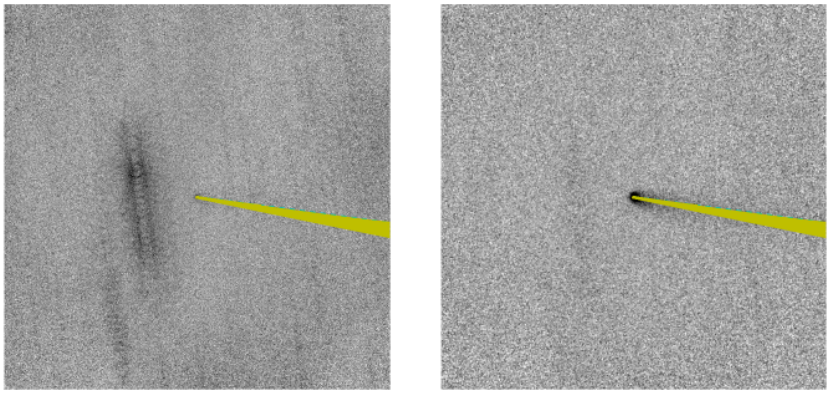

(c) W3 all syndynes and synchrones (d) W4 all syndynes and synchrones

Figure 4.47: The data and results for C/2006 Q1. The overlays are the same as in Figure 4.46, but without panels (e) and (f)

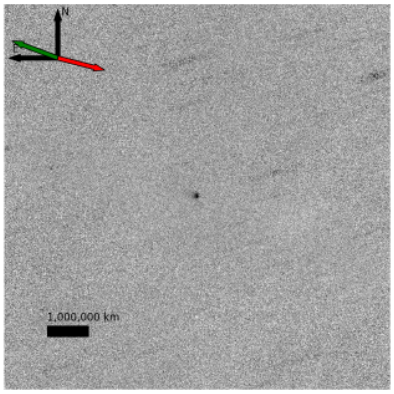


(a) W3 data

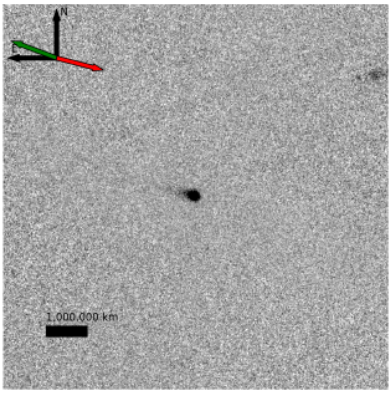


(b) W4 data

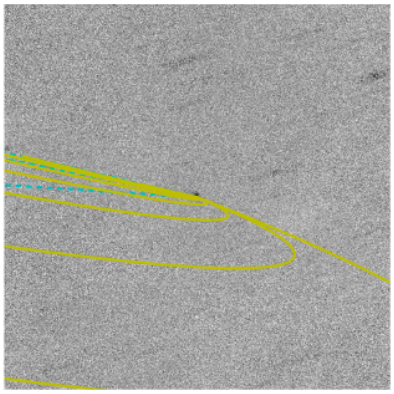

(c) W3 all syndynes and synchrones

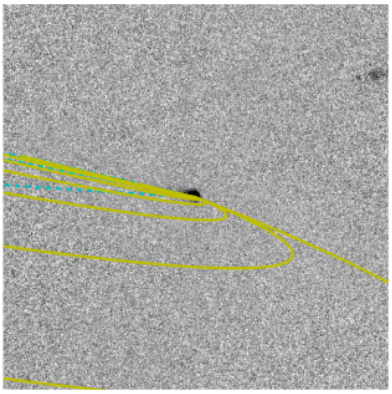

(d) W4 all syndynes and synchrones

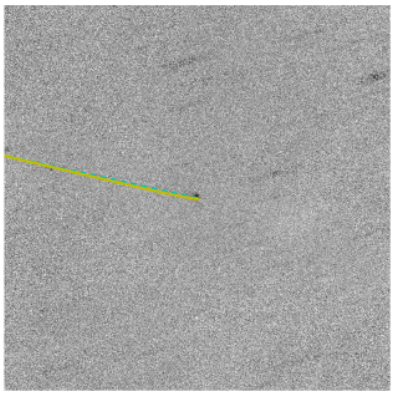

(e) W3 hand-fit model

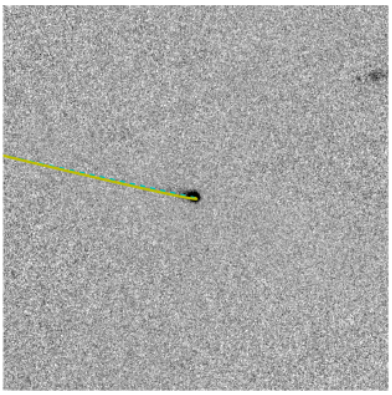

(f) W4 hand-fit model

Figure 4.48: The data and results for C/2006 S3. The overlays are the same as in Figure 4.46

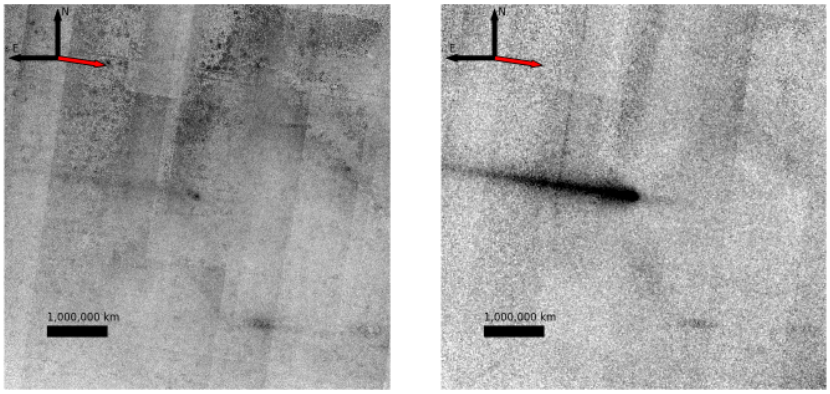


(a) W3 data (b) W4 data

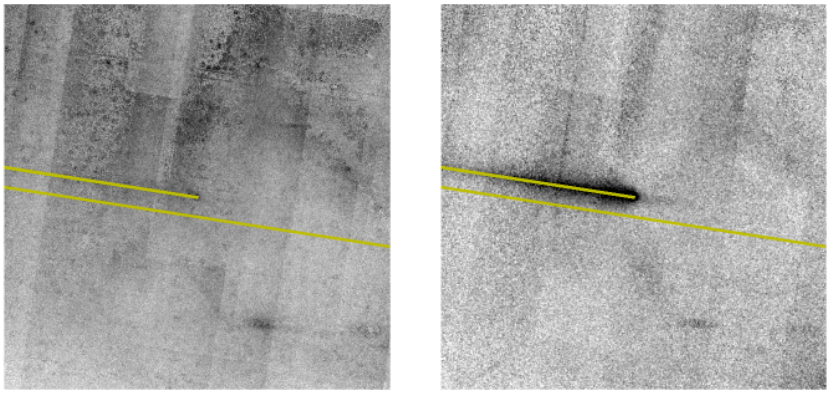

(c) W3 all syndynes and synchrones (d) W4 all syndynes and synchrones

Figure 4.49: The data and results for C/2007 N3. The overlays are the same as in Figure 4.46, but without panels (e) and (f)

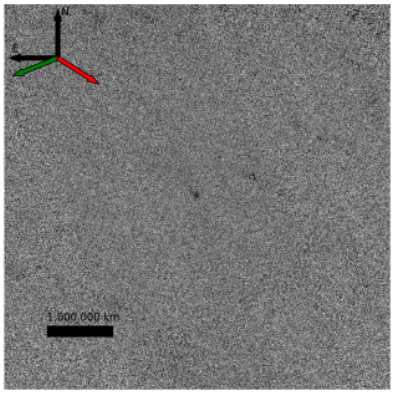


(a) W3 data

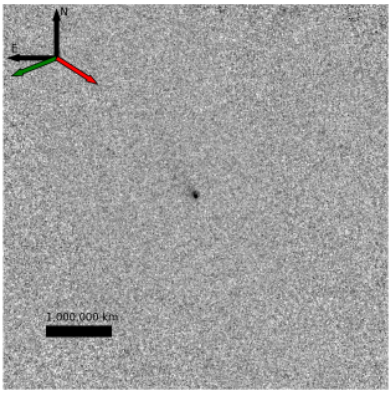


(b) W4 data

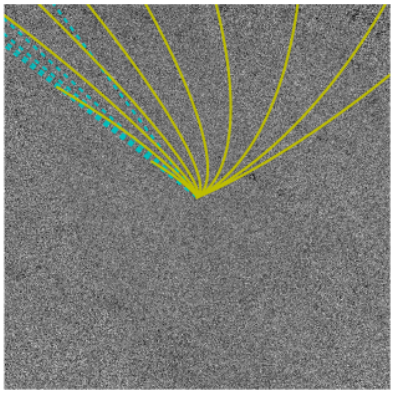

(c) W3 all syndynes and synchrones

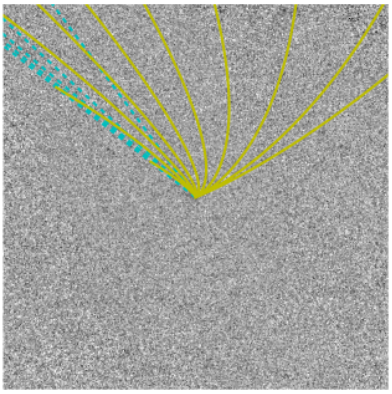

(d) W4 all syndynes and synchrones

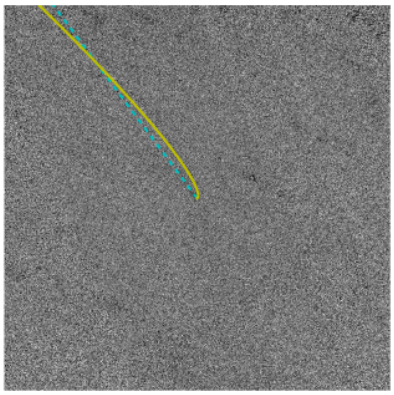

(e) W3 hand-fit model

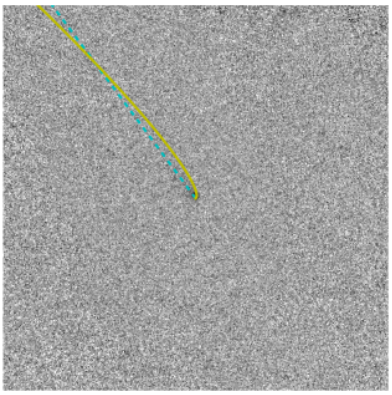

(f) W4 hand-fit model

Figure 4.50: The data and results for C/2008 Q1 (A). The overlays are the same as in Figure 4.46

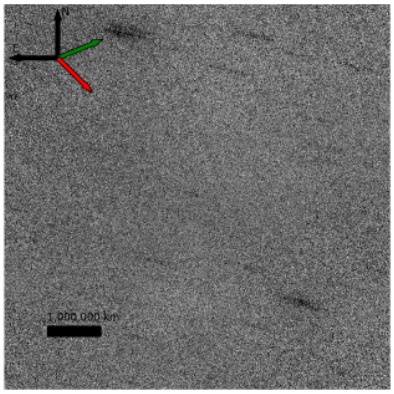

(a) W3 data

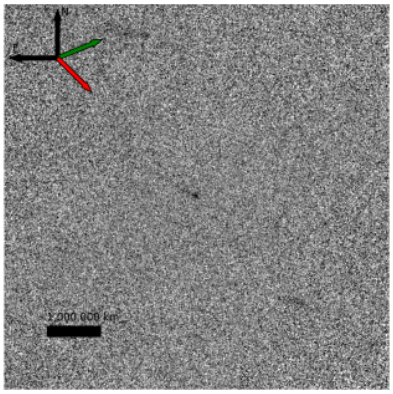

(b) W4 data

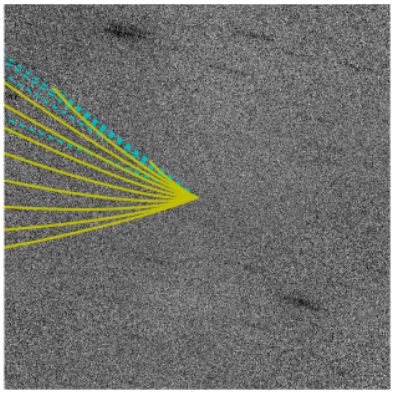

(c) W3 all syndynes and synchrones

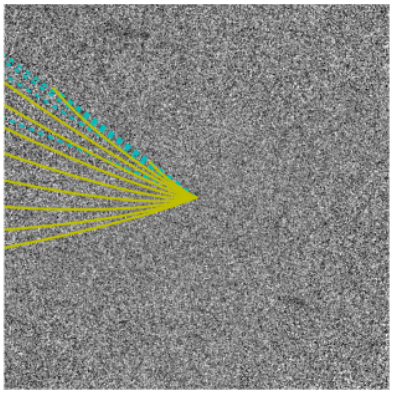

(d) W4 all syndynes and synchrones

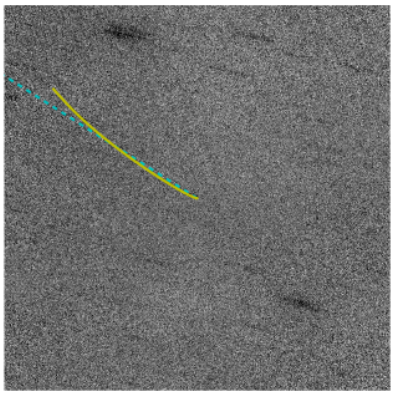

(e) W3 hand-fit model

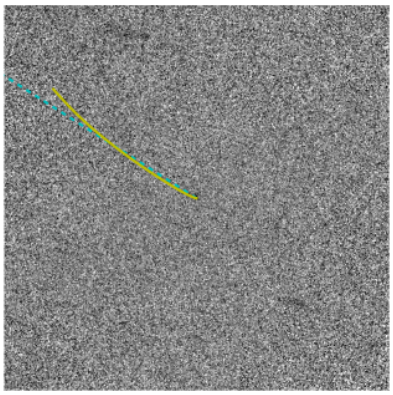

(f) W4 hand-fit model

Figure 4.51: The data and results for C/2008 Q1 (B). The overlays are the same as in Figure 4.46

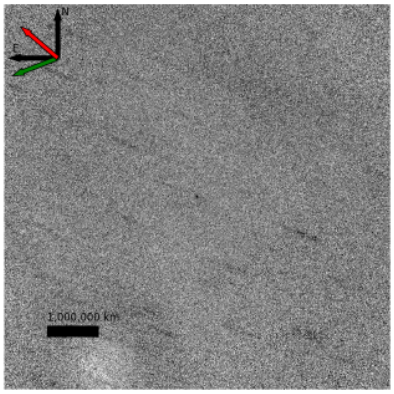


(a) W3 data

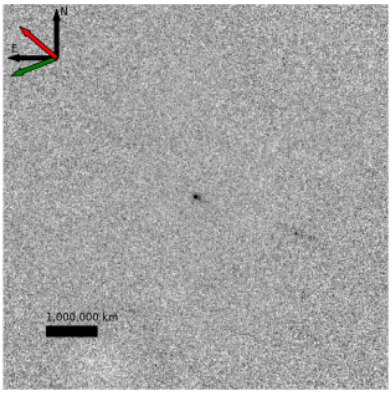


(b) W4 data

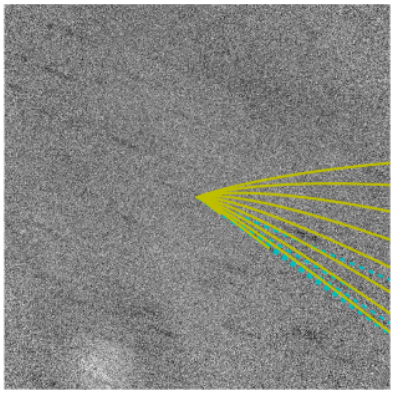

(c) W3 all syndynes and synchrones

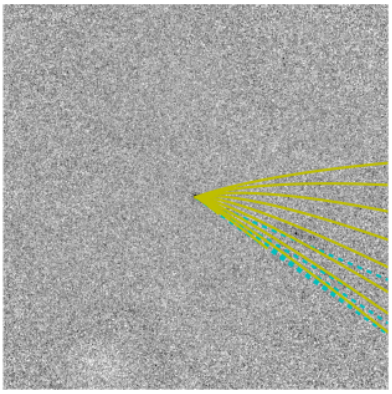

(d) W4 all syndynes and synchrones

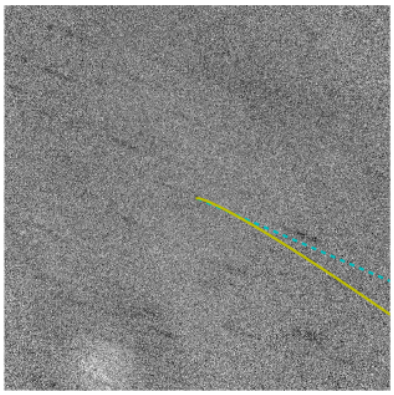

(e) W3 hand-fit model

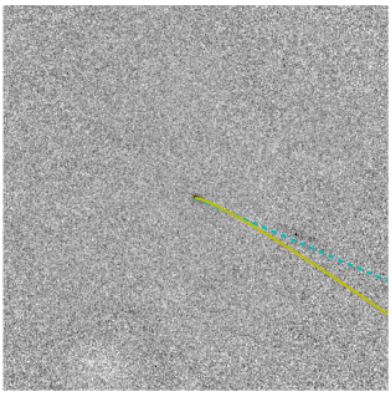

(f) W4 hand-fit model

Figure 4.52: The data and results for C/2009 F2 (A). The overlays are the same as in Figure 4.46

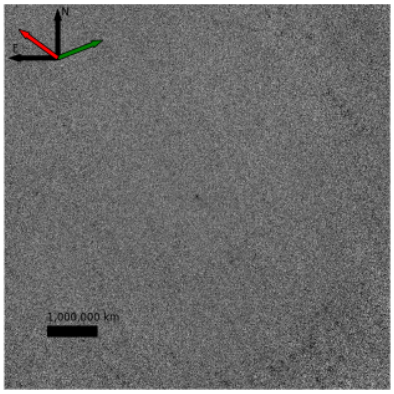


(a) W3 data

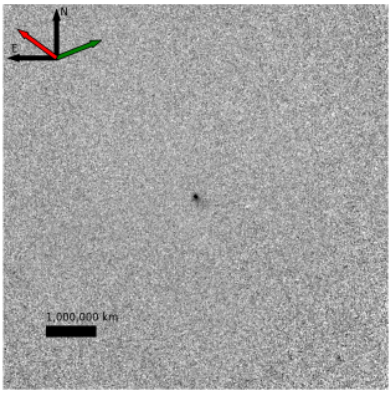


(b) W4 data

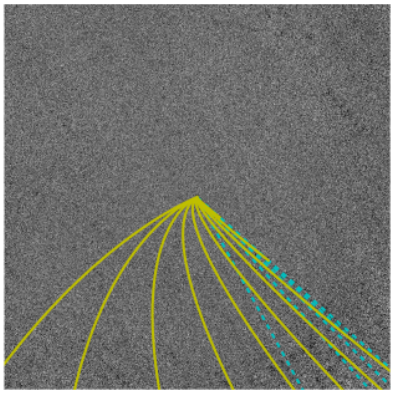

(c) W3 all syndynes and synchrones

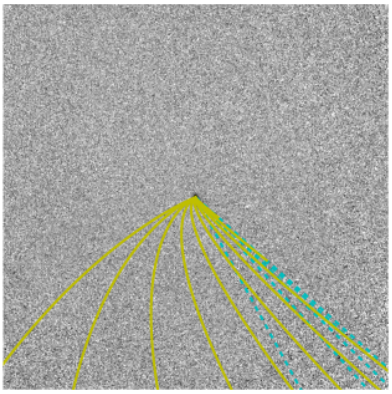

(d) W4 all syndynes and synchrones

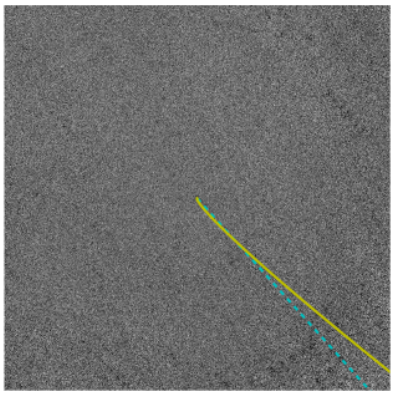

(e) W3 hand-fit model

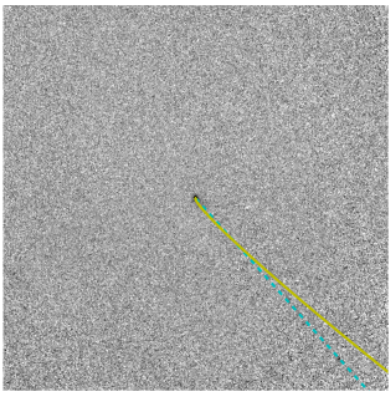

(f) W4 hand-fit model

Figure 4.53: The data and results for C/2009 F2 (B). The overlays are the same as in Figure 4.46

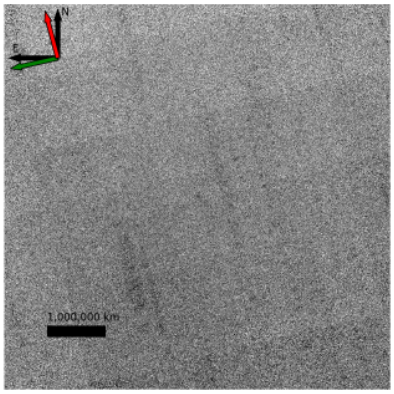


(a) W3 data

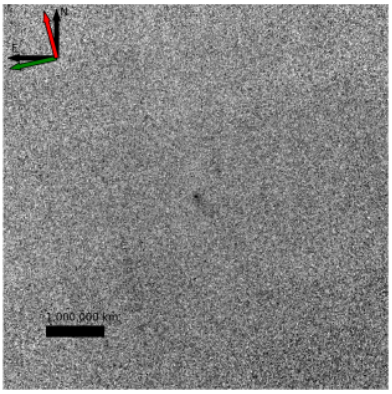


(b) W4 data

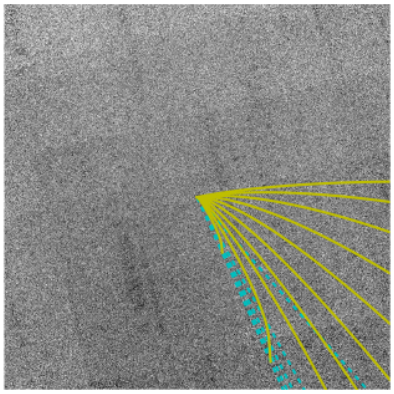

(c) W3 all syndynes and synchrones

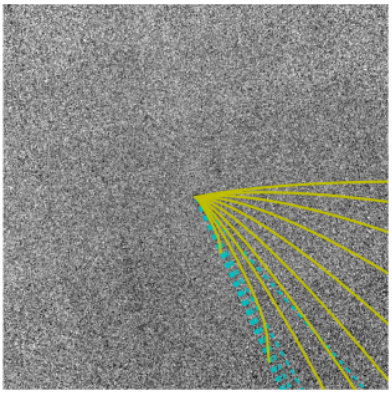

(d) W4 all syndynes and synchrones

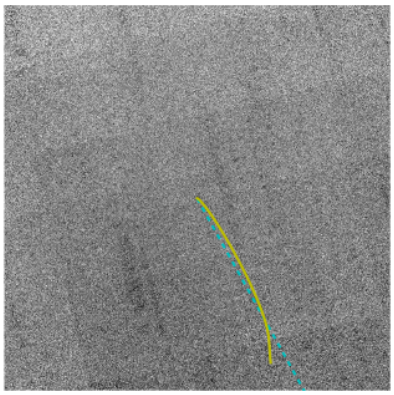

(e) W3 hand-fit model

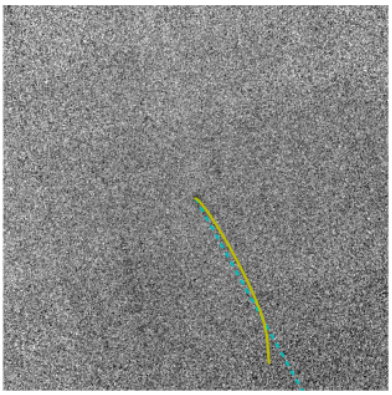

(f) W4 hand-fit model

Figure 4.54: The data and results for C/2009 F5 (A). The overlays are the same as in Figure 4.46

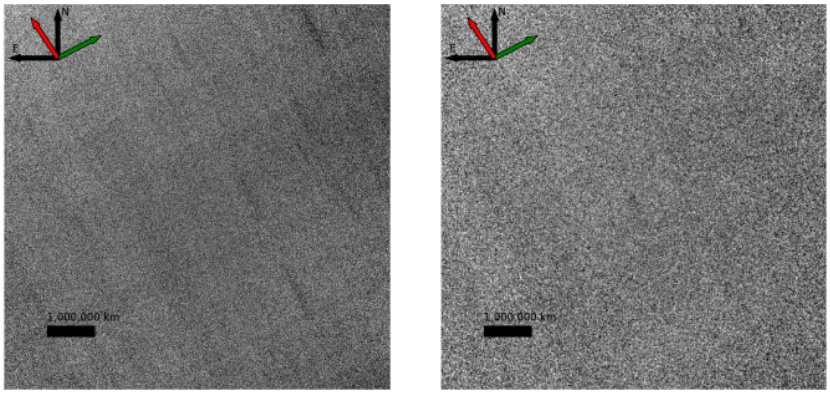


(a) W3 data

(b) W4 data

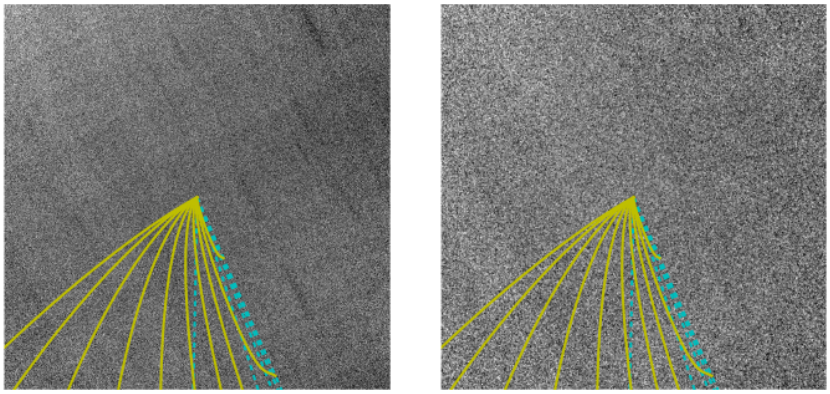

(c) W3 all syndynes and synchrones

(d) W4 all syndynes and synchrones

Figure 4.55: The data and results for C/2009 F5 (B). The overlays are the same as in Figure 4.46, but without panels (e) and (f)

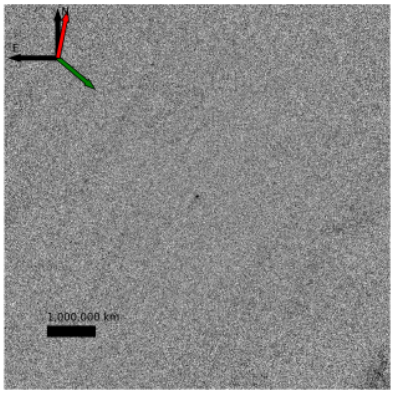


(a) W3 data

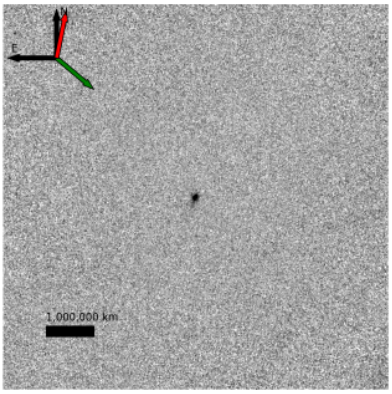


(b) W4 data

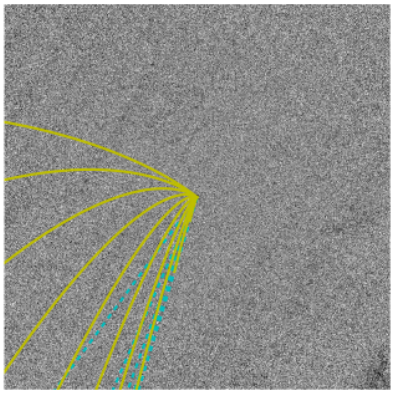

(c) W3 all syndynes and synchrones

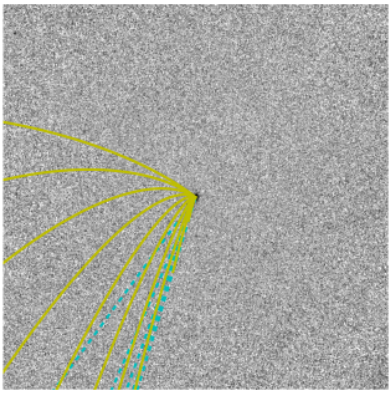

(d) W4 all syndynes and synchrones

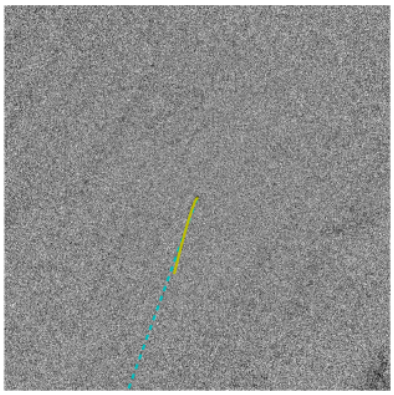

(e) W3 hand-fit model

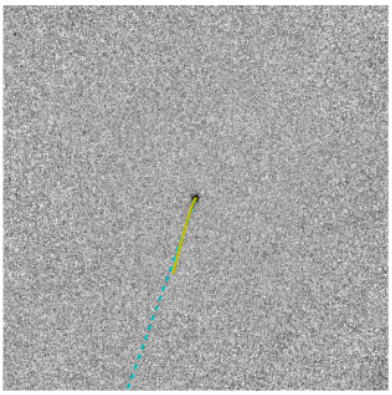

(f) W4 hand-fit model

Figure 4.56: The data and results for C/2009 T1. The overlays are the same as in Figure 4.46

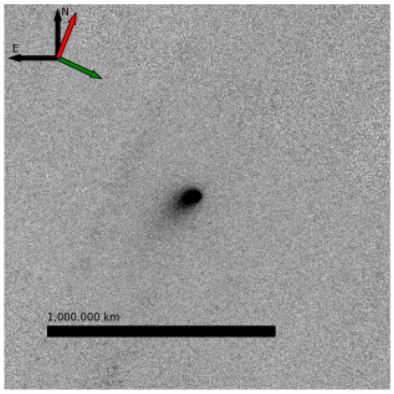


(a) W3 data

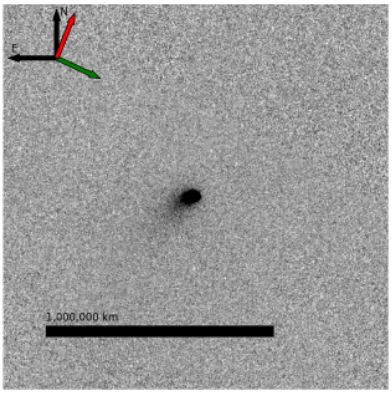


(b) W4 data

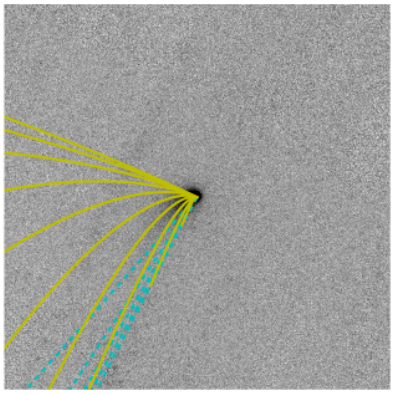

(c) W3 all syndynes and synchrones

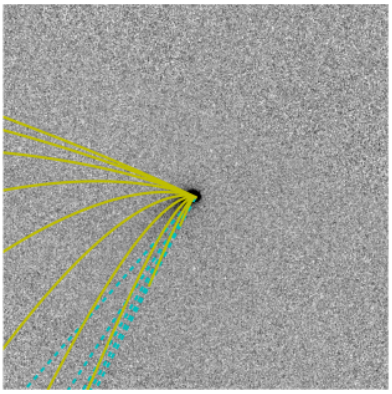

(d) W4 all syndynes and synchrones

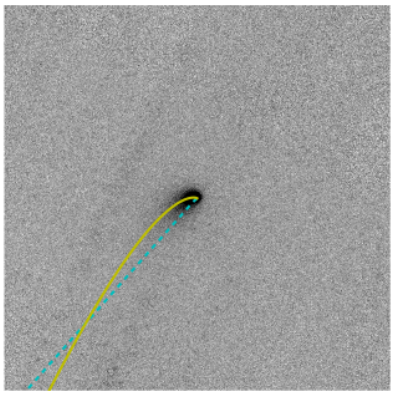

(e) W3 hand-fit model

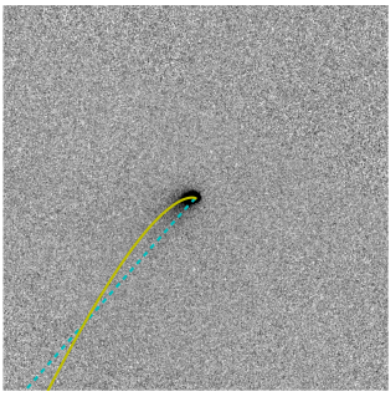

(f) W4 hand-fit model

Figure 4.57: The data and results for C/2009 U3. The overlays are the same as in Figure 4.46

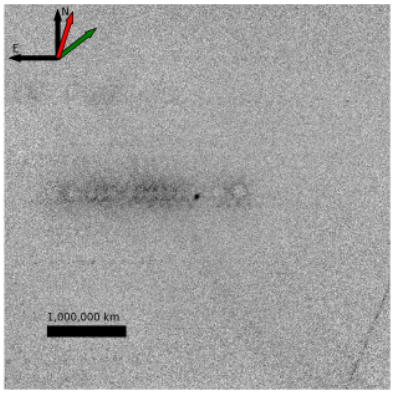


(a) W3 data

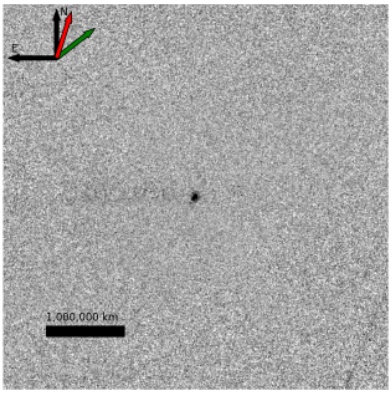


(b) W4 data

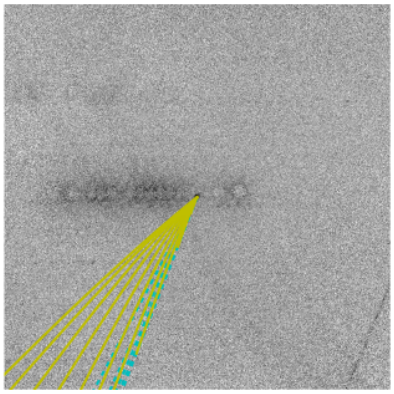

(c) W3 all syndynes and synchrones

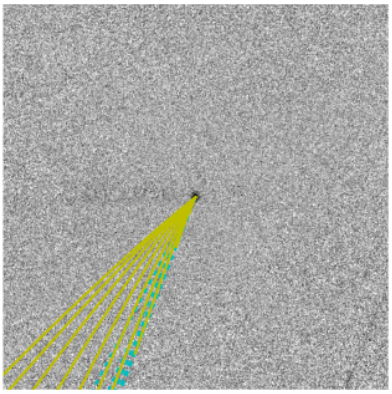

(d) W4 all syndynes and synchrones

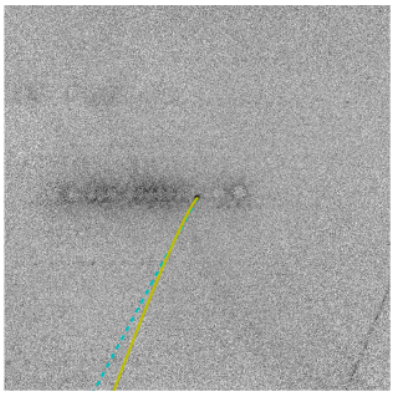

(e) W3 hand-fit model

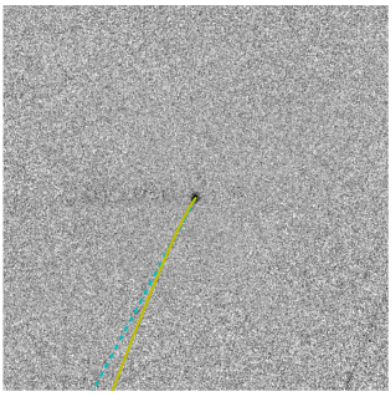

(f) W4 hand-fit model

Figure 4.58: The data and results for C/2009 Y1. The overlays are the same as in Figure 4.46

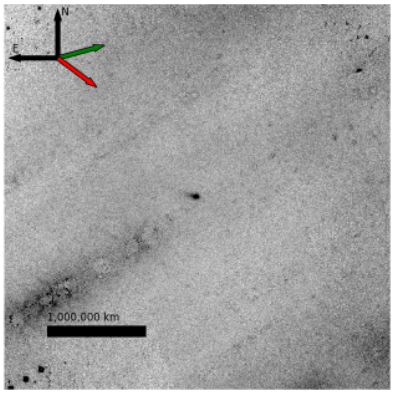


(a) W3 data

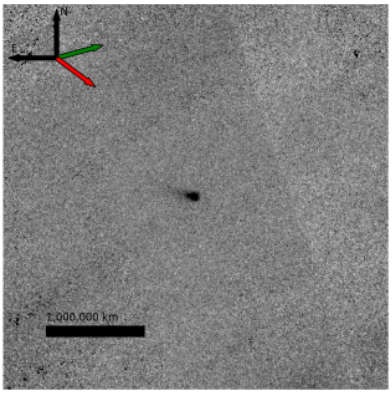


(b) W4 data

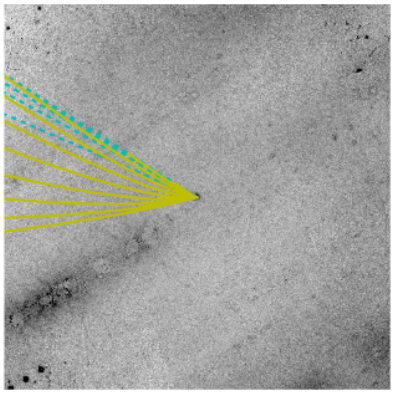

(c) W3 all syndynes and synchrones

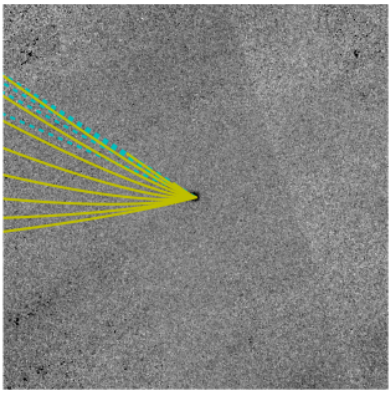

(d) W4 all syndynes and synchrones

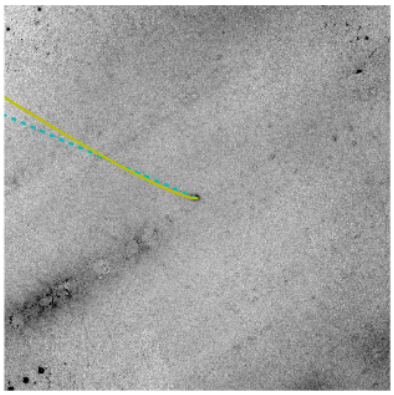

(e) W3 hand-fit model

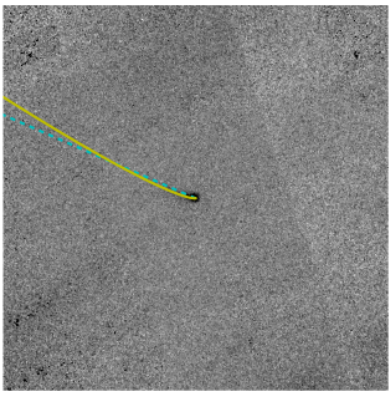

(f) W4 hand-fit model

Figure 4.59: The data and results for C/2010 A4. The overlays are the same as in Figure 4.46

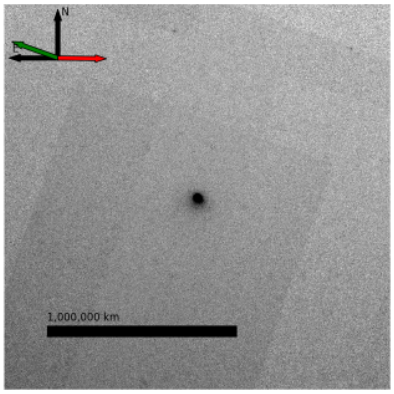


(a) W3 data

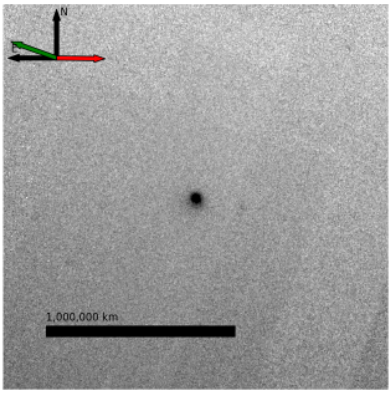


(b) W4 data

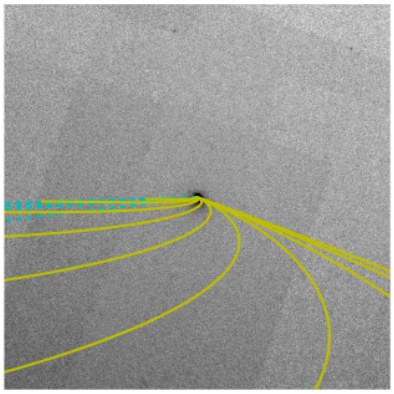

(c) W3 all syndynes and synchrones

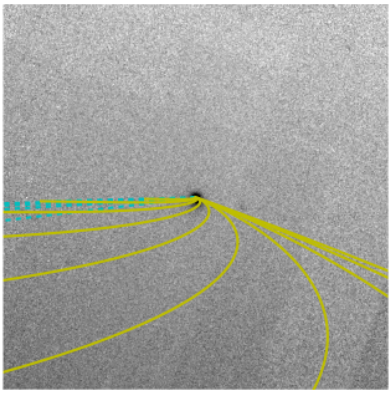

(d) W4 all syndynes and synchrones

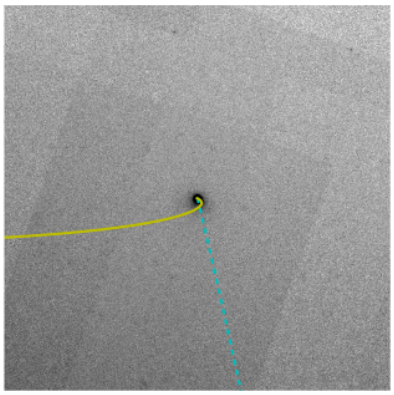

(e) W3 hand-fit model

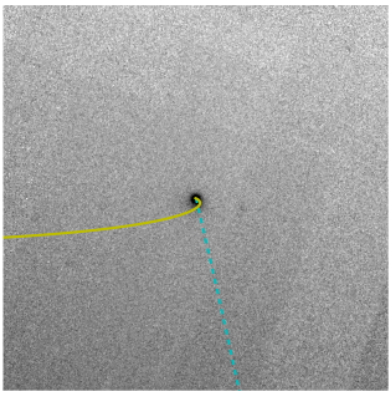

(f) W4 hand-fit model

Figure 4.60: The data and results for C/2010 DG56 (B). The overlays are the same as in Figure 4.46

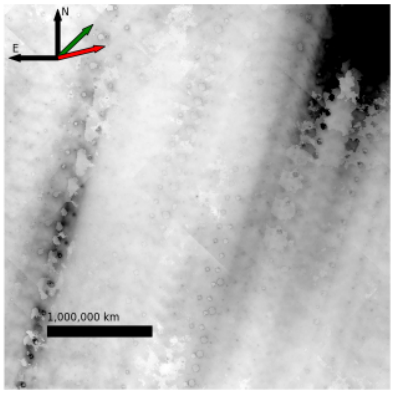


(a) W3 data

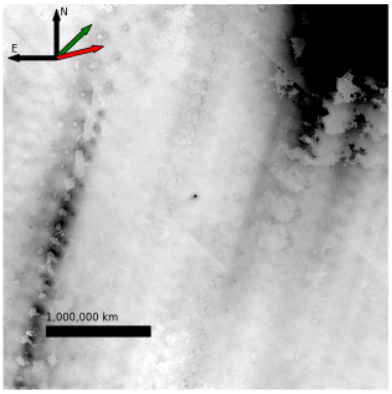


(b) W4 data

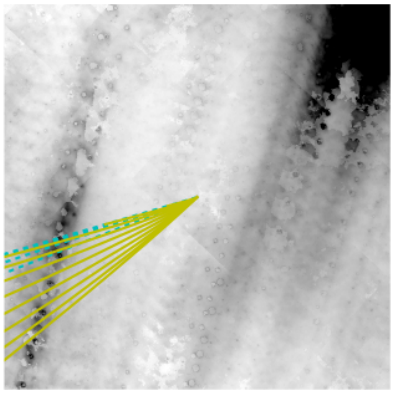

(c) W3 all syndynes and synchrones

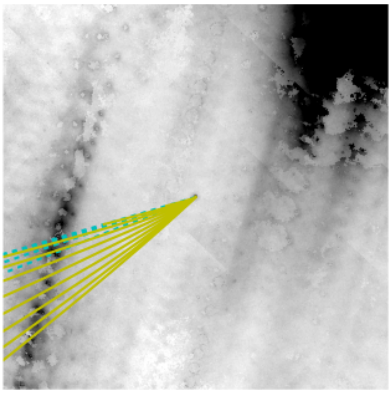

(d) W4 all syndynes and synchrones

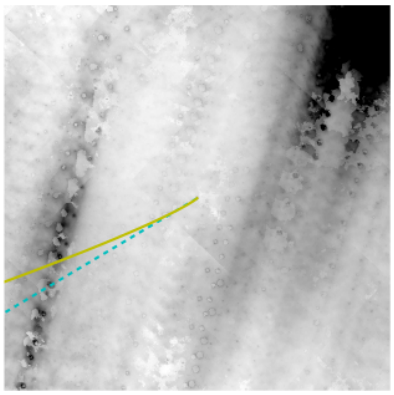

(e) W3 hand-fit model

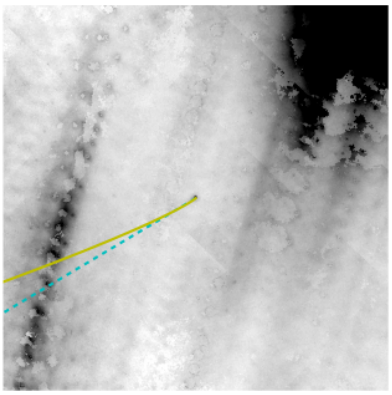

(f) W4 hand-fit model

Figure 4.61: The data and results for C/2010 FB87 (B). The overlays are the same as in Figure 4.46

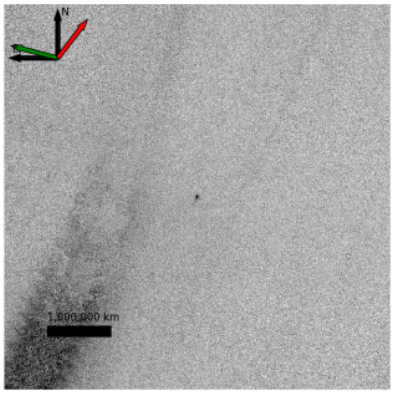


(a) W3 data

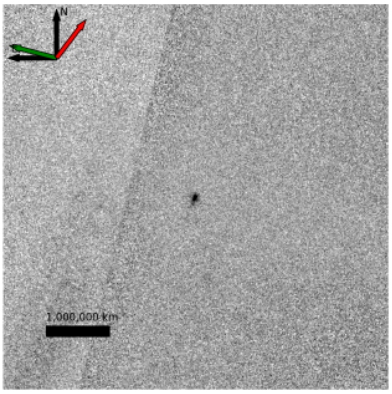


(b) W4 data

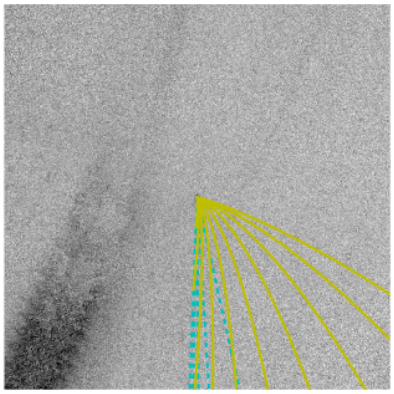

(c) W3 all syndynes and synchrones

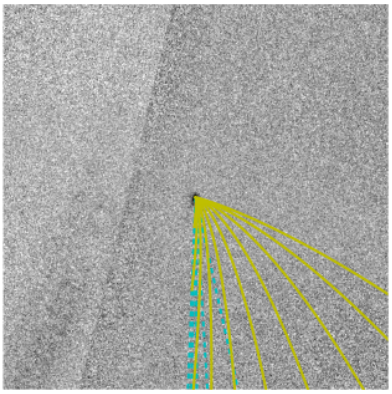

(d) W4 all syndynes and synchrones

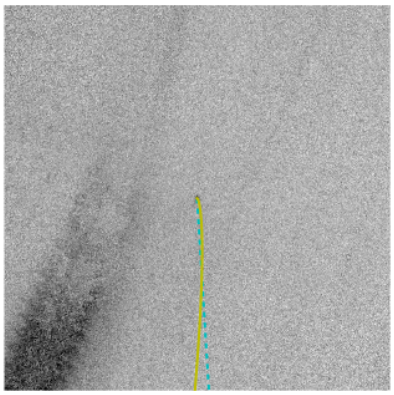

(e) W3 hand-fit model

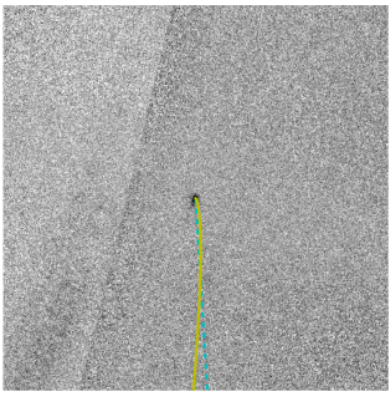

(f) W4 hand-fit model

Figure 4.62: The data and results for C/2010 G3 (A). The overlays are the same as in Figure 4.46

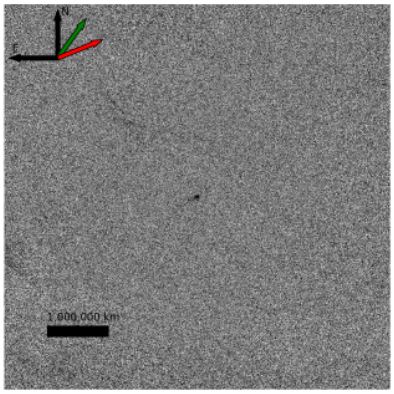


(a) W3 data

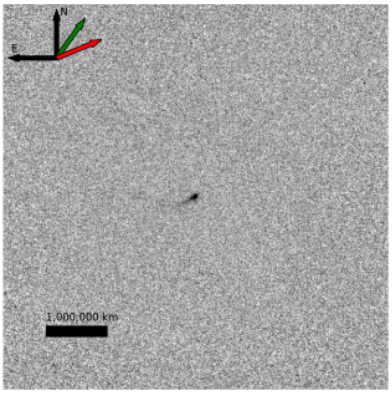


(b) W4 data

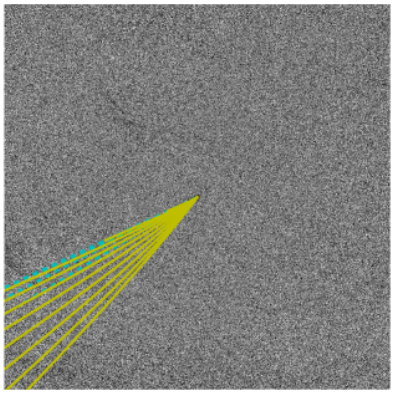

(c) W3 all syndynes and synchrones

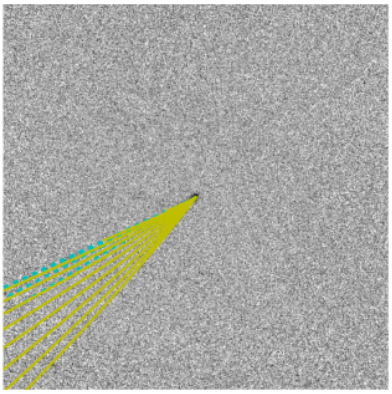

(d) W4 all syndynes and synchrones

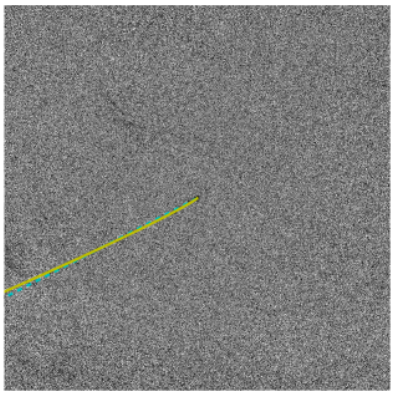

(e) W3 hand-fit model

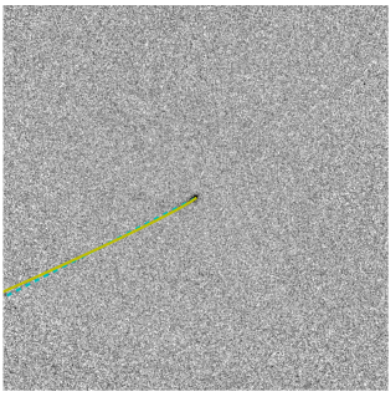

(f) W4 hand-fit model

Figure 4.63: The data and results for C/2010 G3 (B). The overlays are the same as in Figure 4.46

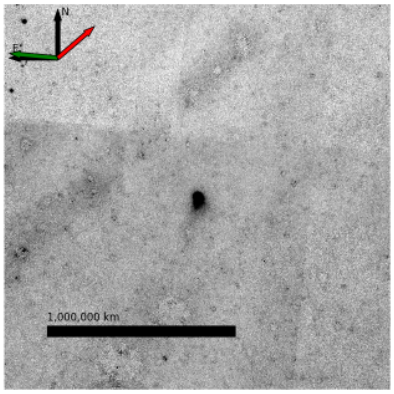


(a) W3 data

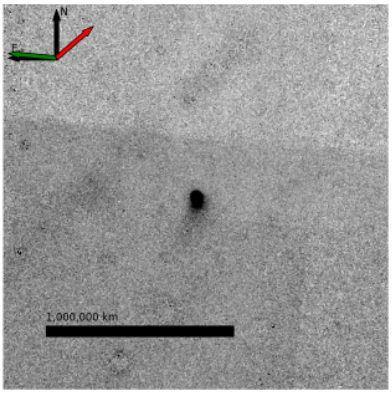


(b) W4 data

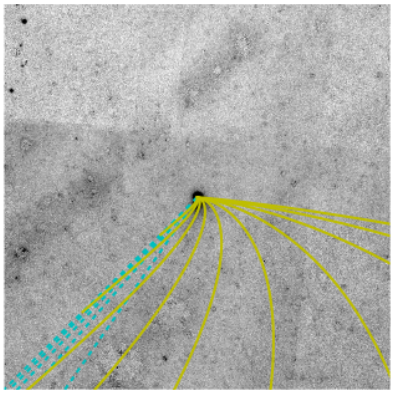

(c) W3 all syndynes and synchrones

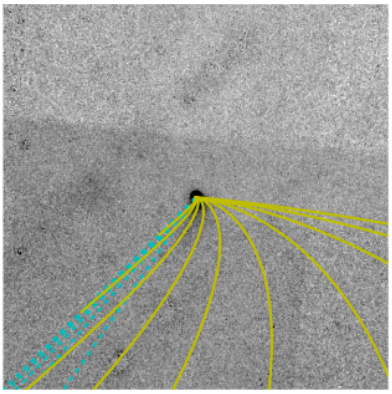

(d) W4 all syndynes and synchrones

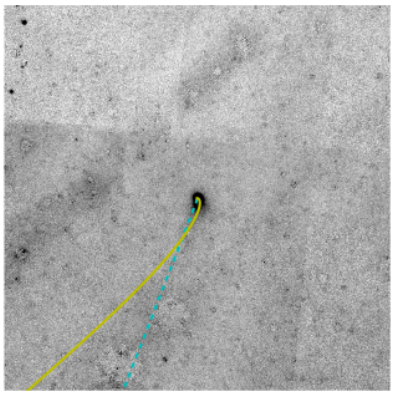

(e) W3 hand-fit model

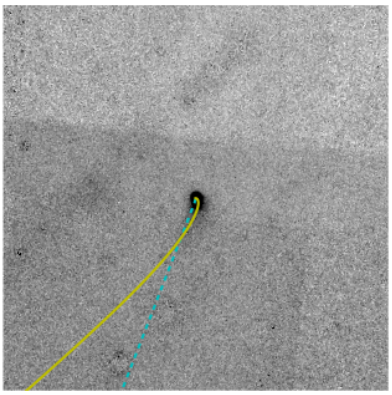

(f) W4 hand-fit model

Figure 4.64: The data and results for C/2010 J1 (A). The overlays are the same as in Figure 4.46

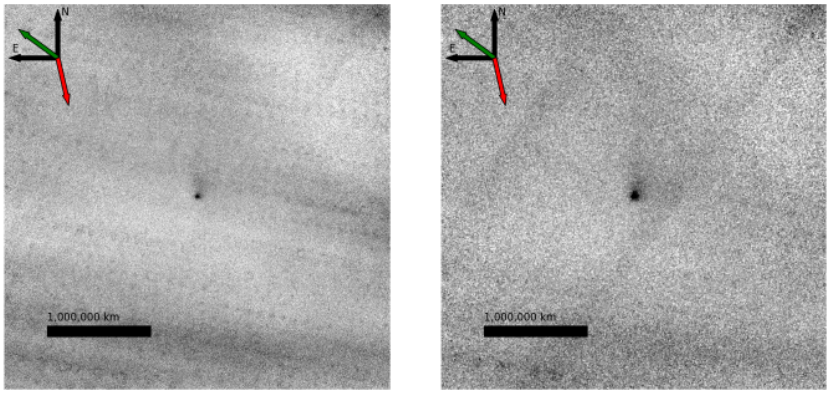


(a) W3 data

(b) W4 data

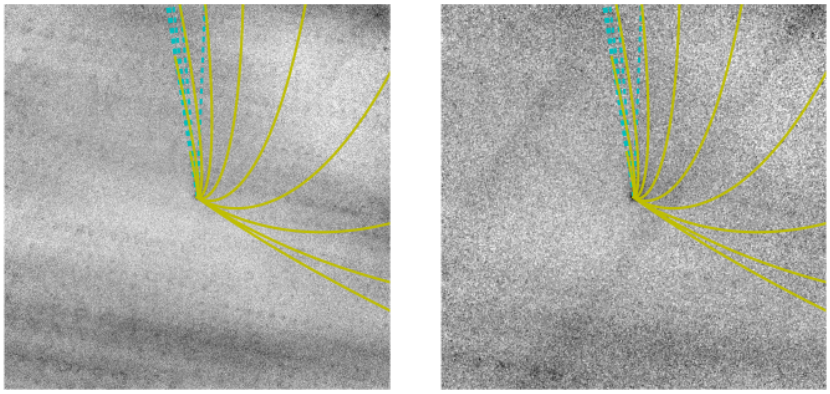

(c) W3 all syndynes and synchrones

(d) W4 all syndynes and synchrones

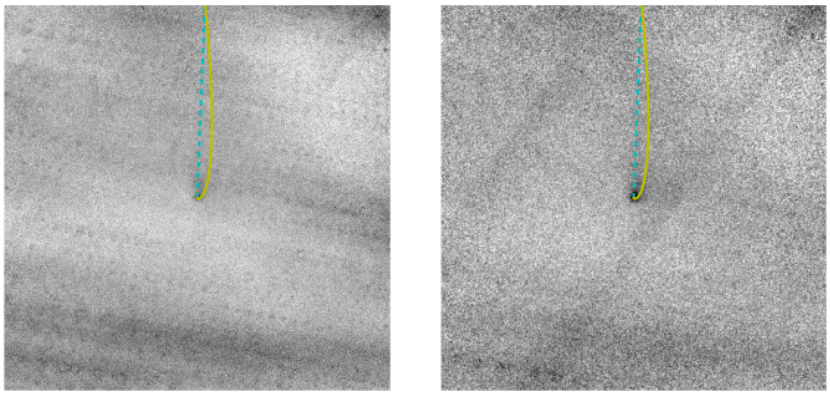

(e) W3 hand-fit model

(f) W4 hand-fit model

Figure 4.65: The data and results for C/2010 L4. The overlays are the same as in Figure 4.46

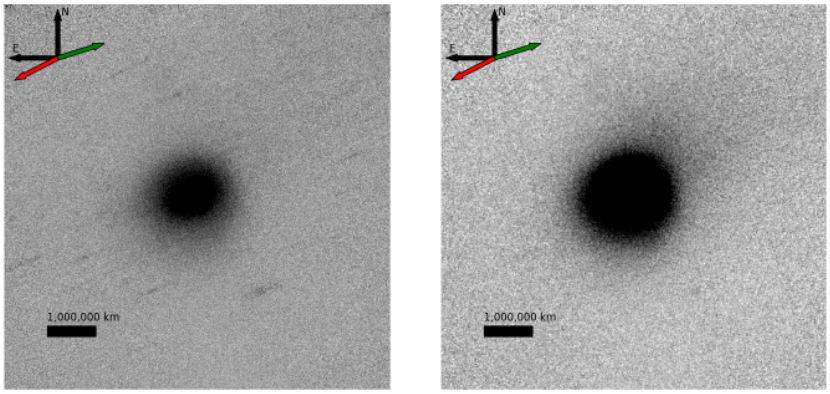


(a) W3 data

(b) W4 data

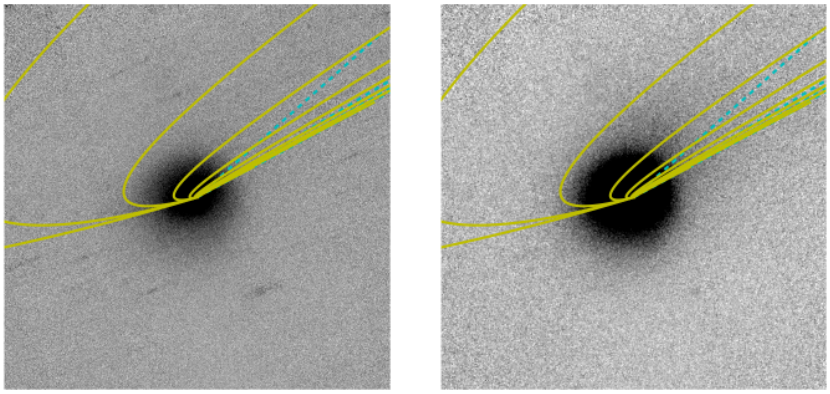

(c) W3 all syndynes and synchrones

(d) W4 all syndynes and synchrones

Figure 4.66: The data and results for 29P. The overlays are the same as in Figure 4.46, but without panels (e) and (f)

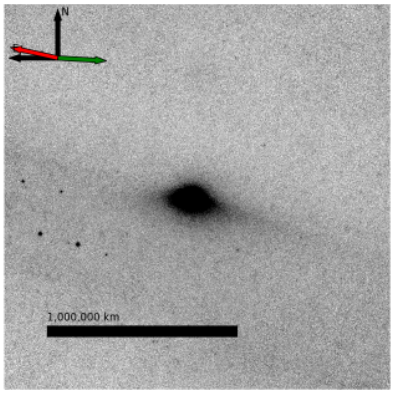


(a) W3 data

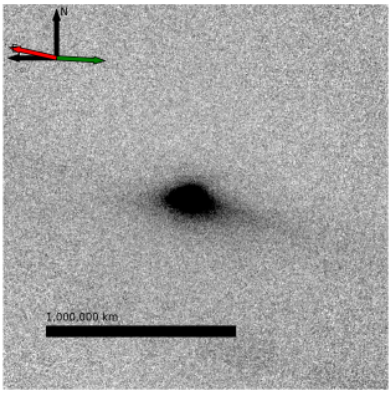


(b) W4 data

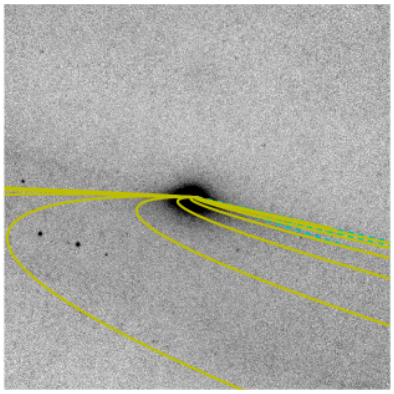

(c) W3 all syndynes and synchrones

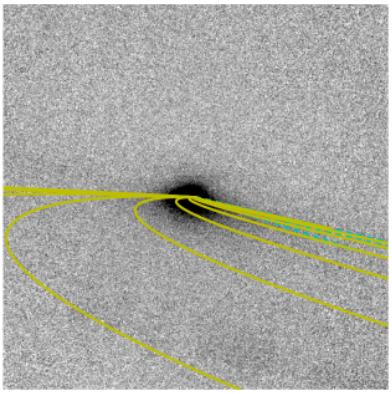

(d) W4 all syndynes and synchrones

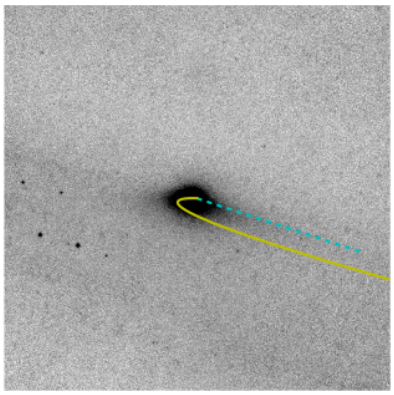

(e) W3 hand-fit model

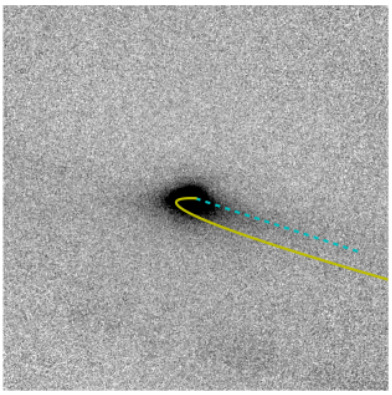

(f) W4 hand-fit model

Figure 4.67: The data and results for 30P. The overlays are the same as in Figure 4.46

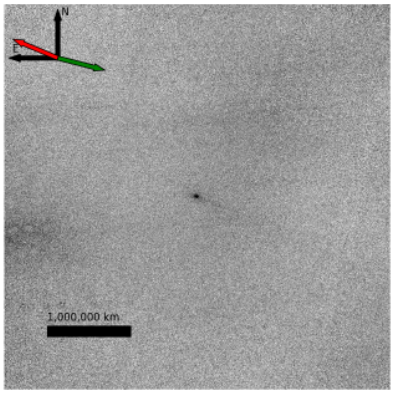


(a) W3 data

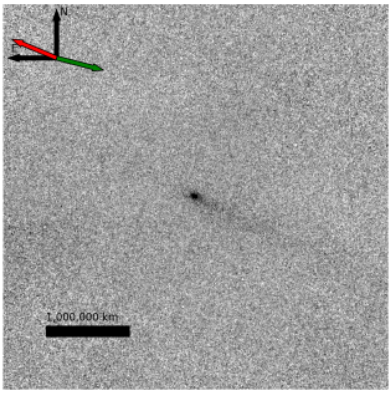


(b) W4 data

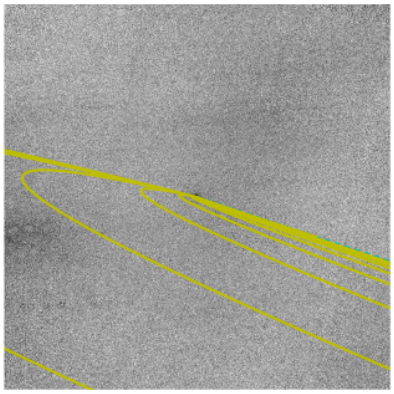

(c) W3 all syndynes and synchrones

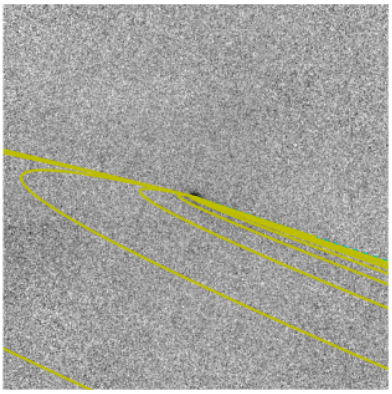

(d) W4 all syndynes and synchrones

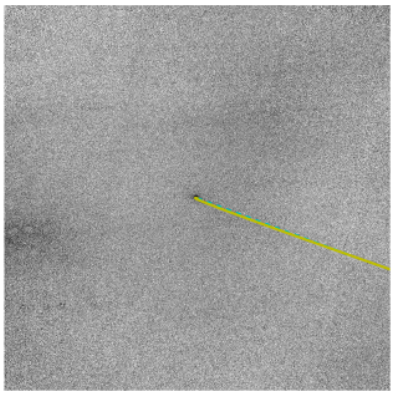

(e) W3 hand-fit model

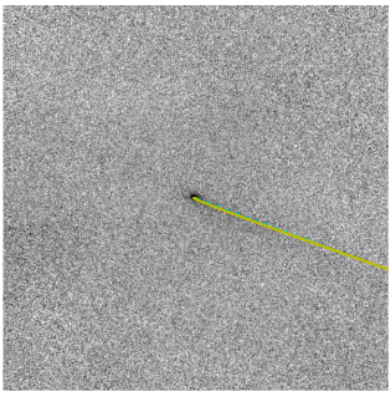

(f) W4 hand-fit model

Figure 4.68: The data and results for 47P. The overlays are the same as in Figure 4.46

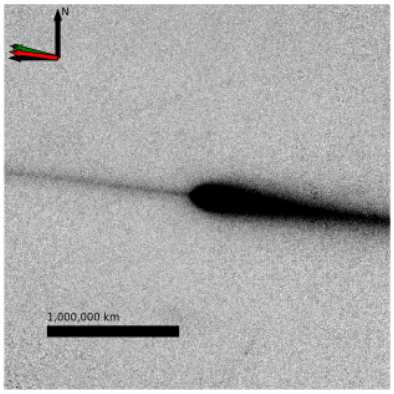


(a) W3 data

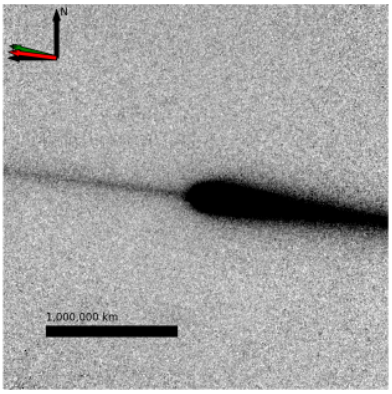


(b) W4 data

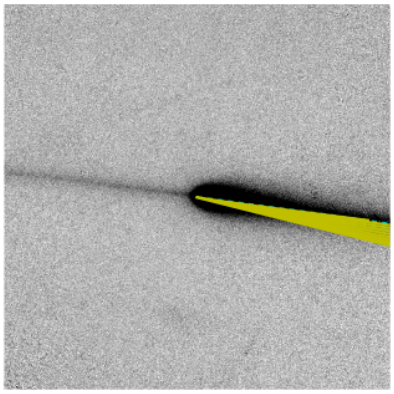

(c) W3 all syndynes and synchrones

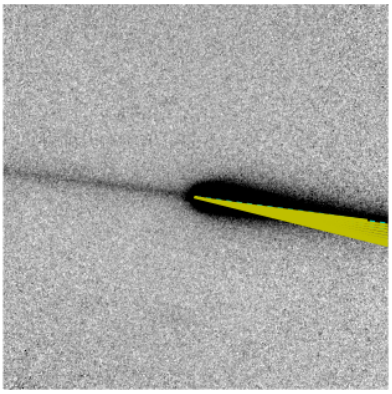

(d) W4 all syndynes and synchrones

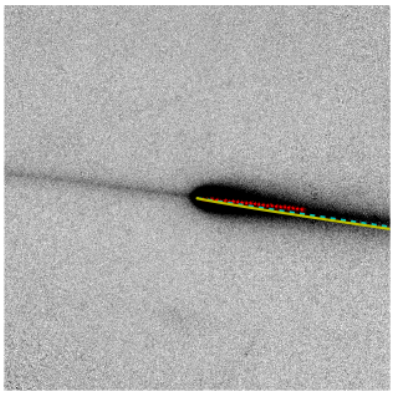

(e) W3 hand-fit model

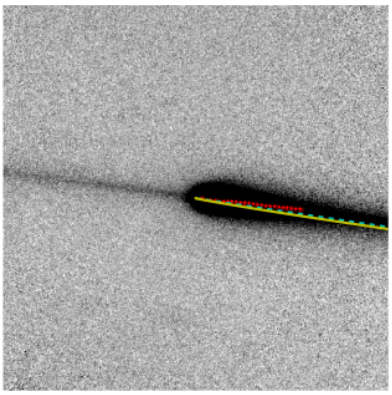

(f) W4 hand-fit model

Figure 4.69: The data and results for 65P. The overlays are the same as in Figure 4.46

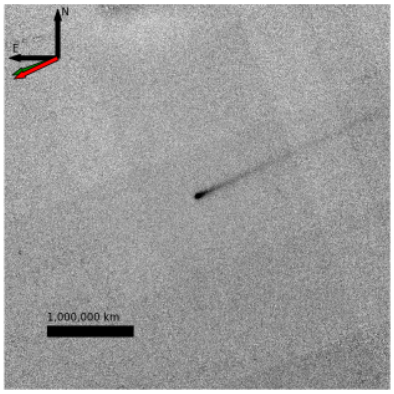


(a) W3 data

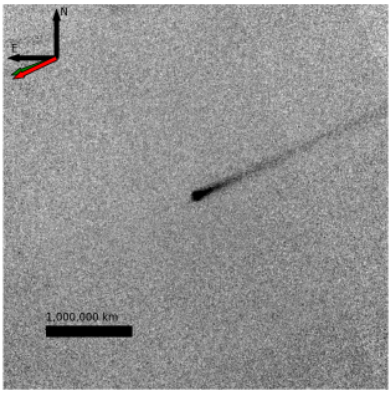


(b) W4 data

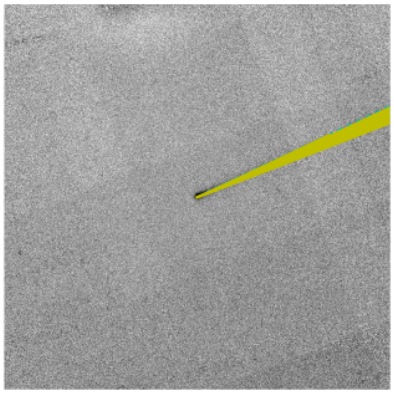

(c) W3 all syndynes and synchrones

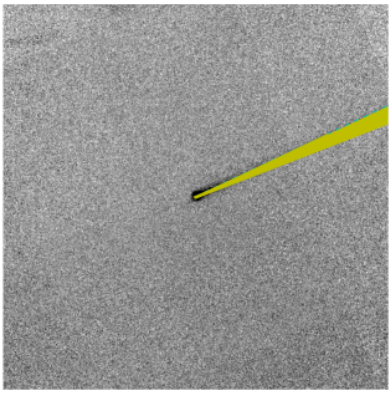

(d) W4 all syndynes and synchrones

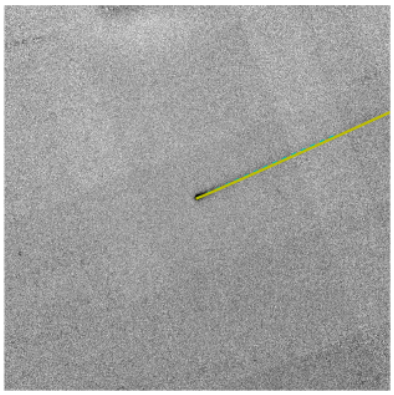

(e) W3 hand-fit model

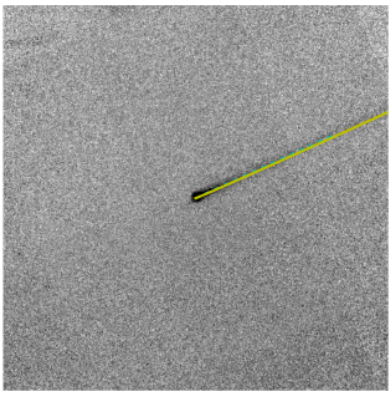

(f) W4 hand-fit model

Figure 4.70: The data and results for 74P (A). The overlays are the same as in Figure 4.46

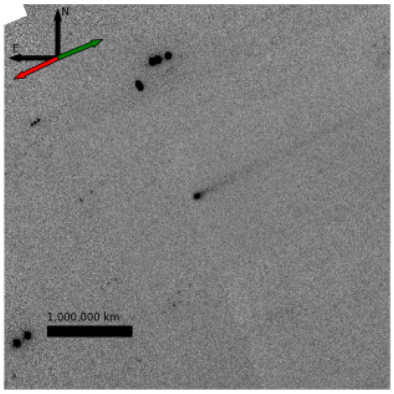


(a) W3 data

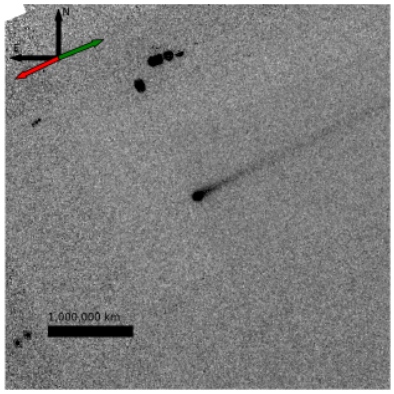


(b) W4 data

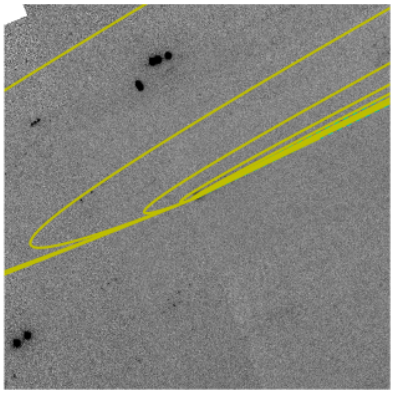

(c) W3 all syndynes and synchrones

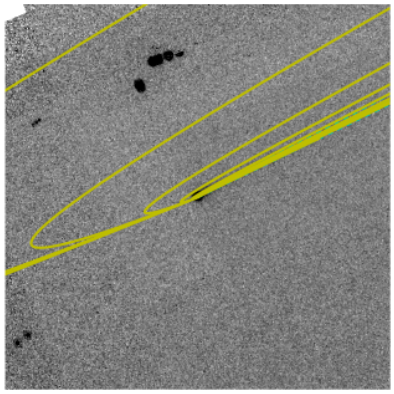

(d) W4 all syndynes and synchrones

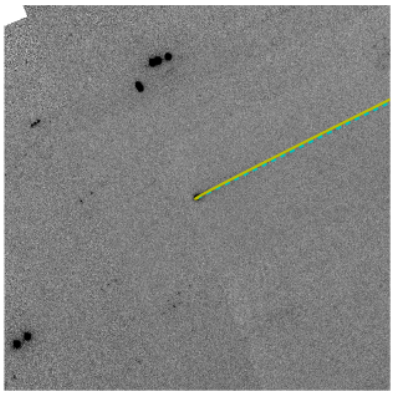

(e) W3 hand-fit model

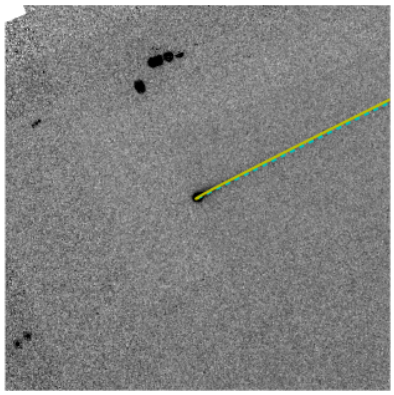

(f) W4 hand-fit model

Figure 4.71: The data and results for 74P (B). The overlays are the same as in Figure 4.46

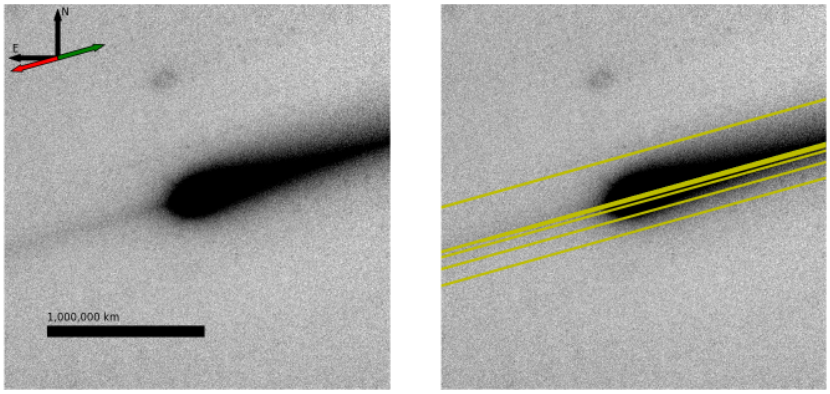


(a) W3 data (b) W3 all syndynes and synchrones

Figure 4.72: The data and results for 81P. The overlays are the same as in Figure 4.46, but without panels (c)-(f)

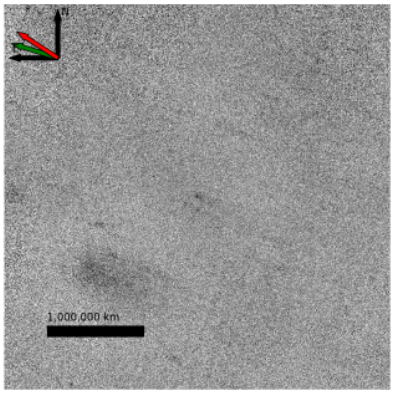


(a) W3 data

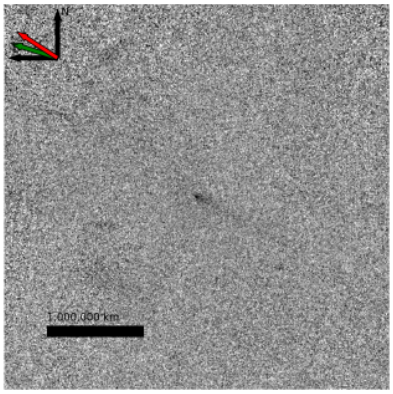


(b) W4 data

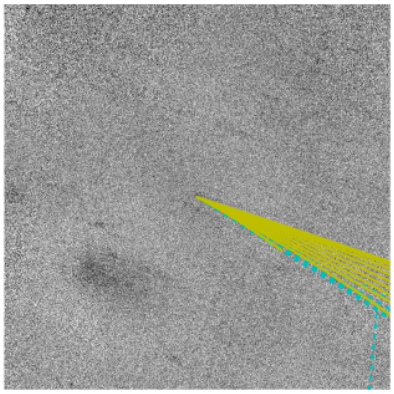

(c) W3 all syndynes and synchrones

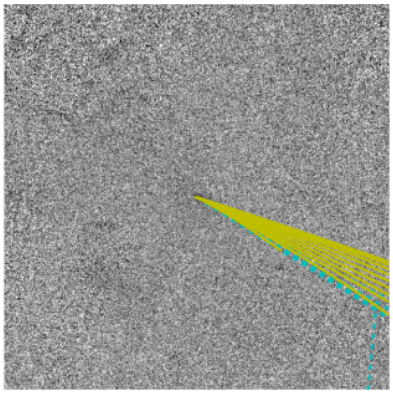

(d) W4 all syndynes and synchrones

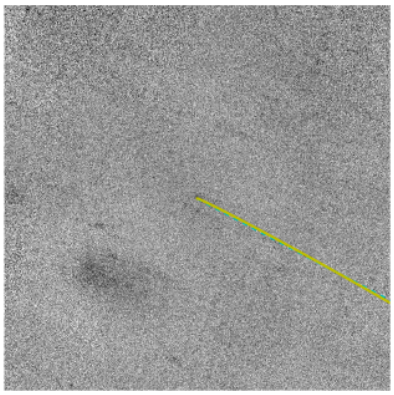

(e) W3 hand-fit model

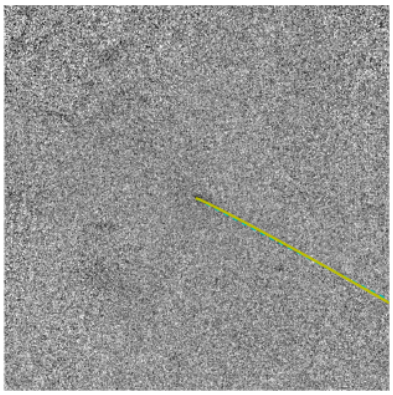

(f) W4 hand-fit model

Figure 4.73: The data and results for 89P. The overlays are the same as in Figure 4.46

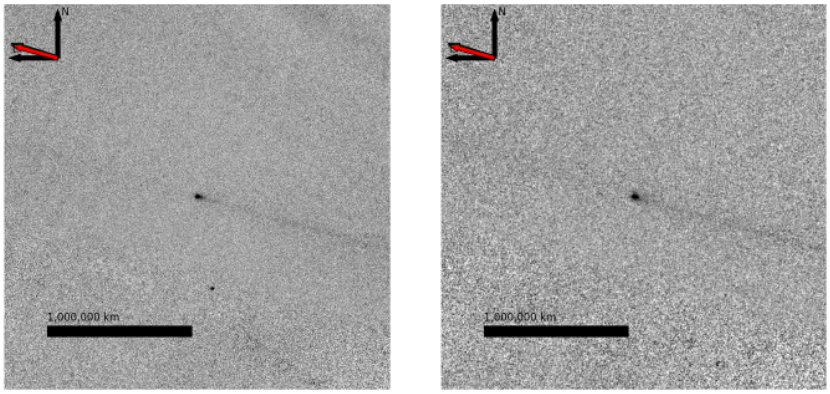


(a) W3 data (b) W4 data

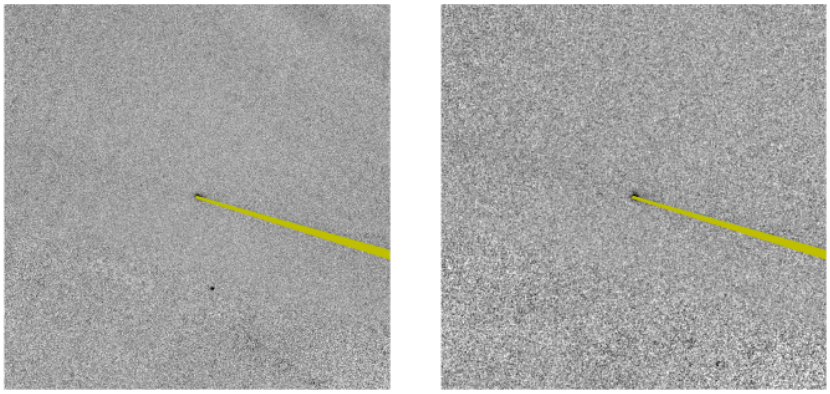

(c) W3 all syndynes and synchrones (d) W4 all syndynes and synchrones

Figure 4.74: The data and results for 103P. The overlays are the same as in Figure 4.46, but without panels (e) and (f)

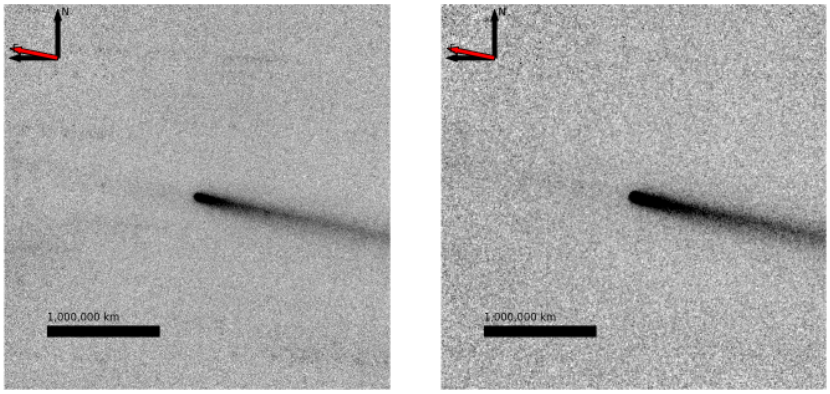


(a) W3 data (b) W4 data

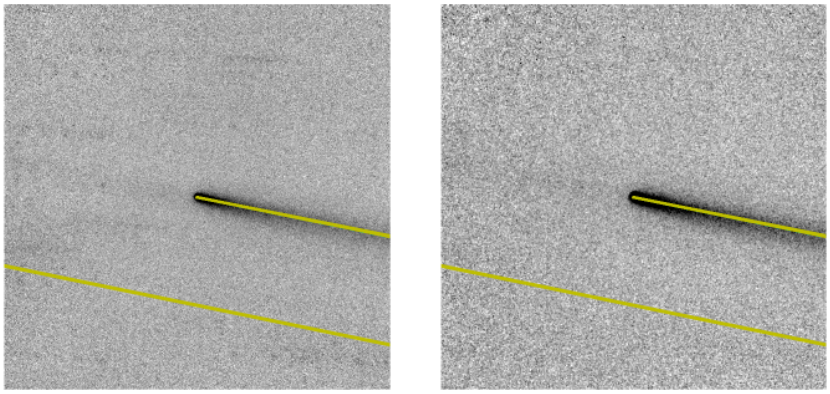

(c) W3 all syndynes and synchrones (d) W4 all syndynes and synchrones

Figure 4.75: The data and results for 116P. The overlays are the same as in Figure 4.46, but without panels (e) and (f)

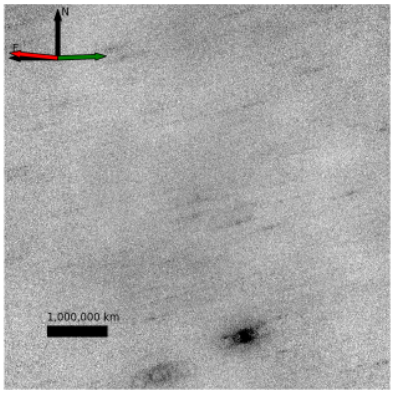


(a) W3 data

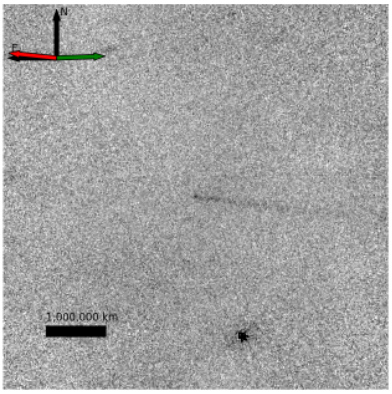


(b) W4 data

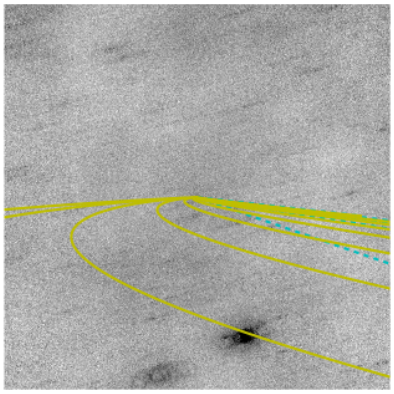

(c) W3 all syndynes and synchrones

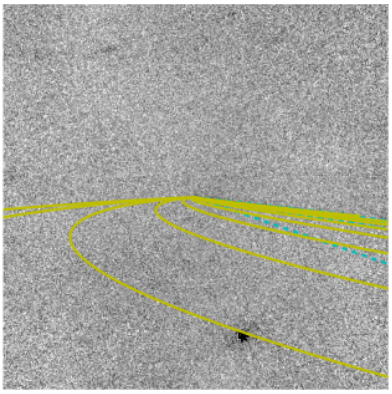

(d) W4 all syndynes and synchrones

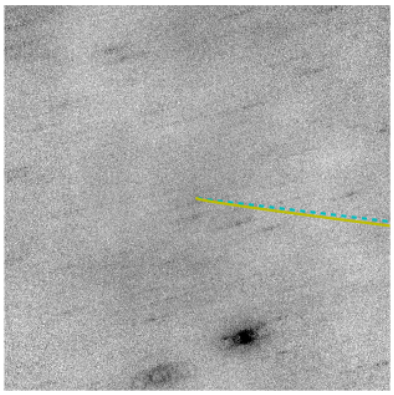

(e) W3 hand-fit model

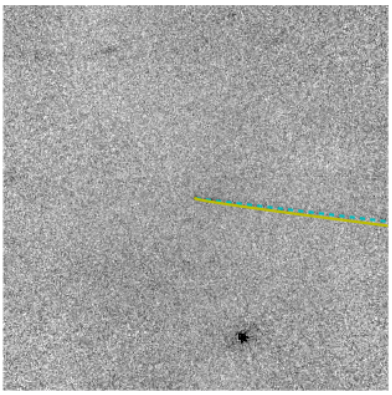

(f) W4 hand-fit model

Figure 4.76: The data and results for 117P. The overlays are the same as in Figure 4.46

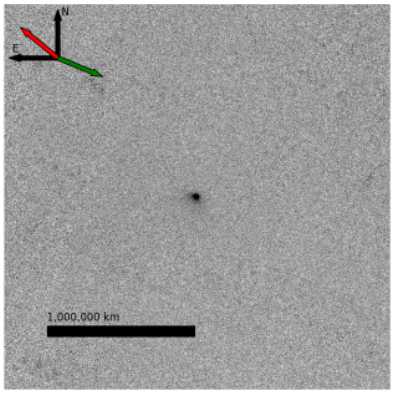


(a) W3 data

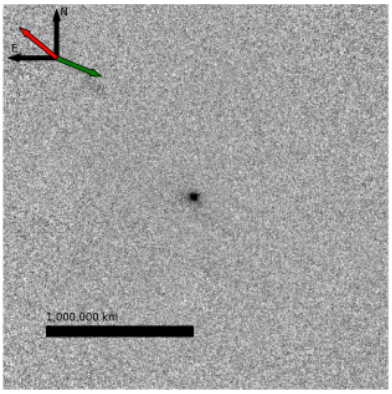


(b) W4 data

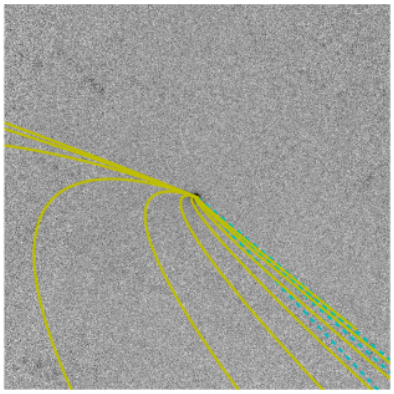

(c) W3 all syndynes and synchrones

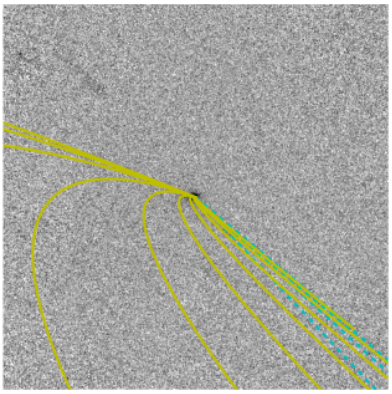

(d) W4 all syndynes and synchrones

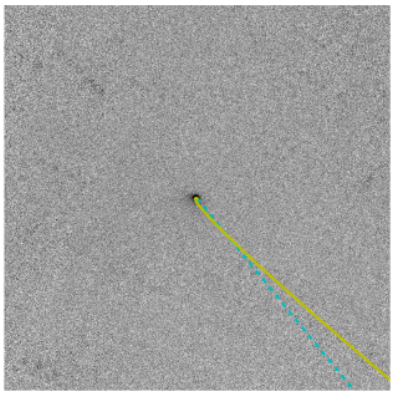

(e) W3 hand-fit model

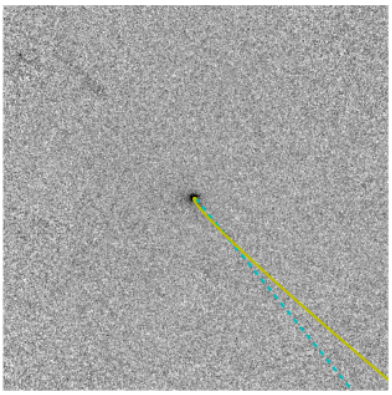

(f) W4 hand-fit model

Figure 4.77: The data and results for 127P. The overlays are the same as in Figure 4.46

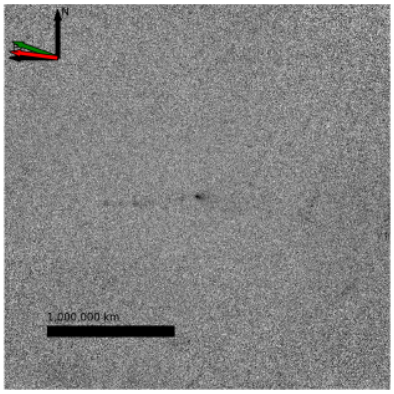


(a) W3 data

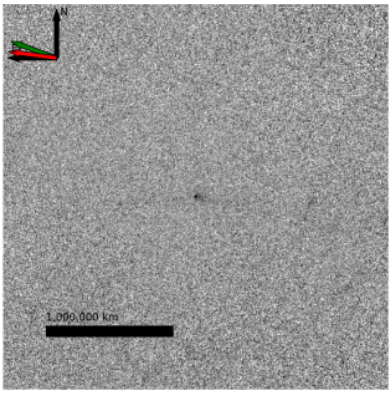


(b) W4 data

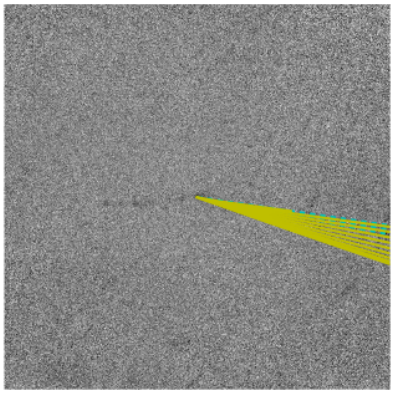

(c) W3 all syndynes and synchrones

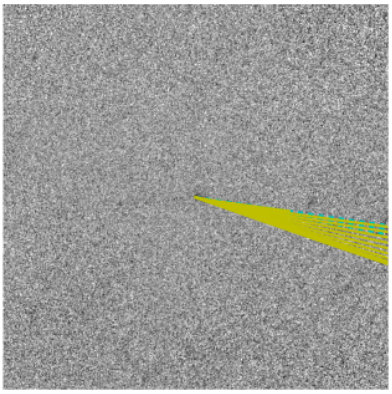

(d) W4 all syndynes and synchrones

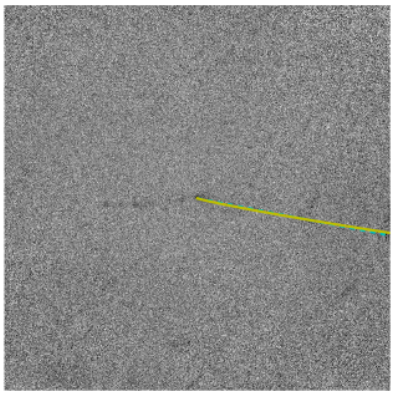

(e) W3 hand-fit model

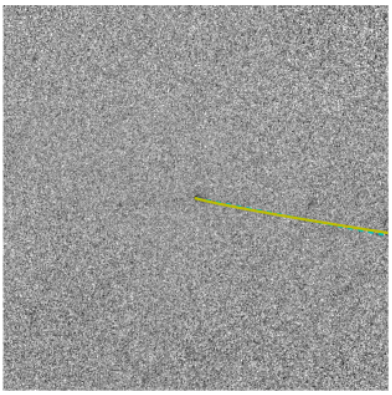

(f) W4 hand-fit model

Figure 4.78: The data and results for 142P. The overlays are the same as in Figure 4.46

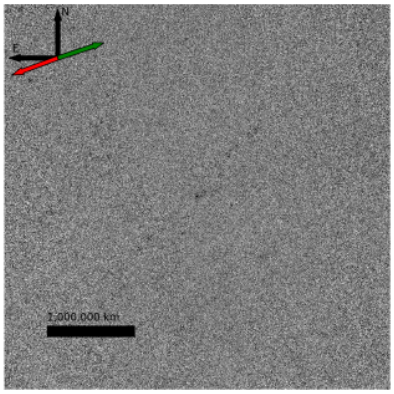


(a) W3 data

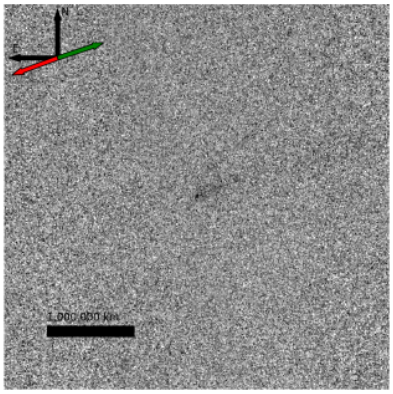


(b) W4 data

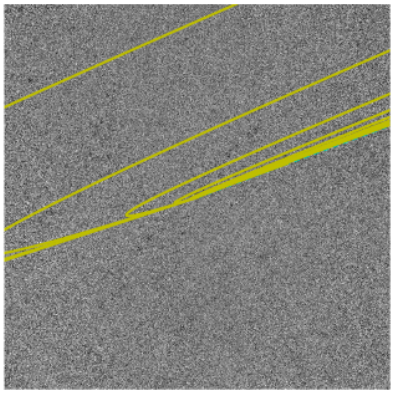

(c) W3 all syndynes and synchrones

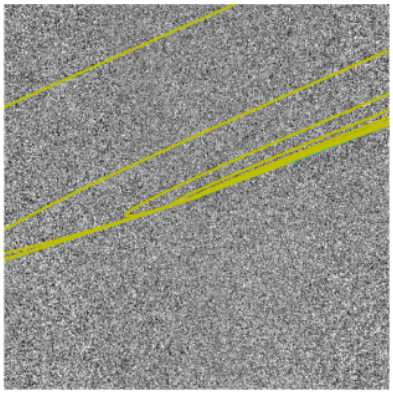

(d) W4 all syndynes and synchrones

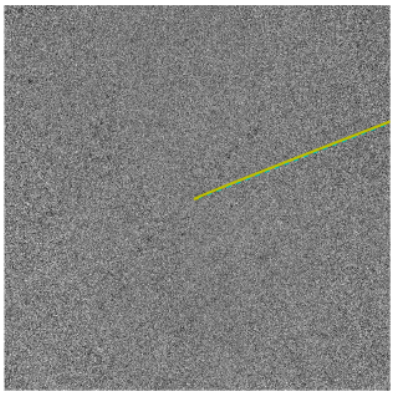

(e) W3 hand-fit model

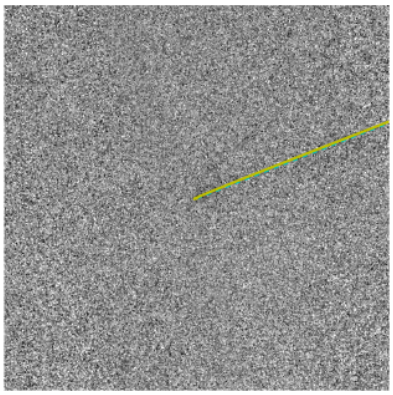

(f) W4 hand-fit model

Figure 4.79: The data and results for 145P. The overlays are the same as in Figure 4.46

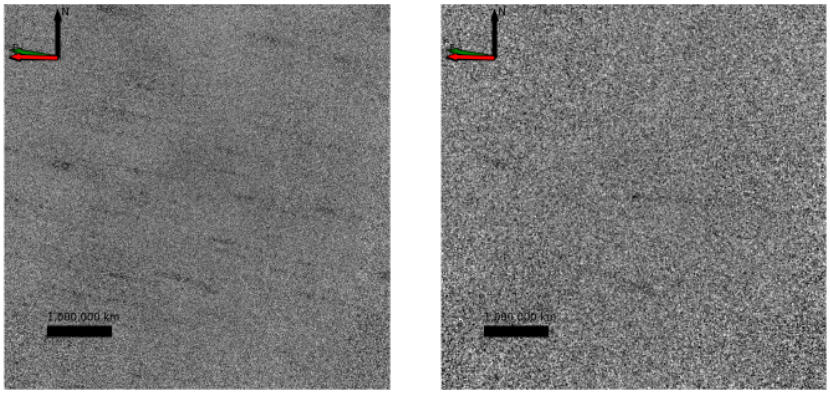

(a) W3 data



(b) W4 data

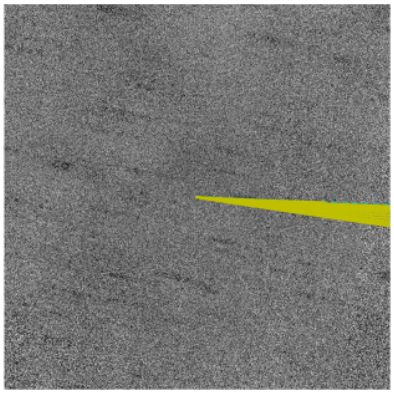

(c) W3 all syndynes and synchrones

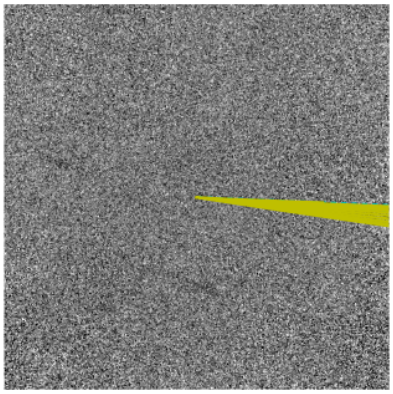

(d) W4 all syndynes and synchrones

Figure 4.80: The data and results for 158P. The overlays are the same as in Figure 4.46, but without panels (e) and (f)

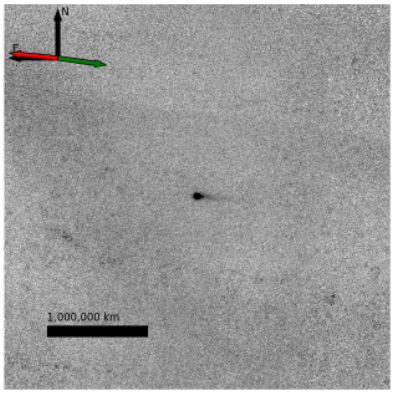


(a) W3 data

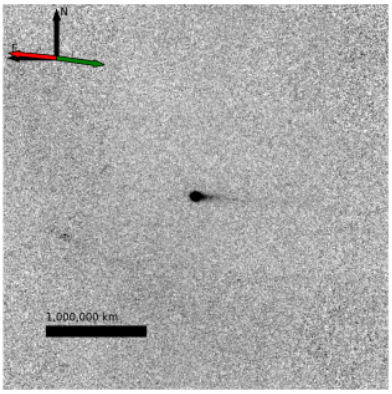


(b) W4 data

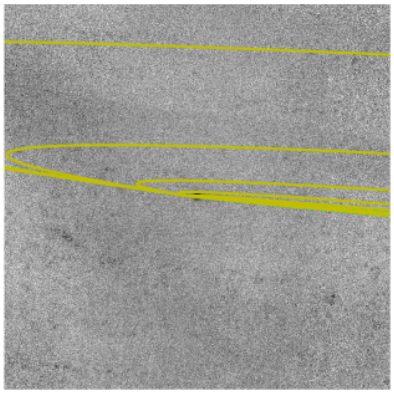

(c) W3 all syndynes and synchrones

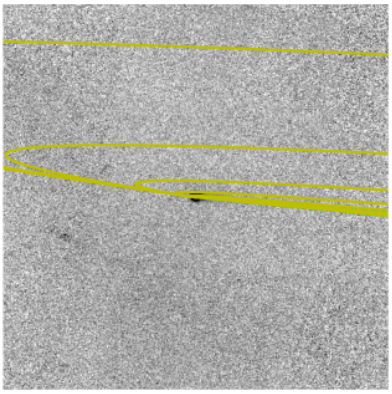

(d) W4 all syndynes and synchrones

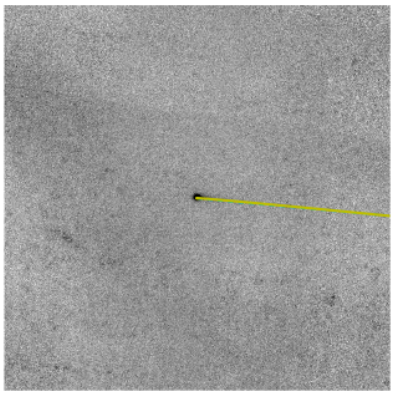

(e) W3 hand-fit model

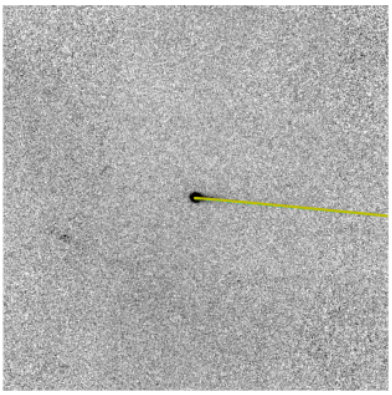

(f) W4 hand-fit model

Figure 4.81: The data and results for 203P. The overlays are the same as in Figure 4.46

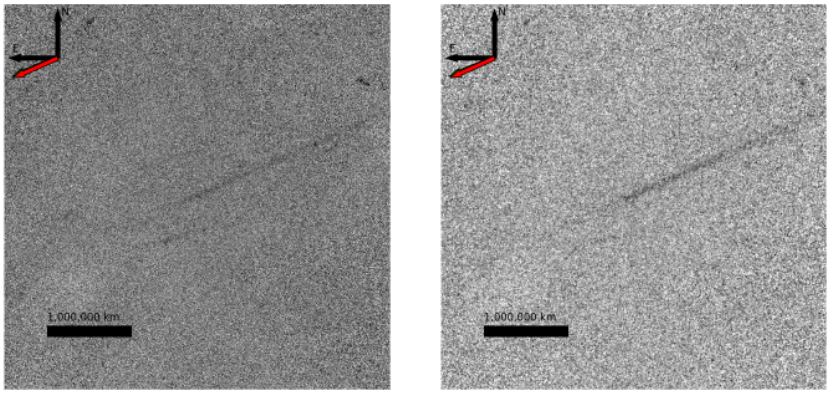


(a) W3 data

(b) W4 data

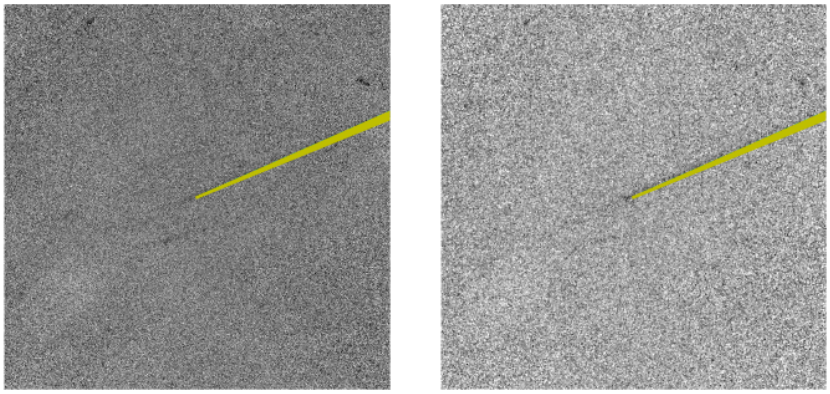

(c) W3 all syndynes and synchrones

(d) W4 all syndynes and synchrones

Figure 4.82: The data and results for 213P (A). The overlays are the same as in Figure 4.46, but without panels (e) and (f)

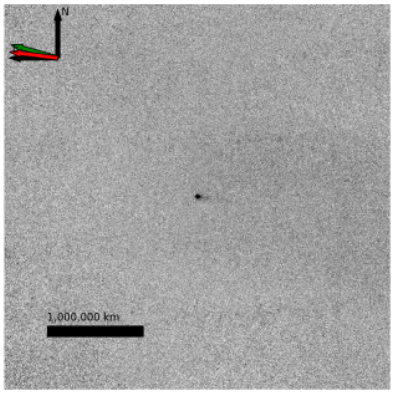


(a) W3 data

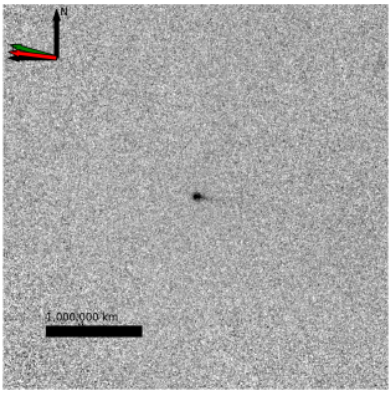


(b) W4 data

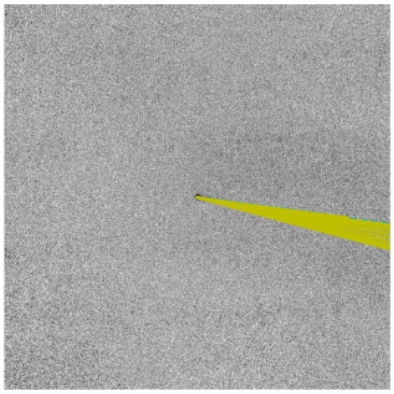

(c) W3 all syndynes and synchrones

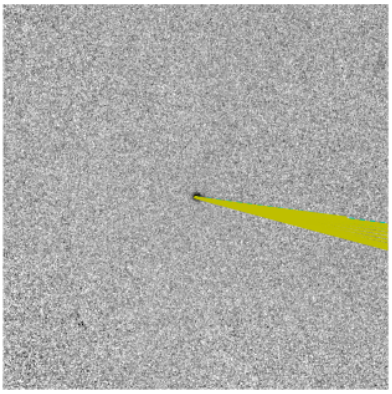

(d) W4 all syndynes and synchrones

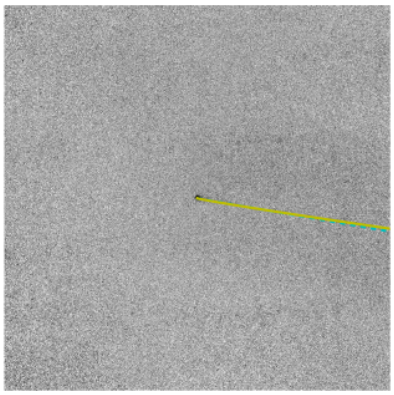

(e) W3 hand-fit model

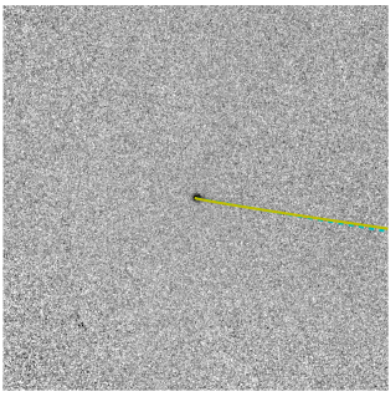

(f) W4 hand-fit model

Figure 4.83: The data and results for 215P. The overlays are the same as in Figure 4.46

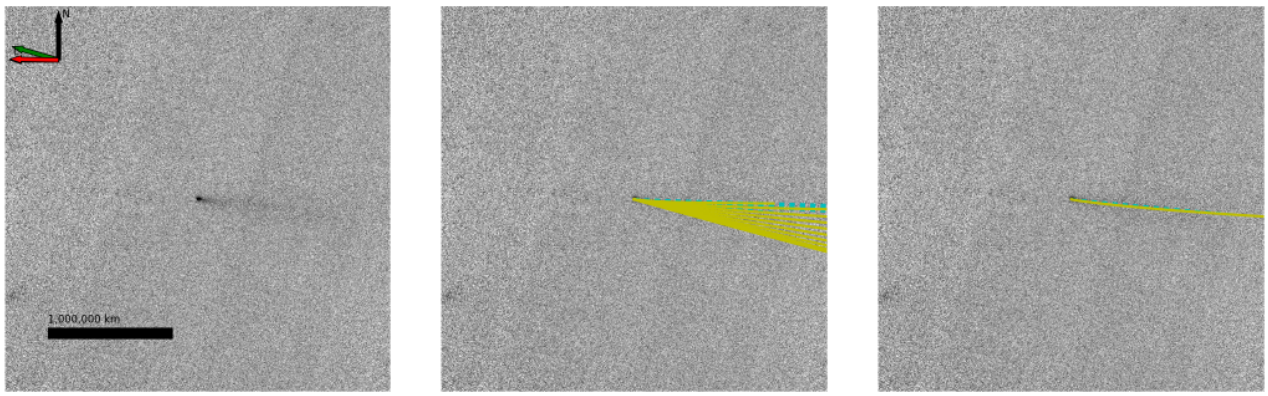


(a) W3 data (b) W3 all syndynes and synchrones (c) W3 hand-fit model

Figure 4.84: The data and results for 219P. The overlays are the same as in Figure 4.46

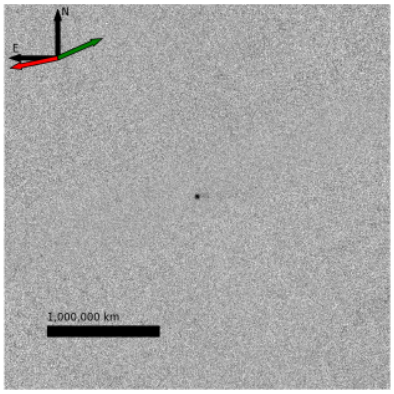


(a) W3 data

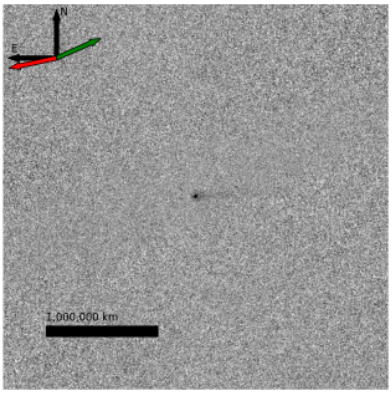


(b) W4 data

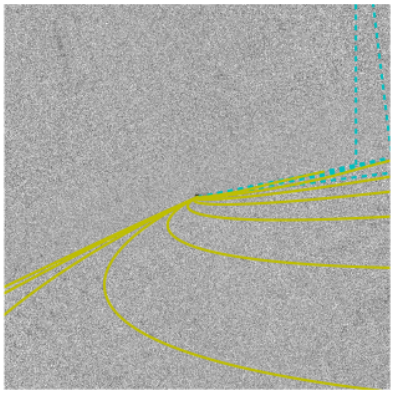

(c) W3 all syndynes and synchrones

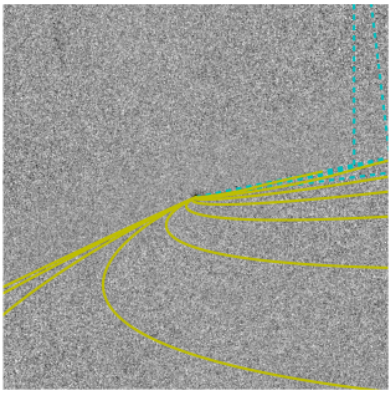

(d) W4 all syndynes and synchrones

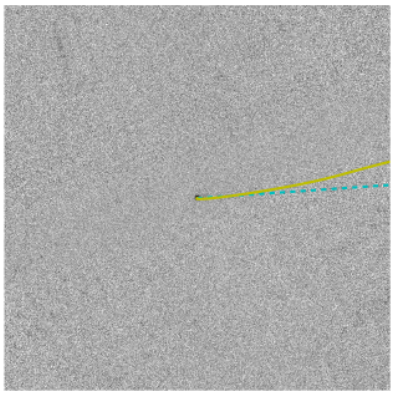

(e) W3 hand-fit model

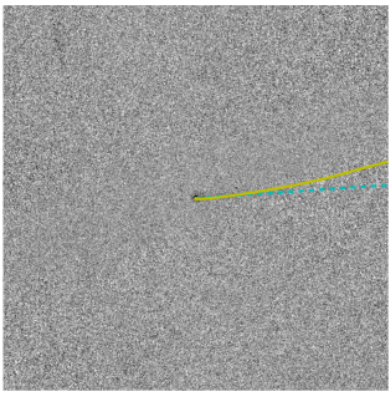

(f) W4 hand-fit model

Figure 4.85: The data and results for 230P. The overlays are the same as in Figure 4.46

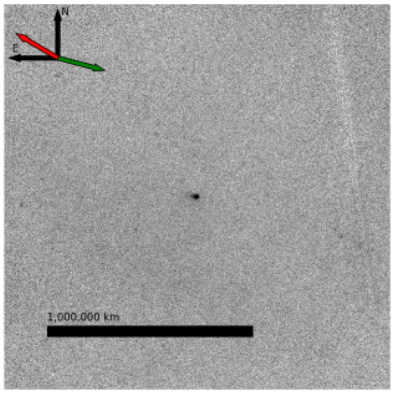


(a) W3 data

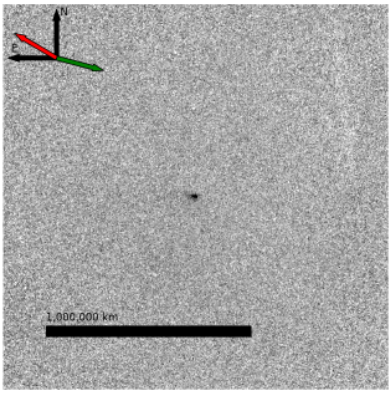


(b) W4 data

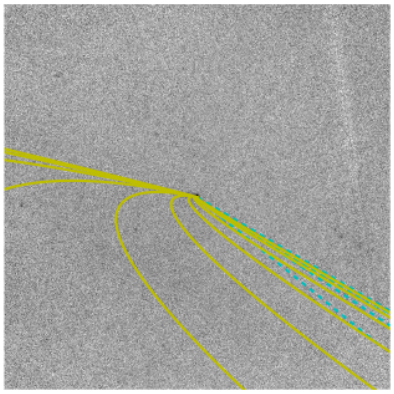

(c) W3 all syndynes and synchrones

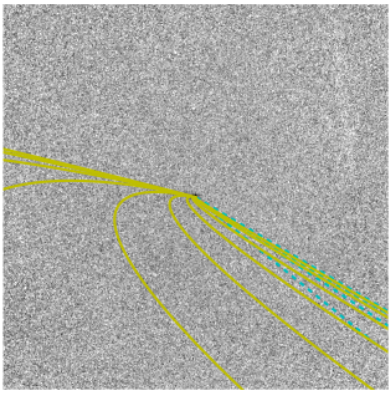

(d) W4 all syndynes and synchrones

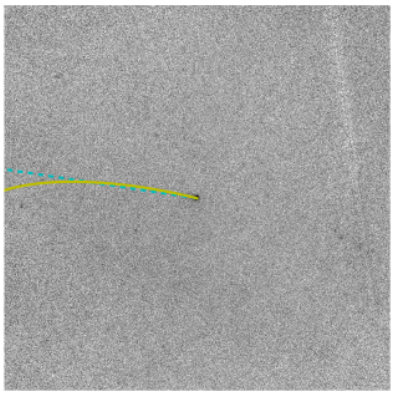

(e) W3 hand-fit model

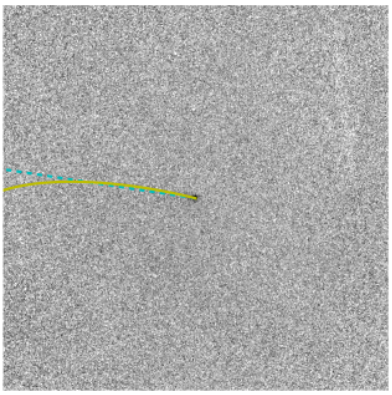

(f) W4 hand-fit model

Figure 4.86: The data and results for 233P. The overlays are the same as in Figure 4.46

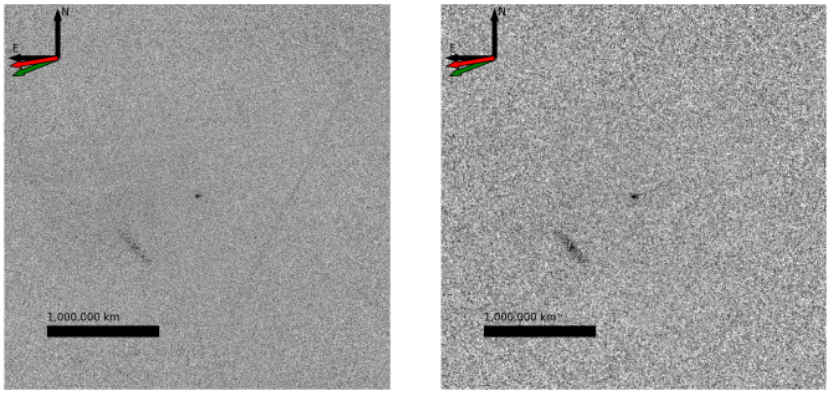


(a) W3 data

(b) W4 data

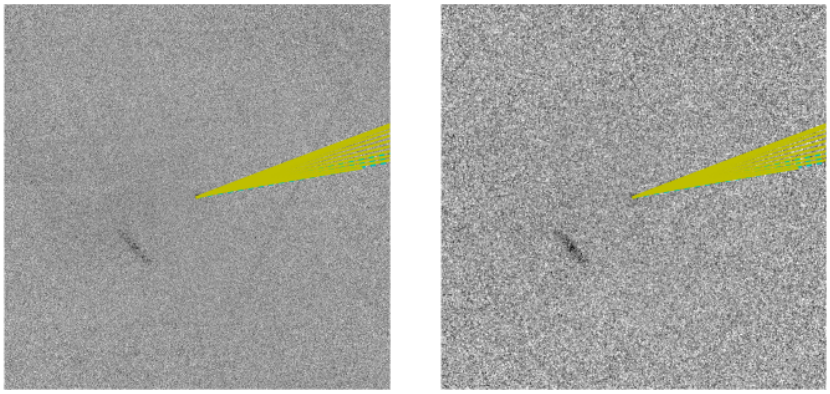

(c) W3 all syndynes and synchrones

(d) W4 all syndynes and synchrones

Figure 4.87: The data and results for 234P (A). The overlays are the same as in Figure 4.46, but without panels (e) and (f)

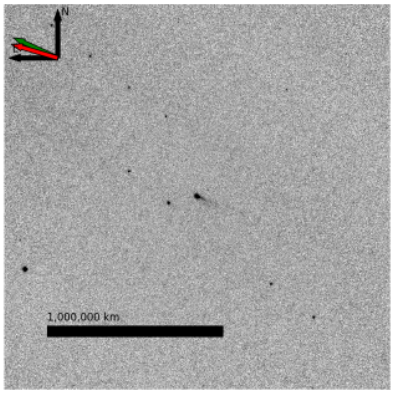


(a) W3 data

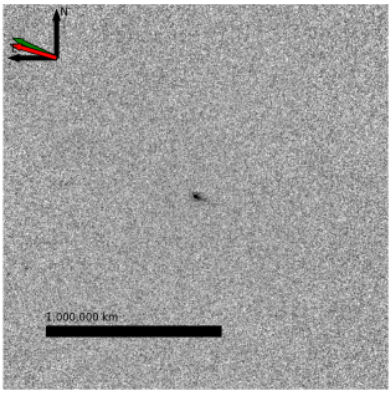


(b) W4 data

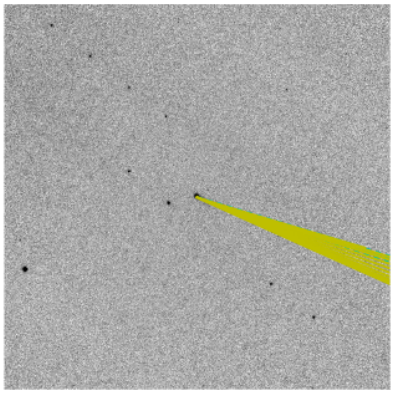

(c) W3 all syndynes and synchrones

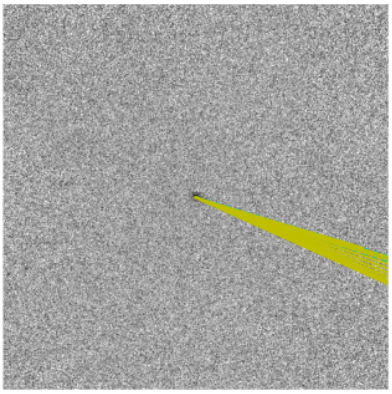

(d) W4 all syndynes and synchrones

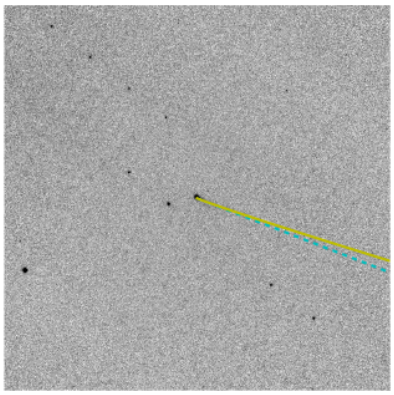

(e) W3 hand-fit model

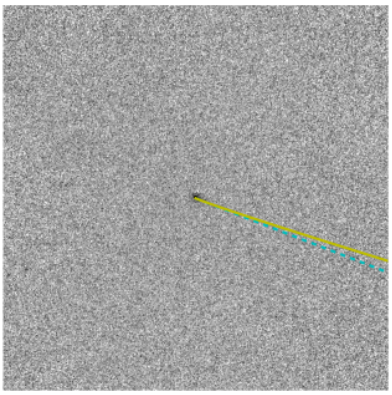

(f) W4 hand-fit model

Figure 4.88: The data and results for 236P (A). The overlays are the same as in Figure 4.46

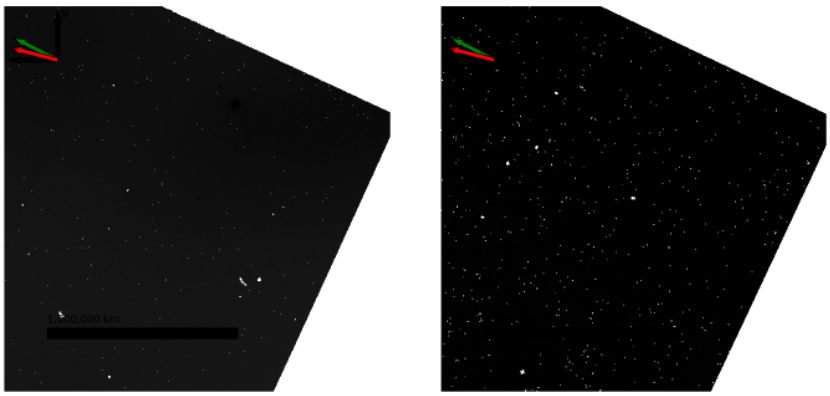

(a) W3 data



(b) W4 data

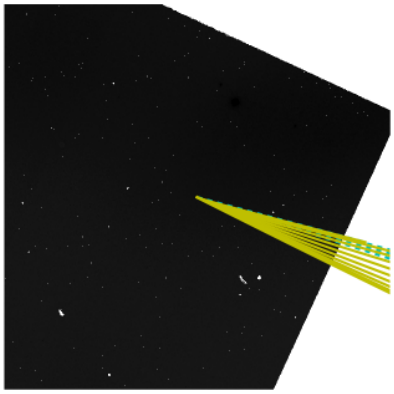

(c) W3 all syndynes and synchrones

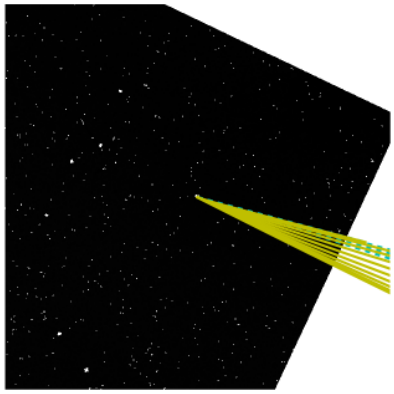

(d) W4 all syndynes and synchrones

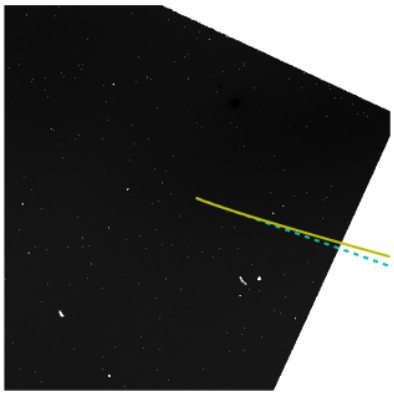

(e) W3 hand-fit model

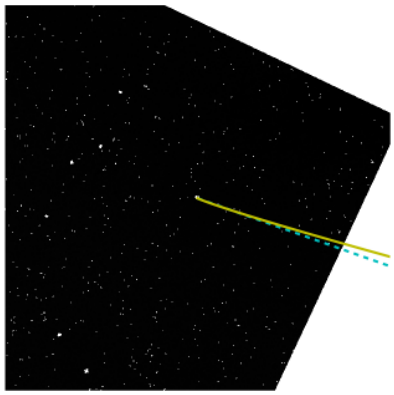

(f) W4 hand-fit model

Figure 4.89: The data and results for 236P (B). The overlays are the same as in Figure 4.46

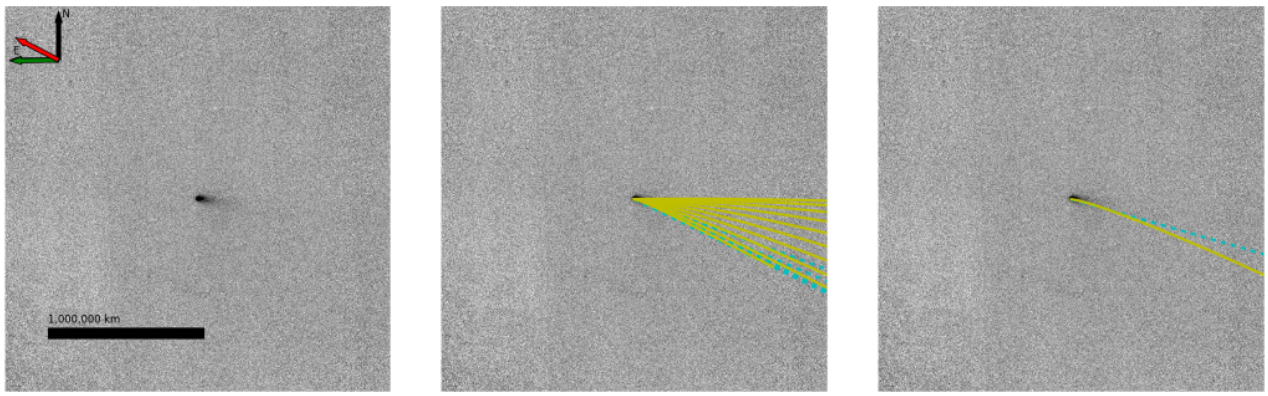


(a) W3 data (b) W3 all syndynes and synchrones (c) W3 hand-fit model

Figure 4.90: The data and results for 240P. The overlays are the same as in Figure 4.46

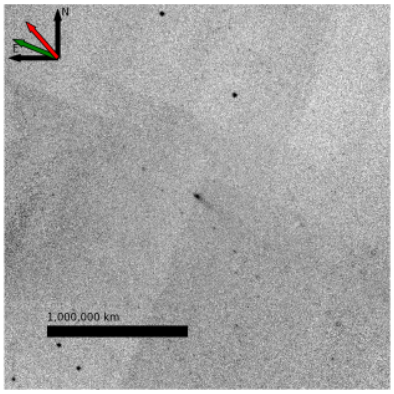


(a) W3 data

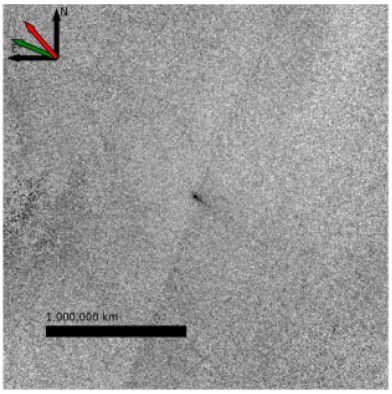


(b) W4 data

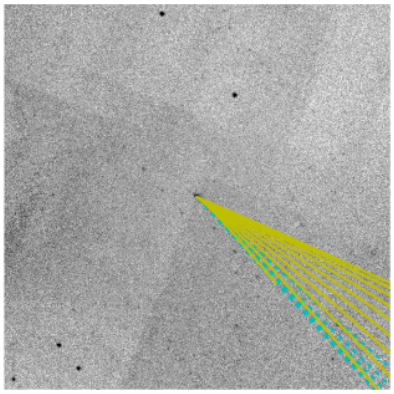

(c) W3 all syndynes and synchrones

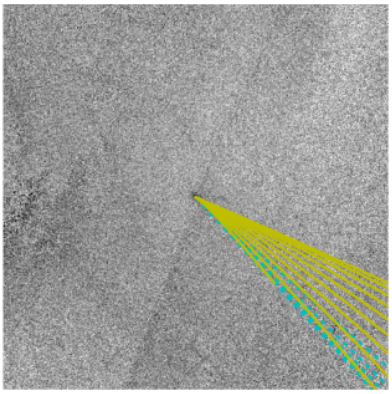

(d) W4 all syndynes and synchrones

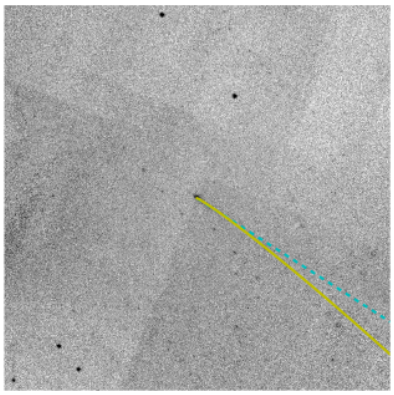

(e) W3 hand-fit model

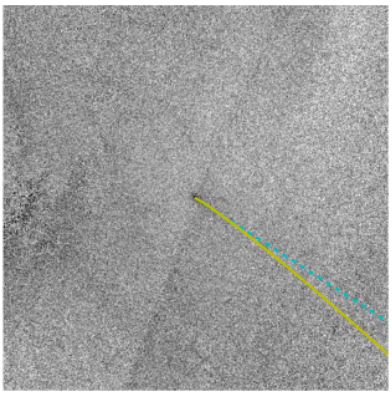

(f) W4 hand-fit model

Figure 4.91: The data and results for 245P. The overlays are the same as in Figure 4.46

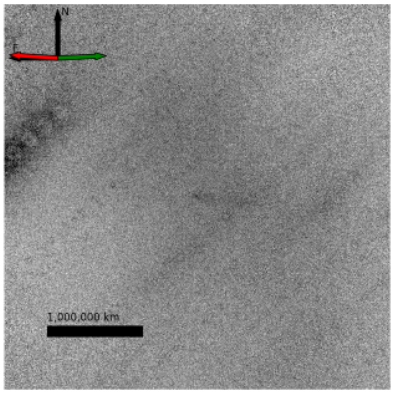


(a) W3 data

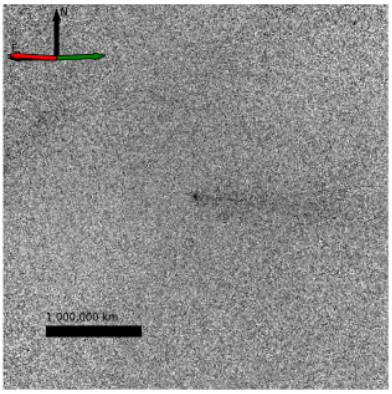


(b) W4 data

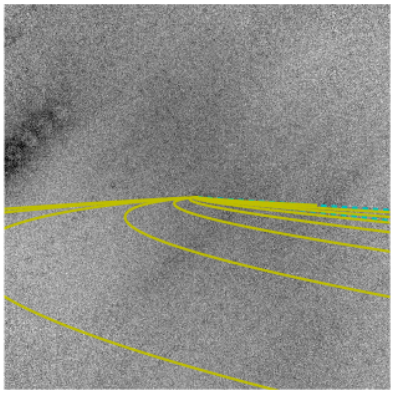

(c) W3 all syndynes and synchrones

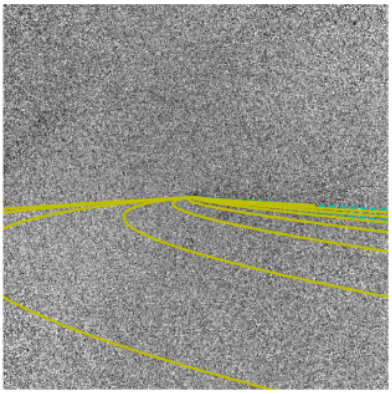

(d) W4 all syndynes and synchrones

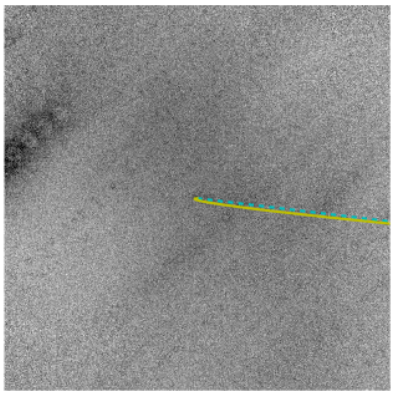

(e) W3 hand-fit model

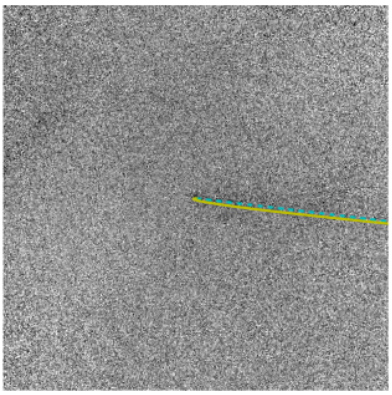

(f) W4 hand-fit model

Figure 4.92: The data and results for P/2008 J3. The overlays are the same as in Figure 4.46

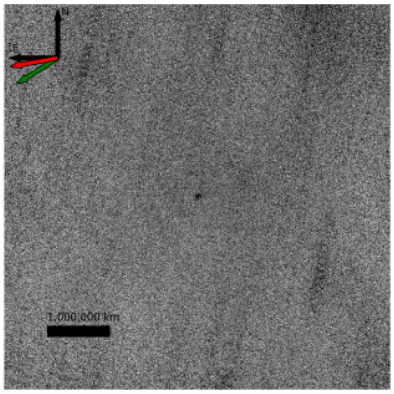


(a) W3 data

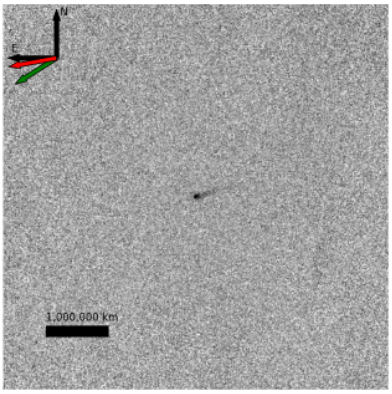


(b) W4 data

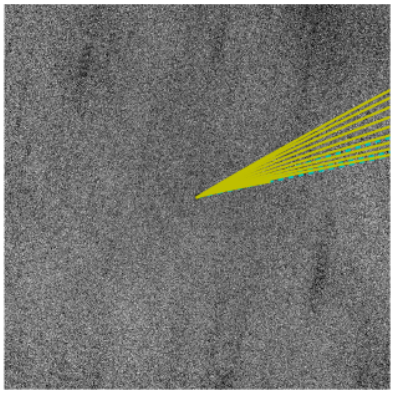

(c) W3 all syndynes and synchrones

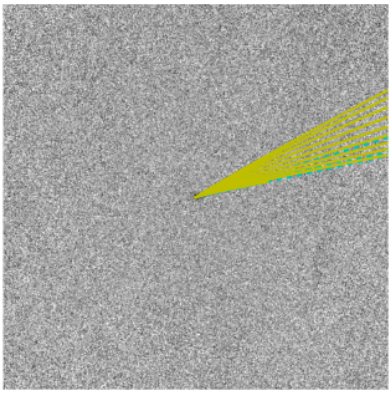

(d) W4 all syndynes and synchrones

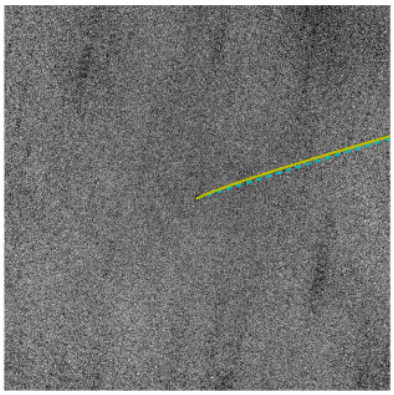

(e) W3 hand-fit model

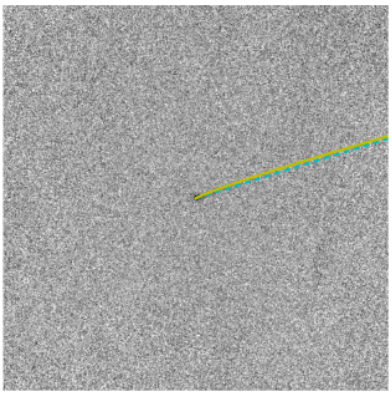

(f) W4 hand-fit model

Figure 4.93: The data and results for P/2008 Y3 (A). The overlays are the same as in Figure 4.46

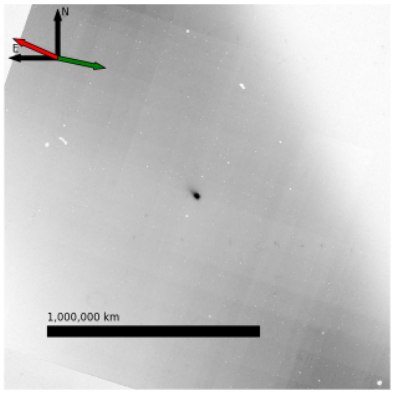


(a) W3 data

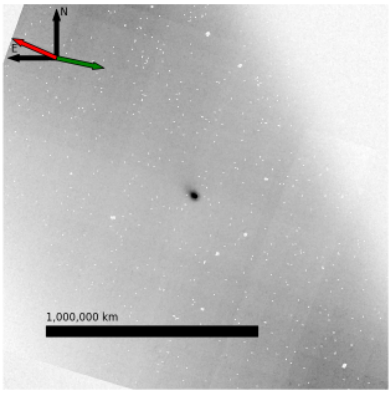


(b) W4 data

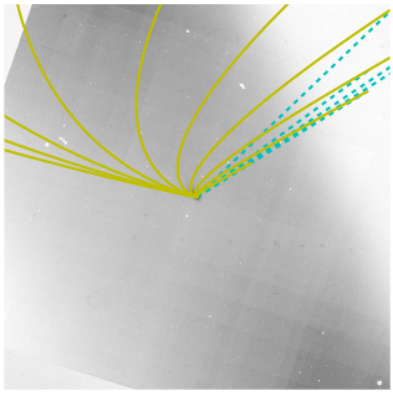

(c) W3 all syndynes and synchrones

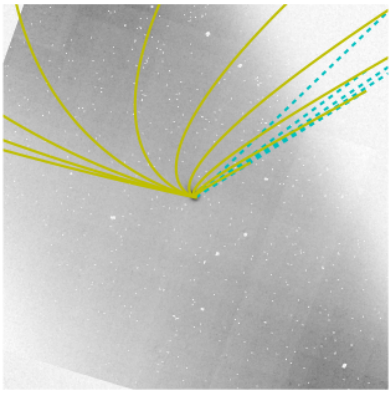

(d) W4 all syndynes and synchrones

Figure 4.94: The data and results for P/2009 T2. The overlays are the same as in Figure 4.46, but without panels (e) and (f)

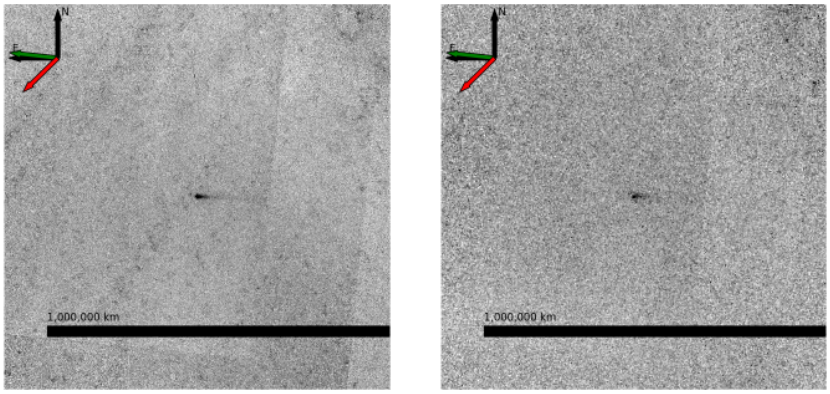


(a) W3 data

(b) W4 data

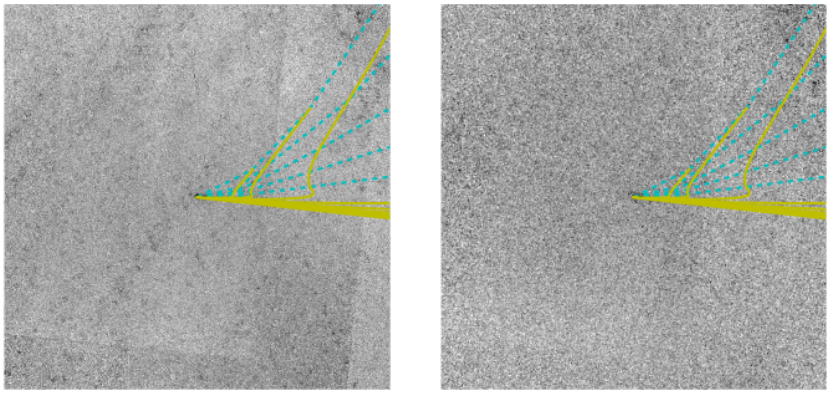

(c) W3 all syndynes and synchrones

(d) W4 all syndynes and synchrones

Figure 4.95: The data and results for P/2009 WX51. The overlays are the same as in Figure 4.46, but without panels (e) and (f)

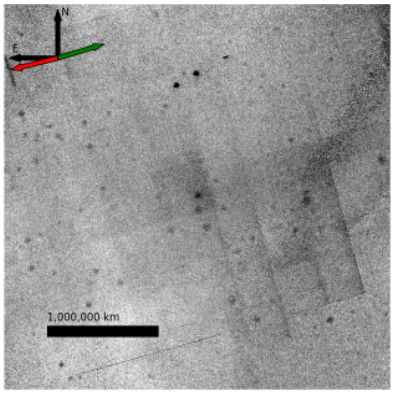


(a) W3 data

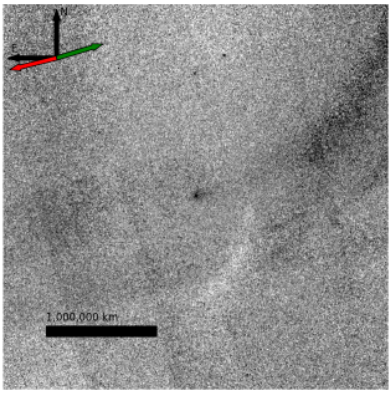


(b) W4 data

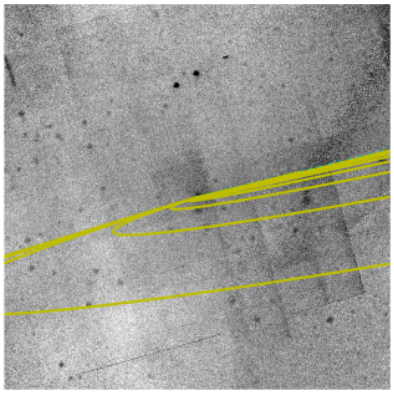

(c) W3 all syndynes and synchrones

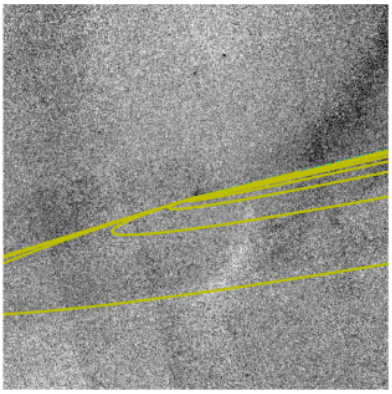

(d) W4 all syndynes and synchrones

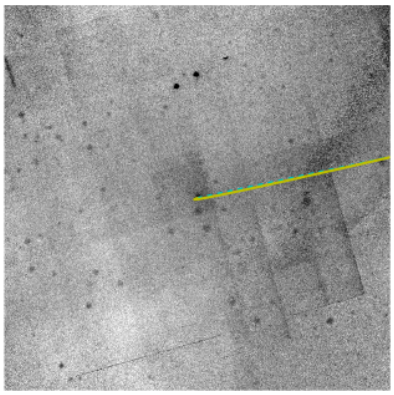

(e) W3 hand-fit model

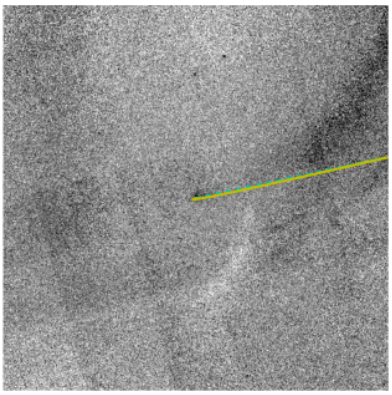

(f) W4 hand-fit model

Figure 4.96: The data and results for P/2010 A1. The overlays are the same as in Figure 4.46

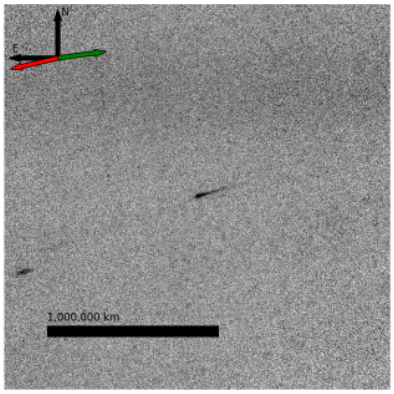


(a) W3 data

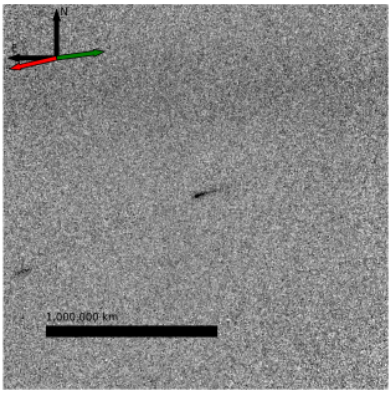


(b) W4 data

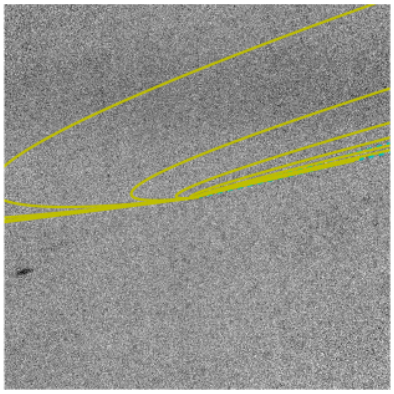

(c) W3 all syndynes and synchrones

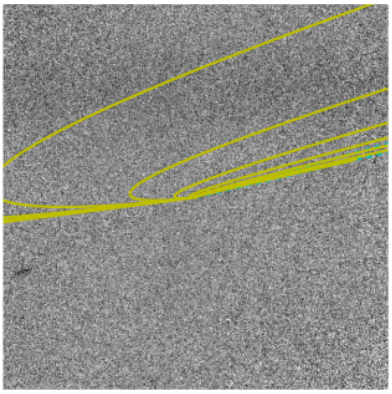

(d) W4 all syndynes and synchrones

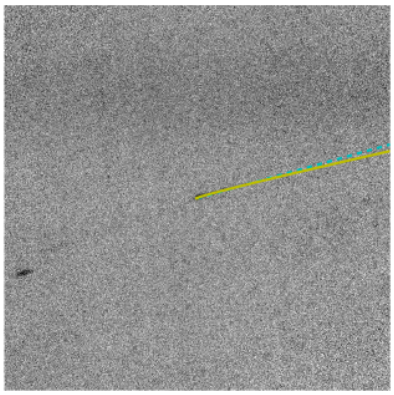

(e) W3 hand-fit model

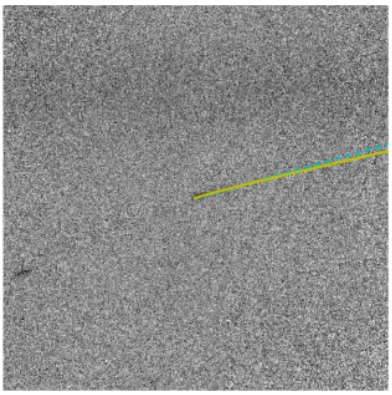

(f) W4 hand-fit model

Figure 4.97: The data and results for P/2010 A2. The overlays are the same as in Figure 4.46

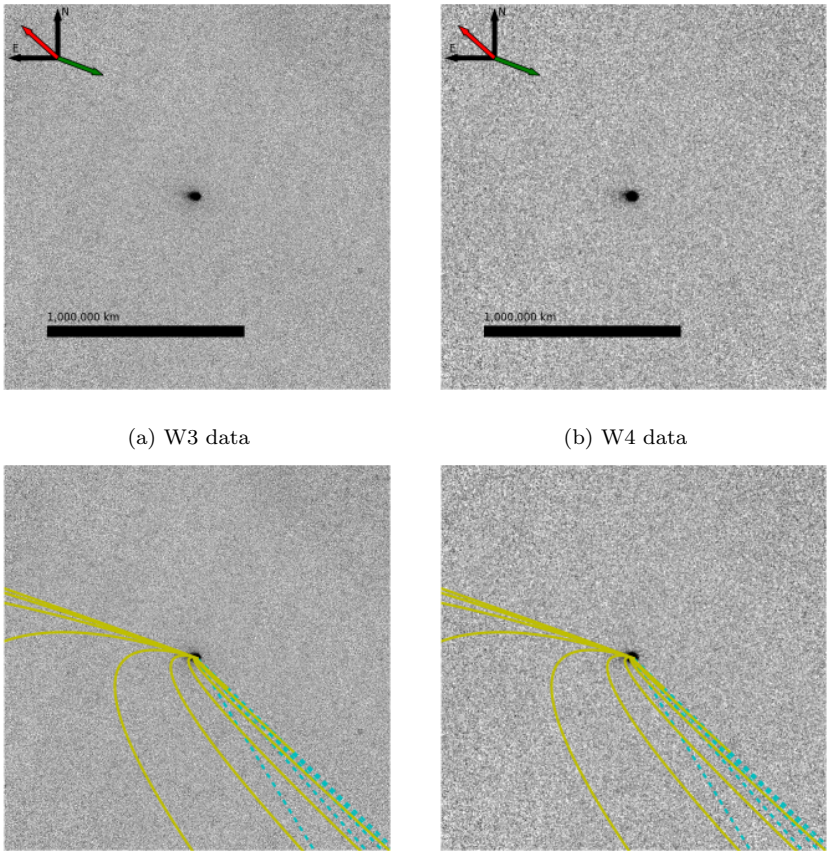


(a) W3 data

(b) W4 data

(c) W3 all syndynes and synchrones

(d) W4 all syndynes and synchrones

Figure 4.98: The data and results for P/2010 A3. The overlays are the same as in Figure 4.46, but without panels (e) and (f)

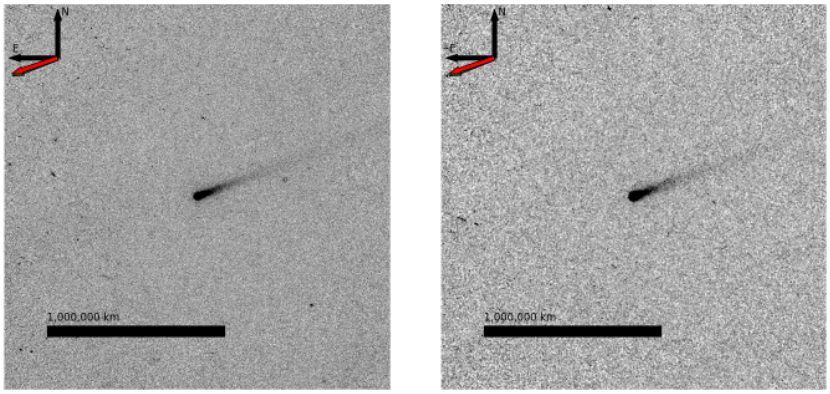


(a) W3 data

(b) W4 data

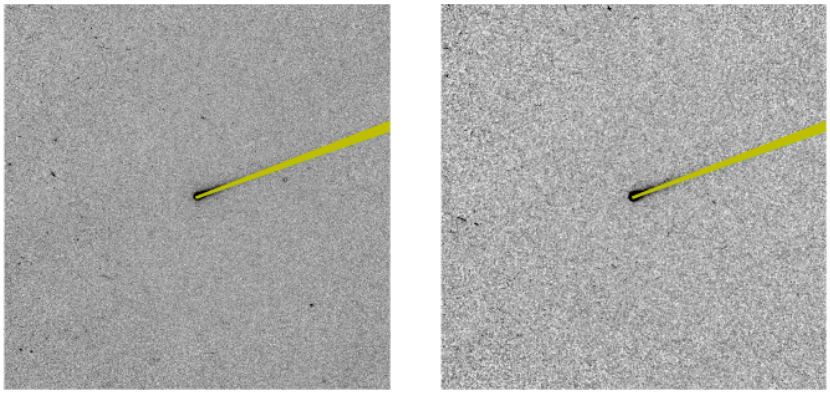

(c) W3 all syndynes and synchrones

(d) W4 all syndynes and synchrones

Figure 4.99: The data and results for P/2010 A5. The overlays are the same as in Figure 4.46, but without panels (e) and (f)

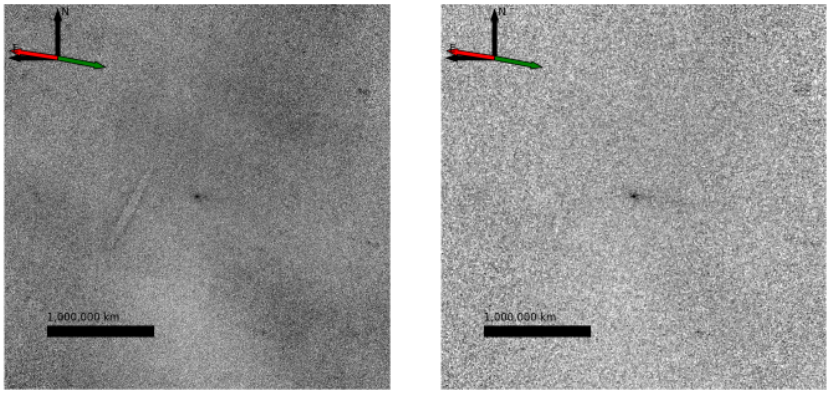


(a) W3 data (b) W4 data

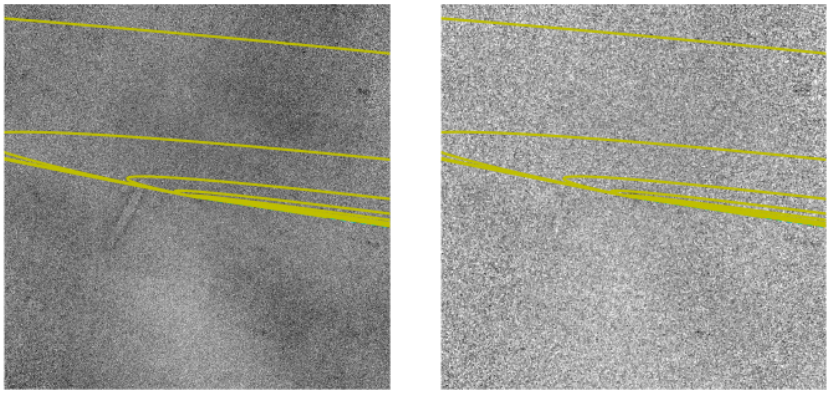

(c) W3 all syndynes and synchrones (d) W4 all syndynes and synchrones

Figure 4.100: The data and results for P/2010 D1. The overlays are the same as in Figure 4.46, but without panels (e) and (f)

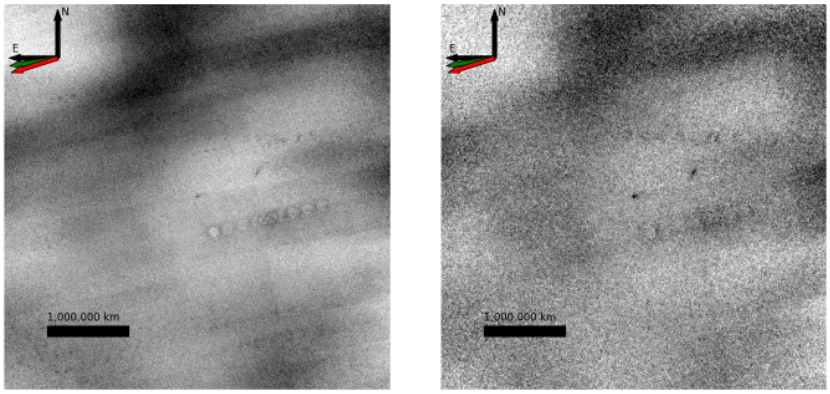


(a) W3 data

(b) W4 data

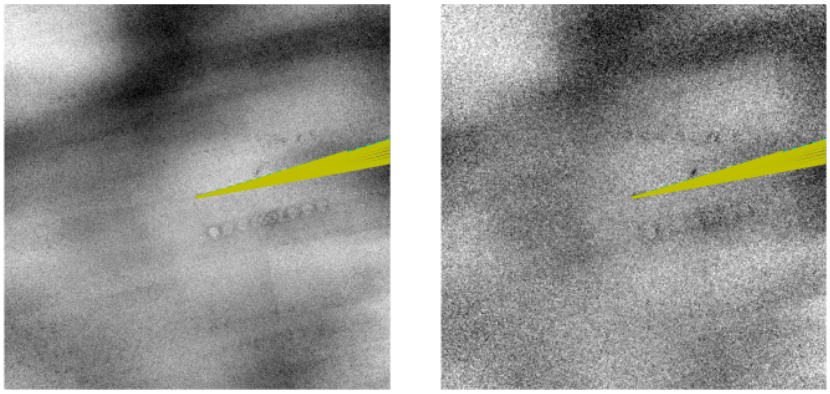

(c) W3 all syndynes and synchrones

(d) W4 all syndynes and synchrones

Figure 4.101: The data and results for P/2010 J5. The overlays are the same as in Figure 4.46, but without panels (e) and (f)

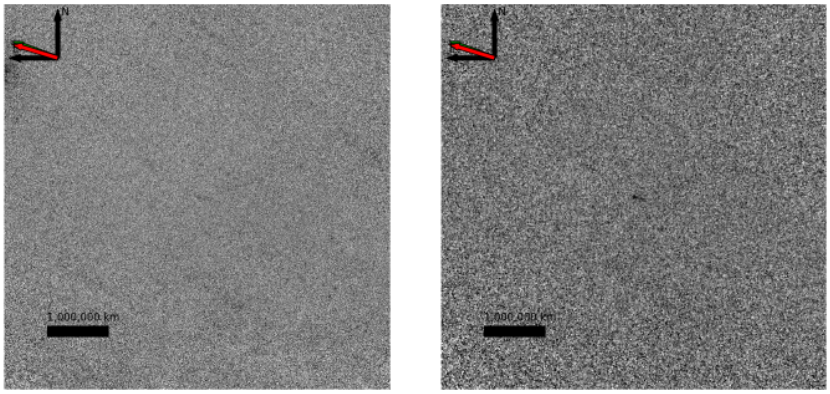


(a) W3 data (b) W4 data

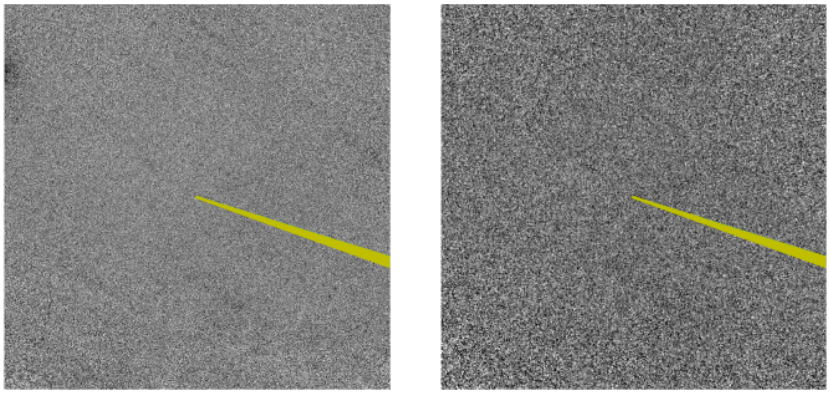

(c) W3 all syndynes and synchrones (d) W4 all syndynes and synchrones

Figure 4.102: The data and results for P/2010 U1. The overlays are the same as in Figure 4.46, but without panels (e) and (f)

# CHAPTER 5
# DISCUSSION

## 5.1 General observations about the results

Before I go into detail, I will state some general observations about the results from the models shown in Chapter 4. Note that the meta-analysis described in this chapter was only done for the W4 results for the well-fit comets, since, as shown in Figure 2.2, cometary dust is brightest in this band and thus the results are more robust.

1. There is a wide range of morphology and activity levels present in the dust tails of both LPCs and SPCs imaged by WISE.

2. For both the LPCs and the SPCs, most of the comets had dust tails that were comprised of large (∼mm to cm sized) particles.

3. The majority of the dust tails were the result of emission that occurred several months to several years prior to the observations.

4. Our results suggest that all of the comets showed strong emission that begins at or before perihelion.

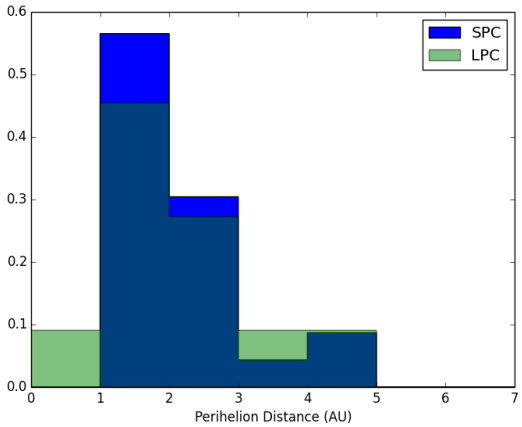


(a) Perihelion distance of each comet.

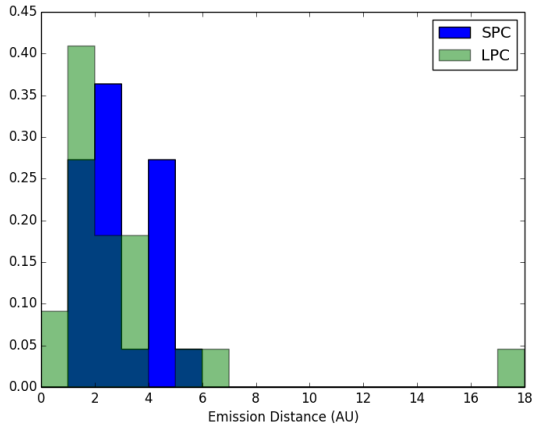


(b) Heliocentric distance at which strong activity occurred for each comet.

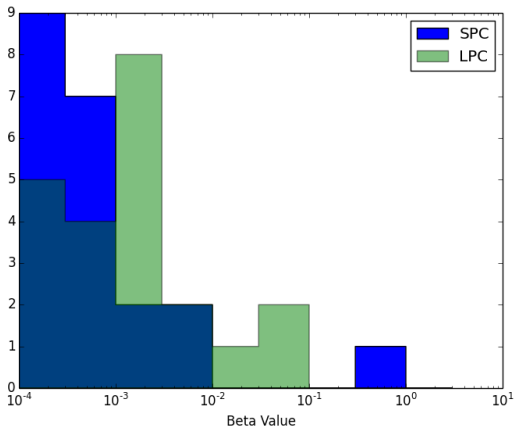


(c) Beta value for each comet.

Figure 5.1: Histograms using data from the comets that were well-fit in W4. The overlap between LPCs and SPCs is shown in gray-blue. The values for (a) and (b) were normalized for ease of comparison between the two populations.

We will now examine some histograms as we begin to analyze the results obtained in the previous chapter. Figure 5.1 shows histograms of the perihelion distance, fitted heliocentric distance of strong emission, and beta value of each comet in W4 that was fit well by the tail-fitting program. The histograms in panels (a) and (b) have been normalized so that the number of objects in each set does not skew the perception of the results. We can see that in all three panels, the SPCs and the LPCs overlap in their range of heliocentric distances and particle sizes. In particular, the distribution of perihelion distances is similar, and is thus unlikely to be a source of bias in the results.

In order to test whether the overlap is significant, we can employ the Kolmogorov-Smirnov test (K-S test), which is a statistical measurement that can be used to determine whether two samples are drawn from the same distribution. Note that one of the strengths of this test is that the distributions do not need to be normal. Additionally, it also works equally well whether the values are linear or logarithmically spaced. When we run a K-S test on the beta values for the LPCs and the SPCs, we get a two-tailed p value of 0.265 (insignificant at the $\sim 1\sigma$ level), suggesting that the two samples may be drawn from the same population. The K-S test for for the heliocentric distance of strong emission for the LPCs and SPCs yields a two-tailed p value of 0.167, (insignificant at the $\sim 1.5\sigma$ level), again suggesting that the two populations are not significantly different.

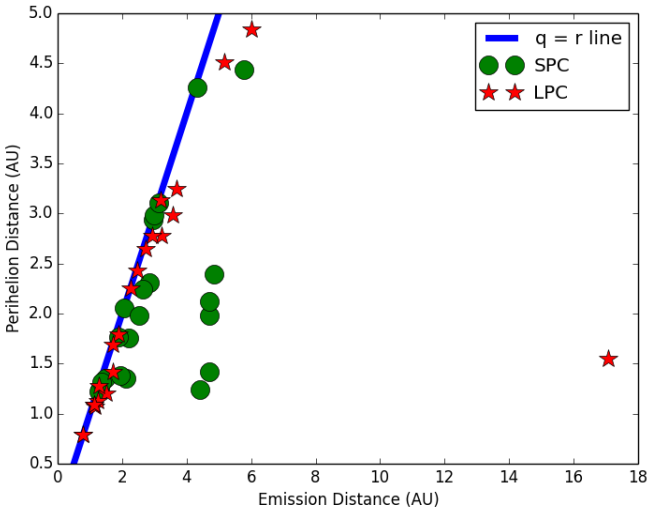


(a) The entire set of the results.

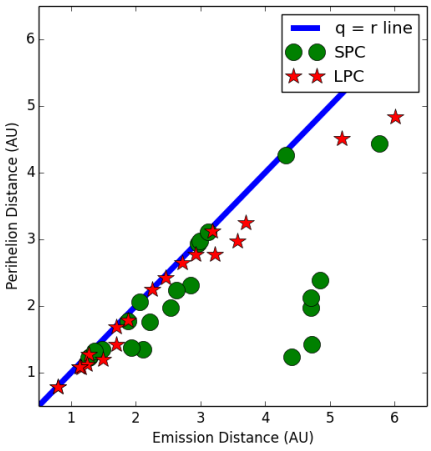


(b) Here the horizontal and vertical axes have been between 0.5 to 6.5 AU to show the relationship between emission distance and perihelion.

Figure 5.2: The heliocentric distance of strong emission for each comet compared to perihelion distance for the W4 well fit comets.

When we plot the results as scatter plots, some interesting trends become more clear. Perhaps the most interesting trend is that, using the comets with well-fit W4 tails, we can see that the LPCs nearly always have strong emission close to perihelion, while the SPCs may have strong emission either at close to perihelion, or sometimes well before perihelion (see Figure 5.2). For the SPCs, we can see a clustering of comets which have strong emission at ∼4-5 AU, well before their respective perihelion distances. This is perhaps evidence for an additional effect which will require further investigation at a later time. We can calculate the Pearson's product-moment correlation coefficient (PPMCC), a measure of the linear dependence of two variables, in order to quantify these results. Note that a PPMCC of +1 corresponds to variables which are perfectly positively correlated, 0 corresponds to no correlation, and -1 corresponds to perfectly negative correlation. For the LPCs, we first

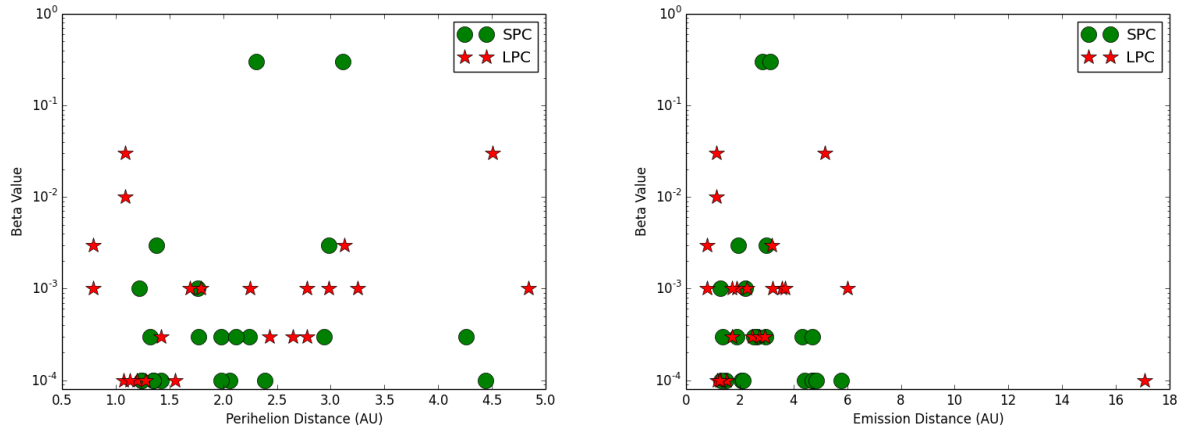


(a) The perihelion distance of each comet vs. the best-fit beta value for that comet.

(b) The heliocentric distance at which strong emission occurred vs. beta for each comet.

Figure 5.3: Using the W4 data for the well-fit comets to examine the relationship between beta and heliocentric distance.

remove C/2009 P1 (see 4.2.1.16) from the results, since its emission distance (∼17.1 AU) is over 4 standard deviations (3.3 AU) away from the median of the entire set (2.06 AU). When we calculate the PPMCC, we get a result of 0.99, which suggests to an extremely high probability that the perihelion distance and distance of strongest emission are correlated. When we calculate the PPMCC for the SPCs, the results are significantly less correlated, with a result of 0.56. This suggests that for the SPCs there is a very weak correlation between perihelion distance and distance of strongest emission.

Another potentially useful way to examine the results is to look at the relationship between $\beta$ and perihelion distance, as well as $\beta$ and emission distance (Figure 5.3). The figures show that for both LPCs and SPCs there does not seem to be much correlation between particle size and perihelion distance, or particle size and emission distance. Additionally, the distribution of LPCs and SPCs on both panels of the figure overlaps entirely, suggesting

that the dust particles in LPCs and SPCs are of similar size. This is not consistent with the results obtained by Lisse [2002], who found that LPCs generally have smaller dust grains than SPCs. We note, however, that our results also show that we do not see very many comets which primarily emit small dust grains, which may explain why the results in this dissertation differ from those found by Lisse [2002]. Additionally, we note that we do not see a clear correlation between perihelion distance and particle size, as was found by Reach et al. [2007].

Although we do not see any correlation between perihelion distance and dust particle size, it is interesting to note that we do see activity in a number of both LPCs and SPCs with small ($q$ <1.8 AU) perihelion distances. This is quite different than the results obtained by the SEPPCoN survey [Kelley et al., 2013], where they found that all the JFCs in their sample with $q$ <1.8 AU were inactive.

## 5.2 Comets with multiple observations

There were 3 LPC and 2 SPC comets with well-fit tails that were observed twice by WISE: C/2008 N1 (Holmes) (4.2.1.9), C/2010 J4 (WISE) (4.2.1.18), C/2010 L5 (WISE) (4.2.1.19), 19P/Borrelly (4.2.2.3), and 67P/Churymov-Gerasimenko (4.2.2.5). These multi-epoch observations give us the opportunity to investigate the temporal aspect of the dust properties, and

to do a consistency check on our modeling techniques. We can see that for two of the comets (C/2010 J4 and C/2010 L5) the BFSc for each pair of comets is quite similar, suggesting that the program does a good job of finding the heliocentric distance at which the comets had the strongest emission. For the other three comets (C/2008 N1, 19P, and 67P), the BFSc is significantly different, suggesting that either the dust tail changed between the observations or the program did not do a good job of finding the best-fit model. The interesting result here is that for the LPCs, the BFSds for each pair of comets in both wavelengths suggests that the size of the dust particles increased between observations, while the BFSds for the SPCs suggests that the size of the dust particles remains the same between observations. A visual inspection of the figures for C/2008 N1 (Figures 4.9 and 4.10) suggests that this result may be spurious, since the BFSc for Figure 4.10 does not seem to quite line up with the fitted tail points. The particle size results for the remaining comets seems to be real.

A natural question to ask is why might the size of the particles increase between observations for C/2010 J4 and C/2010 L5? We note that for both of these comets, the time between the pairs of observations was rather short (11 days for C/2010 J4 and 32 days for C/2010 L5), and the BFSc suggests that the dust was emitted fairly recently ($<\sim$1-3 months before the observations). Additionally, the dust grains were relatively small for both comets ($\beta$=0.03-0.01 for C/2010 J4, and $\beta$=0.003-0.001 for C/2010 L5). For 19P and 67P, the observation pairs were $\sim$5 months apart, the BFSc for each observation suggests the dust grains

were several years old, and the grains were large ($\beta = 0.0001$). Thus, the we are looking at two very different types of tails in each case. It is possible that the difference in grain size for C/2010 J4 and C/2010 L5 is due to small grains being swept away by the solar wind, or perhaps even disintegrating.

## 5.3 Dynamically new comets

Comets which are "dynamically new" are of particular interest when looking at a large sample of comets, because they are likely entering the inner solar system for the first time since their formation in the protoplanetary disk Dones et al. [2004], and thus may be even more "pristine" than other comets. Comets are categorized as dynamically new when they satisfy the criterion

$$E \equiv \frac{1}{a} < 10^4 \tag{5.1}$$

where $E$ is the "energy" of the orbit (a measure of how strongly bound the comet is to the sun), and $a$ is the semi-major axis. Of the 19 LPCs with well-fit tails, 4 were "dynamically new", and one was a borderline case. The four dynamically new comets were C/2006 OF2 (Figure 4.1), C/2007 Q3 (Figure 4.5), C/2008 FK75 (Figure 4.8), and C/2008 T2 (Figure 4.12), with the borderline case of C/2009 K5 (Figure 4.16). When we examine the results presented in Table 4.1, we can see that these comets behave remarkably similarly to the

other, not dynamically new, comets in the data set. This suggests that, at least on the large end of the particle size scale which is sampled in this data set, the dynamically new comets emit dust grains in a similar manner to comets which have previously entered the inner solar system.

## 5.4 Initial velocity calculation for nearly edge-on comets

For comets with very small orbit plane angle separation, the analysis methods described here cannot be used to determine the size and age of the particles, since the models are stacked on top of one another, making them indistinguishable (c.f. C/2007 N3, Figure 4.49). However, these cases are useful in helping to constrain the initial velocity at which particles leave the nucleus. Since the gravitational and radiation pressure forces acting on the dust are central forces, if no other forces or initial velocities are acting on the dust, all the particles should stay in the comet's orbital plane. That is, any spread in the location of the dust from the comet's orbital plane is due to the initial particle velocity.

The procedure for estimating the initial particle velocity is presented for C/2007 N3, but can be extended to all comets with very small orbit plane angle separation. Since this analysis has shown that most comets emit large dust close to perihelion, we will assume that the dust in tail was emitted at perihelion (409 days before observation, for the case of C/2007

N3) and has a beta value of 0.0001. Next, the comet image is rotated such that the comet orbital plane is horizontal. Since having a low orbit plane angle separation means that we are looking into the plane of the comet's orbit, this causes the tail to also be horizontal. The $\beta$= 0.0001 syndyne is clipped to 409 days, and is also rotated. Since the end of the syndyne represents the location of $\beta = 0.0001$ particles that left the comet 409 days ago, we use this as the location to estimate the initial velocity of these particles. Next, a vertical slice is taken along the column where the syndyne ends, and a Gaussian is fit to the tail. The width of the Gaussian is a measure of the spread in the tail, that is, how far from the comet's orbital plane the dust has traveled since it was emitted. For C/2007 N3, the width of the Gaussian is 43.1 pixels. Since the mosaicked WISE images have a pixel scale of 1"/pixel, this means that the particles have moved 43.1" in the 409 days since they were emitted. We must then convert the angular size to physical units (as in Equation 3.9), using $\Delta = 4.94$ AU at the time of observation and $\delta = 43.1$", this yields a physical distance of 154420 km. Converting the time since emission from days to seconds and dividing the distance traveled by the time yields an initial velocity of $\sim$0.004 km/s, or 4 m/s. This is slightly faster than the result obtained by using Equation 3.8, which yields an initial particle velocity of $\sim$0.001 km/s.

## 5.5 The data set as an ensemble

Figures 5.2 and 5.3 and shows us that while the LPC and SPC dust is similar in terms of particle size, the nature of the emission is quite different. LPCs tend to have strong emission only close to perihelion, when they are undergoing the strongest thermal processing, while SPCs have a wider range of thermal environments under which they produce strong emission. It is particularly interesting to note that the relationship between strong emission distance and perihelion distance for the LPCs is present over a wide range of perihelion distances, from <1 AU to over 6 AU. This may imply that the LPCs have undergone significant thermal alteration during previous perihelion passages, possibly causing a depletion in volatiles and thus only show strong emission when they are in the warmest part of their orbit.

We also note that, particularly for the LPCs, there does not seem to be a clustering in the heliocentric distance at which strong emission occurs. That is, there does not seem to be a heliocentric distance at which many comets all begin to activate: the distance at which emission occurs seems to be directly related only to the comet's perihelion distance. For the SPCs, we can see a clustering of comets which have strong emission at ∼4-5 AU (10P, 67P (January observation), 100P, 213P, and 237P), well before their respective perihelion distances. The orbits of these comets are not dissimilar to the rest of the comets in the data set, so the cause for this clustering is unknown at this time and will be investigated

further once the other aspects of the data set (including $CO/CO_2$ production rates) are incorporated.

While interpreting the results presented here, we caution that, while the relationship between the heliocentric distance at which strong emission occurs and perihelion distance seems to be very strong, there is the possibility that it is enhanced due to biases in our methods. That is, the comets for which the tail fitting method works well may have dust which is inherently different that those comets for which the tail fitting method does not work well. For example, the dust tails of the non-well-fit comets may be older, and thus fainter, than the well-fit tails, which could mean that the dust was emitted earlier in the comet's orbit.

Another possible bias in these results is due to the wavelength at which these comets were observed. The results presented here only use the W4 (22 $\mu$m) band, and thus are mostly insensitive to particles smaller than 22 $\mu$m. As such, these images are mostly insensitive to recent emission, since the large particles to which these images are sensitive would still be so close to the comet's nucleus that they would not be able to be distinguished from the coma surrounding the nucleus. That is, when a comet emits particles with a range of sizes, the small particles move quickly away due to solar radiation pressure, while the large particles slowly move away from the nucleus. If a comet is seen in, say, the visible wavelength range shortly after the dust is emitted, a tail consisting of small particles may be seen. However,

if that comet is simultaneously imaged in the infrared, the tail may appear much fainter or have a much different morphology, since the small particles do not emit in the infrared, and the large particles, which do emit in the infrared, are still very close to the nucleus.

## 5.6 Comparisons with results from other surveys

As mentioned in the previous section, the results that we find here are somewhat different than those found by previous studies of cometary dust tails. Lisse [2002] found that the dust tails of LPCs and SPCs are generally comprised of different sized particles, with LPCs having smaller dust grains. We find that the particles in the dust tails of LPCs and SPCs are of similar size, on the order of mm to cm, and that many of the dust tails of both LPCs and SPCs are several years old. These two results are likely to be intimately connected: since WISE is most sensitive to large particles (due to smaller particles not being able to efficiently emit light at mid-infrared wavelengths), it is also most sensitive to dust that is older, since, due to small relative velocity between these larger particles and the nucleus, it takes longer for them to form into a tail. We note, however, that in some comets presented here, we did find dust that was small ($\sim$10's of $\mu$m) and young ($\sim$10's of days old). As described in Section 5.2 above, we saw two comets with new ($<\sim$1-3 months old) dust that

seems to be comprised of larger particles as the tail ages. This is an intriguing result which will warrant further investigation.

Additionally, Reach et al. [2007] found that comets with a smaller perihelion distance had more massive dust trails, and suggest that the reason for this might be the evolution of the size of the particles remaining in the trail due to long-term thermal evolution in the inner solar system. The results we obtain here are consistent with Reach's results: for the comets with multi-epoch observations, the later observations suggest that the average particle size in the tail is increasing with time. Of course this does not mean that the mass of the tail is increasing; rather, it suggests that the smaller particles are being preferentially swept away by solar radiation pressure, thereby leaving the larger particles behind.

When we compare our results to those obtained by the SEPPCoN survey [Kelley et al., 2013, Reach et al., 2013], we can note some interesting differences in the our results. First, Kelley et al. [2013] found that cometary activity was much more common post-perihelion than pre-perihelion. In the results presented in this dissertation, we have found that all the comets with dust tails emit that dust at or before perihelion. However, we have not yet examined the inactive comets in the WISE dataset, which may change our understanding of these results. Second, Kelley et al. [2013] found that all the comets in that study with $q$ <1.8 AU were inactive. While none of the comets which overlap between the two surveys had such small perihelion distances, 17 SPCs with $q$ <1.8 AU were found in our WISE

survey to have a dust tail (see Table 2.1), suggesting the presence of ongoing activity in these objects. Three of these comets were imaged at heliocentric distances of >4 AU, the distance at which most comets in the SEPPCoN survey were imaged. In future work, we will fold in the inactive comets seen by WISE to better compare the results of the two surveys. Third, Reach et al. [2013] found that there was not a sharp transition between $CO_2$ and $H_2O$ dominated activity as a function of heliocentric distance. While the results here do not measure the activity driver directly, we note that we do not see a distinct change in dust grain size with the heliocentric distance at which the strong activity occurred, thus suggesting that the transition from $CO_2$ and $H_2O$ dominated activity is a smooth one.

Note that while (relatively) uniform infrared population studies of SPCs/JFCs have been done before with Spitzer, this is the first time that this has been done for LPCs. While Lisse [2002] has done a population study via a literature review, the results presented here are the first large-scale survey of LPCs. IRAS [Matson, 1986, Sykes et al., 1986, Sykes and Walker, 1992] did have ∼10 LPCs, but the pixel scale on the images was so large that it is hard to say much about the detailed structure of the tails. The WISE mission has thus allowed us to develop the most complete picture we have to date of the nature of LPC dust as an ensemble.

# CHAPTER 6
# THE FUTURE OF COMETARY STUDIES

## 6.1 This Data Set

As we examine the images and tables presented in Chapter 4 and the meta-analysis presented in Chapter 5, it becomes clear that we have only just begun to scratch the surface of this incredibly rich data set. The meta-analysis presented in Chapter 5 has only focused on the W4 results for the well-fit comets, and, with care, can be extended to include even more of the data. We have used dynamical models to estimate the sizes and ages of the particles which comprise the dust tails of these comets, but we can extend this analysis to extract even more information about the activity of these comets, including dust production rates, photometry, particle size distribution, and initial particle velocity. We can also include the inactive comets seen by WISE in order to get a more complete understanding of why and how comets activate.

### 6.1.1 Dust Production Rate

In optical light observations, the dust production rate of comets can be parameterized by the quantity $Af\rho$, where $A$ is the grain albedo, $f$ is the filling factor of the grains, and $\rho$ is the radius of the aperture at the comet [Ahearn et al., 1984]. Since this quantity removes viewing geometry factors from its calculation, it can be used to compare dust production in comets under a variety of observing conditions. Kelley et al. [2013] extended this concept to thermal emission via the quantity $\epsilon f\rho$, where $\epsilon$ is the effective emissivity of the dust grains, and $f$ and $\rho$ remain the same as before. This quantity can be calculated from the flux in the images as described in Kelley et al. [2013]. Table 1, from Kelley et al. [2013] shows a sampling of $\epsilon f\rho$ values for a variety of comets. A significant next step in the analysis process of the WISE comet data set will be to calculate $\epsilon f\rho$, where possible, for each comet and compare the results of that analysis to the results found by Kelley et al. [2013].

### 6.1.2 Particle Size Distribution and Mie Modeling

As described in Bauer et al. [2011], we can use the thermal flux from W3 and W4, and the reflected light in W1 to calculate a particle size distribution (PSD) of the dust. This method assumes that emission primarily comes from particles with size on the same order as the emitted wavelength. For each wavelength band, this yields an estimate of the number of

particles ($n_g$) of a certain size ($m_g$). The slope of $n_g$ vs. $m_g$ can then be calculated, giving a PSD.

The derived PSD information that we get from both the Finson-Probstein analysis and the photometry described above can then be used as a starting point for Mie modeling of the dust spectral energy distribution (SED). Mie modeling can then be used to attempt to extract further higher-order compositional and physical information about the dust grains. While only 3 or 4 data points are available per comet, and while that is not enough to find a unique answer for the dust properties, it is still enough to constrain carbon-to-silicate ratios in the grains, as well as to constrain the importance of the 10 and 20 $\mu$m silicate emission features. Fernández et al. [2012] has done a proof-of-concept analysis of this technique on some cometary WISE data. This analysis technique, using a combination of dynamical and photometric information, represents a powerful extension to the analysis presented in this dissertation, and mimics what has been done in the past with e.g. COBE imaging of comets [Lisse et al., 1998]. This is in contrast to the typical dust analysis that only uses dynamics and photometry separately.

### 6.1.3 Initial Particle Velocity

The initial velocity of dust particles as they are lifted off the nucleus by the sublimating gas is an interesting property to measure, since it can give a sense of the gas pressure at the comet's surface, potentially yielding insights into properties of the nucleus. The effect of initial velocity on the first-order Finson-Probstein models is to spread the dust out from the curves shown in the analysis presented here [Lisse et al., 1998]. Comets with a low orbit plane angle, which could not be used in our analysis to estimate the sizes and ages of the particles, are of particular use for this kind of analysis, since any spreading in the tail is due to the initial velocity of the particles rather than particles of different sizes and ages becoming spread out from the effects of solar radiation pressure.

### 6.1.4 Comets without a Dust Tail

In order to fully understand the implications of the activity of the comets presented in this work, it is important to also look at the dynamical properties of the WISE-detected comets that did not present a dust tail in W3 and/or W4. That is, comparisons in terms of orbital elements between the comets with a tail and those without a tail may yield additional insights into why some comets had a dust tail and some did not. It is possible that the differences

are due to different perihelion distances, or perhaps due to the dynamical age of the comet, that is, how long it has been on its current orbit.

## 6.2 Assumptions and Limitations of the Finson-Probstein Method

The dynamical modeling technique used throughout this dissertation, known as Finson-Probstein modeling, is a simple, yet powerful, tool that can give good estimates of the sizes and ages of cometary dust tail particles. However, in its simplicity, it makes a number of assumptions and approximations about the true complex nature of cometary dust. The first assumption is that the only forces acting upon the dust are solar radiation pressure and solar gravity. While this has proven to be a good approximation for many comets, there are some comets (e.g., Hale-Bopp, [Kramer et al., 2014]) which require the use of the Lorentz force to explain the motion of the dust particles. Additionally, the model assumes that the dust particles leave the surface of the comet with zero relative velocity, which we know to not be true. This limitation is ameliorated by the fact that, at the large scales used in this analysis, adding an initial velocity to the particles only widens the the tail rather than changing its shape [Lisse et al., 1998]. Furthermore, the best-fit models described in Section 4.2 only show a single best-fit $\beta$ value and particle age, while a real comet emits a range of particle sizes over a period of time.

Despite these limitations, this modeling technique does an excellent job of estimating the sizes and ages of dust particles in comets with a wide range of dust tail morphologies and particle characteristics. The power of this data set lies in its large size, which can smooth over some of the limitations of this modeling technique. Because the technique is applied uniformly across the data set, any biases are applied uniformly, thereby increasing the robustness of the results.

## 6.3 The NEOWISE Reactivation Mission

In August 2013, the WISE mission was restarted as NEOWISE, with the renewed goal of detecting and characterizing more small bodies, including near-earth objects, other asteroids, and comets. The shortest two wavelength bands, W1 and W2, remain operational. The spacecraft will continue to collect data for about 3 years, after which time its orbit will have decayed to the point where scattered sunlight will compromise the image quality. Since late December 2013, the spacecraft has restarted its all-sky survey, and has discovered many new objects, including (as of this writing) two comets. Based on the number of comets detected in W1 and W2 during the prime WISE mission, we expect that at least 40 comets will be imaged per year, for a total of about 120 over the course of the extended mission. Since the thermal flux from the dust is much lower in W1 and W2 than W3 and W4, we expect

that we will not see nearly as many significant dust tails in the new comets. However, we will still be able to constrain dust and gas production rate, as well as nucleus signal. Data for comet C/2009 K5 (Section 4.2.1.15 and Figure 4.16), presented in this dissertation, was collected during the post-cryogenic phase of the WISE mission in October 2010, and is an example of the quality of the results that may be obtained for particularly bright comets seen by NEOWISE during the extended mission.

## 6.4 Other cometary studies

When we consider the results presented in this dissertation and consider the future of cometary sciences, it becomes clear that we are moving away from the historical paradigm of studying single objects and moving into the era of population studies. While in-depth analysis of individual objects can sometimes yield new insights, population studies allow us to finally begin to answer the question: what is a typical comet? At this point, it is still too early to say, but perhaps we can speculate as to the kinds of data which would might assist us in answering that question.

While the number of objects that were part of this study is large enough to yield some preliminary statistically significant results, an even larger data set, perhaps of 500+ comets, would help to solidify the results and might even yield some new insights. We have seen that

the LPCs nearly all tend to have strong emission close to perihelion, and that, while many SPCs also follow this trend, there may be a clustering of objects which have strong emission at ∼4-5 AU. Adding more objects to this analysis could help to strengthen the results we've obtained here, and perhaps yield insights as to why some of the SPCs exhibit behavior that is different from the rest of the population.

Another way to understand the nature of cometary activity would be to send a spacecraft to follow a comet as it passed through different thermal regimes on its orbital path. This is actually precisely the science goal of the *Rosetta* mission [Glassmeier et al., 2007], which coincidentally arrived at its target (67P/Churymov-Gerasimenko, hereafter 67P) on the day before this dissertation was turned in to the author's committee. The spacecraft will orbit 67P as it approaches perihelion, measuring and monitoring the comet as it passes through different thermal regimes using a suite of instruments. The instruments will give us an unprecedented, detailed view of the dust and gas environment in the coma, as well as on 67P's surface itself with the instruments on the *Philae* lander.

The *Rosetta* mission will help to give some "ground truth" to Earth-based telescopic observations, since the comet was well-characterized before the spacecraft arrived. As we learn how 67P changes during the course of its orbit, we will be able to put previously-obtained remote sensing observations (such as the ones described in Section 4.2.2.5) into context. This mission will also help to answer one of the fundamental questions of cometary

science: how refractory materials on the nucleus are lifted off the surface and implanted into the coma and eventually the dust tail.

Perhaps the most powerful studies will be those with in-depth spacecraft analysis of single objects tied with broad population studies. The population study allows the details of individual comets to be averaged out, while the spacecraft mission allows a detailed understanding of a single object. We expect that the results of the *Rosetta* mission will help to move the field of cometary science in that direction.

The most likely scenario is that fully understanding cometary dust will require a combination of the methods described here, and perhaps even new methods that are yet to be developed. What we can say for sure it that the field is rapidly evolving, and our understanding of the nature of cometary dust continues to grow with each new population study, including the one presented in this dissertation.

# REFERENCES

M. F. Ahearn, D. G. Schleicher, R. L. Millis, P. D. Feldman, and D. T. Thompson. Comet Bowell 1980b. *AJ*, 89:579–591, April 1984. doi: 10.1086/113552.

M. F. A'Hearn, R. C. Millis, D. O. Schleicher, D. J. Osip, and P. V. Birch. The ensemble properties of comets: Results from narrowband photometry of 85 comets, 1976-1992. *Icarus*, 118:223–270, December 1995. doi: 10.1006/icar.1995.1190.

M. F. A'Hearn, M. J. S. Belton, W. A. Delamere, L. M. Feaga, D. Hampton, J. Kissel, K. P. Klaasen, L. A. McFadden, K. J. Meech, H. J. Melosh, P. H. Schultz, J. M. Sunshine, P. C. Thomas, J. Veverka, D. D. Wellnitz, D. K. Yeomans, S. Besse, D. Bodewits, T. J. Bowling, B. T. Carcich, S. M. Collins, T. L. Farnham, O. Groussin, B. Hermalyn, M. S. Kelley, M. S. Kelley, J.-Y. Li, D. J. Lindler, C. M. Lisse, S. A. McLaughlin, F. Merlin, S. Protopapa, J. E. Richardson, and J. L. Williams. EPOXI at Comet Hartley 2. *Science*, 332:1396–, June 2011. doi: 10.1126/science.1204054.

J. M. Bauer, R. G. Walker, A. K. Mainzer, J. R. Masiero, T. Grav, J. W. Dailey, R. S. McMillan, C. M. Lisse, Y. R. Fernández, K. J. Meech, J. Pittichova, E. K. Blauvelt, F. J.

Masci, M. F. A'Hearn, R. M. Cutri, J. V. Scotti, D. J. Tholen, E. DeBaun, A. Wilkins, E. Hand, E. L. Wright, and WISE Team. WISE/NEOWISE Observations of Comet 103P/Hartley 2. *ApJ*, 738:171, September 2011. doi: 10.1088/0004-637X/738/2/171.

J. M. Bauer, E. Kramer, A. K. Mainzer, R. Stevenson, T. Grav, J. R. Masiero, R. G. Walker, Y. R. Fernández, K. J. Meech, C. M. Lisse, P. R. Weissman, R. M. Cutri, J. W. Dailey, F. J. Masci, D. J. Tholen, G. Pearman, E. L. Wright, and WISE Team. WISE/NEOWISE Preliminary Analysis and Highlights of the 67p/Churyumov-Gerasimenko near Nucleus Environs. *ApJ*, 758:18, October 2012. doi: 10.1088/0004-637X/758/1/18.

N. Biver, D. Bockelée-Morvan, J. Crovisier, P. Colom, F. Henry, R. Moreno, G. Paubert, D. Despois, and D. C. Lis. Chemical Composition Diversity Among 24 Comets Observed At Radio Wavelengths. *Earth Moon and Planets*, 90:323–333, March 2002.

N. Biver, D. Bockelée-Morvan, P. Colom, J. Crovisier, G. Paubert, A. Weiss, and H. Wiesemeyer. Molecular investigations of comets C/2002 X5 (Kudo-Fujikawa), C/2002 V1 (NEAT), and C/2006 P1 (McNaught) at small heliocentric distances. *A&A*, 528:A142, April 2011. doi: 10.1051/0004-6361/201016250.

A. P. Boss. Temperatures in Protoplanetary Disks. *Annual Review of Earth and Planetary Sciences*, 26:53–80, 1998. doi: 10.1146/annurev.earth.26.1.53.

J. A. Burns, P. L. Lamy, and S. Soter. Radiation forces on small particles in the solar system. *Icarus*, 40:1–48, October 1979. doi: 10.1016/0019-1035(79)90050-2.

L. Colangeli, E. Bussoletti, C. C. Pestellini, M. Fulle, V. Mennella, P. Palumbo, and A. Rotundi. ISOCAM Imaging of Comets 65P/Gunn and 46P/Wirtanen. *Icarus*, 134:35–46, July 1998. doi: 10.1006/icar.1998.5944.

J. Crovisier, N. Biver, D. Bockelée-Morvan, J. Boissier, P. Colom, and D. C. Lis. The Chemical Diversity of Comets: Synergies Between Space Exploration and Ground-based Radio Observations. *Earth Moon and Planets*, 105:267–272, September 2009. doi: 10.1007/s11038-009-9293-z.

L. Dones, P. R. Weissman, H. F. Levison, and M. J. Duncan. Oort Cloud Formation and Dynamics. In D. Johnstone, F. C. Adams, D. N. C. Lin, D. A. Neufeeld, and E. C. Ostriker, editors, *Star Formation in the Interstellar Medium: In Honor of David Hollenbach*, volume 323 of *Astronomical Society of the Pacific Conference Series*, page 371, December 2004.

M. Duncan, H. Levison, and L. Dones. *Dynamical evolution of ecliptic comets*, pages 193–204. 2004.

E. Epifani, L. Colangeli, M. Fulle, J. R. Brucato, E. Bussoletti, M. C. De Sanctis, V. Mennella, E. Palomba, P. Palumbo, and A. Rotundi. ISOCAM Imaging of Comets

103P/Hartley 2 and 2P/Encke. *Icarus*, 149:339–350, February 2001. doi: 10.1006/icar.2000.6546.

Y. R. Fernández, J. M. Bauer, N. H. Samarasinha, T. Grav, A. K. Mainzer, J. R. Masiero, B. E.A. Mueller, R. G. Walker, L. M. Woodney, C. M. Lisse, and K. J. Meech. Characterization of the nucleus, coma, and outbursts of comet 29p/schwassmann-wachmann 1. In *Asteroids, Comets and Meteors*, 2012.

M. C. Festou, H. U. Keller, and H. A. Weaver. *A brief conceptual history of cometary science*, pages 3–16. 2004.

M. J. Finson and R. F. Probstein. A theory of dust comets. I. Model and equations. *ApJ*, 154:327–352, October 1968. doi: 10.1086/149761.

K.-H. Glassmeier, H. Boehnhardt, D. Koschny, E. Kührt, and I. Richter. The Rosetta Mission: Flying Towards the Origin of the Solar System. *Space Sci. Rev.*, 128:1–21, February 2007. doi: 10.1007/s11214-006-9140-8.

R. Gomes, H. F. Levison, K. Tsiganis, and A. Morbidelli. Origin of the cataclysmic Late Heavy Bombardment period of the terrestrial planets. *Nature*, 435:466–469, May 2005. doi: 10.1038/nature03676.

O. Hainaut, R. M. West, B. G. Marsden, A. Smette, and K. Meech. Post-perihelion observations of comet P/Halley. IV. r=16.6 and 18.8AU. *A&A*, 293:941–947, January 1995.

O. R. Hainaut, A. Delsanti, K. J. Meech, and R. M. West. Post-perihelion observations of comet 1P/Halley. V: $r_h$ = 28.1 AU. *A&A*, 417:1159–1164, April 2004. doi: 10.1051/0004-6361:20035658.

M. S. Kelley, Y. R. Fernández, J. Licandro, C. M. Lisse, W. T. Reach, M. F. A'Hearn, J. Bauer, H. Campins, A. Fitzsimmons, O. Groussin, P. L. Lamy, S. C. Lowry, K. J. Meech, J. Pittichová, C. Snodgrass, I. Toth, and H. A. Weaver. The persistent activity of Jupiter-family comets at 3-7 AU. *Icarus*, 225:475–494, July 2013. doi: 10.1016/j.icarus.2013.04.012.

K. E. Kraemer, C. M. Lisse, S. D. Price, D. Mizuno, R. G. Walker, T. L. Farnham, and T. Mäkinen. Midcourse Space Experiment Observations of Small Solar System Bodies. *AJ*, 130:2363–2382, November 2005. doi: 10.1086/444536.

E. A. Kramer, Y. R. Fernandez, J. M. Bauer, R. A. Stevenson, A. K. Mainzer, T. Grav, J. Masiero, R. G. Walker, C. M. Lisse, and The WISE Team. WISE/NEOWISE Observations of WISE/NEOWISE-discovered Cometary Dust Tails. In *AAS/Division for Planetary Sciences Meeting Abstracts*, volume 45 of *AAS/Division for Planetary Sciences Meeting Abstracts*, page 413.12, October 2013.

E. A. Kramer, Y. R. Fernandez, C. M. Lisse, M. S. P. Kelley, and L. M. Woodney. A dynamical analysis of the dust tail of Comet C/1995 O1 (Hale-Bopp) at high heliocentric

distances. *Icarus*, 236:136–145, July 2014. doi: 10.1016/j.icarus.2014.03.033.

H. F. Levison. Comet Taxonomy. In T. Rettig and J. M. Hahn, editors, *Completing the Inventory of the Solar System*, volume 107 of *Astronomical Society of the Pacific Conference Series*, pages 173–191, 1996.

H. F. Levison and M. J. Duncan. The long-term dynamical behavior of short-period comets. *Icarus*, 108:18–36, March 1994. doi: 10.1006/icar.1994.1039.

H. F. Levison, M. J. Duncan, R. Brasser, and D. E. Kaufmann. Capture of the Sun's Oort Cloud from Stars in Its Birth Cluster. *Science*, 329:187–190, June 2010. doi: 10.1126/science.1187535.

C. Lisse. On the Role of Dust Mass Loss in the Evolution of Comets and Dusty Disk Systems. *Earth Moon and Planets*, 90:497–506, June 2002. doi: 10.1023/A:1021519408600.

C. M. Lisse, M. F. A'Hearn, M. G. Hauser, T. Kelsall, D. J. Lien, S. H. Moseley, W. T. Reach, and R. F. Silverberg. Infrared Observations of Comets by COBE. *ApJ*, 496: 971–991, March 1998. doi: 10.1086/305397.

C. M. Lisse, Y. R. Fernández, M. F. A'Hearn, E. Grün, H. U. Käufl, D. J. Osip, D. J. Lien, T. Kostiuk, S. B. Peschke, and R. G. Walker. A tale of two very different comets: ISO and MSX measurements of dust emission from 126P/IRAS (1996) and 2P/Encke (1997). *Icarus*, 171:444–462, October 2004. doi: 10.1016/j.icarus.2004.05.015.

A. Mainzer, J. Bauer, T. Grav, J. Masiero, R. M. Cutri, J. Dailey, P. Eisenhardt, R. S. McMillan, E. Wright, R. Walker, R. Jedicke, T. Spahr, D. Tholen, R. Alles, R. Beck, H. Brandenburg, T. Conrow, T. Evans, J. Fowler, T. Jarrett, K. Marsh, F. Masci, H. McCallon, S. Wheelock, M. Wittman, P. Wyatt, E. DeBaun, G. Elliott, D. Elsbury, T. Gautier, IV, S. Gomillion, D. Leisawitz, C. Maleszewski, M. Micheli, and A. Wilkins. Preliminary Results from NEOWISE: An Enhancement to the Wide-field Infrared Survey Explorer for Solar System Science. *ApJ*, 731:53, April 2011. doi: 10.1088/0004-637X/731/1/53.

A. K. Mainzer, P. Eisenhardt, E. L. Wright, F.-C. Liu, W. Irace, I. Heinrichsen, R. Cutri, and V. Duval. Preliminary design of the Wide-Field Infrared Survey Explorer (WISE). In H. A. MacEwen, editor, *UV/Optical/IR Space Telescopes: Innovative Technologies and Concepts II*, volume 5899 of *Society of Photo-Optical Instrumentation Engineers (SPIE) Conference Series*, pages 262–273, August 2005. doi: 10.1117/12.611774.

F. J. Masci and J. W. Fowler. AWAIC: A WISE Astronomical Image Co-adder. In D. A. Bohlender, D. Durand, and P. Dowler, editors, *Astronomical Data Analysis Software and Systems XVIII*, volume 411 of *Astronomical Society of the Pacific Conference Series*, page 67, September 2009.

D. Matson, editor. *The IRAS Asteroid and Comet Survey: Preprint Version No. 1.* JPL D-3698, 1986.

K. J. Meech and J. Svoren. *Using cometary activity to trace the physical and chemical evolution of cometary nuclei*, pages 317–335. 2004.

A. Morbidelli, H. F. Levison, K. Tsiganis, and R. Gomes. Chaotic capture of Jupiter's Trojan asteroids in the early Solar System. *Nature*, 435:462–465, May 2005. doi: 10.1038/nature03540.

T. G. Müller, P. Ábrahám, and J. Crovisier. Comets, Asteroids and Zodiacal Light as Seen by Iso. *Space Sci. Rev.*, 119:141–155, August 2005. doi: 10.1007/s11214-005-8067-9.

M. J. Mumma and S. B. Charnley. The Chemical Composition of CometsEmerging Taxonomies and Natal Heritage. *ARA&A*, 49:471–524, September 2011. doi: 10.1146/annurev-astro-081309-130811.

M. J. Mumma, P. R. Weissman, and S. A. Stern. Comets and the origin of the solar system - Reading the Rosetta Stone. In E. H. Levy and J. I. Lunine, editors, *Protostars and Planets III*, pages 1177–1252, 1993.

M. J. Mumma, B. P. Bonev, G. L. Villanueva, L. Paganini, M. A. DiSanti, E. L. Gibb, J. V. Keane, K. J. Meech, G. A. Blake, R. S. Ellis, M. Lippi, H. Boehnhardt, and K. Magee-Sauer. Temporal and Spatial Aspects of Gas Release During the 2010 Apparition of Comet 103P/Hartley 2. *ApJ*, 734:L7, June 2011. doi: 10.1088/2041-8205/734/1/L7.

T. Ootsubo, H. Kawakita, S. Hamada, H. Kobayashi, M. Yamaguchi, F. Usui, T. Nakagawa, M. Ueno, M. Ishiguro, T. Sekiguchi, J.-i. Watanabe, I. Sakon, T. Shimonishi, and T. Onaka. AKARI Near-infrared Spectroscopic Survey for $CO_2$ in 18 Comets. *ApJ*, 752:15, June 2012. doi: 10.1088/0004-637X/752/1/15.

D. Prialnik and A. Bar-Nun. On the evolution and activity of cometary nuclei. *ApJ*, 313: 893–905, February 1987. doi: 10.1086/165029.

W. T. Reach, M. S. Kelley, and M. V. Sykes. A survey of debris trails from short-period comets. *Icarus*, 191:298–322, November 2007. doi: 10.1016/j.icarus.2007.03.031.

W. T. Reach, M. S. Kelley, and J. Vaubaillon. Survey of cometary $CO_2$, CO, and particulate emissions using the Spitzer Space Telescope. *Icarus*, 226:777–797, September 2013. doi: 10.1016/j.icarus.2013.06.011.

D. O. Schleicher and A. Bair. Chemical and physical properties of comets in the lowell database: Results from 35 years of narrow-band photometry. In *Asteroids, Comets and Meteors*, 2014.

R. Stevenson, J. M. Bauer, E. A. Kramer, T. Grav, A. K. Mainzer, and J. R. Masiero. Lingering Grains of Truth around Comet 17P/Holmes. *ApJ*, 787:116, June 2014. doi: 10.1088/0004-637X/787/2/116.

M. V. Sykes and R. G. Walker. Cometary dust trails. I - Survey. *Icarus*, 95:180–210, February 1992. doi: 10.1016/0019-1035(92)90037-8.

M. V. Sykes, L. A. Lebofsky, D. M. Hunten, and F. Low. The discovery of dust trails in the orbits of periodic comets. *Science*, 232:1115–1117, May 1986. doi: 10.1126/science.232.4754.1115.

G. M. Szabó, L. L. Kiss, and K. Sárneczky. Cometary Activity at 25.7 AU: Hale-Bopp 11 Years after Perihelion. *ApJ*, 677:L121–L124, April 2008. doi: 10.1086/588095.

G. M. Szabó, K. Sárneczky, and L. L. Kiss. Frozen to death? Detection of comet Hale-Bopp at 30.7 AU. *A&A*, 531:A11, July 2011. doi: 10.1051/0004-6361/201116793.

K. J. Walsh, A. Morbidelli, S. N. Raymond, D. P. O'Brien, and A. M. Mandell. Populating the asteroid belt from two parent source regions due to the migration of giant planets"The Grand Tack". *Meteoritics and Planetary Science*, 47:1941–1947, December 2012. doi: 10.1111/j.1945-5100.2012.01418.x.

E. L. Wright, P. R. M. Eisenhardt, A. K. Mainzer, M. E. Ressler, R. M. Cutri, T. Jarrett, J. D. Kirkpatrick, D. Padgett, R. S. McMillan, M. Skrutskie, S. A. Stanford, M. Cohen, R. G. Walker, J. C. Mather, D. Leisawitz, T. N. Gautier, III, I. McLean, D. Benford, C. J. Lonsdale, A. Blain, B. Mendez, W. R. Irace, V. Duval, F. Liu, D. Royer, I. Heinrichsen, J. Howard, M. Shannon, M. Kendall, A. L. Walsh, M. Larsen, J. G. Cardon, S. Schick,

M. Schwalm, M. Abid, B. Fabinsky, L. Naes, and C.-W. Tsai. The Wide-field Infrared Survey Explorer (WISE): Mission Description and Initial On-orbit Performance. *AJ*, 140: 1868, December 2010. doi: 10.1088/0004-6256/140/6/1868.

B. Yang and G. Sarid. Crystalline Water Ice In Outburst Comet P/2010 H2. In *AAS/Division for Planetary Sciences Meeting Abstracts #42*, volume 42 of *Bulletin of the American Astronomical Society*, page 951, October 2010.